Dynamics and Precursor Signs for Phase Transitions in Neural Systems

A thesis

submitted in fulfilment

of the requirements for the degree

of

Doctor of Philosophy

at

The University of Waikato

by

Ehsan Negahbani

THE UNIVERSITY OF
WAIKATO
Te Whare Wānanga o Waikato

March 2015

Abstract

This thesis investigates neural state transitions associated with sleep, seizure and anaesthesia. The aim is to address the question: How does a brain traverse the critical threshold between distinct cortical states, both healthy and pathological? Specifically we are interested in sub-threshold neural behaviour immediately prior to state transition. We use theoretical neural modelling (single spiking neurons, a network of these, and a mean-field continuum limit) and *in vitro* experiments to address this question.

Dynamically realistic equations of motion for thalamic relay neuron, reticular nuclei, cortical pyramidal and cortical interneuron in different vigilance states are developed, based on the Izhikevich spiking neuron model. A network of cortical neurons is assembled to examine the behaviour of the gamma-producing cortical network and its transition to lower frequencies due to effect of anaesthesia. Then a three-neuron model for the thalamocortical loop for sleep spindles is presented. Numerical simulations of these networks confirms spiking consistent with reported *in vivo* measurement results, and provides supporting evidence for precursor indicators of imminent phase transition due to occurrence of individual spindles.

To complement the spiking neuron networks, we study the Wilson–Cowan neural mass equations describing homogeneous cortical columns and a 1D spatial cluster of such columns. The abstract representation of cortical tissue by a pair of coupled integro-differential equations permits thorough linear stability, phase plane and bifurcation analyses. This model shows a rich set of spatial and temporal bifurcations marking the boundary to state transitions: saddle-node, Hopf, Turing, and mixed Hopf–Turing. Close to state transition, white-noise-induced subthreshold fluctuations show clear signs of critical slowing down with prolongation and strengthening of autocorrelations, both in time and space, irrespective of bifurcation type.

Attempts at *in vitro* capture of these predicted leading indicators form the last part of the thesis. We recorded local field potentials (LFPs) from cortical and hippocampal slices of mouse brain. State transition is marked by the emergence and cessation of spontaneous seizure-like events (SLEs) induced by bathing the slices in an artificial cerebral spinal fluid containing no magnesium ions. Phase-plane analysis of the LFP time-series suggests that distinct bifurcation

classes can be responsible for state change to seizure. Increased variance and growth of spectral power at low frequencies ($f < 15$ Hz) was observed in LFP recordings prior to initiation of some SLEs. In addition we demonstrated prolongation of electrically evoked potentials in cortical tissue, while forwarding the slice to a seizing regime. The results offer the possibility of capturing leading temporal indicators prior to seizure generation, with potential consequences for understanding epileptogenesis.

Guided by dynamical systems theory this thesis captures evidence for precursor signs of phase transitions in neural systems using mathematical and computer-based modelling as well as *in vitro* experiments.

Dedication

I dedicate this thesis—

To my wife Mahsa for her love and countless supports

To my parents Mr. Hosseingholi Negahbani and Ms. Anvar Abdollahi for their endless love

And to my sister Mahnaz for her encouragements.

Acknowledgements

First and foremost, I would like to express my gratitude to my chief supervisor, Associate Professor D. Alistair Steyn-Ross. His knowledge and passion in physics and neural modelling motivated me to do this PhD. Alistair's great creativity, endless patience and ongoing supports made it possible to overcome difficult aspects of my research and discover its interesting parts. Thank you Professor Jamie Sleigh for opening the fascinating neuroscience world to my eyes. My sincere thanks go to Professor Moira L. Steyn-Ross for her guidance through theoretical analysis of mean-field models of this thesis. I would like to also thank Dr Marcus T. Wilson for his valuable comments about the manuscript of thesis, and Dr Logan Voss for training me the *in vitro* electrophysiology techniques.

I would also like to acknowledge the Marsden Fund of Royal Society of New Zealand for a PhD scholarship, and the Fisher and Paykel Healthcare for a study award.

Contents

List of Figures

List of Tables

Acronyms and Abbreviations

1-D, 2-D one-dimensional, two-dimensional

AAS ascending activating system

AMPA α-amino-3-hydroxy-5-methyl-4 isoxazole propionic acid (a fast excitatory neurotransmitter)

AP action potential

aCSF artificial cerebrospinal fluid

CSD critical slowing down

CSF cerebrospinal fluid

EEG electroencephalogram

EP evoked potential

EPSC excitatory postsynaptic current

EPSP excitatory postsynaptic potential

FFT fast Fourier transform

FS fast-spiking cortical inhibitory interneuron

GABA γ-aminobutyric acid (an inhibitory neurotransmitter)

HH Hodgkin-Huxley

IPSC inhibitory postsynaptic current

IPSP inhibitory postsynaptic potential

LFP local field potential

PSP postsynaptic potential

rms root-mean square

RS regular-spiking (an excitatory pyramidal cortical neuron)

RTn reticular thalamic nucleus inhibitory neuron

SLE seizure-like event

TC thalamocortical relay excitatory neuron

WC Wilson–Cowan

Chapter 1

Preamble

Thesis overview

This thesis is a report of comprehensive theoretical, computer-based and *in vitro* investigations to identify early signs of phase transitions in neural systems.

The thesis proceeds as follows.

Chapter 2 starts with an overview of the basic principles of neurophysiology, and the functional structure of cortex and thalamus. The underlying mechanism of anaesthesia-induced transformation of electroencephalogram (EEG) to lower frequencies, sleep spindles and burst suppression pattern are described. These neural phenomena are of interest since, from dynamical systems point of view, their occurrence is mediated by a phase transition. We discuss the various modelling approaches employed in the thesis, and give a brief survey of phase transitions observed in a diverse range of dynamical systems in ecology, climate records, dielectrics, cancer, neural models and *in vivo* measurements.

In **Chapter 3** I extend previous work on the subthreshold behaviour of the H. R. Wilson cubic spiking neuron. My theoretical and numerical examinations reveal an increase in spectral power of the fluctuations of soma voltage prior to firing of an action potential (AP), providing an early warning indication of phase transition. I then apply a similar fluctuation analysis to the Izhikevich neuron, a simplified quadratic model with manual reset on spiking, examining the voltage response for signs of precursor warning signals. Four neural types are studied in detail: cortical regular spiking (RS), cortical fast spiking (FS), thalamic relay (TC), and reticular thalamic nucleus (RTn) neurons. These neurons are of interest since they are the major neural types of cortex and thalamus, and play important role in generation of gamma and spindle oscillations. The original Izhikevich models are modified to produce certain brain rhythms: RS neuron is modified to demonstrate burst-suppression pattern; a hyperpolarization activated cation current (I_h) is introduced into TC neuron to make it a spindle pace-maker; the RTn neuron is modified to burst in response to incoming excitations when it is hyperpolarized. The

dynamics of these models are studied in detail, and precursor signs of phase transition (AP firing or bursting) demonstrated.

Using the spiking neurons developed in Chapter 3, **Chapter 4** presents evidence of early warnings of phase transitions in two population-induced neural phenomena: Transition from gamma to low frequency oscillations in the cortex due to induction of anaesthesia, and generation of sleep spindles in a thalamocortical network. Bistability and flickering prior to transition to low frequency oscillations, and increased variance of voltage fluctuations prior to initiation of a spindle, are observed in these networks.

Complementing the spiking neural modelling of Chapters 3 and 4, **Chapter 5** presents a detailed study of a mean-field neural model. The dynamical behaviour of the Wilson–Cowan (WC) equations of a homogeneous (space independent) cortex and its possible phase transitions are investigated, and clear signs of critical slowing down are observed prior to state transitions. This continuum model supports both numerical and analytical subthreshold investigations, with simulation results confirming theoretical predictions.

Chapter 6 studies the dynamics of the WC cortical rod. The introduction of space gives rich dynamical behaviour arising from a range of temporal, spatial and spatiotemporal instabilities mediated by distinct bifurcations: temporal Hopf and saddle-node bifurcations, spatial Turing instability, and spatiotemporal Turing-Hopf or mixed mode interaction. Clear signs of critical slowing down in time and space are demonstrated, both theoretically and numerically, close to bifurcation.

Chapter 7 reports a series of *in vitro* experiments in which I was looking for precursor signs of phase transitions in living neural tissue. Artificially induced seizure-like events (SLEs) are selected as an exemplar a neural phase transition. These events can be recorded extracellularly from cortical and hippocampal regions of mouse brain slice, when bathed in a zero-magnesium solution. This chapter elucidates the methodology required for acquiring SLEs with high fidelity frequency content, and demonstrates promising preliminary evidences of increased variance, spectral power in low frequencies, and flickering prior to initiation of individual SLEs. The chapter concludes with a report of prolongation of evoked potentials in cortical slices during slow approach to a seizing mode brought on by gradual washing out of magnesium ions in the bath solution. To my knowledge these preliminary results are the first reported observations of critical slowing down in an *in vitro* neural system.

In **Appendices** I present the verification of wave equations in 1-D Wilson–Cowan rod, details for *in vitro* methods, and MATLAB codes for implementing Whittaker smoother and automatic spindle extractor. All the source codes developed for this thesis are accessible from Research Commons, the open access digital repository of the University of Waikato, New Zealand.

Original contributions

The numerical calculations, theoretical analysis, related computer codes, design and conduction of *in vitro* experiments, analysis and interpretation of experimental results, and most graphic presentations are my own work, except:

- I used MATLAB codes written by D. A. Steyn-Ross to numerically locate the intersections of nullclines of homogeneous WC model of Section 5.2.2.
- M. L. Steyn-Ross developed the theoretical framework for the homogeneous WC model and WC rod.
- L. J. Voss designed and carried out the evoked potential experiments of Section 7.4.

Conference presentations

- E. Negahbani, D.A. Steyn-Ross, J.W Sleigh, M.L. Steyn-Ross, and M.T. Wilson. Theory of dynamical systems describes experimentally observed hippocampal seizure-like events, *Neuroscience 2013*, San Diego, California, USA, Nov 2013
- E. Negahbani, D.A. Steyn-Ross, J.W Sleigh, M.L. Steyn-Ross, and M.T. Wilson. Noise and stimulus-induced leading indicators of state transitions, *The 6th International Workshop on Seizure Prediction*, San Diego, California, USA, Nov 2013
- E. Negahbani, D.A. Steyn-Ross, J.W Sleigh, M.L. Steyn-Ross, and M.T. Wilson. A three-neuron thalamocortical model describes sleep-wake transition of brain, *20th Australian Institute of Physics Congress*, Sydney, Australia, Dec 2012
- E. Negahbani, D.A. Steyn-Ross, M.L. Steyn-Ross, M.T. Wilson, J.W Sleigh, and L. J. Voss. Computational model of anaesthetized cortical area, *New Zealand Institute of Physics Congress*, Wellington, New Zealand, Oct 2011
- E. Negahbani, D.A. Steyn-Ross, M.L. Steyn-Ross, J.W Sleigh, and M.T. Wilson. Hysteresis in single neurons and neural population models, *Mathematical Neuroscience*, Edinburgh, Scotland, Apr 2011
- E. Negahbani, D.A. Steyn-Ross, M.L. Steyn-Ross, J.W Sleigh, and M.T. Wilson. Spectral analysis of epileptic activity in rodent brain slice, *28th International Australian Winter Conference on Brain Research*, Wanaka, New Zealand, Aug 2010
- E. Negahbani, D.A. Steyn-Ross, M.L. Steyn-Ross, J.W Sleigh, and M.T. Wilson. Examining the H.R. Wilson spiking-neuron model: What happens during the time leading up to a spike?, *New Zealand Postgraduate Conference*, Victoria University, Wellington, New Zealand, Nov 2009

Chapter 2

Overview

2.1 Basic neurophysiology

2.1.1 Neurons and synaptic interactions

The central nervous system—including the brain, spinal cord, and peripheral sensory system—is composed of principal cellular elements called *neurons*. Three major structural elements can be identified on a generic neuron (see Fig. 2.1): a *soma* or *cell body* which contains the nucleus of the cell; a treelike *dendrite* structure which samples signals from other neurons and integrates them at the soma; and a fibre or *axon* which transfers neural signals to the other neurons via axon-dendrite points of contact called *synapses*.

Neurons are *excitable* cells which are specialized for the formation, modification and propagation of neural electrical signals. These signals originate from *voltage-sensitive* or *ion-selective* ionic channels located on the membrane. The selective opening and closing of these channels alters the internal ionic concentrations and perturbs the potential difference across the membrane, resulting in intra- and extra-cellular currents. In the quiescent resting state, the neuron interior carries a net negative charge relative to the extracellular space. This charge separation is produced by the ongoing action of sodium/potassium pumps that maintain a *resting membrane potential* of about -60 mV (ranging from -40 to -75 mV in different neurons [Kandel *et al.*, 2000]). A decrease or increase in soma potential relative to rest is called *hyperpolarization* and *depolarization* respectively.

Depolarization of a neuron to a *threshold* level (usually about 15 mV above rest) activates (opens) voltage-sensitive Na^+ channels in the soma membrane, allowing an influx of sodium ions which further depolarize the cell with an accelerating positive feedback leading to generation of an *action potential* (AP) manifest as a sudden jump in membrane potential from -60 mV to about $+50$ mV, the Na^+ equilibrium potential. The membrane voltage then rapidly repolarizes towards resting voltage because of activation of voltage-sensitive K^+ channels (leading to K^+ efflux) coupled with the slow inactivation of Na^+ channels [Kandel *et al.*, 2000].

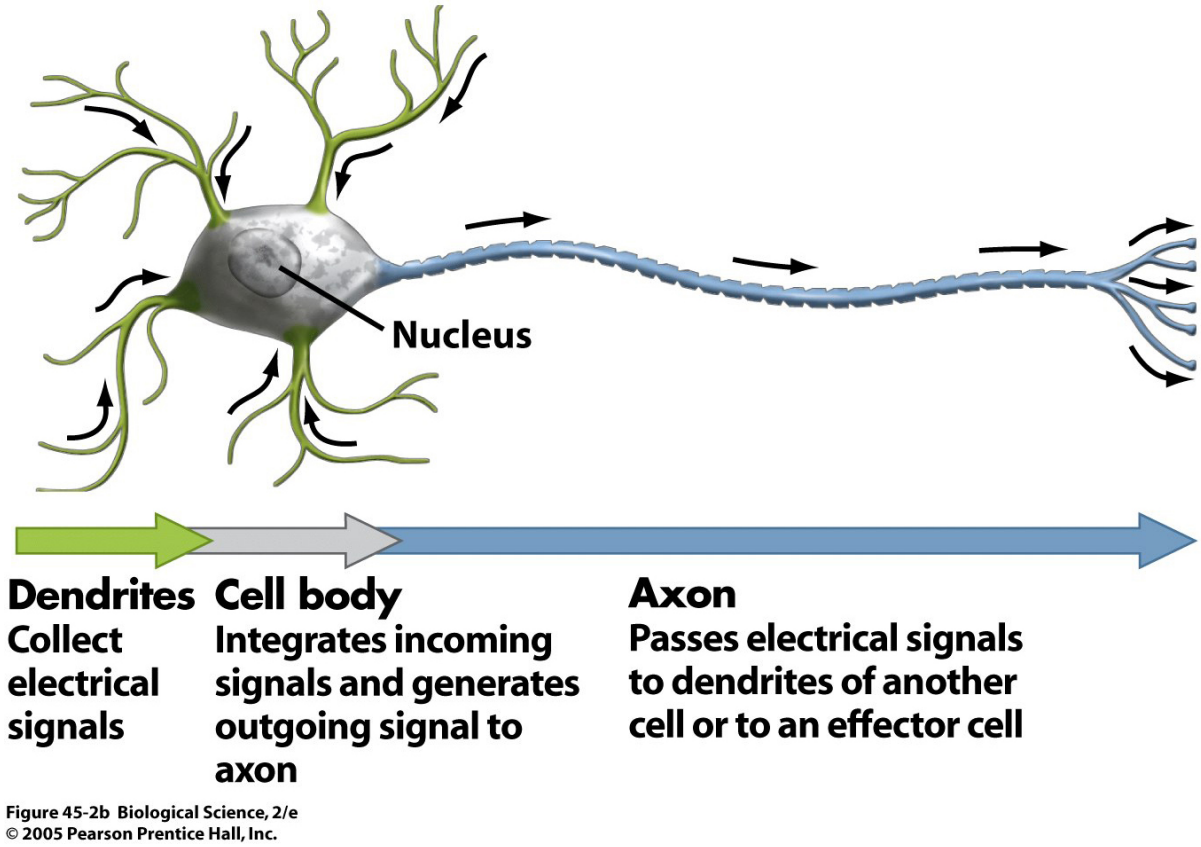

Figure 2.1: Anatomical structure of a generic neuron and the flow of information. The neuron is composed of three main parts: cell body or soma, dendritic tree and the axonal fibre. Image from Freeman *et al.* [2005].

Action potentials are actively transmitted down the axonal fibre towards the synaptic terminals. Synapses are the junctions providing the communication link between neurons (or between a neuron and a muscle cell). Synaptic transmission can be either electrical or chemical, meaning that the neural communication occurs via directly coupled electrical currents, or indirectly through mediation by chemical *neurotransmitters*. Only the chemical synapses are studied in this thesis. Synaptic communication is illustrated in Fig. 2.2. The arrival of an AP causes neurotransmitter release into the synaptic cleft. These neurotransmitters bind to proteins that open ionic channels embedded in the *postsynaptic* neuron, producing postsynaptic currents (PSCs) through, and postsynaptic voltages (PSPs) across, the postsynaptic membrane.

Depending on the type of released neurotransmitters, specific ion channels are activated at the postsynaptic site. If the activity of the presynaptic neuron induces positive-going PSCs in the postsynaptic neuron, then the synapse (and the presynaptic neuron) is declared to be *excitatory*. In contrast, an *inhibitory* synapse (or its presynaptic neuron) suppresses its target by inducing hyperpolarizing PSCs. GABA (γ-aminobutyric acid)—with fast $GABA_A$ and slow $GABA_B$ subtypes—is the major inhibitory neurotransmitter in the central nervous system,

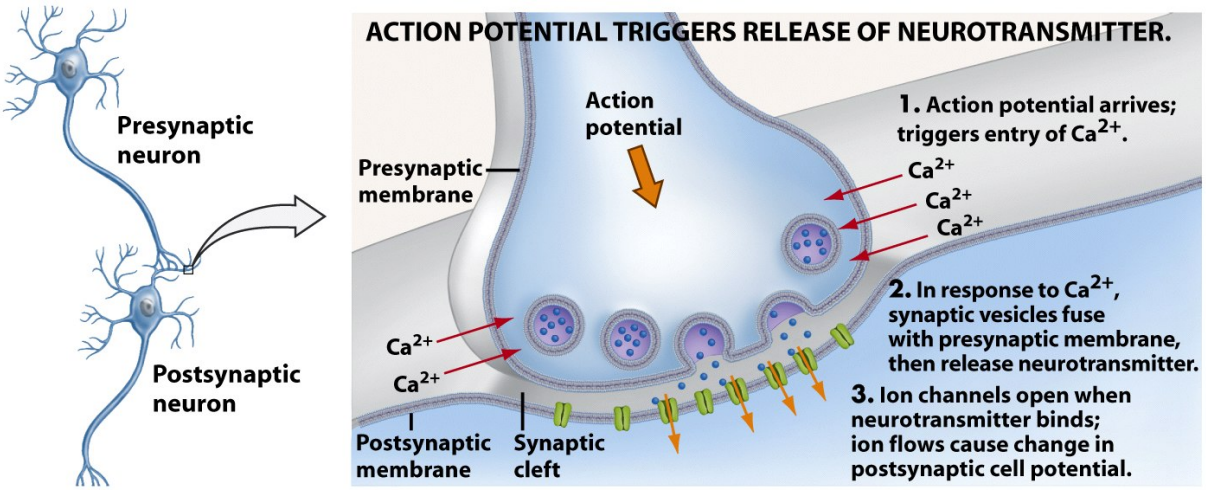

Figure 2.2: Neural communication through a chemical synapse. The action from the presynaptic neuron causes release of neurotransmitters into the synaptic cleft, activating ion channels in the postsynaptic membrane, producing excitatory or inhibitory postsynaptic currents. Image from Freeman *et al.* [2005].

while AMPA (α-amino-3-hydroxy-5-methyl-4-isoxazolepropionic acid) and NMDA (N-methyl-D-aspartate acid) are the main fast and slow excitatory neurotransmitters respectively.

2.1.2 Structure of cortex and thalamus

Human cortex is composed of about 10^{10} excitatory and inhibitory strongly interacting neurons. The cortex is 2–3 mm thick and is often modelled as a set of functional columns[1] oriented perpendicular to the cortical surface. It is traditionally assumed that each column is composed of six layers, numbered from outside to inside. About 80% of cortical neurons are excitatory pyramidal neurons, while the rest are mainly inhibitory interneurons [Braitenberg and Schüz, 1991]. The dendritic trees of pyramidal neurons tend to be aligned in parallel pathways perpendicular to the scalp surface; consequently the flow of synaptic currents in these dendrites form electrical dipoles which are believed to be the source of the electroencephalogram (EEG) signal [Nunez and Srinivasan, 2006]. The random orientation of the dendrite structures of interneurons makes their currents unlikely to play a primary role in EEG formation.

The thalamus is a neural structure at the centre of the brain that is considered traditionally to be a gateway that modulates the flow of sensory information to the cortex. The modern view identifies two additional roles: the last bottleneck for sensory information processing before cortex, via modulatory pathways which feed the thalamus, and participation in higher-order information processing within the cortico-thalamo-cortical feedback loop [Sherman, 2006]. Thalamus also plays important roles in normal or pathological brain rhythms such as slow (0.2–1 Hz)

[1] an organized assembly of excitatory and inhibitory neurons acting cooperatively within a small colume of the cortex

and spindle oscillations [Steriade and Timofeev, 2003]), and spike-and-wave oscillations during epileptic seizures [Granger and Hearn, 2007].

Thalamus is composed of several nuclei, each with distinctive functionality specified in terms of their incoming sensory inputs and targets on layer 6 of neocortex [Sherman and Guillery, 2001]. The three main thalamic subtypes are: excitatory thalamocortical (TC) *relay* neurons that project information to the cortex; inhibitory *reticular nuclei* (RTn) neurons which inhibit the relay neurons; and local interneurons which also inhibit relay neurons.

TC neurons demonstrate two distinct firing patterns under normal waking and hyperpolarized sleep conditions[1]: tonic firing and bursting respectively [Sherman, 2001]. Since the number of spikes in each burst does not depend on the intensity or number of inputs to the neuron, in bursting mode TC cells do not normally transfer any input message to their output targets (depressed responsiveness). However, TC neurons transfer their incoming spikes to cortical targets with high fidelity during wake [Steriade and McCarley, 2005]. The frequency of their tonic response could be in the range of 10–30 Hz, while they show bursts of activity during non-rapid eye movement (NREM) sleep with intraburst frequency of about 200 Hz. A hyperpolarization of about 7–10 mV is normally observed in TC cells while undergoing NREM sleep [Steriade and McCarley, 2005].

2.2 Brain rhythmogenesis

2.2.1 Cortical gamma oscillations

Although cortical gamma oscillations (frequency range above 30 Hz) are thought to play an important role in cognitive tasks in an awake brain, their source has been a matter of debate for many years. Following the suggestion that gamma oscillations arise from the modulation of cortical pyramidal neurons by synchronous inhibition by cortical fast spiking interneurons [Buzsaki *et al.*, 1983; Lytton and Sejnowski, 1991], it has subsequently been proposed that gamma activity is an emergent property of the neural population, and is not due to a specific drive with gamma frequency [Knoblich, 2011]. Kopell *et al.* [2010] and Kann *et al.* [2014] describe the conditions for generation of cortical gamma oscillations:

- Cortical regular spiking (RS) pyramidal neurons are in their excitable regime, firing in response to incoming synaptic inputs from other neurons or brain-stem sources
- These firings excite their downstream fast spiking (FS) inhibitory interneurons, which in turn induce rebound spikes in their RS targets.

[1] The level of depolarization of the thalamic neurons depends on the neurotransmitter level of the ascending activating system (AAS) from brain stem [McCarley and Sinton, 2007]

The recurrence of this cycle produces gamma oscillations in which the time-course of inhibitory synapses of FS neurons plays an important role in modulating frequency content. These oscillations can become slower and larger during emergence of natural sleep or induction of anaesthesia [Steriade *et al.*, 2001; Schiff *et al.*, 2014].

2.2.2 Sleep spindles

Spindles are the EEG hallmark of early stages of the non-rapid eye movement (NREM) sleep. They manifest as transient 12–14 Hz waxing-and-waning patterns lasting 1–3 s, recurring every 3–10 s [Steriade, 2005], and may be associated with loss of awareness and consolidation of memories during early stages of slow-wave sleep (SWS) [Steriade, 2006].

Spindles are produced by the cooperative activity of thalamocortical relay (TC), reticular nuclei (RTn), and corticothalamic regular spiking (RS) neurons. It is known that TC neurons are driven by the slow hyperpolarization-activated cation current I_h during spindle generation [Destexhe and Babloyantz, 1993]. Based on *in vivo* and *in vitro* experiments, Timofeev and Bazhenov [2005] developed a network of spiking cortical and thalamic neurons capable of spindle generation, and gave detailed descriptions about the underlying mechanism for spindle generation. They identified three distinct phases as displayed in Fig. 2.3:

- **Waxing:** spindling is mediated by the activity of RTn neurons
- **Synchronization:** all three neural types oscillate synchronously
- **Waning:** I_h inactivates, and the network desynchronizes

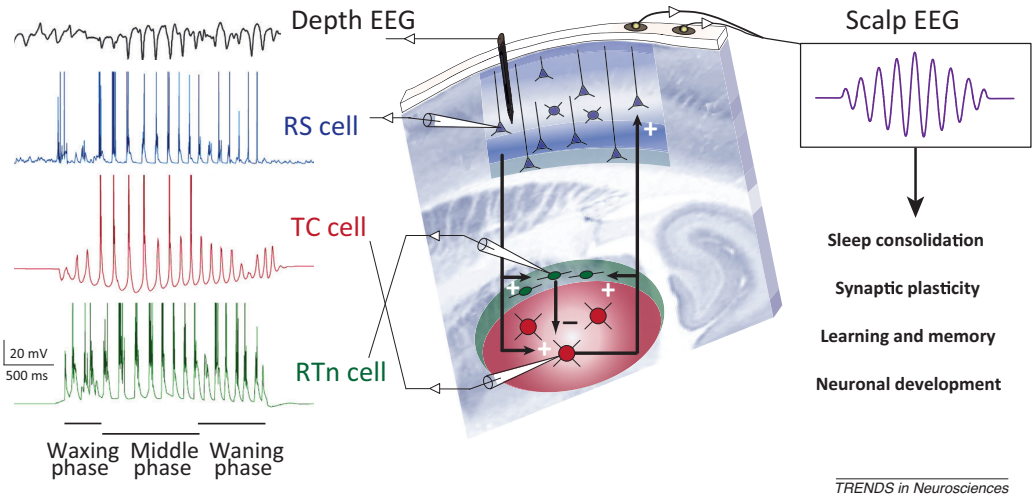

Figure 2.3: Three phases of spindle pattern and their formation in thalamocortical network. Top to bottom: Depth EEG trace, intracellular recordings of cortical regular spiking (RS), thalamocortical (TC), and reticular nuclei (RTn) neurons. The waxing phase is identified by small inhibitory postsynaptic potentials (IPSPs) observed on TC trace due to the activity of RTn neuron. At the synchronized middle phase all three neurons are phase-locked. Desynchronization occurs at waning phase resulting in spindle termination. Spindles can be observed on scalp EEG as population synaptic currents of spindling RS neurons. Image adapted from Astori *et al.* [2013]

2.2.3 Burst suppression

Burst suppression (BS) is a quasiperiodic electroencephalographic pattern characterized by isoelectric flat periods interrupted by transient bursts of low frequency activity (<15 Hz) [Kroeger and Amzica, 2007]. This pattern is frequently observed in very deep levels of anaesthesia [Akrawi *et al.*, 1996], and also in the comatose state [Young, 2000], and in infant encephalopathy [Ohtahara *et al.*, 1987] as a result of after-birth hypoxia. Hypoxia-induced BS pattern is irregular and erratic rather than being quasiperiodic [Roberts *et al.*, 2014].

Lukatch and MacIver [1996] found that BS pattern survives in deafferented cortical network, suggesting the possibility of exclusively cortex-generated BS pattern, in agreement with early work by Hughes [1986] and recent results by Kroeger and Amzica [2007]. A possible neurophysiological mechanism for BS by Ching *et al.* [2012] argues that BS is associated with reduced metabolic rates in the brain arising from a lack of available adenosine triphosphate (ATP). The ATP-sensitive potassium channels can activate under low metabolism conditions, preventing the spiking of cortical neurons, inducing quiescense. This allows ATP to rise so another activity burst can initiate. Using this mechanism, Ching *et al.* [2012] developed a network of Hodgkin-Huxley neurons, and demonstrated many *in vitro* and *in vivo* BS characteristics. Their model-predicted statements about the heterogeneity of bursts (in contrast with the classic homogeneous point of view), and survival of alpha activity[1] during bursts, were confirmed recently by Lewis *et al.* [2013]. A simple model of anaesthesia-induced burst suppression is presented in Chapter 3. The mechanisms underlying generation of hypoxia-induced burst suppression is suggested to be different from anaesthesia-induced ones [Roberts *et al.*, 2014], and the modelling of hypoxia is beyond the scope of the thesis.

2.3 Neural modelling

Neural models aim to describe quantifiable and measurable behaviours of neurons or populations of neurons. They are expressed mathematically as sets of coupled differential equations. Some neural models can be studied analytically, and all models can be simulated numerically using computers to mimic real behaviour and to extend knowledge about neural mechanisms. Models can provide insights into the function of the nervous system and to predict the response of the brain to different stimulations. Potentially, such models could be embedded in hardware and implanted in the human body to assist malfunctioning brain areas. In addition, neural models might allow the "training" of robots or intelligent devices rather than requiring manual programming.[2] This section briefly reviews the spiking neuron and mean-field neural models

[1] Alpha wave with frequency of 8–12 Hz, is the dominant wave of EEG during relaxed wakefulness

[2] `http://www.braincorporation.com/brainos/`

which are of particular relevance to this thesis. Detailed model descriptions are presented in Chapters 3, 5, and 6.

2.3.1 Models of spiking neurons

One of the most important computational models of the spiking neuron was presented by Hodgkin and Huxley [1952]. Based on electrophysiological experiments on squid giant axon, Hodgkin and Huxley identified three voltage-dependent ionic currents responsible for action potential generation:

- persistent K^+ current with four activation gates[1]
- persistent Na^+ current with three activation gates and one inactivation gate
- Ohmic leak current mediated mainly by Cl^- ions

The full set Hodgkin-Huxley equations is

$$\begin{aligned} C\frac{dV}{dt} &= -\underbrace{g_{\mathrm{Na}}^{\max} m^3 h(V-E_{\mathrm{Na}})}_{\mathrm{Na}^+ \text{ current}} - \underbrace{g_{\mathrm{K}}^{\max} n^4 (V-E_{\mathrm{K}})}_{\mathrm{K}^+ \text{ current}} - \underbrace{g_L(V-E_L)}_{\text{Leak current}} + I_{\mathrm{in}} \\ \frac{dm}{dt} &= \frac{1}{\tau_m(V)}(-m+m_\infty(V)) \\ \frac{dh}{dt} &= \frac{1}{\tau_h(V)}(-h+h_\infty(V)) \\ \frac{dn}{dt} &= \frac{1}{\tau_n(V)}(-n+n_\infty(V)) \end{aligned} \tag{2.3.1}$$

where

$$\begin{aligned} m_\infty &= \alpha_m/(\alpha_m+\beta_m), & \tau_m &= 1/(\alpha_m+\beta_m) \\ h_\infty &= \alpha_h/(\alpha_h+\beta_h), & \tau_h &= 1/(\alpha_h+\beta_h) \\ n_\infty &= \alpha_n/(\alpha_n+\beta_n), & \tau_n &= 1/(\alpha_n+\beta_n) \end{aligned} \tag{2.3.2}$$

and

$$\begin{aligned} \alpha_m(V) &= 0.1\frac{25-V}{\exp(\frac{25-V}{10})-1}, & \beta_m(V) &= 4\exp\left(\frac{-V}{18}\right) \\ \alpha_n(V) &= 0.01\frac{10-V}{\exp(\frac{10-V}{10})-1}, & \beta_n(V) &= 0.125\frac{-V}{80} \\ \alpha_h(V) &= 0.07\exp\left(\frac{-V}{20}\right), & \beta_h(V) &= \frac{1}{\exp\frac{30-V}{10}+1} \end{aligned} \tag{2.3.3}$$

[1]The gating particles or gates activate (open) or inactivate (close) ionic channels of the membrane, due to effect of membrane voltage, intracellular or extracellular agents [Kandel *et al.*, 2000]

Here, the voltage-dependence of the ionic conductances are represented by dimensionless weights: m, n, h. Each weight is described by a differential equation with voltage-dependent time-constants ($\tau_{m,h,n}$) and steady-states ($m_\infty, h_\infty, n_\infty,$).

Since HH equations are fourth-order and rather difficult for analytical studies and expensive for numerical simulations, reduced models of AP generation are highly desirable and have been attempted by many researchers. For example, Rinzel [1985] replaced the three HH gating variables by a single inhibitory or recovery variable W:

$$\begin{aligned} C\frac{dV}{dt} &= -g_{\mathrm{Na}}^{\max} m_\infty^3(V)(1-W)(V-V_{\mathrm{Na}}) - g_{\mathrm{K}}^{\max}\left(\frac{W}{S}\right)^4 (V-V_{\mathrm{K}}) - g_L(V-E_L) + I_{\mathrm{in}} \\ \frac{dW}{dt} &= \phi\left(\frac{W_\infty(V)-W}{\tau(V)}\right) \end{aligned} \tag{2.3.4}$$

where $\tau(V) = 5\exp[-(V+10)^2/55^2] + 1$, ϕ is the HH temperature correction factor, and

$$\begin{aligned} W_\infty(V) &= S\left(\frac{n_\infty(V) + S(1-h_\infty(V)}{1+S^2}\right) \\ S &= \frac{1-h_\infty}{n_\infty} \end{aligned} \tag{2.3.5}$$

with m_∞, n_∞, h_∞ following their original HH definitions. Similar simplifications have been proposed by many other researchers, for example, Abbott and Kepler [1990], Joeken and Schwegler [1995] and Wilson [1999][1]. Further simplifications were made by concentrating on the pre-spike behaviour of the neuron (linear regime), without specifying what happens after spike—as represented by leaky integrate-and-fire [Tuckwell, 1988] or resonate-and-fire [FitzHugh, 1966] models. These linear models all have an artificial threshold and a manual reset rule. Although good for mathematical analysis, these models are incomplete because they cannot spike: they lack an accelerating upstroke mechanism for action potential generation, and are just "said to fire" [Izhikevich, 2007].

To restore spiking while retaining mathematical simplicity, the quadratic integrate-and-fire model was introduced by Latham *et al.* [2000]. This formulation captures the nonlinear nature of the spike generation mechanism of real neurons. Rather than using the conductance-based form for the currents responsible for generating action potentials, Latham and his colleagues modelled the spike current as

$$I_{\mathrm{spike}} = -\frac{(V-V_r)(V-V_t)}{R_{\mathrm{cell}}\Delta V} \tag{2.3.6}$$

[1] See Section 3.1 for Wilson spiking neuron model

where $\Delta V = V_t - V_r$ is the nominal gap between resting (V_r) and threshold (V_t) voltages and R_{cell} is the membrane resistance of the cell. After rescaling, the non-dimensional form for the integrate and-fire model can be written [Izhikevich, 2007]:

$$\frac{dV}{dt} = b + V^2; \qquad \text{if} \quad V = V_{\text{peak}}, \quad \text{then} \quad V \leftarrow V_{\text{reset}} \tag{2.3.7}$$

where b is the resting voltage and V_{peak} and v_{reset} are the peak and reset voltages used in the "manual" reset rule. Equation (2.3.7) describes the simplest model for a spiking neuron. However, this model captures only one among many *bifurcation* mechanisms underlying spike generation[1]. Izhikevich [2003] extended the quadratic model by incorporating a slow recovery variable, and showed that this enhanced model is capable of producing spiking and bursting activity of many types of mammalian neurons. The fact that the Izhikevich form preserves a realistic subthreshold (pre-spike) dynamics has made it the model of choice for my single-neuron and network subthreshold investigations of Chapters 3 and 4.

2.3.2 Mean-field models

Complementary to spiking-neuron modelling, the *mean-field* approach describes the collective behaviour of populations of interconnected neurons (excitatory, inhibitory or mixed). These *macroscopic* models can provide insights about the mechanisms underpinning emergent behaviour in neural population, interaction of brain parts—such as thalamus, cortex, hippocampus, and brain stem—and also whole brain dynamics. Here we briefly overview some mean-field models.

- Wilson and Cowan [1972] introduced one of the earliest mean-field models in which the collective behaviour of interacting excitatory and inhibitory cortical neurons are expressed as their mean firing-rates. Based on common anatomical characteristics of the cortex, the model includes both excitatory and inhibitory connections. Excitatory connections are localized while inhibitory connections are allowed to cover broader ranges. Exponentially decaying functions of distance govern the weight of synaptic connections.
- Amari [1971, 1972, 1977] presented a neural model based on the similar concepts followed by Wilson and Cowan. Considering local excitation and long-rage inhibition this model predicts spatially localized solutions (bumps), oscillatory and traveling waves, and transient responses.
- Nunez [1974] considered axonal delays in an infinite, one dimensional (1D) continuum model of excitatory and inhibitory populations introduced by da Silva *et al.* [1974]. Nunez

[1] Different mechanisms underlying the spike generation and other phase transitions will be discussed in Chapters 3–6

investigated the model analytically using wave solutions in 1D and 2D, and consequently predicted global modes with frequencies matching the major cerebral rhythms.

- da Silva *et al.* [1974]; da Silva *et al.* [1976] used a lumped-parameter approach to describe interactions between thalamocortical relay cells and interneurons leading to alpha activity.
- Freeman [1975] modelled the spatiotemporal properties of EEG signals from the olfactory bulb. He considered distinct connection properties within and between different neural sets and formalized the concept of cortical "mass action" by assuming hierarchical interactions between neural aggregates. He noted the importance of synaptic and dendritic delays in the generation of oscillatory behaviour.
- Katznelson [1981] highlighted the importance of cortico-cortical connections by including them in da Silva's model with the cortex represented as a two-dimensional spherical surface. His linearized model predicted oscillations corresponding to alpha and theta rhythms.
- Jansen *et al.* [1993]; Jansen and Rit [1995] retained the nonlinearities of da Silva's 1974 model to produce chaotic activity, and were able to demonstrate normal EEG patterns and evoked potential responses supporting the hypothesis that spontaneous EEG and visually evoked potential are generated by same neural structures in the cortex.
- Wright and Liley [1995] introduced a spatially discretized model of the cortex that included both axonal and dendritic delays. The cortical sheet was subdivided into patches with interconnections formulated with a Green function. The biologically inspired parameter values of this model resulted in outputs more comparable with experimental results, compared with earlier models.
- Robinson *et al.* [1997] replaced the Green function of the Wright and Liley model with a damped wave equation to greatly improve the runtime of numerical methods and enhance spatial resolution. By adopting a continuum form (instead of the discretized Wright and Liley equation) Robinson was able to undertake analytic study of wave properties and their stability.
- The Liley *et al.* [2002] model assumes a homogeneous cortex with long-range (cortico-cortical) and short-range (intra-cortical) connections. This model has been used to demonstrate cortical evoked potentials, travelling waves, and chaotic and noise driven oscillations at realistic EEG frequencies.
- The Waikato model shares many biophysical features with the Wright, Liley, and Robinson models, and contains excitatory and inhibitory neural populations that communicate through local and distant connections at chemical synapses [Steyn-Ross *et al.*, 1999, 2004, 2014]. The significance difference from previous continuum models is the inclusion of electrical synapses (gap junctions) to supplement chemical synaptic connections.

The reminder of this section focuses on the Wilson-Cowan (WC) mean-field model and its applications. Its subthreshold properties will be studied in detail in Chapters 5 and 6.

Cowan [2014] explores general concepts in mean-field modelling and provides a historical review of the WC model, a well-studied neural mass description which has been used extensively to investigate dynamical behaviours of neural systems. Sakaguchi [1988] used the WC model to investigate transition between stationary, oscillatory and excitable states. Borisyuk and Kirillov [1992] performed a bifurcation analysis on this system to describe qualitative behaviour.

Modified versions of the WC formalism have attracted much recent interest. Wang *et al.* [2012] used the homogeneous WC network to generate spike and wave seizures by adding a slow third parameter to permit bursting. Srinivasan *et al.* [2013] investigated the top-down effects of neural background and arousal on activity of single neurons. Meijer and Coombes [2013] impose metabolic limits on synaptic activity by including a refractory time-scale in the dynamics of the synaptic interactions of the model, supporting production of travelling waves in a purely excitatory network. Pasillas-Lepine [2013] proposed necessary conditions for stability of a delayed WC network as a representation of the subthalamo-pallidal feedback loop which may play a critical role in the tremors observed in parkinsonian subjects. Hlinka and Coombes [2012] studied the original WC network with a more realistic structural connectivity[1] that permits inclusion of realistic long-range anatomical connections. They examined the effect of local network dynamics on functional connectivity. Their findings may provide insights into nervous collapse and malfunctions due to local dynamics. Influence of axon propagation delays in neural dynamics [Nunez and Srinivasan, 2014], and analysis of chaotic oscillations in neural systems [Maruyama *et al.*, 2014] are examples of very recent applications of the WC model.

This brief survey of WC-related literature and model applications shows the WC formalism is of foundational importance in computational neuroscience. Its relative simplicity is another reason which motivated me to use it in my theoretical and numerical studies of mean-field subthreshold dynamics. In Chapters 5 and 6 I will show how a range of phase transitions (both temporal and spatial) can be demonstrated by this model.

2.4 Phase transitions in dynamical systems

A dynamical system consists of a set of variables describing the state of the system and a law which describes the evolution of the variables over the time [Meiss, 2007; Izhikevich, 2007]. The governing law can be expressed mathematically using a system of differential equations which quantify how the future state depends on the system input and the previous state. The standard

[1]The original WC formalism assumes a homogeneous structural medium with all-to-all connections between excitatory and inhibitory populations, and an exponentially decaying synaptic strength over space

form for a one dimensional dynamical system with state variable x and governing rule f is usually expressed as [Wiggins *et al.*, 1990]:

$$\frac{dx}{dt} = f(x, \lambda) \tag{2.4.1}$$

where t is time, and λ is the control or *bifurcation* parameter. In general there is no explicit analytical solution for this differential equation, and one must employ numerical integration methods to update the state variable x. A wide range of numerical integrators and their software implementation is introduced in Press *et al.* [1992], among them two methods that are used extensively in this thesis: the fixed-step Euler method, and the fourth-order Runge-Kutta (RK4) method.

Fortunately, numerical integration is not the only way of analyzing dynamical behaviour. Alternative analysis methods include—

- *Phase plane* analysis provides qualitative predictions about system evolution and interaction of system states [Izhikevich, 2007]
- *Steady-state* or *fixed-point* analysis determines the set of resting states at which the system does not evolve, i.e., the solution of $f(x, \lambda) = 0$ Eq. (2.4.1)
- *Linear stability* analysis determines the stability of those steady states relative to small perturbations

These three methods provide insights about the occurrence of a *bifurcation* (sometimes referred as *tipping point* or a *phase transition*) where the system undergoes an abrupt qualitative change. This transition can be result of the disappearance of a steady state, the appearance of a new steady state, or a change in the stability of one of the steady states. These result in distinct bifurcation types (see Golubitsky *et al.* [1988]; Izhikevich [2007] for more details). *Bifurcation theory* is the study of system dynamics as the system explores its state-space by continuous modification of its bifurcation parameter λ [Golubitsky *et al.*, 1988]. Kelso *et al.* [1981] applied bifurcation theory to analyze a biological system, namely human interlimb coordination, in terms of nonlinear limit-cycles. Later, Kelso [1984] reported phase transition and critical behaviour when human subjects performed voluntary hand movements, demonstrating increased variability of phase difference between hand movements when a transition point is approached [Kelso *et al.*, 1986].

It is known that system *resilience* to small perturbations reduces when the bifurcation point is approached [van Nes and Scheffer, 2007]. This behaviour can be quantified by constructing the Jacobian matrix of the linearized form of the system: the real part of the dominant eigenvalue predicts the rate of recovery when disturbed by a small perturbation. Approaching a bifurcation

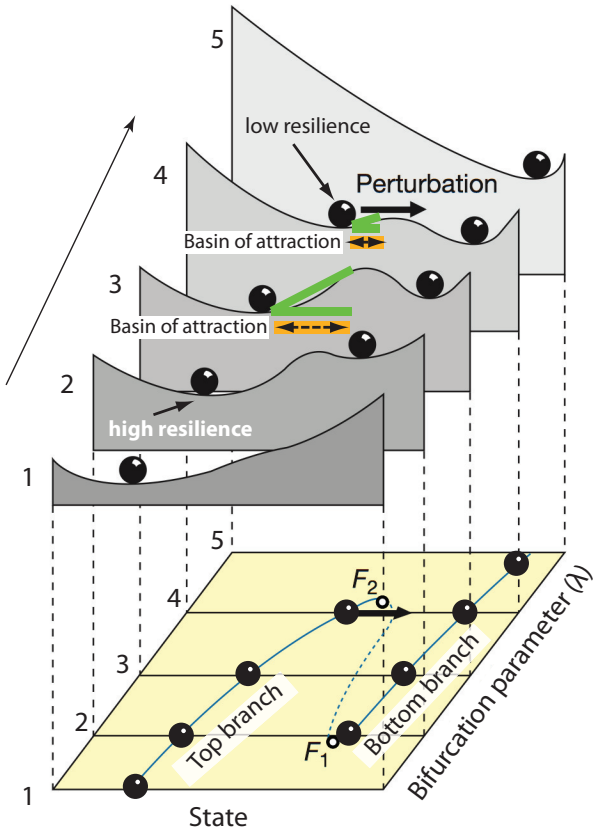

Figure 2.4: Perturbation experiments prior to phase transition in a multistable ecosystem. External conditions act as bifurcation parameter and change the resilience or stability properties of the system as depicted by stability landscapes showing equilibria and their basins of attraction. The hills and peaks indicate stable and unstable steady states. The steady state of the ecosystem versus bifurcation parameter (λ) is displayed in bottom plane. The top and bottom branches are stable while the middle one is unstable. As the $F2$ bifurcation point is approached (indicated by 1–5), the size of the basin of attraction of the top branch and its resilience reduces, the system gets slower in recovering to resting state, and small perturbations may flip the system to the bottom branch. Modified from Scheffer *et al.* [2001].

corresponds to the real part of the eigenvalue tending towards zero, which shrinks the basin of attraction of the steady state and makes the system increasingly "slow" in its recovery [Strogatz, 1994].

The proximity of a system to its tipping point can be discerned from measured time-series if the appropriate variables are sampled *and* if the transition towards the tipping point is slow [Carpenter *et al.*, 2011]. The perturbation method is a straightforward approach to determine the proximity to a tipping point, and is cartooned in Fig. 2.4, where the system response to an externally imposed stimulus is represented. The decay-time of response *increases* prior to phase transition at point F_2; this is what is meant by "slowing down". This idea is applicable even if it is not possible to perturb the system externally, since real world systems are continuously affected by natural perturbations due to the presence of internal or external noise. Slowing down reveals itself in fluctuations displaying increased amplitude and correlation time [Dakos *et al.*, 2008].

Bifurcation theory has been employed to analyze many real-world dynamical systems, and to forecast onset of catastrophic change, for example

- **Population of living organisms.** Veraart *et al.* [2012] studied the sudden collapse of planktonic organisms due to excessive light irradiation. They perturbed the system by removing 10% of the plankton population via dilution, and measured the rate at which the population density recovered. They detected an increased recovery time prior to population collapse.
- **Lake ecosystem.** Catastrophic change in the food web organization of a whole ecosystem was studied by Carpenter *et al.* [2011]. They perturbed the prey-dominated ecosystem of a lake by gradually increasing the population of predator fish, over a three-year period. Since the chlorophyll density responds strongly to food web fluctuations, they analyzed the chlorophyll time-series, and found increased variance and return times prior to transition from prey to predator dominance.
- **Paleoclimatic transitions.** Dakos *et al.* [2008] and Livina and Lenton [2007] studied the paleoclimate records in the times leading to major historic climate transitions: icehouse-greenhouse transition, Sahara desertification. Since it was not possible to apply any perturbation to the system, they focused on the fluctuation analysis of the data, and found increased variance and correlation times prior to regime shifts. A similar study by Held and Kleinen [2004] revealed the existence of precursor signs of bifurcation points in models of climate change.
- **Dielectric liquid breakdown.** Zhang and Zahn [2014] reported electro-optic precursors of critical transitions in dielectric liquids. They found increased spatial variance as an indicator of proximity to electrical breakdown in high-voltage-pulsed transformer oil.
- **Ecological dynamics of cancer.** The "Opinion" article by Korolev *et al.* [2014] suggests investigation of spatial organization of tumors—which has key role in cancer evolution—as a possible indicator of extinction or growth of cancer tissue. They suggested that the response of a tumor to perturbation (for example by a pulsed application of a drug) might quantify closeness to extinction or growth of cancer cells.
- **Transition into and out of depression in human.** van de Leemput *et al.* [2014] have reported increased variance and autocorrelation in the time-series of different emotional, cognitive, and behavioural variables related to depression.

The following two studies are particularly relevant for my thesis:

- **Increased irritability prior to spike generation.** Considering the spike generation as a phase transition, Steyn-Ross *et al.* [2006] presented the first detailed analysis of pre-spike soma voltage fluctuations in the H. R. Wilson model of cortical neuron and squid

axon. They reported increased variance, correlation times and spectral growth at resonant frequencies as signs of critical slowing down.

- **Slowing down prior to "down/up" transitions of the cortical slow oscillations.** Wilson *et al.* [2008] first reported signs of slowing down in *in vivo* experiments in rat brain. Considering the down-to-up transition of cortical slow oscillations (as observed on intracellular voltage signals) as a phase transition, they reported increased fluctuation power and time scale prior to the down-to-up transitions.

Dynamical systems theory and the bifurcation analysis have been applied to describe dynamics of an epileptic brain:

- Using a mean-field model of the thalamocortical loop, Robinson *et al.* [2002] demonstrated distinct steady states, corresponding to normal and seizure states of the brain.
- da Silva *et al.* [2003] considered the occurrence of an epileptic seizure as a sudden qualitative change in underlying physiological characteristics. They proposed a multistable dynamics for the epileptic brain presenting generic dynamical models to explain qualitative differences between absence and limbic seizures.
- In a reduced mean-field model of thalamocortical network, Rodrigues *et al.* [2006] used bifurcation theory to demonstrate thalamic origins of spike-and-wave components for absence seizure.
- By investigating the dynamical bifurcations of a nonlinear neural model, Breakspear *et al.* [2006] predicted both periodic and chaotic dynamics and multistability, both relevant to tonic-clonic and absence seizures.
- Terry *et al.* [2012] demonstrated that subtle alterations of neural connection structures may result in generation of focal seizures, without the requirement for any localized seizing zone.
- Jirsa *et al.* [2014] identified distinct bifurcation types at seizure onset and offset. They introduced a generic "Epileptor" model which is capable of showing general features of different classes of seizures. The authors propose that a seizure initiates when a brain trajectory collides with the separatrix between normal and epileptic states. Model predictions were validated using *in vitro* and *in vivo* experiments.

Motivated by these studies, and using both modelling and *in vitro* approaches, this thesis investigates a range of neural transitions (from spiking single neurons to network emergent phenomena) to identify noise-induced precursors of phase transitions. In addition, preliminary *in vitro* observation of stimulus-induced state change is also included in Chapter 7, providing a link between the theoretical and *in vitro* findings of this thesis and the *in vivo* "probing" experiments of Kalitzin *et al.* [2002, 2005] and Freestone *et al.* [2011]. We demonstrate a characteristic

change of stimulation-evoked potentials prior to pharmacologically-induced state changes in mouse neocortical tissue.

Chapter 3

Dynamical behaviour of spiking single neurons

Patterns of critically slowed fluctuations emerge in dynamical systems when they approach a phase transition point. Anticipation of transition points is significant not only for broadening our knowledge about the functional mechanisms underpinning of state transitions, but also to permit timely preventive intervention in the event of pathological transitions. Phase transitions are common in neural systems. Examples include, but are not limited to, a broad spectrum of events ranging from the firing of a single action potential in an individual neuron, to a global transition in brain state due to seizure occurrence or induction of anaesthesia.

A previous work by Steyn-Ross *et al.* [2006] theoretically predicts and numerically captures the signs of critical-slowing down in the H. R. Wilson model [Wilson, 1999] of a single spiking neuron, as the neuron approaches firing threshold. Here I extend this work by studying the spectrum of the same model. Then I demonstrate precursor critical fluctuations in a reduced spiking neuron model due to Izhikevich [2007]. Four specific neural classes are studied in this chapter:

- Regular spiking (RS) excitatory pyramidal neurons (cortical)
- Fast spiking (FS) inhibitory interneurons (cortical)
- Excitatory thalamocortical (TC) relay neurons (thalamic)
- Inhibitory reticular thalamic nucleus (RTn) neurons (thalamic)

These classes are of interest since they are prevalent in cortex and thalamus, and so play a major role in the generation of natural and pathological brain activities. Some of the models are modified to make them better candidates for use in network simulations of gamma oscillations in wakefulness and spindle generation in sleep (see Chapter 4). In this chapter I first present the models, then their modified forms. I mainly concentrate on the subthreshold voltage fluctuations to elucidate precursor signs of phase transitions.

3.1 Subthreshold dynamics of the Wilson spiking-neuron model

Among the well-known models for action potential (spike) generation in a single nerve cell (neuron) is a model presented by by Wilson [1999, p. 139] as a second-order reduction of the standard fourth-order Hodgkin-Huxley model. Although Wilson's nonlinear model is capable of generating spikes, my interest lies in the period leading up to spike genesis, so I have concentrated on the *below-threshold* behaviour of the Wilson neuron. A 2006 paper by Steyn-Ross *et al.* [2006] showed that a linear Ornstein–Uhlenbeck (OU) analysis is capable of predicting subthreshold behaviour of the nonlinear Wilson model. Briefly, the OU process was originally formulated to describe the velocity of a massive Brownian particle under the influence of opposing random-driving and frictional damping forces. Sometimes is called "mean-reverting", this process tends to approach its mean steady state over the time.

I extend results of Steyn-Ross *et al.* [2006] here with the aim of comparing linear predictions against numerical simulations of the full nonlinear Wilson equations. Specifically, I concentrate on the spectral-amplitude curves for membrane voltage fluctuations, testing the validity of the theoretical fluctuation spectrum.

Wilson's equations describe the deterministic response of an excitable membrane to an injected stimulus current. These equations are expressed as a pair of coupled nonlinear differential equations which I have modified by adding two independent sources of white noise ($\xi_1(t),\ \xi_2(t)$) to represent biological fluctuations.

$$
\begin{aligned}
C\,\frac{dV}{dt} &= -\underbrace{g_{\mathrm{Na}}(V)(V-E_{Na})}_{\text{sodium ion current}} - \underbrace{g_{\mathrm{K}}R\cdot(V-E_{\mathrm{K}})}_{\text{potassium ion current}} + \underbrace{I_{\mathrm{dc}}}_{\text{stimulus current}} + \underbrace{\sigma_I\,\xi_1(t)}_{\text{white-noise disturbance}} \\
\tau_R\,\frac{dR}{dt} &= \underbrace{-R}_{\text{recovery variable}} + \underbrace{G(V)}_{\text{steady-state value of R}} + \underbrace{\sigma_R\,\xi_2(t)}_{\text{white-noise disturbance}}
\end{aligned}
\tag{3.1.1}
$$

where V is the membrane voltage in mV, and R is a dimensionless *recovery variable* representing the combined effect of K^+ channel opening and Na^+ channel closing. The membrane specific capacitance is $C = 1\mu\mathrm{F/cm}^2$. The specific conductances $g_{\mathrm{Na}}(V)$ and $g_{\mathrm{K}} = 26$ carry units $\mathrm{mS/cm}^2$. Here σ_I, σ_R are the amplitudes (standard deviations) of the white noise terms, and the $\xi_{1,2}$ are defined to have zero mean and variance $1/dt$:

$$\xi(t) = \frac{\mathcal{N}(0,1)}{\sqrt{dt}} \tag{3.1.2}$$

where $\mathcal{N}(0,1)$ represents normally distributed random numbers (produced with MATLAB `randn` function) with zero mean and unity variance, and dt is the fixed time-step of the numerical integrator.

By changing the form of $G(V)$ from a linear polynomial to a quadratic, the Wilson model is capable of simulating spike generation in either a **squid axon** or in a **human cortical neuron**. For the squid axon model, $E_{\mathrm{Na}} = 0.55$, $E_{\mathrm{K}} = -0.92$ (meaning +55 and −92 mV respectively), and $\tau_R = 1.9$ ms is the exponential decay time-constant of the R variable. The Na specific conductance and the $G(V)$ function for the squid axon model are given by

$$\begin{aligned} g_{\mathrm{Na}}(V) &= 17.81 + 47.71V + 32.63V^2 \\ G(V) &= 1.35V + 1.03 \end{aligned} \tag{3.1.3}$$

For the human cortical neuron, $E_{\mathrm{Na}} = 0.48$, $E_{\mathrm{K}} = -0.95$ (meaning +48 and −95 mV respectively), and $\tau_R = 5.6$ ms. The Na specific conductance and the $G(V)$ function for this neuron are given by[1]

$$\begin{aligned} g_{\mathrm{Na}}(V) &= 17.81 + 47.58V + 33.8V^2 \\ G(V) &= 0.79 + 1.29V + 3.3(V + 0.38)^2 \end{aligned} \tag{3.1.4}$$

3.1.1 Steady states and eigenvalue analysis

In *steady state* the model variables do not evolve temporally, so the derivatives of the deterministic form of Eqs. (3.1.1) are set to zero[2]:

$$\begin{aligned} F_1(V,R) =& \frac{1}{C}\left[-g_{\mathrm{Na}}(V)(V - E_{\mathrm{Na}}) - g_{\mathrm{K}}R(V - E_{\mathrm{k}}) + I_{\mathrm{dc}}\right] = 0 \\ F_2(V,R) =& \frac{1}{\tau_R}[-R + G(V)] = 0 \end{aligned} \tag{3.1.5}$$

These equations can be solved numerically giving the steady-state coordinate (V^0, R^0) for membrane voltage and recovery variable. The Jacobian matrix of partial derivatives, $\mathbf{J}$, evaluated at the (V^0, R^0) equilibrium point is

$$\mathbf{J} = \left[\begin{array}{cc} \frac{\partial F_1}{\partial V} & \frac{\partial F_1}{\partial R} \\ \frac{\partial F_2}{\partial V} & \frac{\partial F_2}{\partial R} \end{array}\right]_{|(V^0,R^0)} \tag{3.1.6}$$

[1] Wilson's Eq. (9.10) on [Wilson, 1999, p. 147] contains an error: the "3.3" appears as "0.33". This is reported in Wilson's Errata at `http://cvr.yorku.ca/webpages/book.html`.

[2] In the deterministic form of Eqs. (3.1.1), the noise amplitudes are $\sigma_I = \sigma_R = 0$

The real parts of the eigenvalues of this matrix predict growth or decay of small fluctuations about (V^0, R^0), hence the stability of the given steady state. [See Figs. 4, 5 in Steyn-Ross *et al.* [2006] for the steady-state distribution, and eigenvalue structure of integrator and resonator Wilson neurons as a function of the control parameter $I_{\rm dc}$.]

3.1.2 Linear analysis of the nonlinear Wilson equations

By assuming that the membrane is resting at a subthreshold equilibrium point (V^0, R^0), one can linearize Eqs (3.1.1) about the nominated steady state point as,

$$\frac{d}{dt}\begin{bmatrix} v \\ r \end{bmatrix} = -\mathbf{A}\begin{bmatrix} v \\ r \end{bmatrix} + \sqrt{\mathbf{D}}\begin{bmatrix} \xi_1(t) \\ \xi_2(t) \end{bmatrix} \tag{3.1.7}$$

with

$$\begin{aligned} v(t) &= V(t) - V^0 \\ r(t) &= R(t) - R^0 \end{aligned} \tag{3.1.8}$$

defining the fluctuations (instantaneous deviations away from (V^0, R^0)), $\mathbf{A}$ is the 2×2 *drift* matrix, equal to the negative of the Jacobian matrix $\mathbf{J}$, evaluated at the nominated steady state; and $\mathbf{D}$ is the 2×2 *diffusion* matrix [Steyn-Ross *et al.*, 2006]:

$$\mathbf{D} = \begin{bmatrix} \sigma_I^2/C^2 & 0 \\ 0 & \sigma_R^2/\tau_R^2 \end{bmatrix} \tag{3.1.9}$$

Equation (3.1.7) defines a two-dimensional Ornstein–Uhlenbeck process, in which the 2×2 spectrum matrix is [Gardiner, 2004],

$$\mathbf{S}(\omega) = \frac{1}{2\pi}\int_{-\infty}^{\infty} e^{-i\omega\tau}\mathbf{C}(\tau)\,d\tau = \frac{1}{2\pi}(\mathbf{A} + i\omega\mathbf{I})^{-1}\mathbf{D}(\mathbf{A}^{\rm T} - i\omega\mathbf{I})^{-1} \tag{3.1.10}$$

where $\mathbf{I}$ is the 2×2 identity matrix, T is the transpose operator and $\mathbf{C}(\tau)$ is the 2×2 steady-state time-correlation matrix for v and r fluctuations defined as

$$\mathbf{C}(\tau) = \begin{bmatrix} \mathrm{cov}\{v(0), v(\tau)\} & \mathrm{cov}\{v(0), r(\tau)\} \\ \mathrm{cov}\{r(0), v(\tau)\} & \mathrm{cov}\{r(0), r(\tau)\} \end{bmatrix} \tag{3.1.11}$$

with τ as the lag-time. Following Gardiner [2004] one can compute the $\mathbf{C}(\tau)$ as the product of the matrix exponential $\exp(\mathbf{A}\tau)$ with the covariance matrix $\mathbf{\Sigma}$:

$$\mathbf{C}(\tau) = e^{-\mathbf{A}\tau}\mathbf{\Sigma}, \quad \tau \leq 0 \tag{3.1.12}$$

with symmetry property $\mathbf{C}(-\tau) = [\mathbf{C}(\tau)]^{\mathrm{T}}$. The covariance matrix [Gardiner, 2004] is,

$$\mathbf{\Sigma} = \frac{\det(\mathbf{A})\mathbf{D} + [\mathbf{A} - \mathrm{tr}(\mathbf{A})\mathbf{I}]\mathbf{D}[\mathbf{A} - \mathrm{tr}(\mathbf{A})\mathbf{I}]^{\mathrm{T}}}{2\ \mathrm{tr}(\mathbf{A})\det(\mathbf{A})} \tag{3.1.13}$$

where $\det(\cdot)$ and $\mathrm{tr}(\cdot)$ are determinant and trace operators respectively. In this section I examine the $S_{11}(\omega)$ component of the spectrum matrix since this gives the theoretical power spectral density of the membrane voltage fluctuations. This theoretical prediction and the numerically calculated fluctuation spectrum will be studied while the neural model is forwarded towards its firing threshold.

3.1.3 Numerical simulation of nonlinear stochastic Wilson equations

In order to test the predictions of linear theory, a series of numerical simulations of the nonlinear noisy Wilson equations have been performed for both the squid axon and human cortical neuron. I used the Euler-trapezium method which provides a predictor-corrector strategy to compute the membrane voltage time-series[1]. All the simulations were done in the quiescent subthreshold (nonspiking) regime, with care taken to minimize the chance of spike generation. Experimental spectral amplitude curves were computed by averaging Fourier transforms of 500 simulation runs for each case.

Figure 3.1 compares the ideal (Eq. (3.1.10)) and experimental spectra for both human (left panel) and squid axon (right panel) models. For each type of excitable membrane, three different levels of I_{dc} injected current were applied, but the intensity of white-noise stimulations were kept unchanged.

Critical current for spike generation is about 7.7732 μA/cm^2 for squid axon, and 21.4752 μA/cm^2 for human cortical neuron [Wilson, 1999]. Both models show strong growth in spectral energy as the critical current is approached—exactly as predicted by linear Ornstein-Uhlenbeck theory. For the squid axon, the double-sided spectra develop a narrow resonance at $\sim \pm 360$ Hz; in contrast, the resonance frequency is 0 Hz for the human neuron. Theoretical and experimental results show a satisfying compatibility over a wide range of frequency. However, this agreement was only achieved by ensuring that the noise intensity was set sufficiently low that spikes were

[1]The Euler-trapezium update rule to solve the equation $dy/dt = f(t, y)$ is $y_{n+1} = y_n + 0.5\Delta t(f(t_n, y_n) + f(t_{n+1}, y_{n+1}))$, where Δt is the step size.

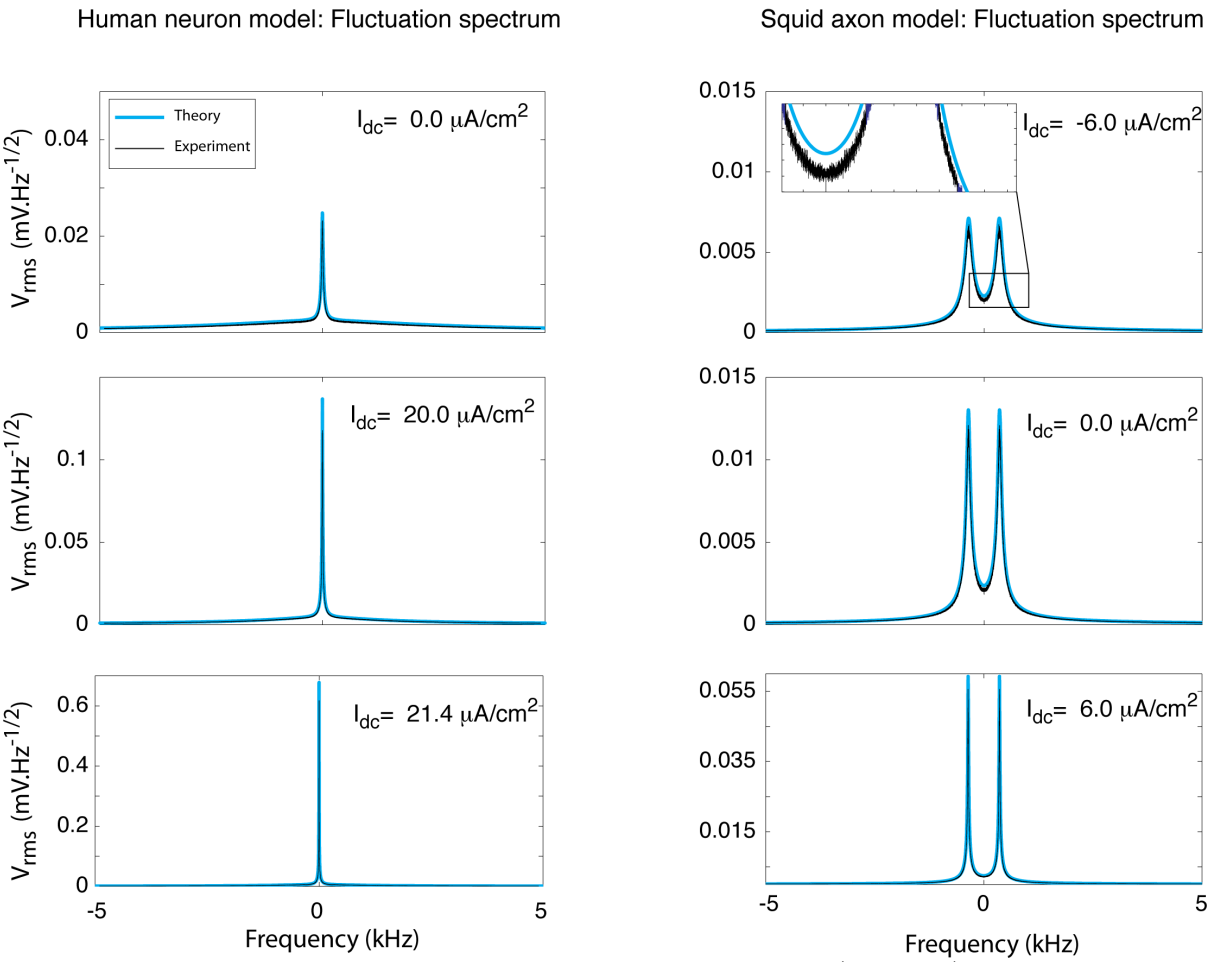

Figure 3.1: Subthreshold spectrum graphs for integrator cortical neuron (left panel), and resonator squid axon (right panel) models. Grey (blue online) traces show the $S_{11}(\omega)$ Ornstein–Uhlenbeck prediction. Black traces show Fourier transform results averaged across 500 independent nonlinear stochastic simulation runs. Integration algorithm is Euler-trapezium with time-step $\Delta t = 0.05$ ms. The noise attenuation followed Steyn-Ross *et al.* [2006]. The critical currents for spike generation are $I_{\rm dc} \simeq 7.7732$, $I_{\rm dc} \simeq 21.4752$ μA/cm^2 for squid axon and human cortical neurons respectively [Wilson, 1999].

never generated during the simulations. This is particularly important for currents that are very close to critical value.

As is evident in the zoomed inset in the bottom-right graph, there remains a tiny discrepancy between experiment and theory. This mismatch seems to be due to the finite length of my numerically generated time-series. By increasing the duration by a factor of 10 (to 10,000 ms), the discrepancy decreases by a factor of 0.75. Another source of spectral error probably arises from the high-frequency aliasing which is the inevitable result of taking the discrete Fourier transform of a non-band-limited process.

The surprising conclusion is that linear stochastic theory can make useful predictions about the onset of strongly nonlinear deterministic behaviour. Neuron susceptibility to small white-noise stimulus grows dramatically as the neuron approaches its spiking threshold. The resulting voltage fluctuations may be communicated to neighbouring neurons via electrical gap-junctions, thus these predictions may have biophysical significance.

Similar subthreshold examinations are performed on a simple Izhikevich spiking neuron model in the next sections. Although the Izhikevich model ignores the after-spike dynamics (simply replaces it with a manual reset rule), it preserves the subthreshold dynamics. As a result it is expected to exhibit signs of critical slowing, just as has been demonstrated in the more biophysically realistic Wilson model.

3.2 Izhikevich model of spiking single neurons

It has been shown that many spiking models can be reduced to two-dimensional systems having a fast voltage and a slower recovery variable representing respectively the activation or inactivation of the ion channels (K^+ and Na^+) [Izhikevich, 2007]. These *reduced models* are a generalization of the *integrate-and-fire* neuron and are an alternative to the very simple *leaky integrate-and-fire* neuron [Shlizerman and Holmes, 2012][1]. In reduced models, only the subthreshold activity of the neurons is tracked, and the mechanism of action potential generation is collapsed into an artificially imposed delta function, followed by a manual reset of the voltage and recovery variables.

Although these models depict neither the curent flows of individual ions, nor the stochastic aspects of channel activity, they are widely used in large network simulations [Shlizerman and Holmes, 2012]. It is standard practice to assume that the fastest channels have reached their steady state in these models. As a result, only the soma voltage and a slow recovery variable are required, making reduced models ideal for *phase plane* analysis.

Eugene M. Izhikevich introduced his reduced spiking neuron model in 2003 [Izhikevich, 2003]. He argues that the governing subthreshold dynamics of the neuron leading to spike generation are more important than the spike shape itself. The Izhikevich model is an abstraction of the standard *Hodgkin-Huxley* neuron and is a generalization of the *quadratic integrate-and-fire* neuron [Izhikevich, 2007].

The governing equations for the Izhikevich neuron, are

$$\begin{aligned} C\frac{dv}{dt} &= k(v - v_r)(v - v_t) - u + I_{\mathrm{dc}} \\ \frac{du}{dt} &= a\left\{b(v - v_r) - u\right\} \\ \text{if} \quad v \geq v_{\mathrm{peak}}, \quad &\text{then} \quad v \leftarrow c, \quad u \leftarrow u + d \end{aligned} \tag{3.2.1}$$

where v is the membrane potential, u is the recovery current, C is the membrane capacitance, v_r is the resting membrane potential, and v_t is the instantaneous threshold potential. The sign

[1] Section 2.3.1 of Chapter 2 introduces the most famous single neuron models.

of b determines whether u is an amplifying ($b < 0$) or resonant ($b > 0$) variable. The recovery rate constant is a. The spike cutoff value is v_{peak}, and the voltage reset value is c. With suitable tuning, this simple model is capable of reproducing spiking and bursting behaviour of many types of mammalian neurons, so is a good choice for simulations of large-scale networks of spiking neurons [Izhikevich, 2007].

3.3 Regular Spiking (RS) Neuron

The pyramidal neuron is the most common excitatory cell type in mammalian cortex [Spruston, 2009]. Most are classified as regular spiking (RS) neuron; although there are *intrinsically bursting* (IB) and *chattering* (CH) pyramidal neurons in different layers of cortex.

Using the simple model (3.2.1) and some *in vitro* data, a typical RS model can be defined as [Izhikevich, 2007, p. 282]:

$$\begin{aligned} 100\frac{dv}{dt} &= 0.7(v+60)(v+40) - u + I_{\text{dc}} \\ \frac{du}{dt} &= 0.03\,\{b(v+60) - u)\} \\ \text{if} \quad v \geq +35, \quad &\text{then} \quad v \leftarrow -50, \quad u \leftarrow u + 100 \end{aligned} \tag{3.3.1}$$

The slope of u-nullcline is controlled by b. This coefficient may have positive or negative values, based on rheobase[1] and the input resistance of the neuron. Depending on the sign of b, the depolarization of v decreases ($b < 0$) or increases ($b > 0$) the recovery current.

In the next sections I will show that the RS neuron shows low frequency fluctuations (Fig. 3.3) when $b < 0$ and is a so-called "integrator", while it demonstrates subthreshold oscillations (Fig. 3.5) for $b > 0$, and is called a "resonator".

3.3.1 Linear stability analysis of integrator RS neuron

I first derive the v- and u-nullcline equations in which the rates of change of the v and u variables are set respectively to zero:

$$\begin{aligned} (v\text{-nullcline}) \quad \frac{dv}{dt} = 0 \quad &\Rightarrow F_1(v,r) = \frac{1}{C}\{k(v-v_r)(v-v_t) - u + I_{\text{dc}}\} = 0 \\ (u\text{-nullcline}) \quad \frac{du}{dt} = 0 \quad &\Rightarrow F_2(v,r) = a\{b(v-v_r) - u\} = 0 \quad \Rightarrow u = b(v-v_r) \end{aligned} \tag{3.3.2}$$

These equations can be rearranged to give u as a function of v. This produces the (u, v) nullclines of Fig. 3.2(a). The location of the v-nullcline depends on I_{dc} (external dc current),

[1] The minimal amplitude of injected current (infinite duration) needed to fire a neuron [Izhikevich, 2007]

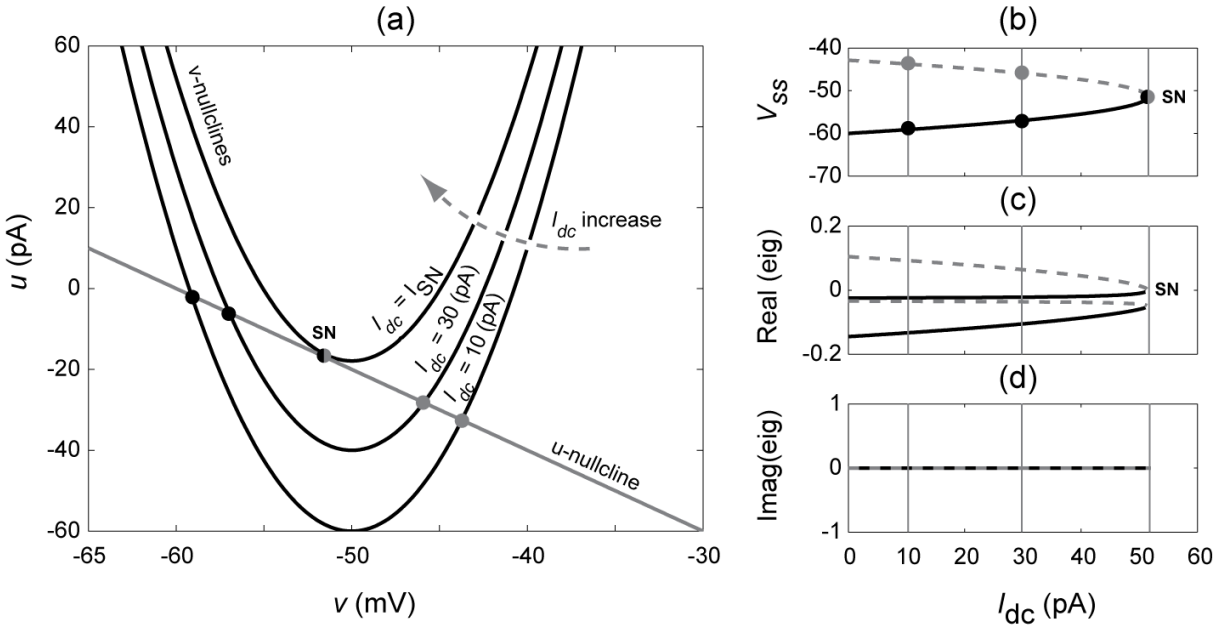

Figure 3.2: Linear stability analysis of the regular spiking (RS) cortical neuron of Eqs. (3.3.1) with $b = -2$. (a) The v (black) and u (gray) nullclines in $u - v$ plane. The intersection of nullclines locates the steady states. Increasing $I_{\rm dc}$ moves the v-nullcline upward. (b) Steady state diagram of the voltage $v_{\rm ss}$ as a function of $I_{\rm dc}$ and the corresponding real (b) and imaginary (c) parts of the system eigenvalues. The upper state (indicated by dashed line) is an unstable node; the bottom branch (solid line) is a stable node. The two branches approach each other and annihilate via saddle-node bifurcation at $I_{\rm dc} = I_{\rm SN}$ where $I_{\rm SN} \simeq 51.4285714285716$ pA.

moving upward with increasing $I_{\rm dc}$. By eliminating u in Eqs. (3.3.2) on obtains

$$kv^2 - v(k(v_t + v_r) + b) + kv_r v_t + v_r b + I_{dc} = 0 \tag{3.3.3}$$

which is the *characteristic* equation of the system giving the intersection point(s) of the two nullclines. The *steady-state* diagram can be extracted from Eq. (3.3.3) using a range of $I_{\rm dc}$ values. The result is displayed in Fig. 3.2(b) for $0 \le I_{\rm dc} \le 60$ pA.

We now linearize the model equations. The governing equations (3.2.1) can be written as

$$\begin{aligned} \frac{dv}{dt} &= F_1(v,u), \quad F_1(v,u) = \frac{1}{C}\left\{k(v - v_r)(v - v_t) - u + I_{\rm dc}\right\} \\ \frac{du}{dt} &= F_2(v,u), \quad F_2(v,u) = a\left\{b(v - v_r) - u\right\} \end{aligned} \tag{3.3.4}$$

We write $v(t) \to v_0 + \hat{v}(t)$ and $u(t) \to u_0 + \hat{u}(t)$ where v_0, u_0 are the stationary values and the $\hat{v}(t), \hat{u}(t)$ are small temporal perturbations of the form $\hat{v}(t) = \delta_v e^{\lambda_1 t}, \hat{u}(t) = \delta_u e^{\lambda_2 t}$ with $\delta_{v,u}$ and $\lambda_{1,2}$ being the amplitude and decay rate of the perturbations respectively. Thus Eqs. (3.3.4)

become

$$\begin{aligned} F_1(u,v) &= F_1(v_0+\hat{v}, u_0+\hat{u}) \\ F_2(u,v) &= F_2(v_0+\hat{v}, u_0+\hat{u}) \end{aligned} \tag{3.3.5}$$

Taylor expanding, and retaining only *linear* terms,

$$\begin{aligned} F_1(u,v) &\approx F_1(v_0,u_0) + \frac{\partial F_1}{\partial v}|_{v_0,u_0}\ \hat{v} + \frac{\partial F_1}{\partial u}|_{v_0,u_0}\ \hat{u} \\ F_2(u,v) &\approx F_2(v_0,u_0) + \frac{\partial F_2}{\partial v}|_{v_0,u_0}\ \hat{v} + \frac{\partial F_2}{\partial u}|_{v_0,u_0}\ \hat{u} \end{aligned} \tag{3.3.6}$$

Noting that $F_1(v_0,u_0) = F_2(v_0,u_0) = 0$, we obtain the linearised system

$$\begin{aligned} \frac{d}{dt}\hat{v} &= \frac{\partial F_1}{\partial v}|_{v_0,u_0}\ \hat{v} + \frac{\partial F_1}{\partial u}|_{v_0,u_0}\ \hat{u} \\ \frac{d}{dt}\hat{u} &= \frac{\partial F_2}{\partial v}|_{v_0,u_0}\ \hat{v} + \frac{\partial F_2}{\partial u}|_{v_0,u_0}\ \hat{u} \end{aligned} \tag{3.3.7}$$

which is equivalent to the matrix form

$$\frac{d}{dt}\begin{bmatrix} \hat{v} \\ \hat{u} \end{bmatrix} = \begin{bmatrix} \frac{\partial F_1}{\partial v} & \frac{\partial F_1}{du} \\ \frac{\partial F_2}{\partial v} & \frac{\partial F_2}{du} \end{bmatrix}_{|_o} \begin{bmatrix} \hat{v} \\ \hat{u} \end{bmatrix} = \mathbf{J}\begin{bmatrix} \hat{v} \\ \hat{u} \end{bmatrix}$$

where

$$\mathbf{J} = \begin{bmatrix} \frac{\partial F_1}{\partial v} & \frac{\partial F_1}{\partial u} \\ \frac{\partial F_2}{\partial v} & \frac{\partial F_2}{\partial u} \end{bmatrix}_{|_o} \tag{3.3.8}$$

is the *stability matrix* of (3.2.1) evaluated at the equilibrium point (v_0, u_0) with F_1, F_2 as derivative functions defined in Eqs. (3.3.4). The eigenvalues of J predict the exponential decay or growth of the system response to small fluctuations around the fixed points (steady-states). Negative values for the real parts of both eigenvalues indicates *stability* of the fixed point while a positive real part of either eigenvalues shows the fixed point is *unstable*. The real and imaginary parts of the eigenvalues are plotted in Fig. 3.2(c, d) respectively. The upper steady state (dashed line) has one real positive and one real negative eigenvalue, characteristic of an *unstable saddle* point. The lower branch (solid line) has a pair of real negative eigenvalues, indicating a *stable node*. The two steady states coalesce at $I_{\mathrm{dc}} = I_{\mathrm{SN}} = 51.4285714285716$ pA and annihilate through *saddle-node* bifurcation. For $I_{\mathrm{dc}} > I_{\mathrm{SN}}$ the two nullclines do not intersect and the state of the system grows without limit towards infinity. This divergence is taken to mean that a

spike event (action potential) has occurred. The Izhikevich model does not have an automatic mechanism to bring the state back to rest; this is why a manual reset is required.

3.3.2 Subthreshold dynamics of integrator RS neuron

In order to explore the dynamics of the RS neuron around its steady state, a white-noise input is added to the external current to render a stochastic version of the RS equations:

$$\begin{aligned} C\frac{dv}{dt} &= k(v-v_r)(v-v_t) - u + I_{\rm dc} + \sigma_v \xi(t) \\ \frac{du}{dt} &= a\left\{b(v-v_r) - u\right\} \\ \text{if} \quad v \geq v_{\rm peak}, \quad &\text{then} \quad v \leftarrow c, \quad u \leftarrow u + d \end{aligned} \tag{3.3.9}$$

where $\sigma_v \xi(t)$ is a small amplitude noise term with characteristics described in Section 3.1.

I perform a series of subthreshold stochastic experiments in which the $I_{\rm dc}$ is used as a control parameter to drive the system towards the threshold of saddle-node (SN) instability. The numerically obtained voltage fluctuations are plotted in Fig. 3.3(a). (The baseline of each trace has been offset to produce the stack graph for a simple visual comparison.) The same noise source is used for all twenty simulations. By increasing $I_{\rm dc}$ (upward arrow), the amplitude of the slow voltage fluctuations grows strongly.

I define ϵ as the normalized distance from $I_{\rm SN}$

$$\epsilon = \frac{I_{\rm SN} - I_{\rm dc}}{I_{\rm SN}} \tag{3.3.10}$$

and plot the logarithm of the variance of each voltage time-series versus corresponding $\log(\epsilon)$. The results are displayed in Fig. 3.3(b) with a dashed line superimposed on the variance values with the slope of -0.5. The logarithmic graph shows a dramatic increase in the variance of the noise-induced subthreshold voltage fluctuations on close approach to the spike generation via SN bifurcation. The slope of -0.5 is in agreement with theoretically reported values for SN bifurcation in the Wilson model of a human integrator spiking neuron [Steyn-Ross *et al.*, 2006], implying a power-law divergence in fluctuation variance,

$$\text{var}(v) \sim \frac{1}{\sqrt{\epsilon}} \tag{3.3.11}$$

This is a general result for any system approaching saddle-node bifurcation, and is valid not only for the Wilson and Izhikevich integrator neurons, but also for mean-field neural populations

such as Wilson-Cowan homogeneous cortex (Chapter 5) and 1-D cortical rod (Chapter 6).

Further analysis can be done on the fluctuation time-series by examining the autocorrelation and power spectrum. We find that the autocorrelation function gets larger and broader when approaching the SN threshold, consistent with a peaking of the spectral density at dc (e.g., see Fig. 3.1). These changes are characteristics of a well-known phenomenon in dynamical systems, namely *critical slowing down*, when the system becomes divergently slower in returning to steady state in response to a subthreshold perturbation.

3.4 RS Neuron as a resonator

It is informative to examine the subthreshold behaviour of the RS neuron when it is configured as a resonator. This is achieved by altering the sign of coefficient b in Eqs. (3.3.1): here we set $b = 5$. The resonator nullclines and steady states are displayed in Fig. 3.4(a), (b). The nullclines are similar to those for the integrator RS neuron, apart from the change in the slope of the u-nullcline. The linear stability eigenvalues are displayed in Fig. 3.4(c,d). The non-zero imaginary part of the eigenvalues in a certain range of $I_{\rm dc}$ implies a non-zero "resonance" frequency of noise-induced oscillations. The real parts of the eigenvalues indicate stability of bottom branch and instability of top branch of steady states.

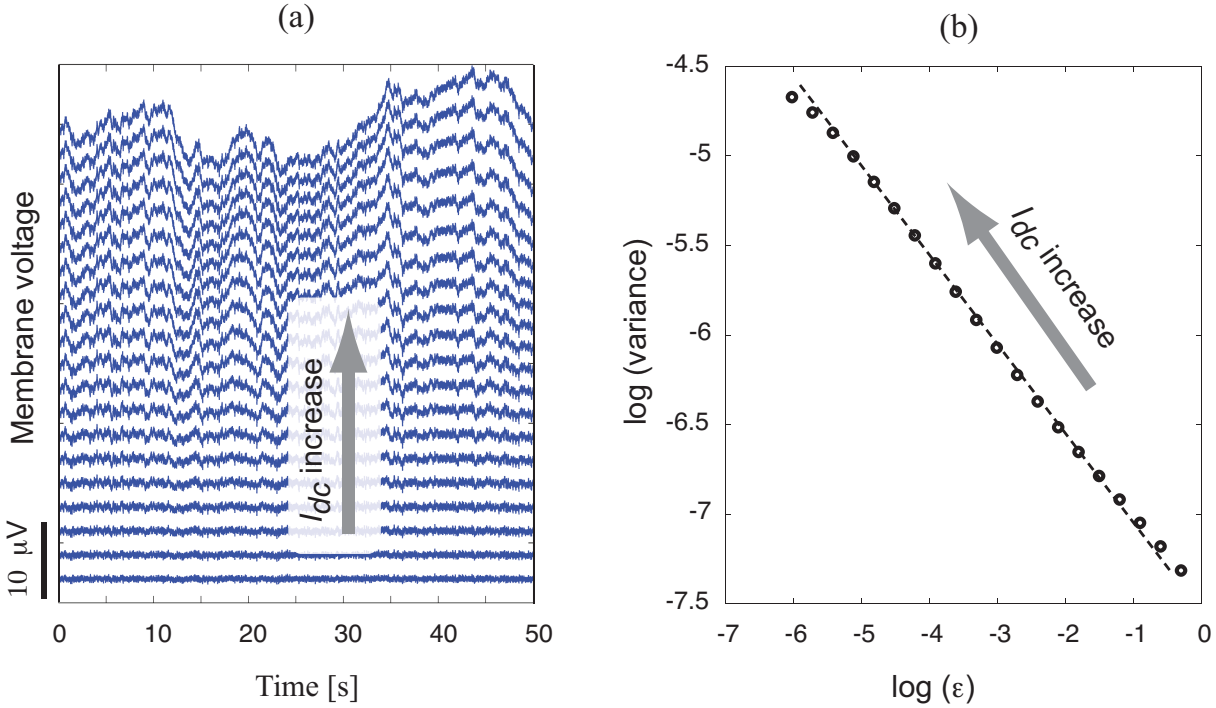

Figure 3.3: Subthreshold dynamics of a regular spiking (RS) neuron. (a) The subthreshold fluctuations of the soma voltage in an Izhikevich model of RS neuron. The traces represent soma voltages (shifted and stacked beside each other for visual comparison) for numerical simulations at 20 different $I_{\rm dc}$ values using an RK4 integrator with time-step $\Delta t = 0.05$ ms. (b) Logarithm of variance of fluctuations as a function of $\log(\epsilon)$ where $\epsilon_j = (-I_j + I_{\rm SN})/I_{\rm SN} = 1/4^j$ with $j \in \{1, 2, \ldots, 20\}$, and $I_{\rm SN} = 51.4285714285716$ pA. The superimposed dashed line has the slope of -0.5. The model parameters are as for Fig. 3.2.

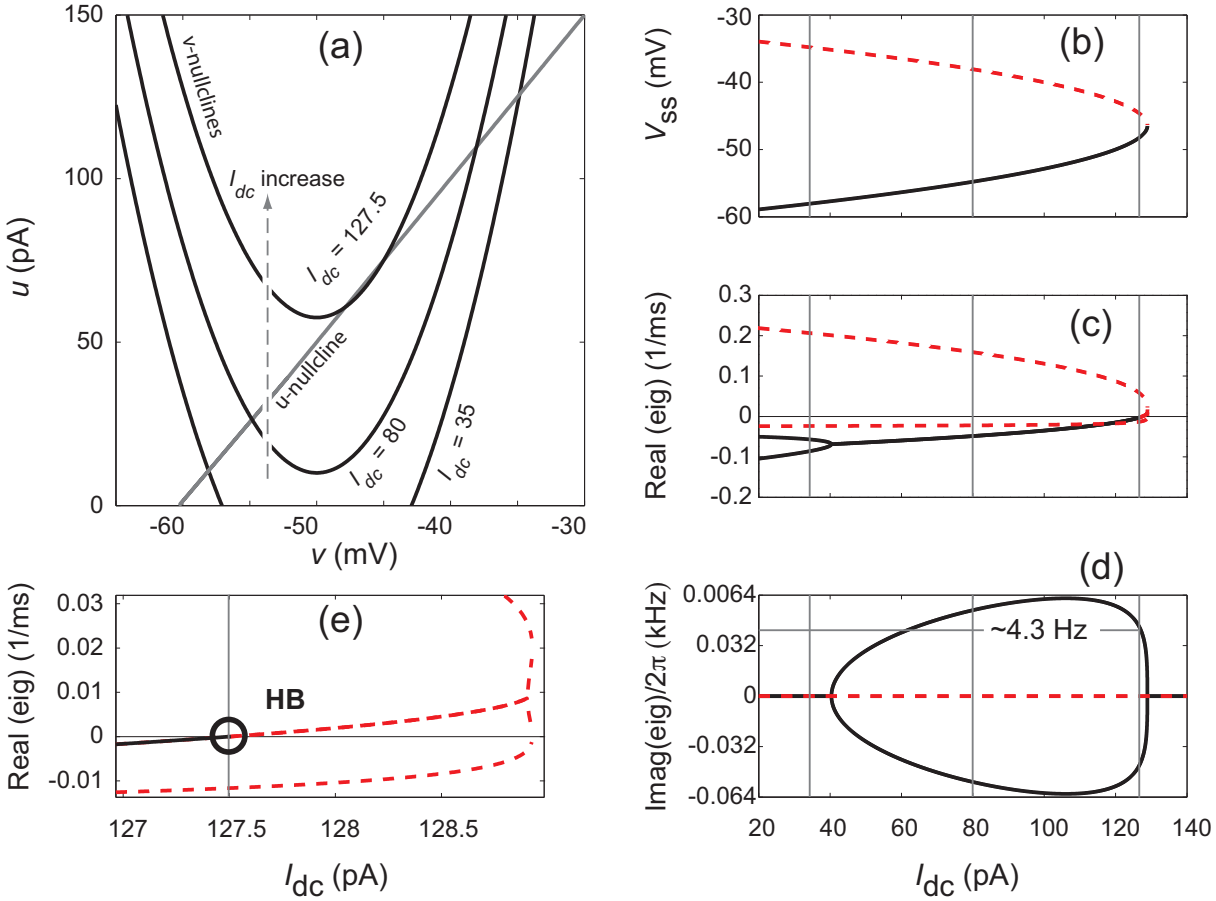

Figure 3.4: Linear stability analysis of the regular spiking (RS) cortical neuron model configured as a resonator. Model parameters are as Fig. 3.2 but with $b = 5$. (a) Nullclines of the system. (b) Steady states as a function of control current I_{dc}. Stable and unstable branches are indicated by solid and dashed lines respectively according to the real part of their corresponding eigenvalues as displayed in (c). (d) Scaled imaginary part of the eigenvalues, predicting the frequency of oscillations as a function of I_{dc}. (e) A detailed view of (c) at Hopf bifurcation (HB); the bottom branch loses stability at $I_{\mathrm{dc}} = I_{\mathrm{HB}} = 127.5$ pA and an action potential is fired.

As the I_{dc} control parameter is increased, the bottom branch undergoes a series of qualitative changes. The bottom branch is a stable node for $I_{\mathrm{dc}} \leq 40$ pA since its eigenvalues are real negative. Increasing I_{dc} gives birth to imaginary parts, changing the stable node to a stable spiralling-in *focus* point. The stable focus changes to an unstable spiralling-out point at $I_{\mathrm{dc}} = 127.5$ pA, since the real part of the eigenvalues become positive as displayed in Fig. 3.4(e). This qualitative change marks a *Hopf bifurcation* (HB), making the bottom branch unstable. Note that both branches are unstable now, and results in the firing of an action potential in the resonator RS neuron.

The subthreshold behaviour of the model is investigated numerically in a series of experiments in which the system is forwarded towards the HB point using I_{dc} as control parameter, while using the same white-noise sequences for all experiments. The results of Fig. 3.5(a) demonstrate pronounced growth in the amplitude of the subthreshold oscillations consistent with diminished resonator damping as the critical point is approached. This is particularly apparent in the

last four experiments displayed in Fig. 3.5(b), revealing emergence of ∼4.3 Hz oscillations as predicted by the linear stability analysis of Fig. 3.4(d). The time-course of the decaying envelope of these subthreshold oscillations is predicted by the real part of the dominant eigenvalue of Fig. 3.4 (c, e). Close approach to the HB point is associated with very small negative real parts of the eigenvalue implying a "slowed" system. Crossing the HB threshold changes the sign of real parts, allowing the subthreshold oscillations to grow unboundedly (resulting in spike generation).

The variance of the subthreshold oscillations is computed and displayed in Fig. 3.5(c) as a function of ϵ where the ϵ is defined as:

$$\epsilon = \frac{I_{\mathrm{HB}} - I_{\mathrm{dc}}}{I_{\mathrm{HB}}} \tag{3.4.1}$$

A significant increase in the variance is evident prior to HB point in the Izhikevich resonator. A dashed line with the slope of -1 is superimposed on the graph showing the same results as previously demonstrated by Steyn-Ross *et al.* [2006] for the Wilson resonator spiking neuron, and implies a power-law divergence:

$$\mathrm{var}(v) \sim \frac{1}{\epsilon} \tag{3.4.2}$$

as generally expected for a dynamical system with a Hopf bifurcation.

In the next section I present a modified form of the RS neuron capable of producing a complex dynamics known as burst-suppression. The subthreshold behaviour of the model will also be studied briefly.

3.5 Modified RS neuron showing burst-suppression (BS) pattern

In this section a modified form of RS resonator neuron is presented which is capable of producing *burst-suppression* (BS) patterns at hyperpolarized membrane potentials[1]. The working mechanism underlying the BS pattern is adopted from works by Cunningham *et al.* [2006] and Ching *et al.* [2012]. These authors model BS using a Hodgkin-Huxley formalism in which the equation for the membrane voltage is,

$$C\frac{dV}{dt} = I_{\mathrm{dc}} - I_{\mathrm{Na}} - I_{\mathrm{K}} - I_{\mathrm{K_{ATP}}} - I_{\mathrm{leak}}$$

[1]See Section 2.2.3 of Chapter 2 for a description of burst-suppression.

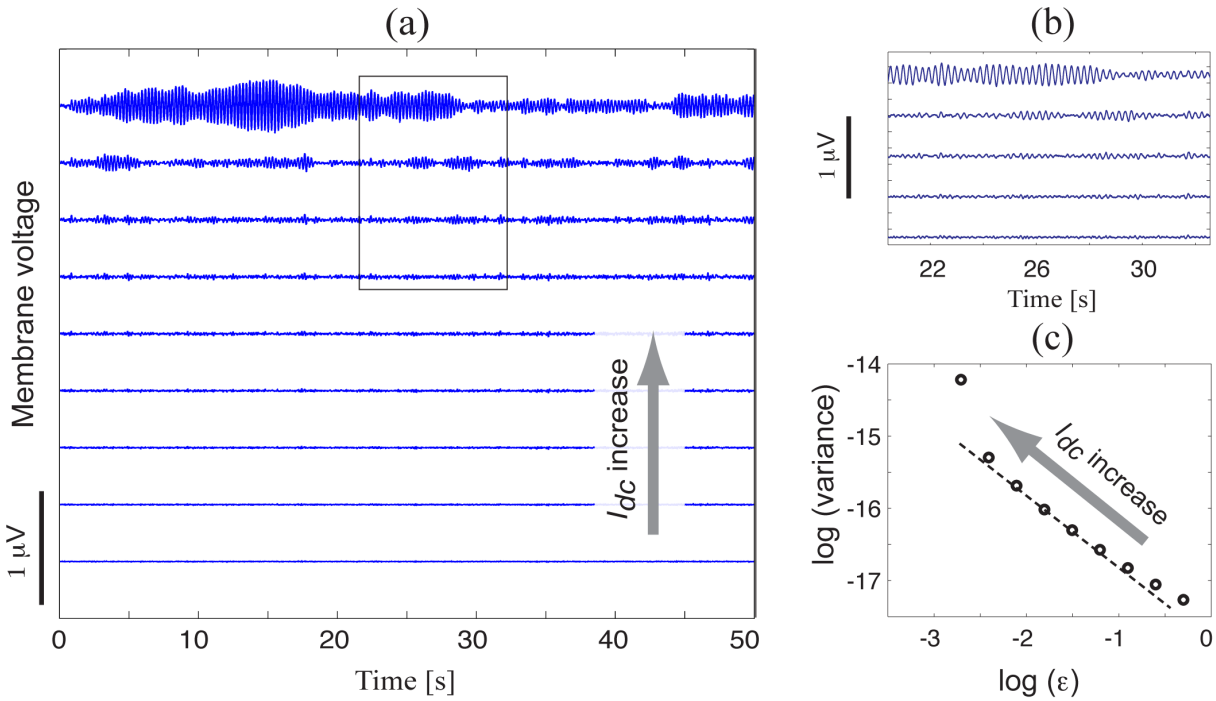

Figure 3.5: Subthreshold dynamics of Izhikevich regular spiking (RS) resonator neuron. (a) White noise-induced subthreshold oscillations while the model is forwarded towards Hopf bifurcation (HB) by stepped increases of I_{dc}. (b) Details of subthreshold oscillations prior to HB showing oscillations with frequency $f \simeq 4.3$ Hz for the top trace. (c) Fluctuation variance corresponding to time-series in (a) as a function of $\log(\epsilon)$ showing a dramatic increase while approaching HB at $I_{\mathrm{dc}} = I_{\mathrm{HB}}$ where $I_{\mathrm{HB}} \simeq 127.5$ pA.

See Cunningham *et al.* [2006]; Ching *et al.* [2012] for the sodium, potassium and leakage currents. The ATP-gated potassium membrane current is,

$$I_{\mathrm{K_{ATP}}} = g_{\mathrm{K_{ATP}}} z (V - E_{\mathrm{K}}) \tag{3.5.1}$$

in which the gating variable z of ATP-sensitive potassium channels depends on ATP concentration:

$$z = \frac{1}{1 + 10[\mathrm{ATP}]} \tag{3.5.2}$$

The concentration of ATP is related to intracellular concentration of sodium ions [Na] and the sodium ionic current I_{Na}, obeying the following differential equations:

$$\begin{aligned} \frac{d[\mathrm{Na}]}{dt} &= F.I_{\mathrm{Na}} - 3K_m[\mathrm{Na}]^3[\mathrm{ATP}] \\ \frac{d[\mathrm{ATP}]}{dt} &= J_{\mathrm{ATP}}([\mathrm{ATP}]_{\max} - [\mathrm{ATP}]) - K_m[\mathrm{Na}]^3[\mathrm{ATP}] \end{aligned} \tag{3.5.3}$$

where $F = 8.8 \times 10^{-5}$ mM·(ms)$^{-1}$(pA)$^{-1}$ is the surface factor (which transforms sodium ionic flow to intracellular concentration), and $K_m = 6 \times 10^{-8}$ (mM)$^{-3}$·(ms)$^{-1}$ is the kinetic constant

of Na^+/K^+-ATPase pump (the main energy consumer neural element [Ames III, 2000]). The parameter $J_{\rm ATP}$ is the production rate of ATP, directly coupled to cerebral metabolism. Manipulation of this parameter could be a proxy for changes in metabolic rate. The baseline value set to $J_{\rm ATP} = 2 \times 10^{-4}$ $(\text{ms})^{-1}$ and is increased over the range of $30 - 50\%$ of baseline to model the *decrease* in metabolic rate due to the effect of anaesthetics and hypothermic effects on cerebral metabolism.

In this section I demonstrate how the mechanism of BS pattern generation can be embedded into an Izhikevich-based model for the cortical RS neuron. We note that the individual ionic currents are not declared explicitly in the Izhikevich scheme: the recovery current u represents the sum of all inward and outward ionic currents. However Eqs. (3.5.1–3.5.3) show the dependence of $I_{\rm K_{ATP}}$ current on [ATP] concentration, which is related to concentration of intracellular sodium [Na], and consequently to the sodium current $I_{\rm Na}$. As a result, the $I_{\rm Na}$ current needs to be incorporated into the Izhikevich model. I choose to represent the $I_{\rm Na}$ current as,

$$I_{\rm Na} \simeq u - u_{\rm ss}$$

i.e., as a departure of u from its steady-state value $u_{\rm ss}$, obtained by setting $du/dt = 0$ in second equation of Eqs. (3.2.1) to give

$$\begin{aligned} \frac{du}{dt} = 0 \quad &\Rightarrow \quad a\{b(v - v_r) - u_{\rm ss}\} = 0 \\ &\Rightarrow \quad u_{\rm ss} = b(v - v_r) \end{aligned}$$

Based on this simplification I propose the following equations for a single pyramidal cell capable of producing a burst suppression pattern at lowered metabolism rates,

$$\begin{aligned} &C\frac{dv}{dt} = k(v - v_r)(v - v_t) - u + I_{\rm dc} + I_{\rm K_{ATP}} + \text{noise} \\ &\frac{du}{dt} = a\{b(v - v_r) - u\} \\ &I_{\rm K_{ATP}} = g_{\rm K_{ATP}} z(v - E_{\rm K}) \\ &z = \frac{1}{1 + 10[\text{ATP}]} \\ &\frac{d[\text{Na}]}{dt} = F.(u - u_{\rm ss}) - 3\text{K}_m[\text{Na}]^3[\text{ATP}] \\ &\frac{d[\text{ATP}]}{dt} = J_{\rm ATP}([\text{ATP}]_{\rm max} - [\text{ATP}]) - K_m[\text{Na}]^3[\text{ATP}] \\ &\text{reset rule:} \quad v \leftarrow -75 \text{ mV}, \quad u \leftarrow u + 100, \quad \text{when} \quad v \geq 35 \text{ mV} \quad \text{(spike cutoff)} \end{aligned} \tag{3.5.4}$$

Table 3.1: Variables (Var) and parameters (Par) of bursting cortical pyramidal neuron based on Izhikevich formalism

Var/Par	Description	Value	Unit
v	membrane potential		mV
u	recovery variable, representative of summation of all all inward and outward ionic currents of membrane		pA
u_{ss}	steady state of recovery variable (used in [ATP] equations)		pA
C	membrane capacitance	100	pF
k	scaling factor, affects the spike width	0.7	mS/mV
v_r	resting membrane potential	-90	mV
v_t	instantaneous threshold potential	-70	mV
I_{dc}	externally applied dc current	127.5	pA
a	rate constant of recovery currents	0.03	$(\text{ms})^{-1}$
b	sensitivity of recovery current to subthreshold membrane fluctuations	5	nS
v_{peak}	spike cutoff value	35	mV
c	voltage reset value	-75	mV
d	reset value of recovery variable	100	pA
$I_{\text{K}_{\text{ATP}}}$	ATP-sensitive potassium current		pA
$g_{\text{K}_{\text{ATP}}}$	maximum conductance of ATP-sensitive K channels	3	nS
z	gating variable of ATP sensitive potassium channels		dimensionless
E_{K}	potassium channel reversal potential	-80	mV
[Na]	concentration of intracellular sodium		mM
[ATP]	concentration of intracellular ATP		mM
$[\text{ATP}]_{\text{max}}$	maximum concentration of intracellular ATP	2	mM
F	surface factor, converts sodium influx to intracellular concentration	2×10^{-4}	$\text{mM}\cdot(\text{ms})^{-1}(\text{pA})^{-1}$
K_m	kinetic constant of NaK-ATPase	3×10^{-6}	$(\text{mM})^{-3}\cdot(\text{ms})^{-1}$
J_{ATP}	production rate of ATP, a surrogate for metabolic rate	2×10^{-4}	$(\text{ms})^{-1}$

See Table 3.1 for definition and parameter values. The values of some parameters differ from the original resonating RS model. These modifications were applied in order to construct an RS model capable of producing a BS pattern under deep anaesthesia. Cortical RS neurons are known to hyperpolarize by about 25–30 mV during BS generation [Steriade *et al.*, 1994]. As a result I lowered the resting membrane potential to $v_r = -90$ mV. Consequently the corresponding spike threshold potential, and the voltage reset values, were set to new values of $v_t = -70$ and $c = -75$ mV respectively.

The resultant 4^{th}-order model is an example of a *fast-slow* bursting system, composed of fast and slow variables with drastically different time courses. The fast subsystem is composed of v, u and [Na] variables while the slow variable is [ATP] level. The time course of the slow subsystem is determined by $J_{\text{ATP}} = 2 \times 10^{-4}$ $(\text{ms})^{-1}$. Such a bursting model can be dissected by freezing the slow variable and using it as the bifurcation parameter to control the the fast subsystem [Izhikevich, 2007, ch. 9]. The v- and u-nullclines of the fast subsystem can be extracted by assuming a fixed value for the slow variable [ATP] and the resultant $I_{\text{K}_{\text{ATP}}}$. According to the

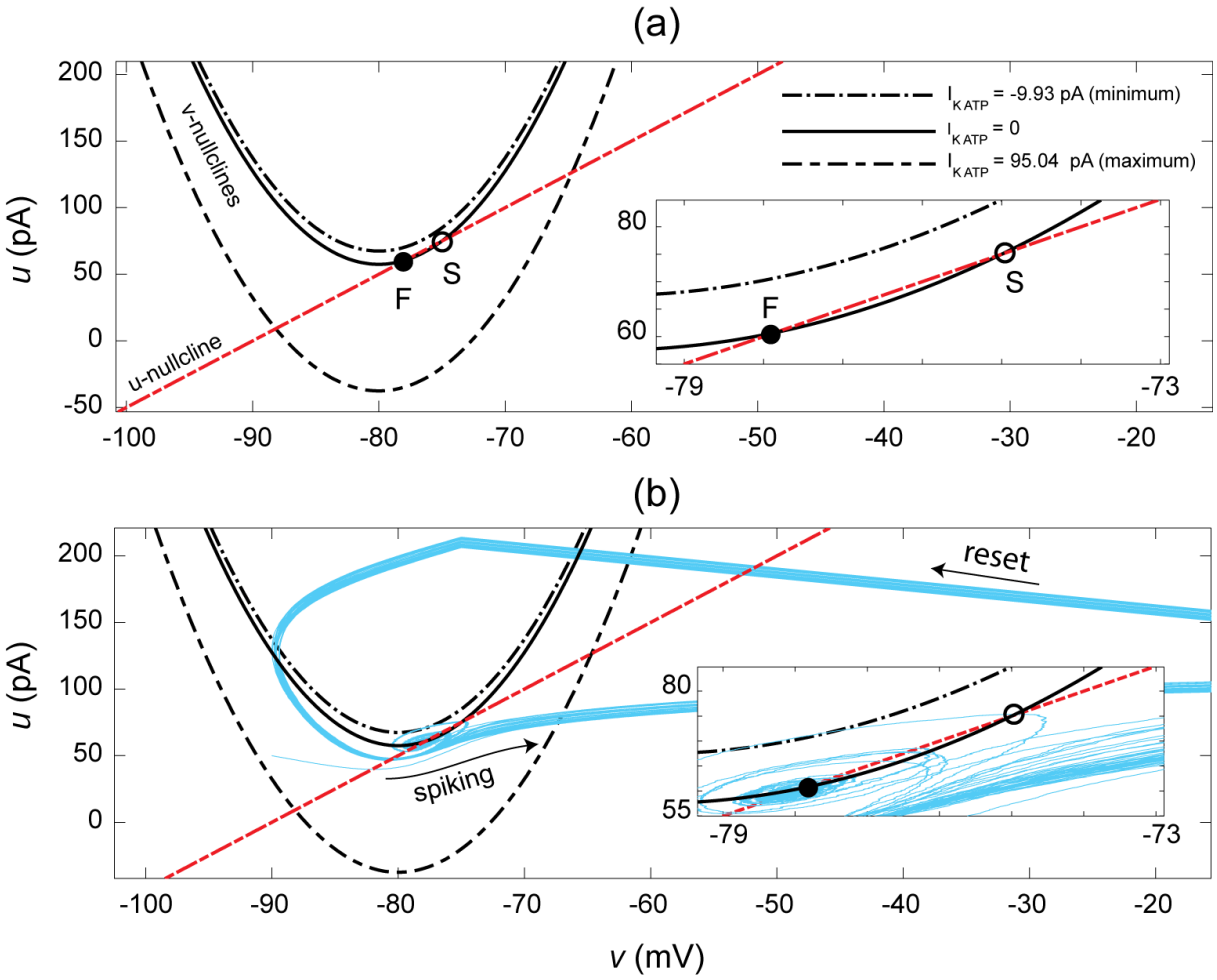

Figure 3.6: Nullclines and trajectories of a hyperpolarized regular spiking (RS) resonator neuron capable of producing burst suppression (BS) pattern as described by Eqs. (3.5.4). (a) The nullclines and their intersections resulting in the generation of a stable spiralling-in focus (F) and unstable saddle (S). The v-nullcline moves vertically according to the variation of slow variable [ATP] or the corresponding $I_{\mathrm{K_{ATP}}}$ values. Considering the numerically obtained range of values for $I_{\mathrm{K_{ATP}}}$, three v-nullclines are superimposed in the figure. (b) The numerically obtained trajectories of the model are superimposed on the nullclines. A fourth-order Runge-Kutta integrator (time step $\Delta t = 0.1$ ms) is used to solve the model equations. See Table. 3.1 for parameter values.

model equations (3.5.4), the variation in the slow variable induces a vertical shift of the v-nullcline. Considering this effect, the nullclines of the model are extracted and displayed in Fig. 3.6(a). Similar to the original resonating RS neuron, the u-nullcline is a line with slope of $b = 5$, and the v-nullcline is a parabola. Using the numerically obtained values for $I_{\mathrm{K_{ATP}}}$, three v-nullclines are plotted in the figure.

When $I_{\mathrm{K_{ATP}}} = 0$, the system is equivalent to the original resonating RS model. As demonstrated for the resonator RS model in Fig. 3.4, the two intersections can be shown to be a stable spiralling-in focus and an unstable saddle point (F and S in the figure respectively). As shown in Fig. 3.6, the revised model parameters lets the system rest at a hyperpolarized membrane potential corresponding to the stable node at $v = -78.5$ mV. The metabolic rate is

low in the hyperpolarized state, so the ATP level slowly recovers to its base value, corresponding to slow *decrease* in $I_{\mathrm{K_{ATP}}}$ (according to the inverse relationship between [ATP] and $I_{\mathrm{K_{ATP}}}$ in (3.5.4), fourth equation). When the ATP-sensitive potassium current reaches its minimum point $I_{\mathrm{K_{ATP}}} = -9.93$ pA, a Hopf bifurcation has already happened, and the stable focus point has changed to an unstable one and then disappeared (similar dynamics as displayed in Fig. 3.4(e)). The v- and u-nullclines do not intersect for $I_{\mathrm{K_{ATP}}} = -9.93$ pA, and the system is unstable. As a result the system starts firing a burst of action potentials.

The generation of action potentials quickly consumes the available ATP which is equivalent to the uptake of $I_{\mathrm{K_{ATP}}}$. This uptake shifts the v-nullcline downward, until two nullclines intersect again, and a new stable focus point is formed. The v-nullcline corresponding to the maximum value of the $I_{\mathrm{K_{ATP}}}$ is also displayed in the Fig. 3.6(a). The numerically obtained $v-u$ trajectory is superimposed on the nullclines and displayed in Fig. 3.6(b). The inset shows that the system is resting around the stable spiralling-in focus point (black circle)[1]. The uptake of ATP makes the focus unstable, and the trajectories grow outwardly towards the spiking threshold, and the system starts another cycle of bursting.

The mechanism of BS generation, maintenance and termination in this model are well illustrated in time-series for membrane potential, intracellular Na and ATP levels, and the corresponding $I_{\mathrm{K_{ATP}}}$ values: see Fig. 3.7. Performing a numerical simulation for 200 s results in the BS pattern generation by an RS neuron as displayed in in (a). In agreement with *in vivo* observations (see Figure 1 in Liley and Walsh [2013] and related citations), variability is apparent in the duration of the suppressed or isoelectric period.

Two bursts are selected from (a) and displayed in (b) with the inset showing the close-up view of the suppressed period in which the RS neuron shows subthreshold oscillations that are closely similar to those of Fig. 3.5 for the standard two-variable resonator RS neuron. Note that it is possible to demonstrate the occurrence of critical slowing-down in this system as well. One can freeze the slow variable [ATP], and analyze the subthreshold oscillations of the system while forwarding it towards Hopf bifurcation. The results are expected to be similar to the subthreshold behaviour of the resonating RS neuron of Sect. 3.4.

The corresponding intracellular ATP level and the sodium concentration are displayed in Fig. 3.7(c). The ATP (dashed line) is consumed during the bursting phase, and recovers slowly to its baseline value during the quiescent phase of the BS pattern. The [Na] increases while bursting, and returns to baseline during the quiescent period. The last trace (d) displays the variations in the $I_{\mathrm{K_{ATP}}}$ level. It is interesting to contrast the slow evolution of [ATP] with the

[1]Note that white noise is applied to the system. As a result the trajectories contain noisy fluctuations.

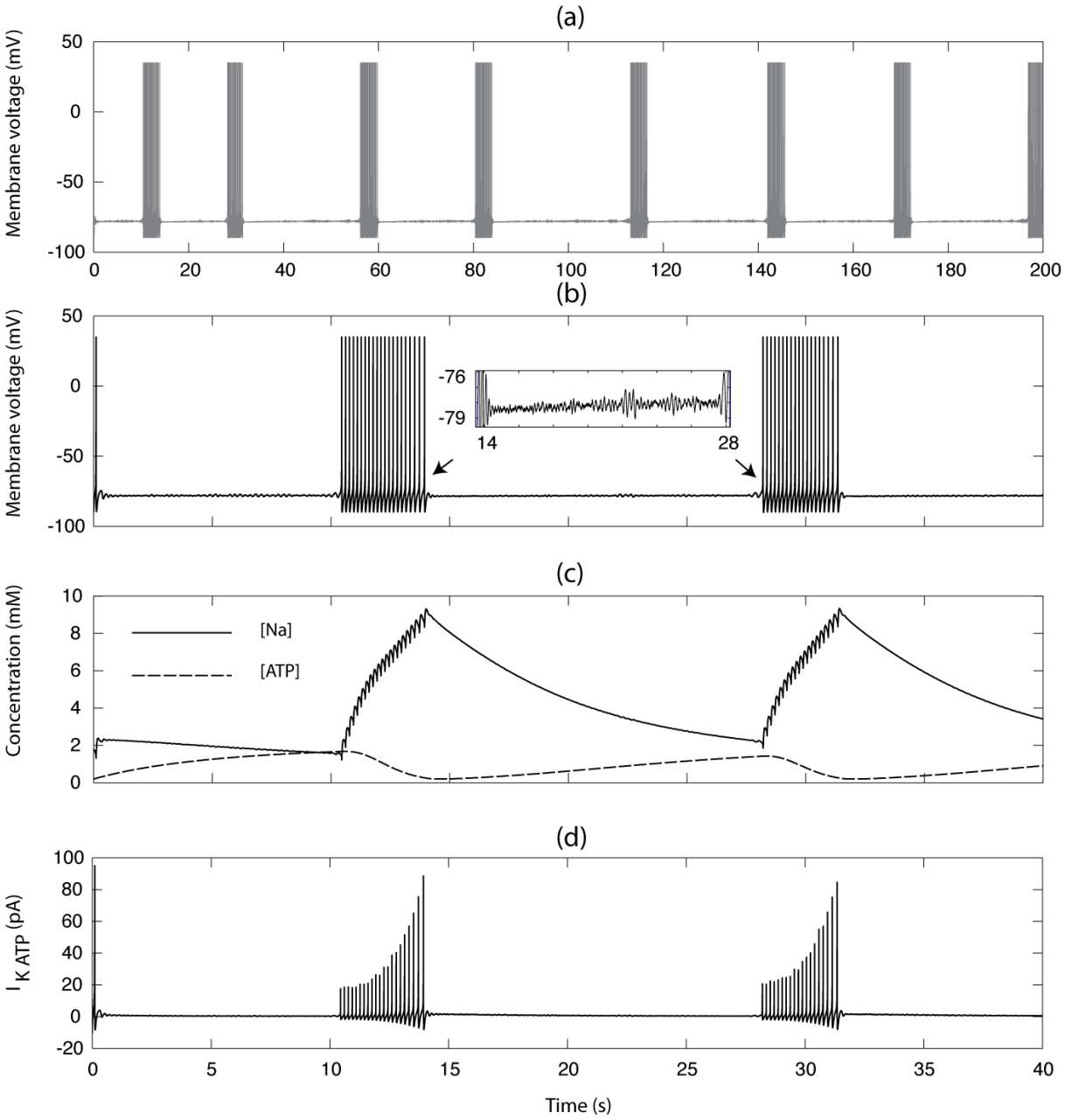

Figure 3.7: Bursting regular-spiking cortical neuron as described by Eqs. (3.5.4) and Table 3.1. (a) Membrane potential of RS neuron showing burst of action potentials with variable length of quiescent periods. (b) A detailed view of two bursts from (a) showing the growth in the subthreshold fluctuations prior to burst generation. (c, d) The corresponding intracellular [Na] concentration, [ATP] level and the ATP-gated potassium current $I_{\mathrm{K_{ATP}}}$. Numerical simulation method is as in Fig. 3.6.

much faster time course of v illustrating clearly the fast-slow dynamics that drives this bursting model.

3.6 Fast spiking (FS) cortical interneurons

The fast spiking (FS) interneurons are the prevalent type of inhibitory neuron in the neocortex and hippocampus, comprising ∼20% of the population of all inhibitory neurons [Kann *et al.*,

2014]. These neurons play an essential role in generation of *gamma oscillations*[1] and can fire up to hundreds of spikes per second during gamma oscillations (hence "fast-spiking"). These neurons also exhibit resonator behaviour (subthreshold oscillations with non-zero frequency and discontinuity in their frequency-current relation), stuttering (random switching between spiking and quiescence) and lack of rebound or post-inhibitory spikes (firing after strong hyperpolarization) [Izhikevich, 2007]. Based on these characteristics Izhikevich [2007] introduced his FS model as

$$
\begin{aligned}
&20\frac{dv}{dt} = (v+55)(v+40) - u + I_{\mathrm{dc}} \\
&\frac{du}{dt} = 0.2\left\{U(v) - u\right\} \quad , U(v) = \begin{cases} 0 & \text{if } v \le v_{\mathrm{b}} \\ 0.025(v - v_{\mathrm{b}})^3 & \text{otherwise} \end{cases} , \; v_{\mathrm{b}} = -55 \text{ mV} \\
&\text{reset rule:} \quad v \leftarrow -45 \text{ mV when } v \ge 25
\end{aligned}
\tag{3.6.1}
$$

with a nonlinear u-nullcline to prevent formation of rebound spike [Izhikevich, 2007].

Following the method introduced in Section 3.3.1, I perform a linear stability analysis on FS neuron. The results of the analysis are displayed in Fig. 3.8, with the steady state diagram of v_{ss} as a function of I_{dc} in (a), and the corresponding real and imaginary parts of eigenvalues of the stability matrix in (b), (c) respectively. Considering the structure of the eigenvalues, one observes occurrence of a Hopf bifurcation (HB) where the real parts of complex eigenvalues change sign at $I_{\mathrm{HB}} \simeq 73.6843750000033$ pA.

I selected four qualitatively different regions of the steady-state diagram corresponding to $I_{\mathrm{dc}} = 20, 73, 74, 90$ pA, indicated by vertical dashed lines in Fig. 3.8 (a-c) marked ①, ②, ③, and ④. The corresponding v- and u-nullclines (black dashed and solid lines respectively) for selected I_{dc} values are plotted in Fig. 3.9 (a-d). For $I_{\mathrm{dc}} = 20$ pA, the two nullclines plotted in (a) have an intersection with two real negative eigenvalues, characteristic of a stable node. A numerically obtained trajectory (blue trace) with an arbitrary starting point (grey circle) is superimposed on the phase plane diagram, showing attraction to the stable node. When the drive current is increased to $I_{\mathrm{dc}} = 73$ pA, the v-nullcline shifts upward and the steady state becomes a stable *focus*. This is confirmed with a numerical simulation showing that a trajectory starting from the vicinity of intersection is attracted spirally into the steady state as displayed in (b). Panel (c) shows the system dynamics when the intersection is an unstable *spiraling out focus* point

[1] Gamma oscillations (frequency range ∼30-100 Hz) are the hallmarks of consciousness and higher cognitive tasks. See Sections 2.2.1, 4.3.

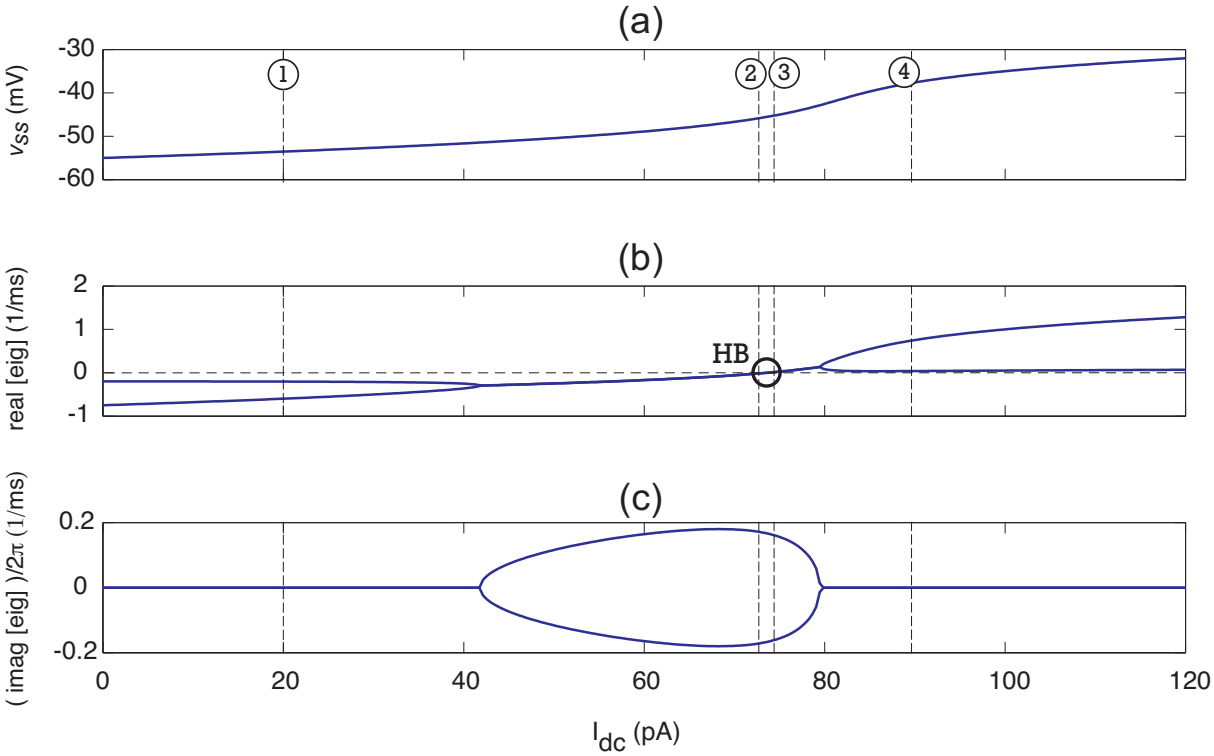

Figure 3.8: Steady states of the fast spiking (FS) cortical neuron. (a) Steady-state voltage as a function of external stimulus current. (b, c) Corresponding real and imaginary parts of the eigenvalues of system. The real parts changes sign at $I_{\rm dc} = I_{\rm HB} \simeq 73.6843750000033$ pA, via Hopf bifurcation (HB).

corresponding to $I_{\rm dc} = 74$ pA. A typical trajectory, started in the vicinity of the intersection, spirals out (not visible in the figure) and grows to full-scale tonic spiking. Considering the eigenvalues for $I_{\rm dc} = 90$ pA, the steady state is an unstable node. All trajectories are repelled away from this steady state (without subthreshold oscillation) and grow to full amplitude spikes as displayed in (d).

The corresponding voltage time-series are displayed in (e-h). Note the existence of subthreshold oscillations in (f), and (g) with frequency of $f \simeq 27.3$ and 26 Hz respectively. These numerically obtained frequencies are in agreement with the theoretical predictions as displayed in Fig. 3.8 (c) as the scaled (divided by 2π) imaginary part of corresponding eigenvalues.

A similar approach as presented in Section 3.3.2 can be employed to analyze the subthreshold response of the FS neuron to small white-noise stimulation during approach to the HB point. One can observe signs of critical slowing down prior to state transition in the FS neuron; these are comparable to those seen in the resonator RS neuron shown in Fig. 3.5.

3.7 Thalamocortical (TC) relay neurons

Thalamocortical (TC) relay neurons are a type of excitatory thalamic neuron that projects sensory information to the cortex. These neurons have two functional modes, *tonic firing* and *bursting*. Izhikevich [2007] presented a simple model of a "typical" TC neuron as,

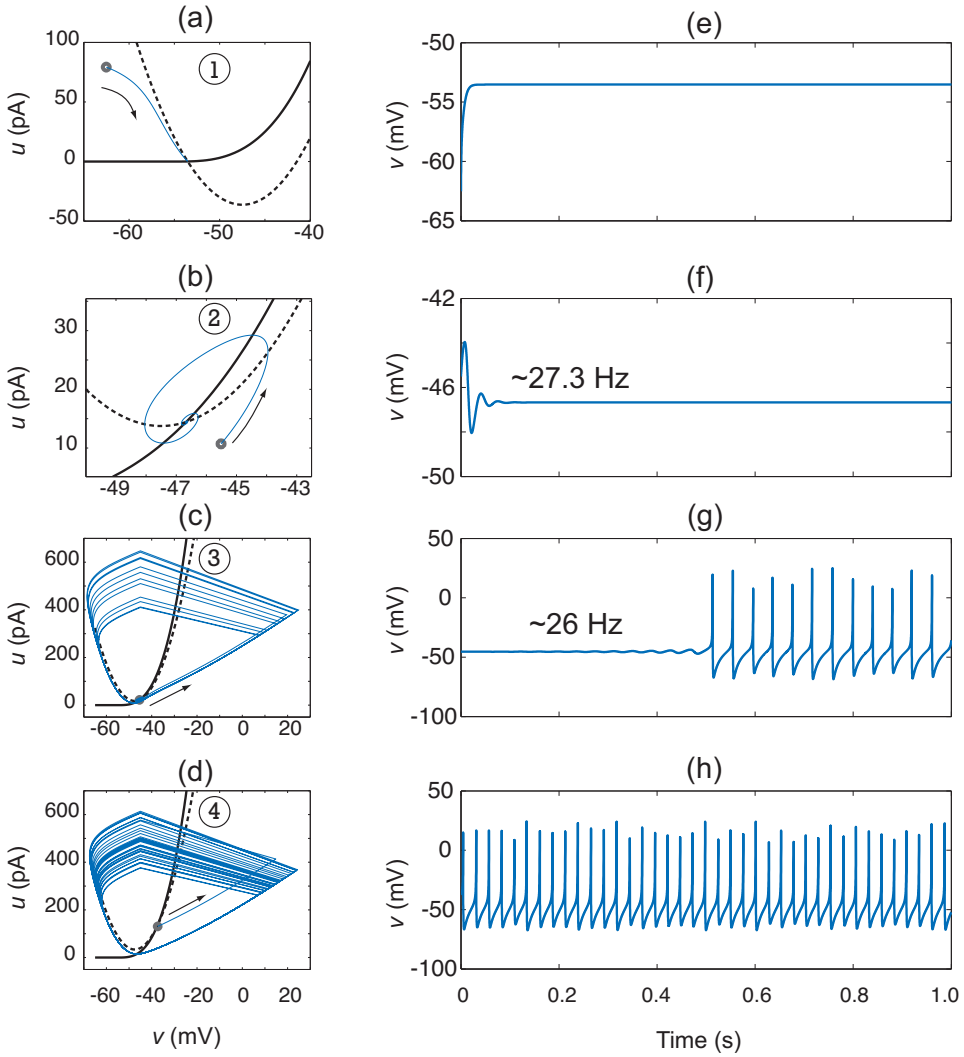

Figure 3.9: Numerical analysis of fast spiking (FS) cortical neuron. Numerical simulation of FS neuron at four selected $I_{\rm dc}$ values (marked ①, ②, ③, and ④) in Fig. 3.8; resulting $v-u$ trajectories (blue) are superimposed on the corresponding v- and u-nullclines (black solid and dashed respectively) in phase planes of (a-d). An RK4 integrator with time step $\Delta t = 0.1$ ms was used. See text for the values of selected dc current. The corresponding voltage traces are plotted in right panels, showing sub- (e, f) and supra-threshold (g, h) response of FS neuron.

$$
\begin{aligned}
200\frac{dv}{dt} &= 1.6(v+60)(v+50) - u + I_{\rm dc} \\
\frac{du}{dt} &= 0.01\left\{b(v+65) - u\right\}, \quad b = \begin{cases} 15 & \text{if } v \le -65 \text{ mV} \\ 0 & \text{otherwise} \end{cases} \\
&\text{reset rule: } v \leftarrow -60 - 0.1u,\ u \leftarrow u + 10, \text{ when } v \ge 35 + 0.1u
\end{aligned}
\tag{3.7.1}
$$

Figure 3.10(a) displays the v-nullcline ($dv/dt = 0$) and u-nullcline ($du/dt = 0$) of this model. The u-nullcline is a piecewise linear function, and is designed to provide both the tonic and bursting firing patterns of the TC neuron. The "spike cutoff" and the "reset" lines are superimposed. Although a theoretical eigenvalue analysis can be done on the model in two

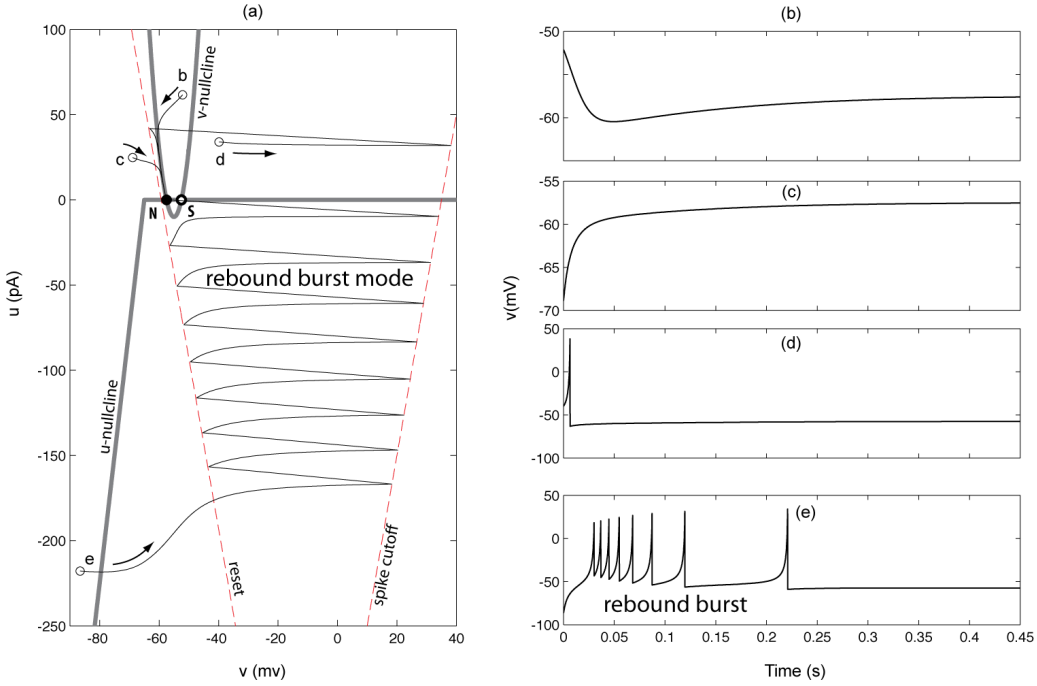

Figure 3.10: The response of Izhikevich model of thalamocortical (TC) relay neuron to different initial soma voltages prior to saddle-node bifurcation. (a) The nullclines (thick grey), reset and spike cutoff lines (dashed) of the model described by Eq. (3.7.1). The model is in a subthreshold mode prior to saddle-node (SD) bifurcation set by $I_{\rm dc} = 30$ pA. The result of four numerical simulations of the model starting from different points are displayed in (b-e). (b, c) Initial values are in the attraction domain of the node (N) point and the trajectories are attracted to the stable node point. When the initial state of the model is out of the attraction domain of N, the trajectories travel towards the "spike cutoff" threshold, where they are instantaneously reset. Note the firing of rebound burst of spikes in (e).

different ranges of v (corresponding to linear pieces of u-nullcline) to determine stability, a qualitative approach can also be employed. In the latter method one numerically obtains the trajectories of the model starting from different regions of the phase-plane. By performing a set of such experiments, one can infer the type of steady points. None of these analyses are shown here, but the result of the numerical approach identifies the node and saddle points, and are displayed as **N** and **S** in Fig. 3.10(a).

After selecting four initial points on different regions of the phase-plane, a series of numerical simulations are performed and the results are shown as the trajectories in (a) and the corresponding voltage time series in (b) to (e). The trajectories in (b) and (c) are attracted to the node, indicating that the attraction domain of the node includes (c) and (b) points in Fig. 3.10(a). If the starting point of the trajectories is beyond the attraction domain of the stable steady-state (d, e), then the trajectories go towards the spike cutoff line, and then reset according. This can result in the firing of a burst of rebound spikes as shown in (e).

Let us study the suprathreshold response of the model when $I_{\rm dc} > I_{\rm SN}$ and the saddle-node bifurcation has already occurred, so the system does not have any steady state. This is shown in Fig. 3.11(a) as the nullcline diagram, and the two selected trajectories. Since there is no

attracting steady-state, the trajectories are increased unboundedly, until they reach the spike cutoff line and then reset.

The "reset ↻ cutoff" loop may repeat several times before the attraction of the trajectories to the tonic spiking limit-cycle. Depending on the start point of the trajectories (determined by the level of hyperpolarization of v, and the value of the recovery variable u), the TC neuron expresses a tonic firing mode (b), or a rebound burst followed by regular tonic mode (c).

3.8 TC neuron with hyperpolarization-activated cation current

The original Izhikevich model of the TC neuron was introduced in the previous section. However it is known that TC neuron is driven by a slow hyperpolarization activated cation current, I_h. Briefly, the Na^+ and K^+ ions flow into the neuron via activated I_h channels in response to membrane hyperpolarization. *In vitro* experiments show that blockade of the I_h current by application of cesium results in elimination of *spindle*-like[1] and slow oscillations in hyperpolarized TC neurons [Destexhe and Babloyantz, 1993]. As a result I_h is believed to have a key role during spindle generation [Destexhe and Babloyantz, 1993; Steriade and McCarley, 2005]. This section presents an extended model of TC neuron including I_h current.

To incorporate the dynamics of the I_h current in the model thalamocortical neuron, I added a third differential equation to augment the original two-variable model:

[1]Spindles are hallmarks of early stages of the slow-wave sleep and are modelled in Section 4.4 of this thesis.

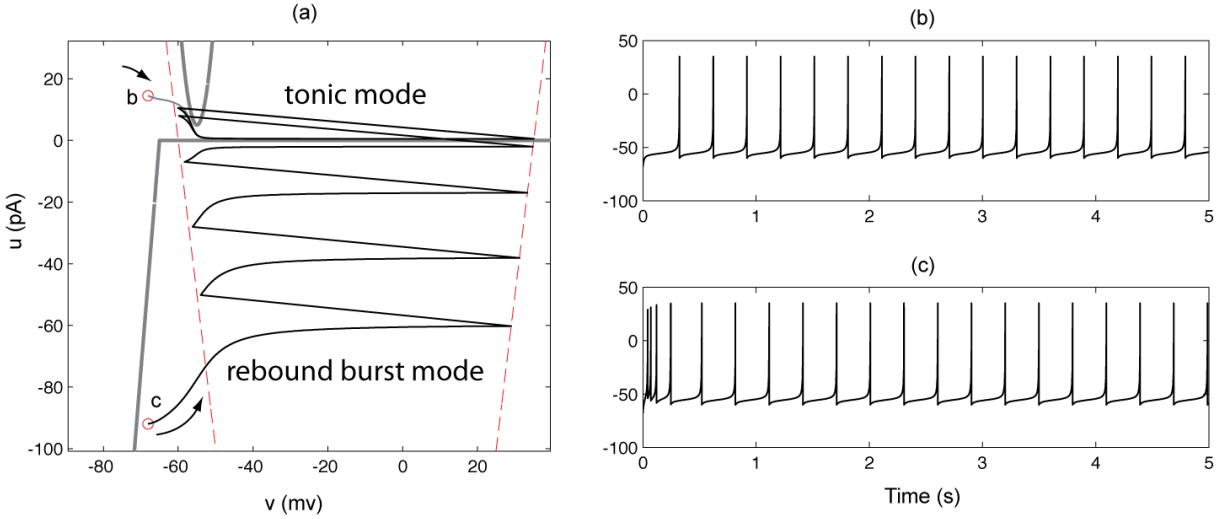

Figure 3.11: The response of Izhikevich model of thalamocortical (TC) relay neuron to different initial soma voltages in suprathreshold regime

Table 3.2: Variables (Var) and parameters (Par) of hyperpolarization-activated thalamocortical relay neuron based on Izhikevich formalism

Var/Par	Description	Value	Unit
v	membrane potential		mV
u	recovery variable, representative of summation of all inward and outward ionic currents		pA
I_h	hyperpolarization-activated cation current		pA
C	membrane capacitance	180	pF
k	scaling factor, affects the spike width	1.6	mS/mV
v_r	resting membrane potential	-65	mV
v_t	instantaneous threshold potential	-55	mV
I_{dc}	externally applied dc current	18	pA
a	rate constant of recovery currents	0.01	$(\text{ms})^{-1}$
a_h	rate constant of I_h currents	3.5×10^{-7}	$(\text{ms})^{-1}$
b	sensitivity of recovery current to subthreshold membrane fluctuations		nS
b_h	sensitivity of I_h to membrane voltage		nS
ϵ	voltage sensitivity to I_h	3	
$I_{h,\text{offset}}$	I_h offset value	-75	pA
v_{peak}	spike cutoff value	35	mV
c	voltage reset value	-65	mV
d	offset value of recovery variable	-15	pA
d_h	offset value of I_h current	-1.3	pA

$$
\begin{aligned}
&C\frac{dv}{dt} = k(v-v_r)(v-v_t) - u + I_{\text{dc}} + \epsilon I_h + \text{noise}\\
&\frac{du}{dt} = a\left\{b(v-v_r) - u\right\}, \qquad b = \begin{cases} 15 & \text{if } v \le -70 \text{ mV} \\ 0 & \text{otherwise} \end{cases}\\
&\frac{dI_h}{dt} = a_h\left\{b_h \cdot v - I_{h,\text{offset}} - I_h\right\}, \quad b_h = \begin{cases} -255.5 & \text{if } v \le -65 \text{ mV} \\ 0 & \text{otherwise} \end{cases}\\
&\text{reset rule: } v \leftarrow c - 0.1u, \quad u \leftarrow u + d, \quad I_h \leftarrow I_h + d_h, \quad \text{when } v \ge v_{\text{peak}} - 1.1u
\end{aligned}
\tag{3.8.1}
$$

See Table 3.2 for description and values of model parameters. Note that the I_h term is now added to the voltage equation. The third equation describes the slow (see a_h value) current which depolarizes the neuron. Ideally the range of allowed values for these parameters should be determined from biological measurements, but that is beyond the scope of this work.

The numerical simulation is used in this section to demonstrate interaction of the system variables, v, u, I_h. Figure 3.12 shows the temporal evolution of v and I_h. Assuming that the

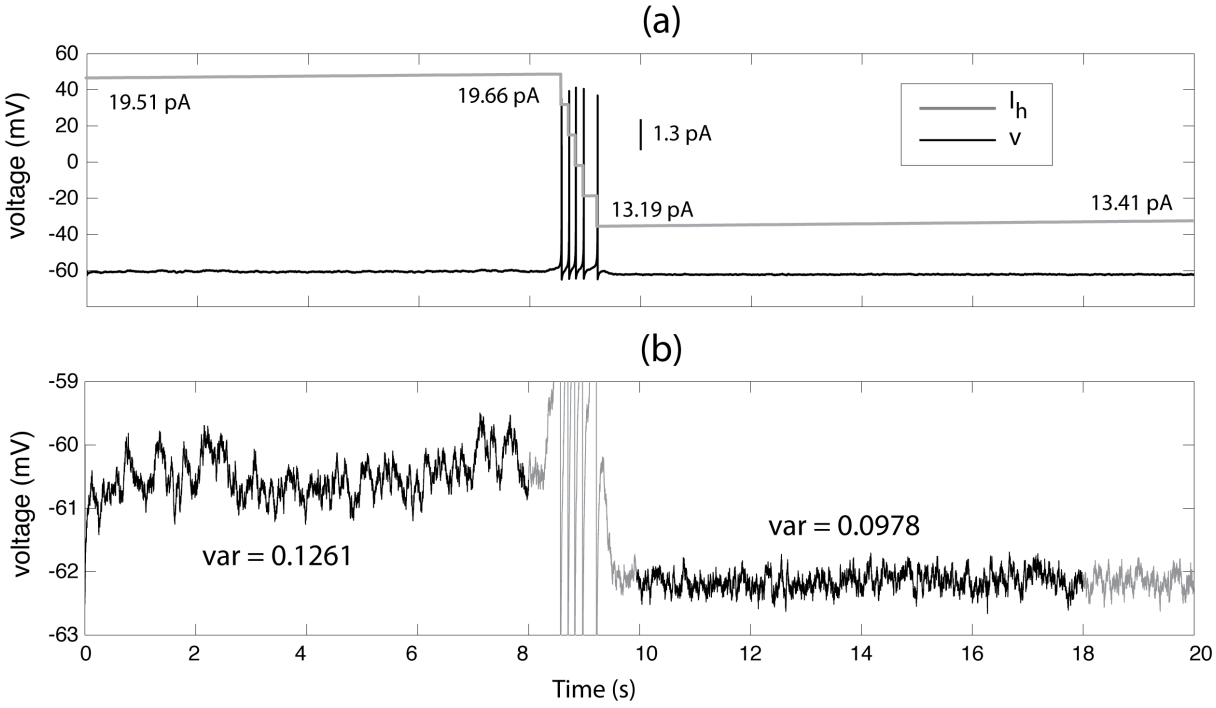

Figure 3.12: Spontaneously generated burst in a model of thalamocortical relay (TC) neuron with hyperpolarization-activated cation current I_h as described by Eqs. (3.8.1). (a) The membrane voltage (black) and I_h (grey) of TC neuron biased with $I_{\rm dc} = 18$ pA and driven with white noise. The I_h current slowly increases from 19.51 to 19.66 pA. This increment depolarizes the neuron towards its firing threshold. Firing of action potentials reduces I_h which results in the slight hyperpolarization of the membrane in return and termination of the burst. (b) A detailed view of subthreshold fluctuation of the membrane voltage. Variance of two 8-sec pre- and post-burst epochs (black) are calculated. The variance is higher prior to burst generation compared to the after-burst period (var $= 0.1261,\ 0.0978$ mV^2) respectively.

neuron is in bursting mode (more specifically in spindle generation mode) and that I_h current is active, I_h increases very slowly while the neuron is resting at $v \approx -61$ mV. The increase in I_h slowly depolarizes the neuron until it fires a burst of action potentials at $t = 8.55$ s. Following the after-spike reset rule described in Eq. (3.8.1), the firing of every action potential subtracts $d_h = 1.3$ pA from I_h (vertical bar in Fig. 3.12(a)). The continious reduction of I_h during burst firing hyperpolarizes the membrane potential to subthreshold levels and the bursting terminates. Another burst will spontaneously emerge when I_h grows to a level capable of depolarizing the cell again. We will shortly see that in an *in vivo*-like condition, consecutive external inhibitory stimuli can promote burst generation in TC neuron.

Before examining the effect of externally induced inhibitions on burst generation, a simple analysis is performed on the subthreshold voltage fluctuations of the model as displayed in Fig. 3.12(b). The aim is to track variance of voltage fluctuations prior to and after bursts.The comparison between variances of two 8-sec voltage epochs—belonging to before- and after-burst periods—shows 22% reduction after the burst generation. The increased variance prior to burst generation is a result of critical slowing down and is consistent with increased sensitivity of

the system in the period leading up to phase transition. One can perform a detailed analysis[1] of the variance by simply *freezing* the slow variable (I_h), and analysing on the fast subsystem composed of v and u variables only.

The remainder of this section examines the model response to pulses of hyperpolarizing current. In *in vivo* conditions when spindles are generated, the hyperpolarizing currents are due to activity of inhibitory reticular nucleus of thalamus.The model behaviour is displayed in Fig. 3.13. To understand the mechanisms underlying spindle generation, the feedback connection from I_h to v is temporarily disconnected as displayed in (a). One can do this simply by setting $\epsilon = 0$ in Eqs (3.8.1). The stimulation train induces temporary hyperpolarization of $v = -76.5$ mV in the membrane potential as displayed in the inset. Each hyperpolarization increases I_h about 0.4 pA, provided that the membrane is hyperpolarized to lower levels than -65 mV (see the definition of b_h parameter in the model). Since the effect of I_h on membrane voltage is suppressed in this experiment, no spiking dynamics occurs in this crippled version of the model.

The mutual interaction between v and I_h variables is restored in Fig. 3.13(b), resulting in bursting. The bursts are produced in response to hyperpolarizing pulses, and are composed of 3–4 consecutive spikes. As described in (a), every stimulation pulse hyperpolarizes the membrane which results in an uptake of I_h current. The increased inflow of I_h depolarizes the TC cell, until the neuron passes firing threshold and generates the first action potential of the burst. This inactivates the I_h channels, blocking the I_h inflow, and reducing the membrane potential. This is modelled by an after-spike reset in I_h. However the neuron is still depolarized and 2–3 further action potentials may be generated. The firing of every spike reduces the I_h level more and more, until the neuron stops spiking. Further stimulation of the neuron can reactivate this mechanism to produce another burst of action potentials after a refractory period of $\sim$2 s.

In Section 4.4 the TC neuron will be incorporated into a thalamocortocal network to model spindle generation.

The next section presents a model for inhibitory thalamic reticular nucleus neuron, which also plays important role in spindle generation.

3.9 Reticular thalamic nucleus neuron (RTn)

Reticular thalamic nucleus (RTn) neurons fire tonic spikes in response to depolarizing incoming signals if they are at rest potential (corresponding to awake state of the brain), but fire bursts of action potentials in response to the same stimuli when they are hyperpolarized (corresponding

[1]The detailed variance analysis is similar to the analysis presented for two RS models in Sections 3.3, 3.4 of this chapter

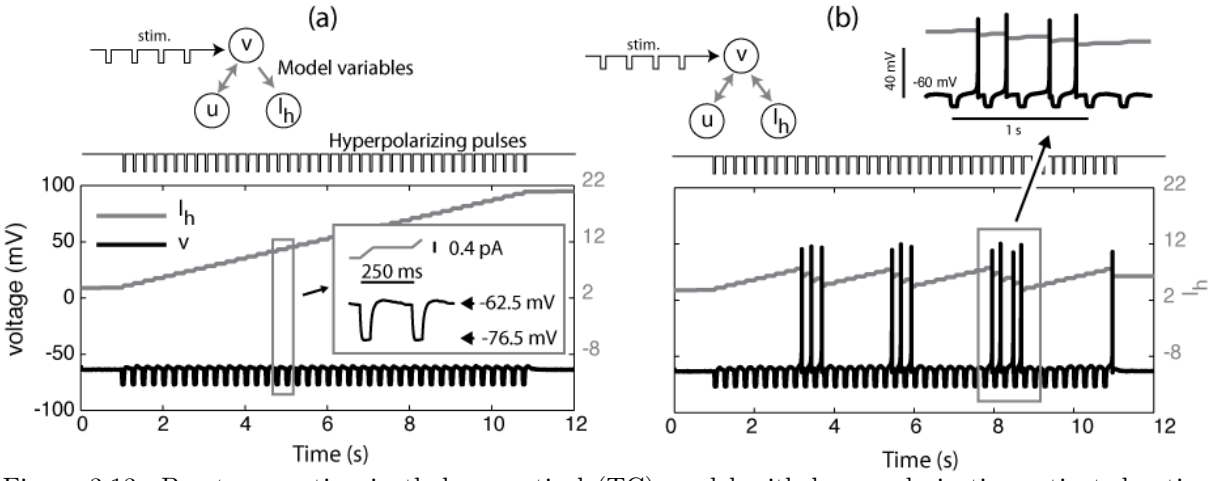

Figure 3.13: Burst generation in thalamocortical (TC) model with hyperpolarization-activated cation current I_h as described by Eqs. (3.8.1). (a) Top, illustration of the model variables when the feedback from I_h to v is disconnected. The hyperpolarizing pulses (pulse width = 50 ms, amplitude = −450 pA, frequency = 4 Hz) are applied to the neuron from $t = 1$ to 11 s. The membrane potential is displayed as a function of time, with I_h current superimposed. The neuron does not fire action potentials. (b) Burst generation in TC model after restoring mutual interaction between v and I_h variables. Same hyperpolarizing pulses are applied to the neuron. The details of the v and I_h variables is displayed in top right corner for a selected period of time. A fourth-order Runge-Kutta integrator with time steps of $\Delta t = 0.1$ ms is used to numerically simulate the model.

to NREM or SWS or light anaesthesia states of the brain). The simple Izhikevich model of RTN neurons follows:

$$
\begin{aligned}
&40\frac{dv}{dt} = 0.25(v+65)(v+45) - u + I \\
&\frac{du}{dt} = 0.015\{b(v+65) - u\},\ b = 10 \text{ if } v \le -65 \text{ and } b = 2 \text{ otherwise} \\
&\text{with reset rule of:} \quad v \leftarrow -55, \quad u \leftarrow u + 10, \quad \text{when} \quad v \ge 0 \quad \text{(spike cutoff)}
\end{aligned}
\tag{3.9.1}
$$

This model emits a rebound spike when it is released from a hyperpolarized potential of about −80 mV to more depolarized potentials around the resting potential (−60 mV). This behaviour is displayed in Fig. 3.14, where the nullclines are plotted in (a) and the numerically obtained trajectory superimposed. The rebound spike generation is produced based on a similar mechanism as displayed in Fig. 3.10 for TC neuron. However the type of the stable point is different as indicated by the numerically obtained trajectories: the trajectory in the inset of Fig. 3.14(a) shows that the steady state is a stable focus point, while the steady state was a stable node for the TC neuron.

The response of this neuron to incoming excitations and inhibitions is demonstrated in Fig. 3.15. The stimuli have a form of rapid excitatory or inhibitory pulses with the width of 20 ms (in the order of the time-course of incoming synaptic currents) and amplitude of +250 and

−100 pA for excitatory and inhibitory stimuli respectively. The "E" and "I" arrows show the neural response to excitatory and inhibitory inputs respectively. The resting neuron ($v_m = -55$ mV) fires single spikes due to both types of incoming stimuli, while the hyperpolarized neuron ($v_m = -68.5$ mV) only fires due to incoming excitations.

A thalamocortical network model of *spindle* generation will be presented in the next chapter with the hyperpolarized RTn neuron as one of the key elements of the model. It is known that hyperpolarized RTns fire bursts of spikes in response to incoming excitatory stimulations [Bazhenov and Timofeev, 2006]. However Fig. 3.15 demonstrated that the original RTn model does not burst when hyperpolarized. I propose a modified form of the RTn model that is capable of burst generation while the neuron is hyperpolarized:

$$
\begin{aligned}
&C\frac{dv}{dt} = k(v - v_r)(v - v_t) - u + I_{\mathrm{dc}} \\
&\frac{du}{dt} = a\{b(v - v_r) - u\}, \qquad b = \begin{cases} 80 & \text{if } u \le -65 \text{ pA} \\ 2 & \text{otherwise} \end{cases} \\
&\text{with reset rule of: } v \leftarrow c + v_{\mathrm{offset}}, \quad u \leftarrow u + d + u_{\mathrm{offset}}, \quad \text{when } v \ge v_{\mathrm{peak}} \\
&v_{\mathrm{offset}} = \begin{cases} -40 & \text{if } u \le -250 \text{ pA} \\ 0 & \text{otherwise} \end{cases}, \qquad u_{\mathrm{offset}} = \begin{cases} 20 & \text{if } u \le -250 \text{ pA} \\ 0 & \text{otherwise} \end{cases}
\end{aligned}
\tag{3.9.2}
$$

Here v_{offset} and u_{offset} are values to be added to the after-spike voltage and recovery variables

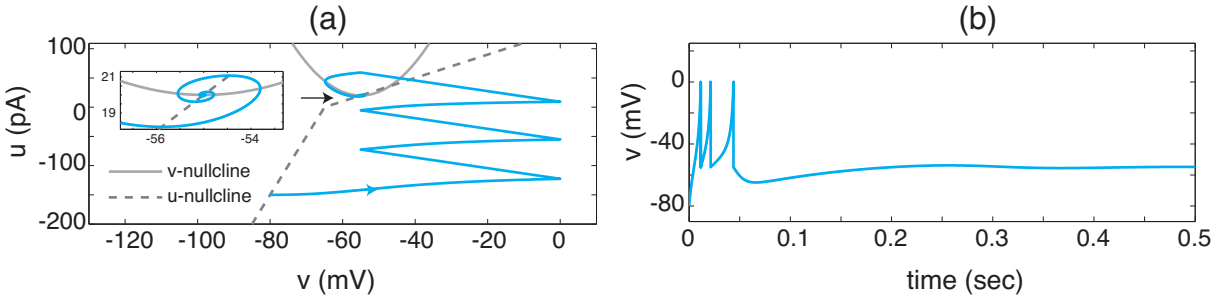

Figure 3.14: Rebound spike generation in original Izhikevich model of reticular thalamic nucleus (RTN) neuron described by Eqs. 3.9.1. (a) The nullclines and the numerically obtained (fourth-order Runge-Kutta method, $\Delta t = 0.01$ ms) trajectory of RTN model upon release from hyperpolarized state of $v = -80$ mV. The inset shows detail of the trajectory while getting attracted to the intersection. The spiralling-in behaviour signals the existence of a stable focus. (b) Corresponding voltage time-series, comparable with *in vivo* measurements as stated in Fig. 8.32 of Izhikevich [2007]. The external stimulus current is set to $I_{\mathrm{dc}} = 45$ pA.

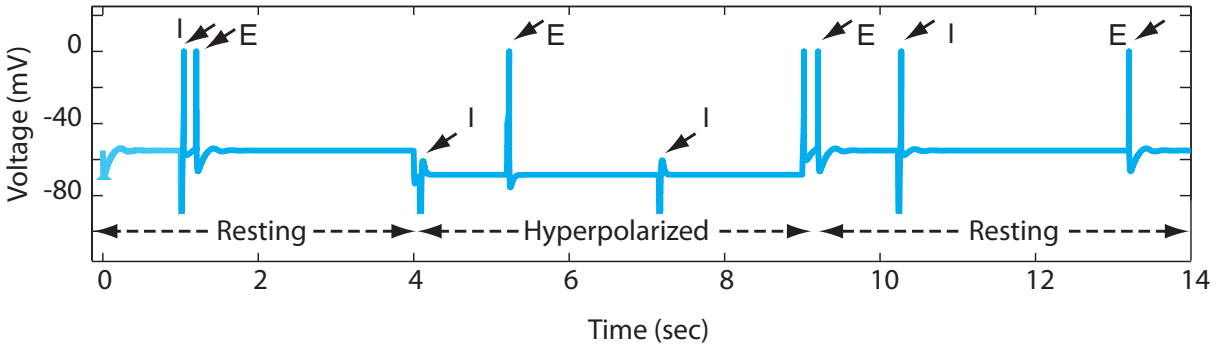

Figure 3.15: The response of resting and hyperpolarized Izhikevich model of reticular thalamic nucleus (RTn) neuron (same neuron as studied in Fig. 3.14) to brief excitatory and inhibitory pulses. The resting neuron fires single spikes to both inhibitory and excitatory inputs (indicated by "I" and "E" arrows respectively), while the hyperpolarized neuron fires only due to excitations.

respectively. The dependence of the offset values on u (and consequently on v) in this modified model distinguishes the spiking behaviour of the RTn neuron in the hyperpolarized state ($v_m = -71$ mV) compared to when it is slightly depolarized ($v_m = -65$ mV). See Table 3.3 for description and values of model parameters.

Figure 3.16(a) displays the membrane voltage of the modified model. Brief excitatory stimuli (pulse width = 8 ms, amplitude = 250 pA) are applied regularly to the neuron. The neuron undergoes a hyperpolarization from $t = 4$ to $t = 8$ s by application of a negative external current. A tonic discharge pattern is observed in response to stimuli while the membrane voltage is at $v_m = -65$ mV; this potential corresponds to the awake state [Steriade and McCarley, 2005, ch. 5]. The figure shows that neuron fires differently when it is hyperpolarized to $v_m = -71$ mV. The hyperpolarization corresponds to natural slow wave sleep (SWS) and can be accompanied with sleep spindles [Steriade and McCarley, 2005]. With a hyperpolarized membrane potential,

Table 3.3: Variables (Var) and parameters (Par) of modified reticular thalamic nucleus neuron, Eq. (3.9.2).

Var/Par	Description	Value	Unit
v	membrane potential		mV
u	recovery variable, representative of summation of all inward and outward ionic currents		pA
C	membrane capacitance	40	pF
k	scaling factor, affects the spike width	0.25	mS/mV
v_r	resting membrane potential	-65	mV
v_t	instantaneous threshold potential	-45	mV
I_{dc}	externally applied dc current	45	pA
a	rate constant of recovery currents	0.015	$(\text{ms})^{-1}$
b	sensitivity of recovery current to subthreshold membrane fluctuations		nS
v_{peak}	spike cutoff value	0	mV
c	voltage reset value	-55	mV
d	offset value of recovery variable	10	pA

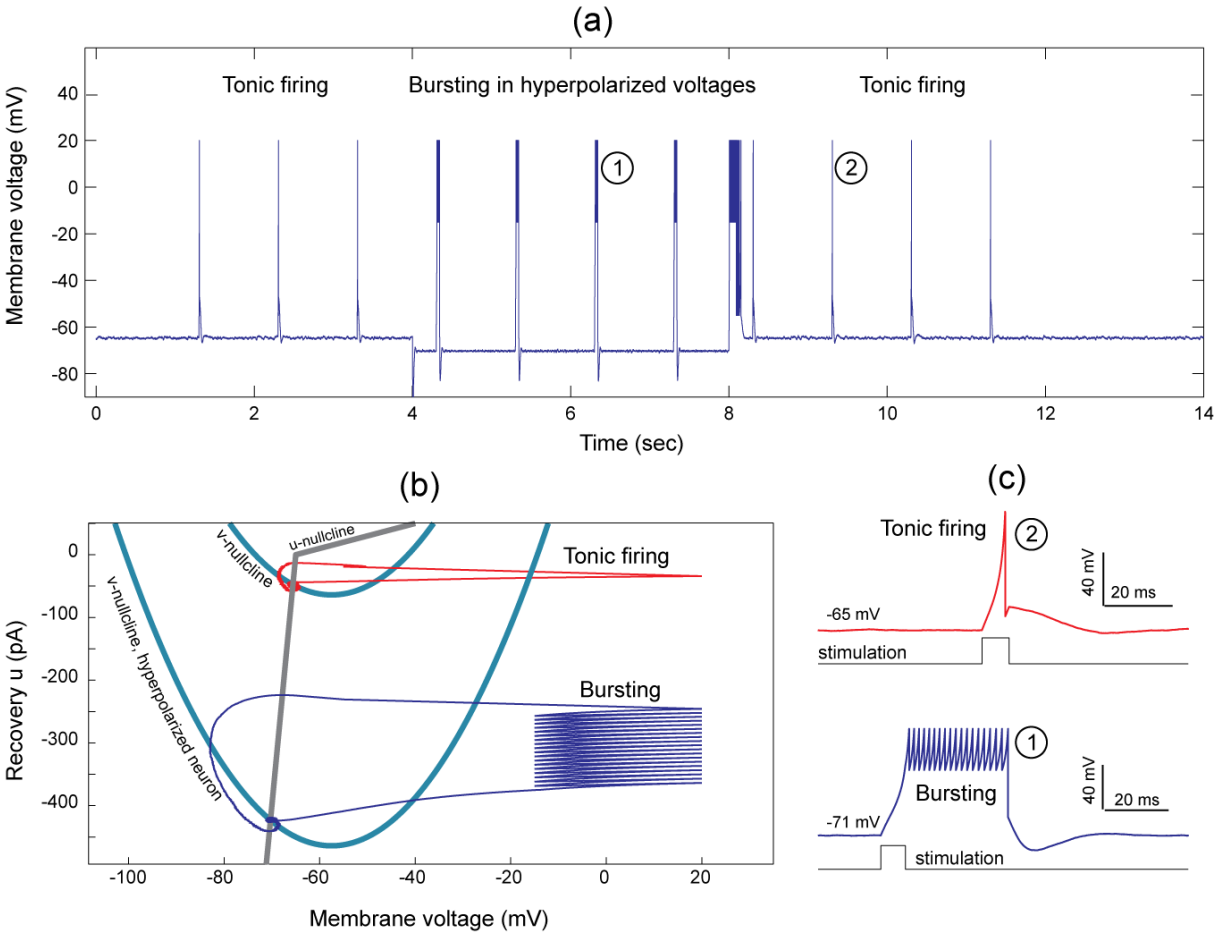

Figure 3.16: Response of the modified model of the reticular thalamic nucleus (RTn) neuron. (a) In response to excitatory current stimulations (applied every 1 s), the neuron fires differently. Tonic firing is produced when the membrane potential is at resting voltage of $v_m = -65$ mV. The neuron generates a burst of action potentials when it is hyperpolarized to $v_m = -71$ mV by application of $I_{\text{hyp}} = -450$ pA. (b) The nullclines of the model showing the effect of hyperpolarization as the downward shift in the location of the v-nullcline. The trajectories of two events from (a)—marked ①, and ②—are superimposed on the nullclines showing the mechanism of bursting in this model. (c) The expanded view of the events from (a) showing two modes of firing for RTn neurons. The corresponding external stimuli are superimposed. $I_{\text{dc}} = 0$ pA. An RK4 integrator with time step $\Delta t = 0.01$ ms was used. Small amplitude white noise is added to I_{dc}.

the neuron fires a burst of action potentials in response to excitatory stimuli.

The nullclines of the model are displayed in Fig. 3.16(b), and are identical to the nullclines of the original RTn model of Fig. 3.14(a). However, the after-spike conditions are different in the new model. The trajectories corresponding to two events in (a) (marked ①, ②, and expanded in (c)) are superimposed on the nullclines, showing the generation of rebound burst when the neuron is hyperpolarized.

3.10 Chapter summary

What happens during the time leading up to action potential generation in a neuron? This chapter tries to answer this question in biophysical models of single spiking neurons using theory

of dynamical systems and numerical simulations. The subthreshold voltage fluctuations are proposed to convey precursor signs prior to occurrence of a phase transition represented by the firing of an action potential. Studying and capturing such signs could be significant in terms of providing theoretical knowledge about the mechanisms by which the brain undergoes switching between its different healthy or pathological rhythms.

The chapter starts with an extension of a previous theoretical and numerical subthreshold analysis of the H. R. Wilson model of cortical neurons. The results show precursors in the spectrum of voltage fluctuations prior to spike generation. As the next step it would be interesting to look for the signs of phase transitions in more complex neural phenomenon rather than a spike generation in a single neuron. However proper models of different neural types (cortical, thalamic, ...) should be developed at first. Although H. R. Wilson model is simpler than original four-dimensional Hodgkin-Huxley model in terms of number of governing equations, more abstract models are better fits for our network simulations.

The number of governing equations and consequently the complexity is reduced in abstract model by retaining only the subthreshold dynamics and replacing the after spike behaviour with a manual reset rule. The Izhikevich model is shown to capture the spiking behaviour of many known neurons *in vitro* and *in vivo*, and is the model of choice in this chapter.

Models of two cortical neural types (excitatory regular spiking RS, and inhibitory fast spiking FS) and two thalamic neural types (excitatory thalamic relay (TC) and inhibitory reticular nucleus neuron RTn) were investigated in the chapter. The subthreshold dynamics of these neurons were studied using the linear stability analysis, and the mechanisms underlying spike generation were described using the bifurcation theory. Then the subthreshold voltage fluctuations were studied, and I found signs of critical slowing prior to bifurcation. Modifications were introduced to the original Izhikevich model to allow more realistic behaviour in some neural types. Specifically, the RS model was altered to capture the metabolic-rate related bursting. A hyperpolarization activated cation current was incorporated into the TC neuron. The original Izhikevich RTn neuron was modified to burst in response to incoming excitation, when the neuron is hyperpolarized. The two latter novel modifications are of importance for generating thalamocortical sleep spindles which will be presented in Chapter 4.

Chapter 4

Slowing down in networks of spiking neurons

The previous chapter demonstrated subthreshold critical fluctuations prior to action potential or burst generation in single-neuron models for cortex and thalamus. Precursor signals can be detected in the time-series for neuron voltage. The vision of the thesis is pursued in this chapter by looking for signs of critical slowing in network assemblies of spiking neurons. The constitutive elements of the network are the modified Izhikevich models described in Chapter 3. These biologically inspired networks are tuned to generate gamma oscillations and sleep spindles. I will show evidence of warning signs in neural activity prior to state transitions.

We begin with a discussion about synaptic interactions, and describe how the local field potential (LFP) can be extracted from the network. A cortical network capable of gamma frequency activity is presented in Section 4.3, and we demonstrate transition to lower frequencies following simulated application of an anaesthetic drug. In Section 4.4 we construct a small network of cortical and thalamic neurons that supports sleep spindles. I demonstrate how signs of critical slowing can be detected in these network generators of gamma and spindle oscillations.

4.1 Synaptic connections

The arrival of a presynaptic action potential (AP) at the synaptic terminal releases neurotransmitters into the synaptic cleft, and these bind to their corresponding receptors in the postsynaptic side of the synapse. This binding may result in the opening of ion channels (directly, or indirectly via secondary messengers) on the postsynaptic site, leading to change in ionic concentrations in- and outside of the postsynaptic dendrite. Depending on the type of neurotransmitter and receptor, the result can be excitation or inhibition of the postsynaptic neuron. The amount of released neurotransmitter and the time-course of the consequent processes should be considered when designing a model for a synaptic interaction. Other details could also be considered in the model such as the delay time after AP arrival and neurotransmitter release.

A realistic synaptic model might consider the separate time-courses of neurotransmitter release and uptake. A detailed model of the synapse is presented by Ledoux and Brunel [2011].

Here the goal is to use a moderately realistic synaptic model that is also computationally efficient in order to facilitate network simulation. Following Ohm's law, synaptic currents can be modelled as the product of the synaptic conductance with the voltage difference across the synapse [Izhikevich and Edelman, 2008]

$$I_{\text{syn}} = g(t)(V_{\text{rev}} - V_{\text{post}}) \tag{4.1.1}$$

where V_{post} is the postsynaptic membrane potential, and V_{rev} is the receptor-dependent reversal potential. The time-dependent conductance $g(t)$ has first-order linear kinetics:

$$\frac{dg}{dt} = \frac{-g}{\tau} \tag{4.1.2}$$

with exponentially decaying solution $g(t) = g_{\max} \exp(-t/\tau)$ where $g_{\max}$ is the maximum conductance and τ is the time-constant.

Following a similar network scheme by Traub *et al.* [2005], I assume that synaptic currents entering a particular neuron sum linearly. Only the inhibitory GABA_A (γ-aminobutyric acid type A) and the excitatory AMPA (α-amino-3-hydroxy-5-methyl-4-isoxazolepropionic acid) mediated synaptic currents are considered here: these neurotransmitters are dominant in the central nervous system. (See Chapter 2 for more descriptions on GABA_A and AMPA currents.)

4.2 Modelling local field potentials (LFPs)

Electroencephalogram (EEG) and local field potentials (LFPs) are common measures of neural activity, but it is not fully understood how they are related to individual neural variables such as ionic currents or membrane potential [Mazzoni *et al.*, 2008]. However, it is known that the EEG and LFP signals are strongly correlated with population activity of *pyramidal* neurons since the dendritic trees of these neurons are aligned in pathways perpendicular to scalp surface, unlike interneurons which have randomly directed dendrites [Nunez and Srinivasan, 2006].

Based on this fact, mean-field (continuum) models are designed to contain variables directly comparable with EEG or LFPs. However, to compare the output of spiking-neuron-based models with experimental data, the EEG or LFP related parameters need to be extracted from the model in a biologically plausible way. Two main approaches are suggested to extract an EEG/LFP-related parameter from the networks of spiking neurons:

1. In several mean-field models it is assumed that the AC component of the EEG voltage is linearly related to the fluctuation of the spatially averaged excitatory soma membrane potentials [**?**Bojak and Liley, 2005; Steyn-Ross *et al.*, 2009]. The same assumption about the origin of EEG signal is made by Ursino and Cara [2006] and Warlaumont *et al.* [2011] in their neuron-by-neuron modelling works. However, because action potentials are strongly low-pass filtered when they propagate through extracellular fluids (and skull and skin for EEG signal), some researchers believe that the membrane potentials are unlikely to sum additively [Stead *et al.*, 2010] to form the LFP or EEG signal. An alternative view asserts that temporal variations in the mean *firing rate* of excitatory neurons is proportional to the EEG and LFP signals [Robinson *et al.*, 1998; Wilson, 1999].
2. Because of the relatively slow dynamics of the post-synaptic currents [Stead *et al.*, 2010], they are highly correlated with EEG and LFP signals [Steriade and McCarley, 2005]. As a result some modellers use total input synaptic current entering pyramidal neurons as a descriptor of neural mass activity (see, e.g., [Logothetis, 2003; Mazzoni *et al.*, 2008; Deco *et al.*, 2008; Ledoux and Brunel, 2011]), while others assume that the EEG and LFP signals are proportional to the mean of AMPA currents emanating from the excitatory population [Ching *et al.*, 2010].

A study by Mazzoni *et al.* [2008] contrasted the soma voltage and synaptic current models for LFP, using "spectral features" and "information content" as comparison criteria. The results showed that the spectrum of mean membrane voltage may not be in complete agreement with LFP signal, but the information content of membrane potential and the LFP signal can be very similar. However both spectral features and information content are in agreement when the average *synaptic current* entering the excitatory neurons is used as a model of LFP. Thus a good representation of the LFP signal can be obtained by averaging the sum of the absolute values of AMPA and $\mathrm{GABA_A}$ currents entering the pyramidal neurons:

$$\mathrm{LFP} = \Sigma_{i=1}^{N} \frac{|I_{\mathrm{AMPA},i}| + |I_{\mathrm{GABA_A},i}|}{N}, \quad N\text{: number of pyramidal neurons} \tag{4.2.1}$$

Mazzoni *et al.* [2008] showed that this is a reasonable approach for modelling LFP, allowing comparison between model output and experimental LFP recordings.

4.3 Modelling cortical gamma oscillations

A mechanism for the generation of *gamma* oscillations—as an example of a population-generated neural rhythm—is now presented. Whittington *et al.* [2000] classify the gamma rhythm as an "inhibition-based oscillation" to emphasize the role of inhibitory neurons in the generation of

these oscillations, and its collapse in the absence of inhibition. Here I demonstrate that a network of excitatory RS neurons and inhibitory FS interneurons can produce gamma activity.

Following Whittington *et al.* [2000], I set the FS neurons in their subthreshold regime, while the RS pyramidals are in their excitable mode firing action potentials (APs) with frequency of $f < 10$ Hz in response to incoming stimuli. The sparse firing of RS neurons depolarizes the FS neurons causing them to fire fast spikes in the 30–40 Hz range, influencing their postsynaptic RS targets. The collective behaviour of the network is reflected on the extracted LFP showing gamma frequency oscillations of frequency $f \simeq 30$ Hz. The gamma wave is a population-induced oscillation in which the excitatory RS neurons activate the inhibitory FS neurons, and the FS neurons respond by sending fast inhibitory postsynaptic currents to their RS targets.

The cortical network is composed of 20 RS and four FS neurons[1], with synaptic connections and network connectivity matrix as displayed in Fig. 4.1 (a, b). A 20×20 connectivity matrix whose elements are "one" is constructed first, representing all-to-all connection prototype. We then introduce uncertainty to the network by randomly zeroing some connections (see Fig. 4.1). Next, we construct the conductance matrix using the connectivity prototype. This matrix provides all the information about the topology of the network, and is used to update synaptic currents at each time-step. A one-line vector based MATLAB code is used for this update:

```
Isyn = sum(   cond.*( repmat(v, N ,1 ) - rev_pot)  );
```

where `Isyn` contains synaptic current of all neurons, `cond` is the conductance matrix, `v` is the membrane voltage vector, `N` is the total number of neurons, and `rev_pot` contains all reversal potentials. The synaptic excitation and inhibition are mediated respectively by AMPA- and $\mathrm{GABA_A}$-type neurotransmitters with reversal potentials $V_r = 0$ and -80 mV. The maximum synaptic conductances between different neurons are set to[2] $g_{\text{RS-RS}} = 0.25$, $g_{\text{RS-FS}} = 0.2$, $g_{\text{FS-RS}} = 0.12$, and $g_{\text{FS-FS}} = 0.025$ nS. The decay times of synaptic conductances are $\tau_{\text{AMPA}} = 2$, and $\tau_{\mathrm{GABA_A}} = 10$ ms. A stochastic term is added to the DC drive current of each neuron in a similar method as described in Section 3.1 by Eq. (3.1.2). The standard deviations of the applied white noise are selected to be $\sigma_I = 0.01$ and $\sigma_E = 0.2$ $\sqrt{\text{ms}}\cdot$pA for FS and RS neurons respectively.

The spiking of individual neurons during a 1-sec interval is displayed as a raster plot in Fig. 4.1(c), top. The RS neurons fire with a frequency of $f_{\text{RS}} \sim 6$ Hz, while the FS neurons fire with the frequency of $f_{\text{FS}} \sim 30$ Hz. The corresponding 1-sec length LFP signal is extracted from

[1] The cortical excitatory and inhibitory neurons compose respectively 80% and 20% of total neural population [Braitenberg and Schüz, 1991]

[2] The parameter values for synaptic interactions are selected to be in the range of a similar study by Izhikevich and Edelman [2008]

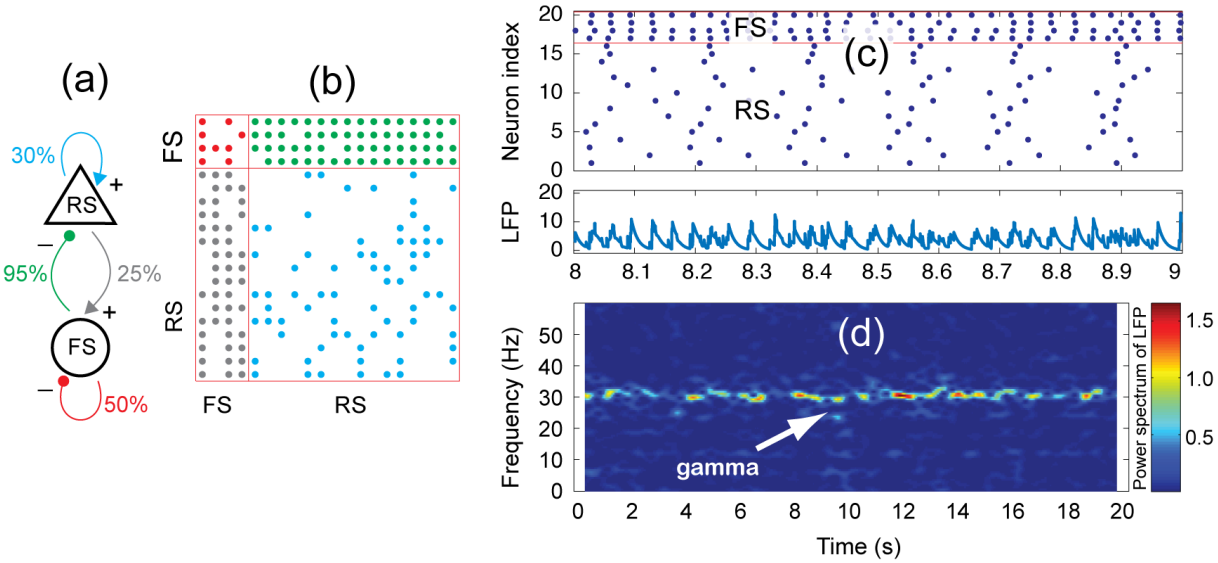

Figure 4.1: Gamma wave generation in Izhikevich-based cortical model composed of 16 regular spiking (RS) excitatory pyramidal neurons and four fast spiking (FS) inhibitory interneurons. (a) Connection diagram between a typical RS-FS pair in the network , showing all possible synaptic connections. Not every RS-FS pair in the network contains all displayed synaptic connections. (b) Connection matrix of the network. Each dot represents a connection between corresponding neurons indicated on the vertical and horizontal axes. We discard randomly selected 5% of all possible inhibitory connections from FS to RS neurons (green dots). This percentage is 25% for RS to FS (grey dots), 70% for RS to RS (blue dots), and 50% for FS to FS connections (red dots), as displayed on connection diagram. (c) Top, one second of the raster plot showing network activity: each dot represents the firing of individual neurons. Bottom, the 1-sec local field potential (LFP) produced as the average of sum of absolute values of the AMPA and $GABA_A$ presynaptic currents impinging on all RS neurons. (d) The frequency-time representation of the full-length (20 s) LFP signal showing the emergent gamma-band oscillation with narrow frequency distribution around $f \sim 30$ Hz. A fourth-order Runge-kutta integrator was used for numerical simulation. The parameters of each RS model are as in Fig. 3.4 and $I_{dc} = 132$ pA. See Eq. (3.6.1) for parameters of each FS neuron, with $I_{dc} = 73$ pA.

the activity of all pyramidal neurons using Eq. (4.2.1), and displayed in Fig. 4.1(c), bottom. The result of spectral analysis on the full-length (20 s) LFP signal is displayed as a time-frequency graph in Fig. 4.1(d). The emergent gamma oscillation is evident in this graph as the result of interaction between cortical RS and FS neural populations.

4.3.1 Transition from gamma to low-frequency oscillations in the cortex

General anaesthetics including volatile gases (isoflurane, desflurane, and sevaflurane) and intravenous drugs (thiopental, etomidate and propofol) increase the amplitude and slow the time-course of $GABA_A$ mediated synaptic currents. See Garcia *et al.* [2010] for a review. In this section it is assumed that only the time-course of $GABA_A$ currents is increased by anaesthetic drug. The dynamics of the gamma-producing cortical network in response to varying τ_{GABA_A} is investigated. Considering two distinct oscillating modes of the cortex (viz gamma and low-frequency bands), the possibility of capturing the precursors of transitions between modes is examined here.

It is known that propofol increases the dwell time of $GABA_A$ neurotransmitters in the synaptic cleft. This results in strengthening of the inhibitory post synaptic currents (IPSCs), and consequently greater hyperpolarization of the postsynaptic neurons. The decay time of $GABA_A$ mediated synaptic currents τ_{GABA_A} can be increased up to three-fold as a model of induction of anaesthesia [Sleigh *et al.*, 2009]. The cortical model is set initially to produce gamma oscillations as a model of the awake state. Then the network response is studied while increasing τ_{GABA_A} decay time. The results are displayed in Fig. 4.2. The spectrogram of the LFP is displayed in (a), with the trend of τ_{GABA_A} superimposed as a dashed line. The spectrum shows the transition from 30-Hz (gamma range) to 6-Hz oscillations, in agreement with activity-suppressing effect of larger τ_{GABA_A} values induced by application of anaesthetic agents.

The LFP shows mixture of high- and low-frequency oscillations for times $25 < t < 35$ s,

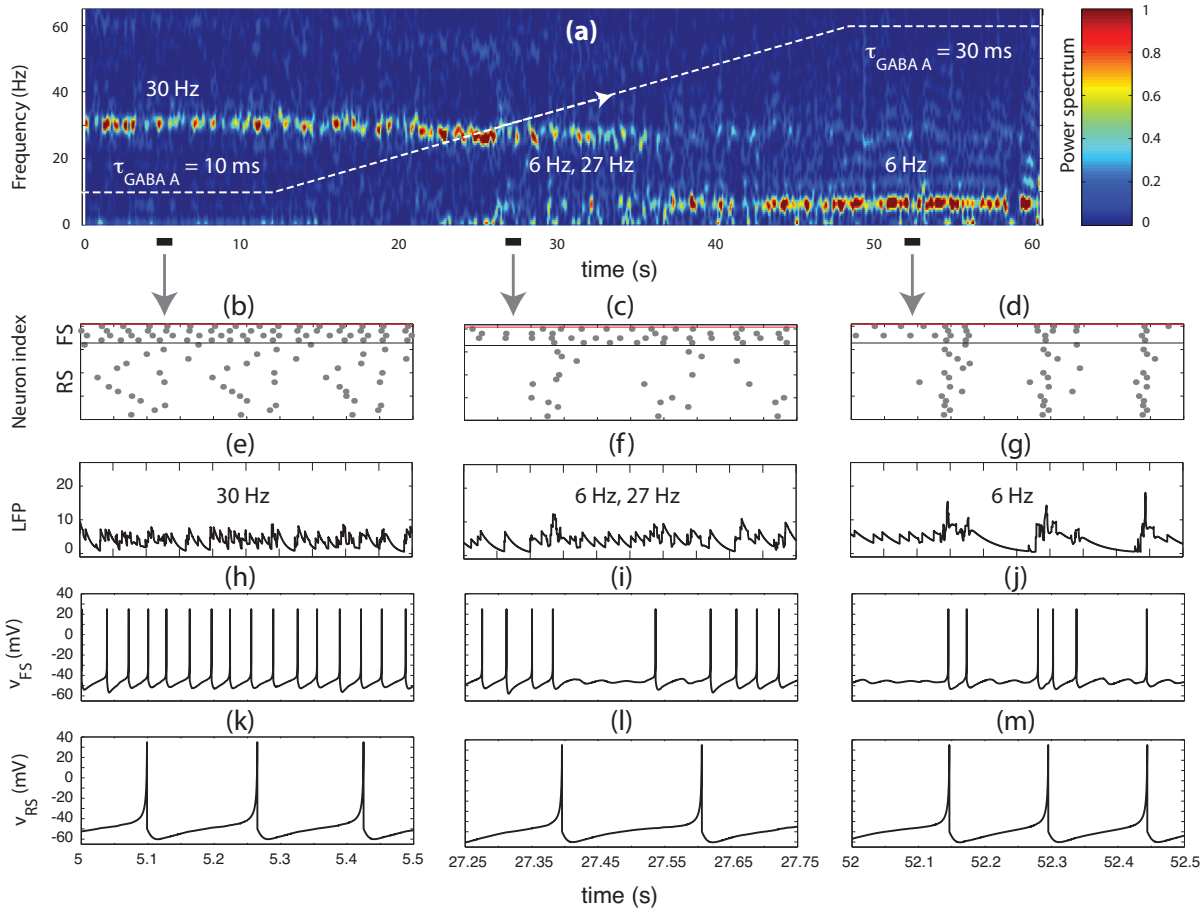

Figure 4.2: Transition from gamma-dominated wakefulness to minimally conscious state. (a) Time-frequency plot of extracted local field potential (LFP). The model is identical to the one in Fig. 4.1 is used here, except the variable τ_{GABA_A} (superimposed dashed line). The initial 30-Hz population frequency switches to 6 Hz as τ_{GABA_A} increases from 10 to 30 ms. The cortex is in a bistable mode when the transition between modes occurs (see spectrum for $25 \leq t \leq 35$ s). (b-d) Raster plots of entire network at three 0.5-s time-periods, (e-g) corresponding LFP signals. (h-j) Corresponding membrane potential of a selected fast spiking (FS) interneuron, (k-m) regular spiking (RS) pyramidal neuron. The transition period is reminiscent of "normal wakefulness" in which the EEG contains two prominent spectral peaks in 3–7 Hz range (theta), and another peak in the 15–30 Hz (beta) range.

reminding the behaviour of a bistable system. The horizontal bars in (a) represent three 0.5-second epochs belonging to three qualitatively different phases of LFP: gamma, low-frequency and bistable modes. The corresponding raster plots (b-d), LFPs (e-g), soma voltage of selected FS (h-j), and RS (k-m) neurons are displayed in the figure. The raster plot in (b) shows *asynchronous* activity of RS and FS neurons during gamma oscillations, while both RS and FS populations fire almost *synchronously* in ∼6 Hz mode as displayed in (d). In bistable-like mode a *weak synchrony* is observed in the RS population, while the FS neurons have a firing rate of ∼27 spikes per second.

A further analysis is performed on the firing rate of RS and FS neurons in gamma (∼30 Hz) and slow (∼6 Hz) modes. Figure 4.3 displays the firing rate of the two selected neurons from the previous simulation. The firing rate of the RS neuron shows a small increase (8%) for RS, while a noticeable decrease (50%) for FS neuron is captured when the oscillation mode changes from 30 to 6 Hz. The change of firing-rates in the model reminds the firing-rate variations across awake and slow-wave-sleep in an *in vivo* experiments by Steriade *et al.* [2001].

The bistability in the transition phase from gamma to slow oscillations is interesting, inviting further investigation. A continuous-cyclic transition of the model (gamma → slow → gamma) can be achieved by an appropriate variation in $\tau_{\mathrm{GABA_A}}$. The resulting LFP signal and the superimposed trend of $\tau_{\mathrm{GABA_A}}$ is displayed in Fig. 4.4(a). The LFP contains high-frequency gamma oscillations at the beginning and the end, but high-amplitude low-frequency oscillations in the middle stage with similarities to SWS or slow-wave anaesthesia.

The time-frequency plot is displayed in Fig. 4.4(b). The appearance and disappearance of low-frequency oscillations are marked with vertical lines. Although the $\tau_{\mathrm{GABA_A}}$ trend has a symmetrical shape, the emergence and termination of slow oscillations occur at different doses

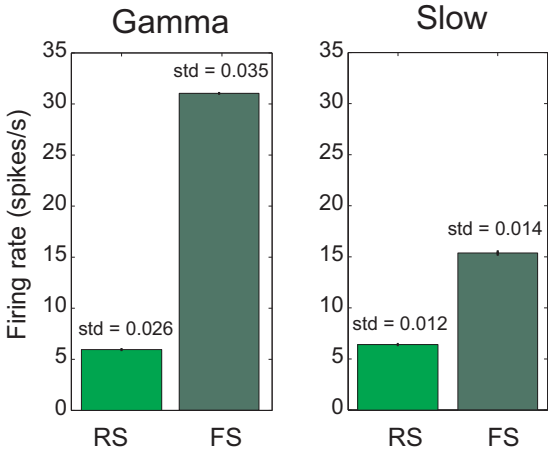

Figure 4.3: Firing rate of individual neurons in gamma and slow oscillations. The firing rate of the two selected regular spiking (RS) and fast spiking (FS) neurons from modelling experiment displayed in Fig. 4.2, during gamma and anaesthesia-induced slow oscillations.

of anaesthetic drug corresponding to $\tau_{\mathrm{GABA_A}} = 23.3,\ 18.32$ ms respectively. This phenomenon is analogous to *anaesthetic induced hysteresis* and is observed in particular neural models which exhibit bistability of stable states under specific conditions [Wilson, 1999; Steyn-Ross, 2002]. These modelling predictions have been supported recently by Friedman *et al.* [2010] in experimental studies on mice and fruit flies. They demonstrated that induction of unconsciousness by general anaesthetics and dissipation of anaesthetic effect is not mediated through identical forward and reverse paths.

A further analysis of the LFP is performed to investigate the possible early signs of state transition of LFP. The full-length LFP signal is displayed again in Fig. 4.5(a) for convenience. Three 3-s length epochs (horizontal bars) are selected from qualitatively different stages of the LFP time series. These epochs are plotted in (b-d). We compute the corresponding discrete Fourier transforms (implemented by MATLAB's `FFT` function), and extract the normalized amplitude spectrum:

$$\text{Amplitude spectrum of LFP} = \frac{1}{T_{\mathrm{s}} L} |\texttt{FFT}\,\{\text{LFP}\}\,| \tag{4.3.1}$$

where $T_{\mathrm{s}} = 0.1$ ms is the sampling interval (equal to the time step of the RK4 integrator), and $L = 30000$ is the length of the epoch. Amplitude spectra are plotted in Fig. 4.5(e-g).

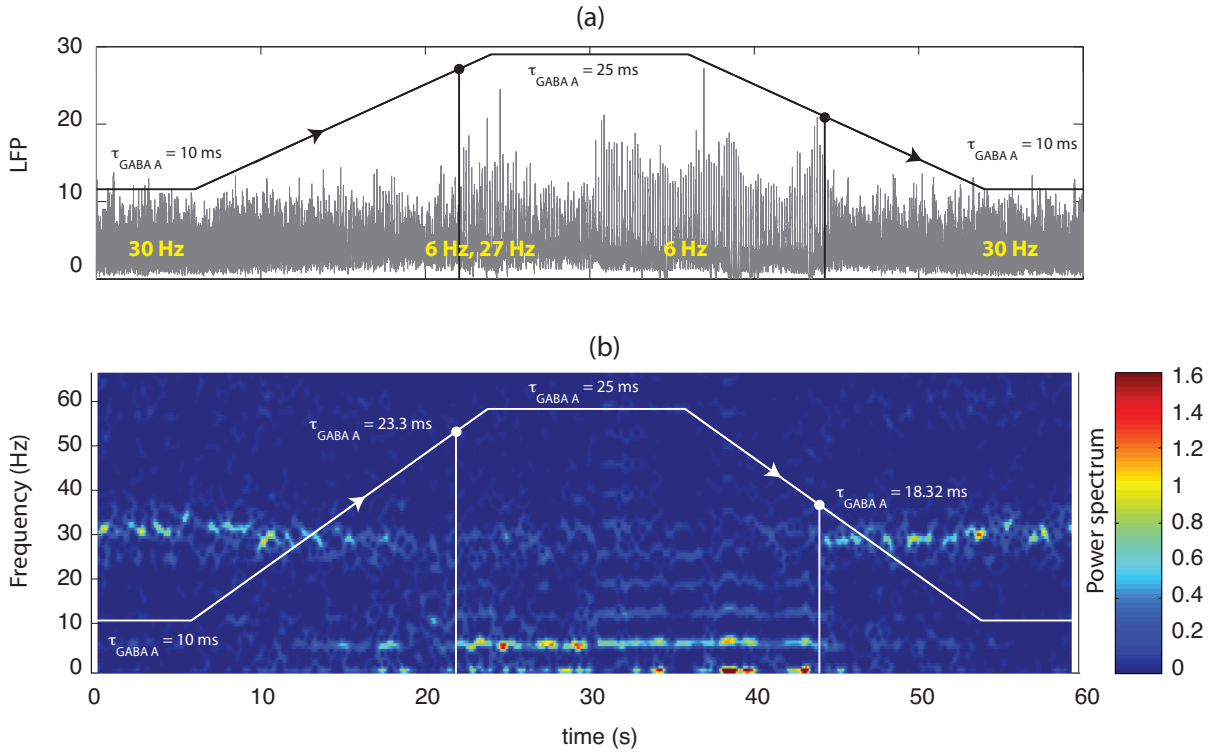

Figure 4.4: Hysteresis in the gamma-slow-gamma transition loop. (a) LFP when the activity of cortical network switches between gamma and slow oscillations by appropriate variation of $\tau_{\mathrm{GABA_A}}$ (superimposed black trace) from 10 ms in the baseline to 30 ms in the peak. (b) Time-frequency analysis of the LFP. The vertical lines highlight emergence and termination of low-frequency oscillations. Although $\tau_{\mathrm{GABA_A}}$ varies symmetrically, the emergence and termination of slow oscillations occur asymmetrically, implying a hysteresis effect.

These results show dominance of 30.82 Hz in (e), almost equal contribution of the $f = 5.79$ and $f = 28.69$ Hz components in (f), and the dominance of $f = 6.41$ Hz mode in (g). The simultaneous existence of two frequencies (corresponding to two distinct states of the system) is evident in (f), which can be interpreted as a sign of approaching a bistable region, with the possibility of an upcoming phase transition.

This section demonstrated how a simple network of spiking neurons can be developed to capture aspects of cortical activity in the fully "conscious" state that supports gamma-range oscillations. Network oscillations under the influence of anaesthesia (represented as a lengthening of the time-course of $GABA_A$ mediated inhibitory currents) was investigated. Interesting dynamical behaviours—bistability, and hysteresis—were observed near the transition regime before the system switches to a new oscillation mode, reminding us of the precursors announcing a bifurcation point.

In the next section I present a model for sleep spindles in a corticothalamic network of Izhikevich neurons with a focus on phase transitions.

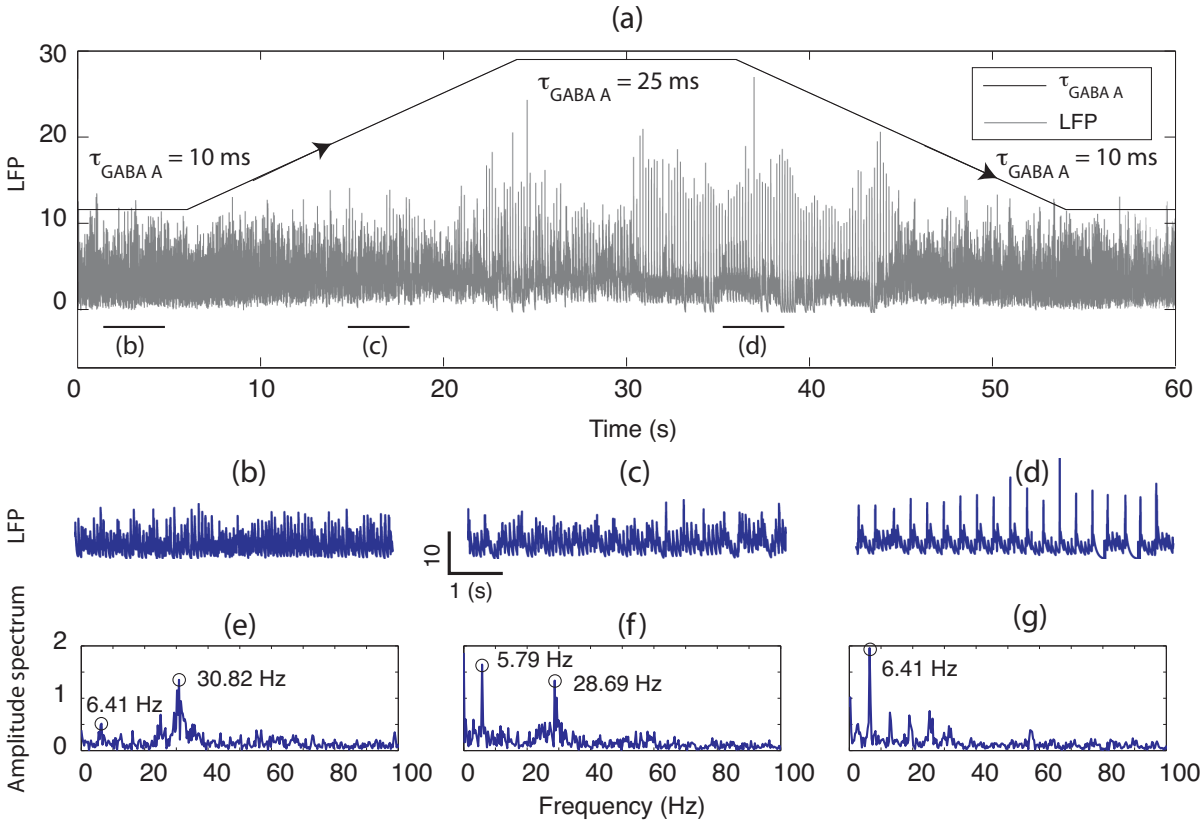

Figure 4.5: Appearance of alternative states in cortical network. (a) The LFP and τ_{GABA_A} trend from Fig. 4.4(a) replotted here for convenience. (b-d) Guided by the trend of the τ_{GABA_A}, three 3-s epochs were selected (horizontal bars) showing: normal activity, transition, and the low-frequency mode. (e-g) Amplitude spectrum showing bistability of the LFP in transition phase (f).

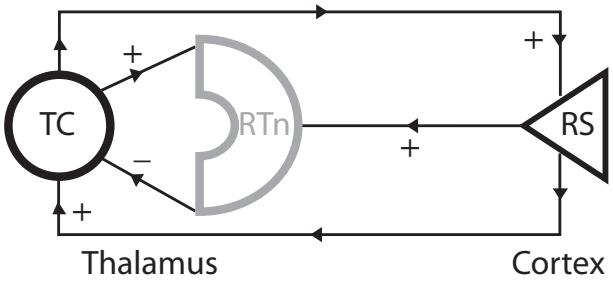

Figure 4.6: Structure of the thalamocortical model capable of producing spindles. There is a mutual connection between relay (TC) and reticular nuclei (RTn) neurons. The pyramidal regular spiking (RS) neuron of the cortex excites both thalamic neurons and receives feedback excitation from TC.

4.4 Increased sensitivity prior to sleep spindles

Here I demonstrate how a three-neuron thalamocortical network can be developed to generate sleep-related spindles. Then I examine the subthreshold fluctuations of individual neurons, and the behaviour of the LFP signal. I will look specifically for signs of increased sensitivity prior to spindle generation as a generic precursor of phase transitions in dynamical systems.

4.4.1 Sleep spindle modelling

Sleep spindles are produced through the interaction between thalamus and cortex [Steriade *et al.*, 1997; Steriade and McCarley, 2005]. The main neural types responsible for generation, maintenance and termination of spindles are thalamic TC, RTn, and cortical RS neurons. Cortical FS neurons do not contribute directly in any phase of spindle activity, although they are important in functional "deafferentation" of cortex through modulation of neocortical gamma activity by thalamic-originated spindles and hippocampal-originated sharp-wave-rippples [Peyrache *et al.*, 2011; Ayoub *et al.*, 2012]. Following theories of spindle generation and adopting corresponding models and experimental results of Destexhe *et al.* [1998], Bazhenov *et al.* [1998, 2002], Timofeev and Bazhenov [2005], and Bonjean *et al.* [2011] a simple model of thalamocortical network is constructed using only three types of neuron. Figure 4.6 shows the model structure: mutual connections between thalamocortical relay (TC) and reticular nuclei (RTn) neurons, and excitatory connections to and from the cortical RS neuron.

When the brain produces sleep spindles, the RS neurons are in bistable or excitable mode, and fire occasionally in response to excitation received from other brain areas, mainly as a result of sensory inputs. The cortically sourced random action potentials from RS excite both TC and RTn neurons. This excitation produces a subthreshold depolarization on the TC neuron, but induces bursts of action potentials (APs) in the RTn neuron, causing strong and persistent hyperpolarization of the TC neuron. The hyperpolarization-activated cation current (I_h) of the

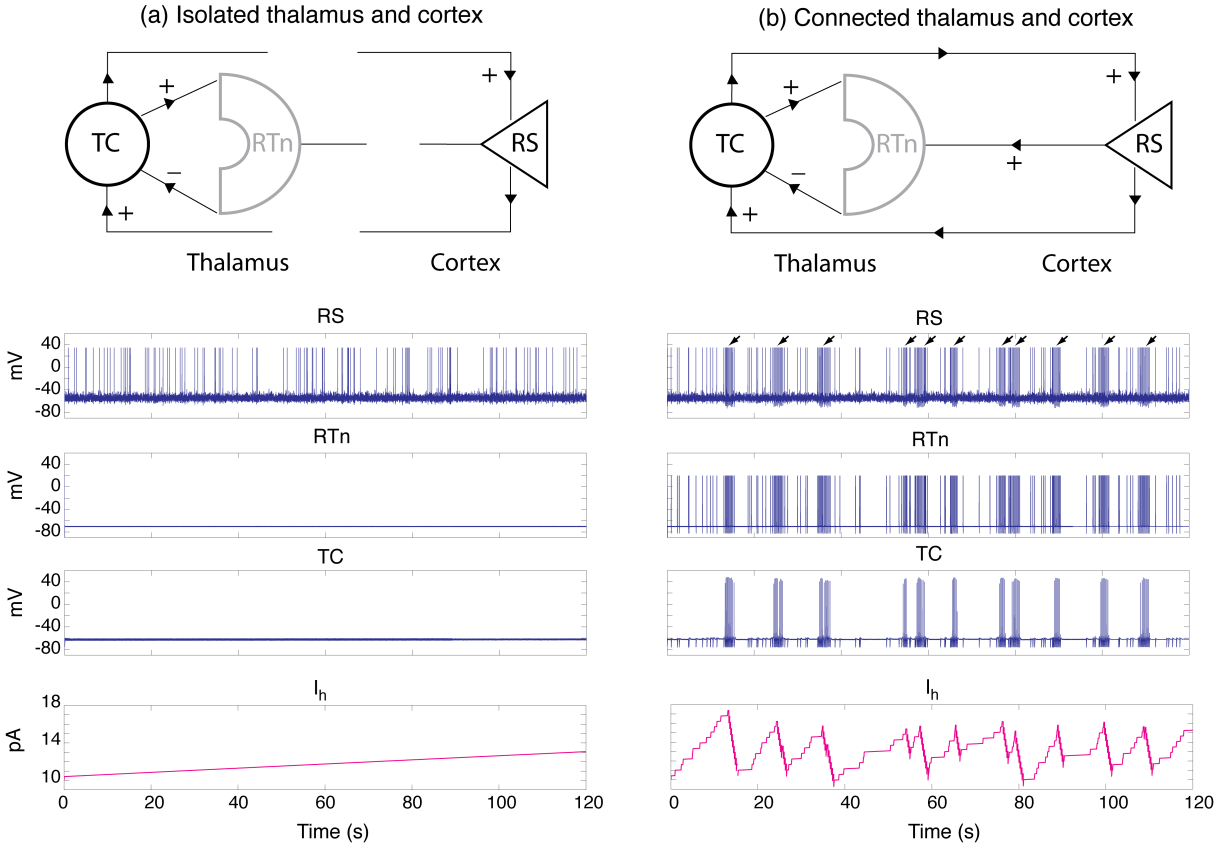

Figure 4.7: Spindle generation in the network of Fig. 4.6. The membrane voltage of three neural types and the I_h current of TC neuron are displayed. The drive currents of the neurons are $I_{\text{dc}} = -450, 80, 18$ pA for RTn, RS, and TC neurons respectively. The maximum synaptic conductances are $g_{\text{RTn-TC, max}} = 40$, $g_{\text{TC-RTn, max}} = 10$, $g_{\text{TC-RS, max}} = 5$, $g_{\text{RS-RTn, max}} = 6$, $g_{\text{RS-TC, max}} = 1.5$, $g_{\text{RS-RS, max}} = 1$ nS. The synaptic decay times are $\tau = 15, 5, 7$ ms for GABA_A, thalamic AMPA and cortical AMPA respectively. A fourth-order Runge-Kutta integrator with fixed time-step of $\Delta t = 0.1$ ms was used to solve the model equations.

TC neuron becomes active due to incoming inhibition from RTn[1], and may cause TC to cross firing threshold, so that it generates a burst of action potentials.

Bursting of the TC neuron excites its RTn and RS targets, resulting in generation of a synchronous spindle pattern in all three neurons. However TC firings inactivate the I_h current, causing hyperpolarization of TC neuron. This terminates the bursting of the TC neuron and consequently other neurons. The next spindle will be initiated by another random firing of the cortical RS neuron.

Based on the presented mechanism, two numerical simulations are performed in this section showing the activity of thalamic and cortical neurons during spindle generation. First, we isolate the cortex from the thalamus. Simulation results are displayed in Fig. 4.7(a), showing the random firing of RS neuron, while the thalamic neurons are in their quiet mode with sub-threshold fluctuations (not visible in the figure). The hyperpolarization activation current (I_h) of TC neuron is also displayed (bottom trace), demonstrating a very slow dynamics, compared

[1]Recall that I_h is a depolarizing current—see Section 3.8

to the fast dynamics of the spiking. The gradual uptake of I_h slowly depolarizes the TC neuron. Note that in a longer simulation of isolated thalamus and cortex, one may eventually observe TC firing at elevated values for I_h. However, the generated action potentials will quickly supress I_h, returning the TC membrane potential to hyperpolarized state with only noise-induced subthreshold fluctuations.

In the second experiment, the mutual connections between thalamus and cortex are restored. This results in repeated emergence and termination of synchronous spindles by all three neurons as indicated by arrows in top trace of Fig. 4.7(b). The spindles are extracted automatically (see Appendix C.2), and indicated by dashed line in Fig. 4.8(a). The resultant traces of spindle-width and the inter-spindle gaps are displayed in Fig. 4.8(b, c) respectively. The mean spindle width is 2.1 s, and the mean distance between consecutive spindles is 7.5 s. These results are in good agreement with their corresponding *in vivo* values of 0.5–3 and 5–15 s respectively [Bonjean *et al.*, 2011].

The interaction of individual neurons as described earlier can be realized more clearly by a closer look at the activity of the neurons as displayed in Fig. 4.9. The top trace shows random firing of an isolated RS neuron. Then the same neuron (with same applied noise) is connected to the rest of the network, and its membrane voltage displayed in the second trace. The first four APs fired by RS induce isolated bursts of APs in RTn (third trace), and small depolarization on TC (fourth trace) and a step increase in I_h current of TC neuron (last trace). The spindling initiates after firing of the fifth AP by RS neuron (indicated by star symbol), when the I_h has reached a level capable of depolarizing the TC neuron to its firing threshold.

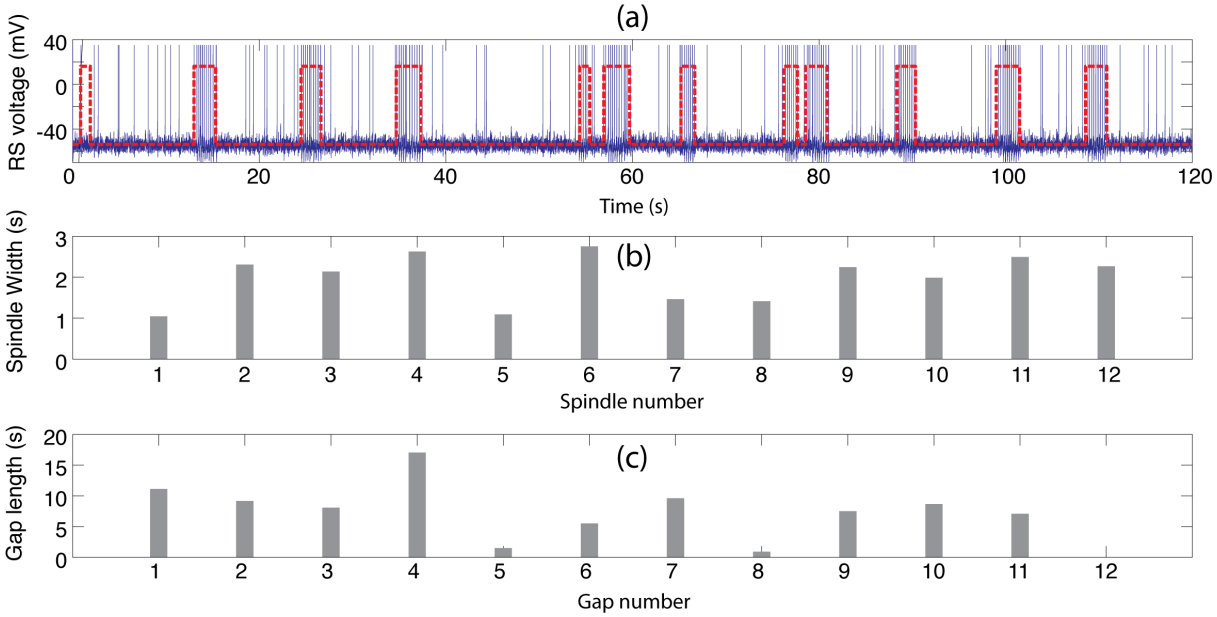

Figure 4.8: Extraction of spindle-width and interspindle gaps

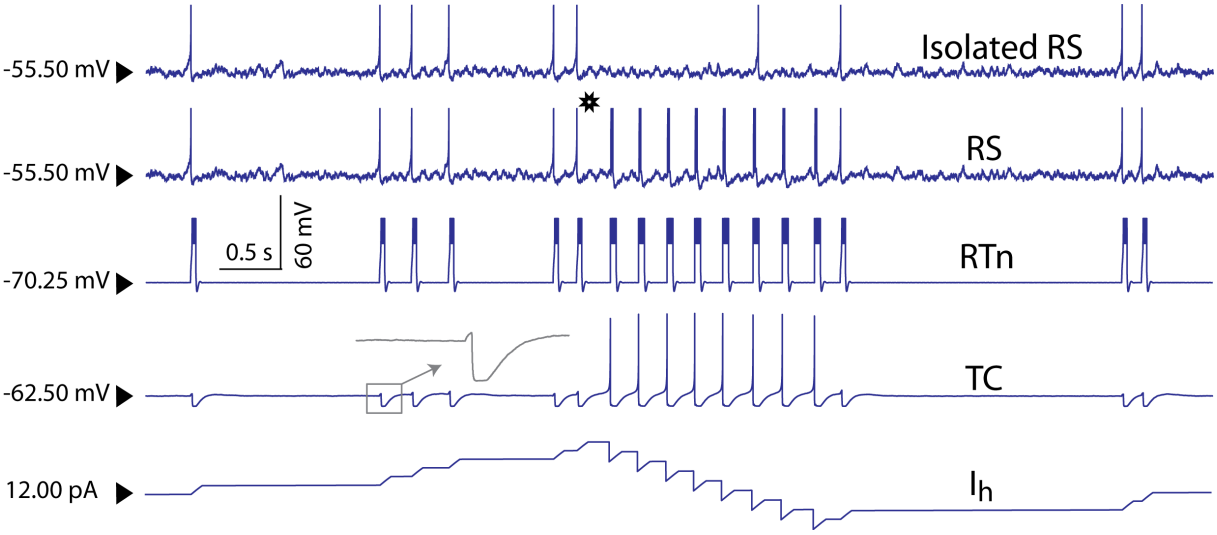

Figure 4.9: Detailed view of activity of individual neurons while a single spindle emerges and fades out. This particular spindle is the first one selected from the experiment displayed in Fig. 4.7.

4.4.2 Increased sensitivity prior to spindle initiation

The quiescent and bursting phases of a spindle pattern can be considered as two distinct dynamical modes for underlying neural system. Here I look for precursor signs of transitions in the spindling network. Among the three neural types, the best candidate to capture precursor activity is the TC neuron due to its slow-fast dynamic and its key role in spindle generation—although we will shortly examine RS and RTn neurons as well. Consider the activity of TC neuron as displayed in right panel of Fig. 4.7. The high-pass filtered or "rough" part of the TC voltage is extracted using a Whittaker filter[1] and displayed in Fig. 4.10(a). Two interburst periods (framed parts) are selected and plotted in Fig. 4.10(b, c). In the following its described how the variance of membrane fluctuations during inter-burst period is calculated and analyzed prior to spindle initiation.

One can track the variance of subthreshold fluctuations by sliding a temporal window on the time-series and extracting the instantaneous variance value at every step. This method is not straightforward to implement in our case due to interruptions by small spikelets. These spikelets contaminating the interburst period (indicated by star symbols in (c)) are due to TC response to excitations and inhibitions originating from RS and RTn neurons respectively. Only the spikelet-free parts of interburst periods are considered as potential conveyors for signs of upcoming burst. Two spikelet-free epochs are selected for each interburst period, belonging to start and end phases of the period, and their variances are compared. Fig. 4.10(b, c) displays the details of two interburst periods with extracted spikelet-free epochs in blue along with variance

[1]The smoothing factor and the sampling frequency of Whittaker filter are 10,000,000, 10,000 respectively

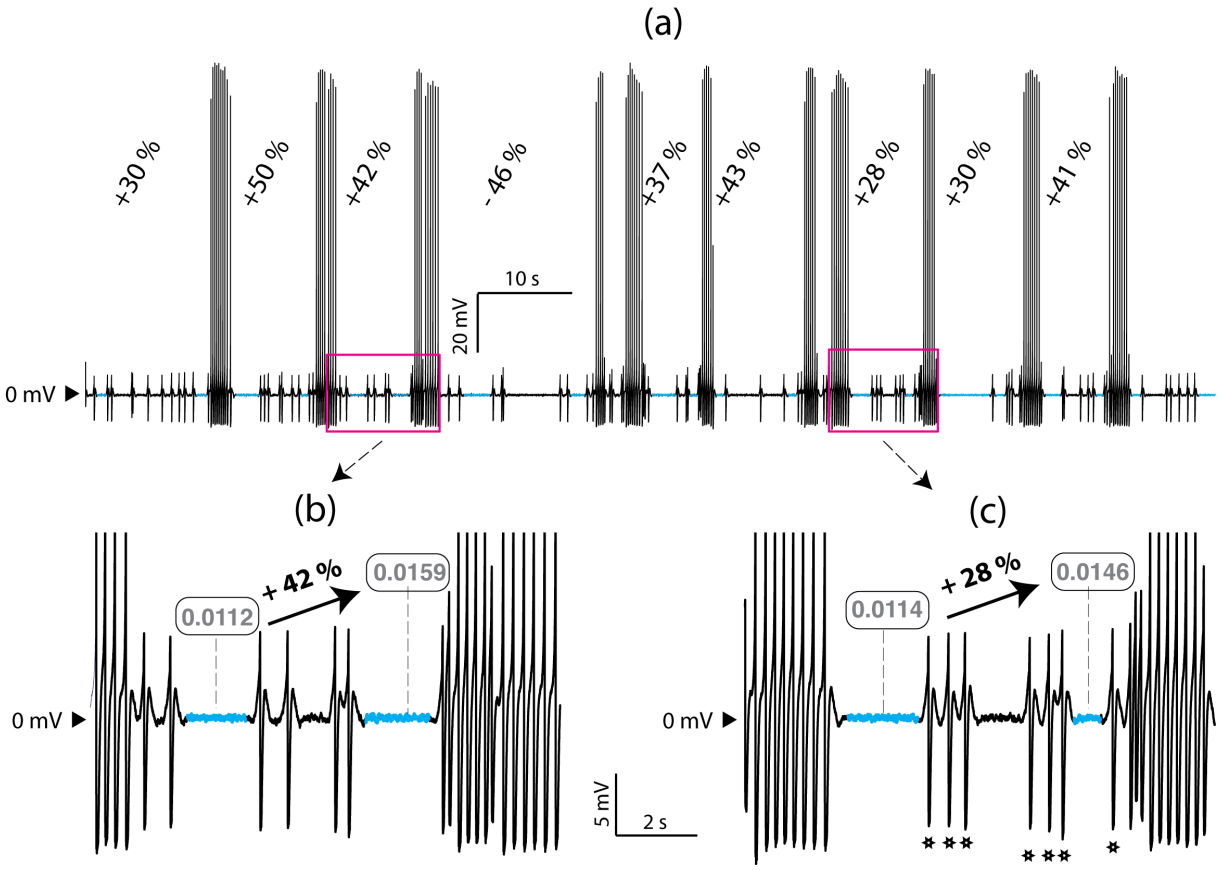

Figure 4.10: Increased variance of thalamocortical (TC) fluctuation prior to spindle generation. (a) TC membrane voltage during spindle generation in the network. The percentages demonstrate the growth in the fluctuation variance within inter-spindle periods. The variance increases noticeably in eight periods, but decreases in one periods. (b, c) Detailed view of two inter-spindle periods from (a). The inter-spindle periods are interrupted by spikelets (star symbols in (c)). Two spikelet-free epochs (blue) from beginning and end phases of each inter-spindle period are selected for further analysis. The framed numbers display normalized variance of corresponding epochs. Spikelet-free epochs vary in length from 0.5 to 4 s.

values and growth rates. In this simulation, 90% of spindle events are preceded by a growth in the interburst variance. The average variance increase is ∼40%

The same analysis is performed on the subthreshold voltage fluctuation of the RS neuron. Unlike the TC results, the variance of the RS interburst periods does not show a consistent trend in fluctuation variance. The corresponding high-pass filtered RS activity during two interspindle periods displayed in Fig. 4.10(b,c) are displayed in Fig. 4.11(a,b) respectively. The highlighted (grey) epochs of fluctuations and their variance values are displayed in the figure, showing no trend for the variance on the way towards spindle generation. Similar null results were found for RTn fluctuations (results not shown). Thus only the subthreshold voltage fluctuations of the TC neuron seemed to show precursor growth fluctuation amplitude prior to spindle generation.

A further variance analysis was performed on a longer TC time-series containing 33 inter-spindle periods; see Table 4.1. About 75% of spindles were preceded by a large increase in the voltage fluctuations. The initiation and termination phases of interspindle periods have an

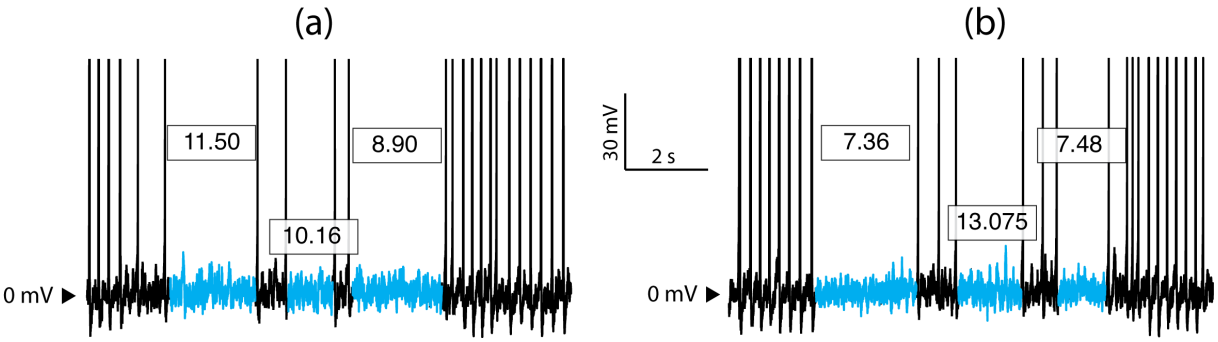

Figure 4.11: Variance analysis in spindling regular spiking (RS) neuron. The activity of RS neuron during two selected inter-burst periods is displayed. Displayed numbers are the variances of highlighted (grey) time-series in $(\text{mV})^2$, and show no trend in the period leading to burst generation.

average variance of 0.0189 and 0.0288 $(\text{mV})^2$ respectively, showing an average growth of 32%. These results show the increased variance in the time leading up to a spindle initiation, which can be interpreted as a precursor sign of phase transition.

4.5 Chapter summary

After examining the subthreshold fluctuations of individual neurons in Chapter 3, I extended the investigations to networks of spiking neurons in this chapter. Following a brief discussion about synaptic interactions, I selected a network measure for local field potential (LFP). Using the models of single neurons developed in Chapter 3, small networks were presented to model two distinct neural phenomena, namely cortical gamma oscillations and thalamocortical sleep spindles. The network model for gamma activity produced results comparable to *in vivo* observations. The transformation of gamma oscillations to slower oscillations due to the effect of anaesthesia was investigated. Interestingly, the network LFP displayed, bistability and hysteresis across the transition from gamma to slow oscillations. Such behaviours can be interpreted as precursors of phase transitions, reminding us of flicker hallucination and pre-epileptic/pre-migraine auras.

A three-neuron model of thalamocortical network capable of producing sleep spindles was constructed. The spindle-generation mechanisms were informed by previous work based on

Table 4.1: Variance growth in the thalamocortical (TC) fluctuations prior to spindle initiation. The network structure is displayed in Fig. 4.6. Model parameters are as right panel of Fig. 4.7. A total of 33 interspindle periods were analyzed using similar approach as in Fig. 4.10; among these 25 spindles were successfully predicted by 32% growth in the fluctuation variance of inter-spindle periods. Variance of beginning and end phases are displayed in the form of `average`±`standard deviation`, with units $(\text{mV})^2$.

Number of interspindle periods	Variance at the begining	Variance at the end	Average variance growth (%)
25	0.019±0.004	0.029±0.005	**+32**

the Hodgkin-Huxley formalism. Using the Izhikevich-based models of Chapter 3, the proposed network produces spindles which are comparable with *in vivo* results. Subthreshold voltage fluctuations of individual neurons were investigated prior to spindle initiation. The TC neuron demonstrated increased variance of subthreshold fluctuations prior to spindle generation, consistent with critical slowing down. Unlike the TC neuron, the RS and RTn neuron did not show signs of critical slowing. Because of the insignificant contribution of TC subthreshold activity in synaptic currents, the LFP signal is not expected to demonstrate increased variance prior to spindle initiation.

The network models presented in this chapter supported the possibility of capturing precursors of phase transitions at least, in a model. The study of phase transitions and corresponding precursors will be continued in the next two chapters using the Wilson-Cowan mean-field cortical model. We will see how such mean-field models provide a solid frame-work for both theoretical and numerical examination of neural systems and their phase transitions.

Chapter 5

Subthreshold analysis of spatially-homogeneous Wilson–Cowan model

We are motivated by the idea that computational modelling of seizure events may provide insights about epileptogenesis. It is known that both microscopic (ion channels, synapses) and network-scale macroscopic neural phenomena have role in seizure generation, maintenance and termination. As a result both scales should be considered in designing the computational models of the mechanisms underlying seizures. Both *detailed network* and *mean-field* models are used vastly to model behaviour of epileptic neural populations [Ullah and Schiff, 2009; Fisher *et al.*, 2005]. However we choose mean-field approach which enables us to to perform theoretical analysis of the model beside numerical simulations.

The Wilson–Cowan equations as one of the foundation mean-field models, has been used to model multiple aspects of neural functions (see Chapter 1 for a review). Here we use this model to investigate the system dynamics prior to different bifurcation types which may control seizure-induced state transitions. Our hypothesis is that distinct bifurcation types accompany the emergence and termination phases of seizures, so we seek *precursor signals* or *leading indicators* that may be detected prior to such state transitions. This chapter tests our hypothesis using a spatially-homogeneous form of the Wilson–Cowan model that can exhibit both bifurcations: saddle-node and Hopf. Looking for evidence of *critical slowing*, the variance and autocorrelation of model-generated excitatory firing rates will be analyzed while approaching those bifurcation points. We will show that numerical results confirm theoretical predictions about system behaviour.

The chapter starts with a complete introduction of the original Wilson–Cowan equations in Section 5.1. We analyse the spatially-homogeneous limiting form in Section 5.2. The linearized form of the model and its stability analysis is presented in 5.2.2, 5.2.3. Then we derive the

steady-state distribution curve in 5.2.4. Section 5.2.5 shows how the system demonstrates two different bifurcation types, and leading indicators can be captured prior to these bifurcations. The chapter concludes with a summary in Section 5.3.

5.1 Wilson–Cowan model for excitable tissue

The introduction of Hodgkin–Huxley model in 1952 [Hodgkin and Huxley, 1952] motivated many neural modellers to include detailed descriptions of individual neurons and their structural components such as ionic channels and dendrites. This trend towards ever increasing detail was reversed in the approach adopted by Hugh R. Wilson and Jack D. Cowan, when they realized the necessity of developing a neural mass model to describe interactions of thousands of neurons within a localized population [Wilson and Cowan, 1972]. This adoption of a neural continuum was necessary to model parts of brain which are associated with higher functions such as learning, memory and pattern recognition, since these functional parts of nervous system require coordinated input produced by large numbers of neurons, and this scale is too vast to contemplate modelling at the level of single neurons. In addition, the global nature of functions such as pattern recognition cannot be inferred from the action of single cells. Wilson and Cowan recognized that local interactions between individual neurons are largely random; however such interactions on a large scale can give rise to very precise neural functions, similar to the way in which the random Brownian motion of individual molecules of fluid can organize into an orderly laminar flow when viewed macroscopically. Thus the Wilson–Cowan model emphasizes properties of *populations* of neurons rather than the behaviour of *individual* cells.

The Wilson–Cowan model describes average spike frequency of a neural population (instead of membrane voltage of single neuron) as a function of continuous time (instead of discrete timing of spike events). The major simplifying assumption is that all functions of brain activity arise from interactions between excitatory and inhibitory populations, so the state variables for the model are E and I representing the excitatory and inhibitory spike frequencies respectively. Based on known neuroanatomy, Wilson and Cowan assumed a random, dense connectivity between individual cells, allowing at least one connection between any two cells in the network.

Wilson and Cowan neglected spatial interactions in their 1972 paper in order to investigate temporal dynamics of a localized cortical column; they then extended their model to spatially distributed neural populations in their 1973 paper [Wilson and Cowan, 1973], and modelled 1D lines and 2D sheets of cortical and thalamic tissue.

The $E(t)$ and $I(t)$ functions were defined originally as the proportion of excitatory and inhibitory subpopulations which fire in unit time. It is assumed that the firing fraction at time $(t+\tau)$ is given by the proportion of cells which are *not* in their refractory period *and* which also

receive a threshold excitation at time t. This excitation is composed of synaptic inputs from other neurons in the network, plus external input entering each subpopulation. The resulting equations governing the dynamics of localized populations of neurons are [Wilson and Cowan, 1972]:

$$\begin{aligned} E(t+\tau) &= \left[1 - \int_{t-r}^{t} E(t')\mathrm{d}t'\right] \cdot \mathcal{S}_e \left(\int_{-\infty}^{t} \alpha(t-t') \left[c_1 E(t') - c_2 I(t') + P(t')\right] dt'\right) \\ I(t+\tau') &= \left[1 - \int_{t-r}^{t} I(t')\mathrm{d}t'\right] \cdot \mathcal{S}_i \left(\int_{-\infty}^{t} \alpha(t-t') \left[c_3 E(t') - c_4 I(t') + Q(t')\right] dt'\right) \end{aligned} \tag{5.1.1}$$

where r is the absolute refractory period (in ms), and $P(t)$, $Q(t)$ are time-dependent external inputs to E and I subpopulations respectively (in $(\mathrm{ms})^{-1}$). The proportion of excitatory cells which are not in the refractory period (i.e., which are sensitive) is given by $\left[1 - \int_{t-r}^{t} E(t')\mathrm{d}t'\right]$. The $\mathcal{S}_{i,e}$ (in /ms) are *subpopulation response functions* which give the expected firing rate of the excitatory and inhibitory subpopulations based on the average excitation (in mV) they receive. It is assumed that individual cells sum their excitatory and inhibitory inputs with weights represented by c_i coefficients (which are unitless numbers representing the average number of excitatory or inhibitory synapses per cell), and that the effect of stimulations decay with a time course $\alpha(t)$ (in mV). It is also assumed that to be a sensitive cell and for it to reach threshold excitation are statistically independent events. As discussed in the literature review, subpopulation response functions are normally selected to have monotonically increasing sigmoidal forms as inspired by experimental single-cell and population-response curves.

Wilson and Cowan used a *temporal coarse graining* to simplify equations (5.1.1) and thereby eliminated the temporal integrals which have less biological significance than the sigmoidal response functions. They defined $\bar{f}(t)$, the coarse-grained average of a time dependent variable $f(t)$,

$$\bar{f}(t) = \frac{1}{s} \int_{t-s}^{t} f(t')\, dt'$$

where s is some appropriately chosen interval over which the moving time-average is computed. Wilson and Cowan showed that temporal responses evolving over time courses shorter than s are not significant for their modelling purposes, so they replaced the time-integrals in the right-hand side of Eq. (5.1.1) with their corresponding coarse-grained representations as

$$\begin{aligned} \int_{t-r}^{t} E(t')\, dt' &\to r\bar{E}(t) \\ \int_{-\infty}^{t} \alpha(t-t')E(t')\, dt' &\to k\bar{E}(t) \end{aligned}$$

where k is a constant in mV·ms. They also replaced $E(t+\tau)$ and $I(t+\tau')$ with their corresponding coarse-grained equivalents $\bar{E}(t+\tau)$ and $\bar{I}(t+\tau')$, and then with their truncated Taylor expansions,

$$\begin{aligned}\bar{E}(t+\tau) &\simeq \bar{E}(t) + \tau\frac{d\bar{E}}{dt} \\ \bar{I}(t+\tau') &\simeq \bar{I}(t) + \tau\frac{d\bar{I}}{dt}\end{aligned}$$

Thus the simplified form of equations (5.1.1) is arrived at:

$$\begin{aligned}\tau\frac{\mathrm{d}\bar{E}}{\mathrm{d}t} &= -\bar{E} + (1 - r\bar{E}) \,.\, \mathcal{S}_e\left[k\left(c_1\bar{E} - c_2\bar{I} + P(t)\right)\right] \\ \tau'\frac{\mathrm{d}\bar{I}}{\mathrm{d}t} &= -\bar{I} + (1 - r\bar{I}) \,.\, \mathcal{S}_i\left[k'\left(c_3\bar{E} - c_4\bar{I} + Q(t)\right)\right]\end{aligned} \tag{5.1.2}$$

where k and k' are constants given by the area under the respective temporal response function (with units mV·ms), so represent synaptic strengths.

Applying phase-plane analysis to these simplified equations, Wilson and Cowan demonstrated the existence of limit cycles, multiple steady states and hysteresis loops. Dynamical aspects of a slightly modified form of equations (5.1.2) will be studied in detail in the present chapter (in sections 5.2, 6.1) to elucidate subthreshold behaviour as well as different bifurcation mechanisms leading to distinct phase transitions.

Wilson and Cowan's 1972 paper describes the excitatory and inhibitory interactions in localized (space independent) populations. These populations are considered as functional columns with high degree of redundancy, meaning that clusters of neurons have similar response function [Shadlen and Newsome, 1994]. The cortical columns are linked via lateral inter-column connections, forming a 2D sheet of excitable tissue. Considering lateral connections, Wilson and Cowan incorporated a spatial domain as the basis for their 1973 spatiotemporal model.

Figure 5.1 illustrates how an assembly of cortical columns can form a cortical sheet as a representative of cortical tissue. Equations (5.1.2) describe the behaviour of a single cortical column; the spatially extended version of this model as governed by equations (5.1.3) describes the average behaviour a 1D neural line comprised of interacting columns. The authors assumed that

- The sheet is homogeneous (uniform distribution of neurons across the sheet)
- The sheet is isotropic (lateral connectivity is a function of distance only)
- Individual neurons temporally and spatially summate incoming excitations
- All possible types of connection between excitatory and inhibitory neurons are allowed: $E \to E,\ E \to I,\ I \to E,\ I \to I$.

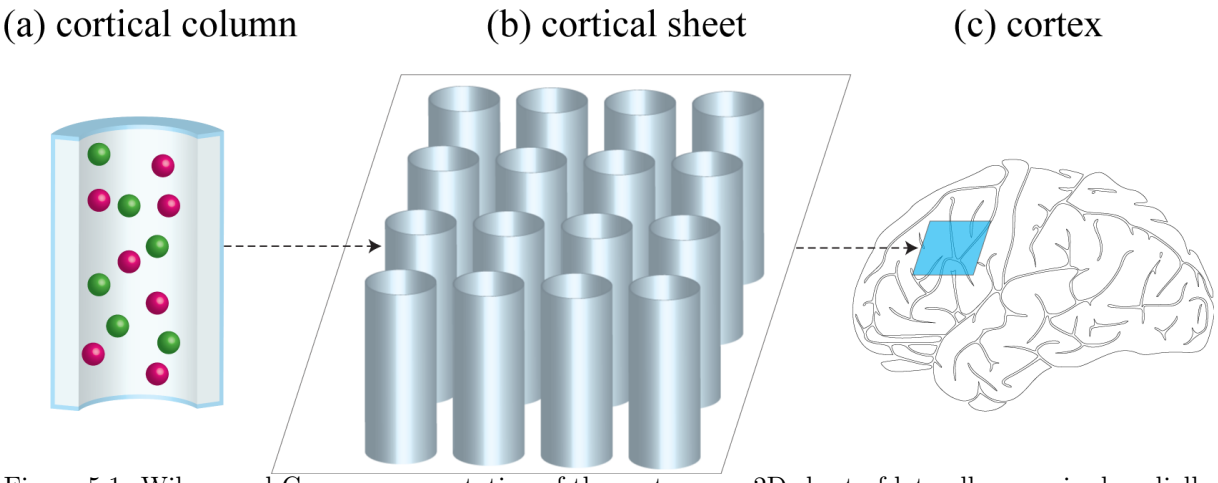

Figure 5.1: Wilson and Cowan representation of the cortex as a 2D sheet of laterally organized, radially redundant cortical columns. (a) A cortical column is composed of densely packed and interconnected excitatory and inhibitory neurons (connections not shown). Equations (5.1.2) describe the average activity of interacting excitatory and inhibitory neurons within an individual cortical column. Each column has cross-sectional area 1 mm^2 and length 2.7 mm in human, containing an average of 20000 neurons [Wilson and Cowan, 1973]. (b) Model of cortical sheet as part of cortex (c) developed by incorporating lateral interconnections (not shown) between columns to describe the average behaviour of cortical and thalamic sheets as described by Eq. (5.1.3). [Cortex modified from `http://all-free-download.com/`]

Connectivity of neurons of type j to neurons of type k is described by the functions β_{jk} (unitless) which were selected to be a monotonicaly decaying function of space. Accounting for the spatial summation of incoming synaptic signals received by individual neurons, Wilson and Cowan introduced their model of cortical and thalamic nervous tissue [Wilson and Cowan, 1973]. After applying temporal coarse-graining, their space-dependent model reads:

$$\begin{aligned}
\mu\frac{\partial}{\partial t}\langle E(x,t)\rangle &= -\langle E(x,t)\rangle + [1 - r_e\langle E(x,t)\rangle] \\
&\quad .\mathcal{S}_e\Big[\alpha\mu\left[\varrho_e\langle E(x,t)\rangle \otimes \beta_{ee}(x) - \varrho_i\langle I(x,t)\rangle \otimes \beta_{ie}(x) + \langle P(x,t)\rangle\right]\Big] \\
\mu\frac{\partial}{\partial t}\langle I(x,t)\rangle &= -\langle I(x,t)\rangle + [1 - r_i\langle I(x,t)\rangle] \\
&\quad .\mathcal{S}_i\Big[\alpha\mu\left[\varrho_e\langle E(x,t)\rangle \otimes \beta_{ei}(x) - \varrho_i\langle I(x,t)\rangle \otimes \beta_{ii}(x) + \langle Q(x,t)\rangle\right]\Big]
\end{aligned} \tag{5.1.3}$$

where $\otimes$ denotes a 1D spatial convolution defined by

$$X(x) \otimes Y(x) \equiv \int_{-\infty}^{\infty} X(x')Y(x - x')\,dx'$$

The $\varrho_{e,i}$ (in $(\mu\text{m})^{-1}$) are the surface density of excitatory and inhibitory neurons in a 1D homogeneous and isotropic tissue; μ (in ms) is the neuronal membrane time constant; α (in mV) is the maximum amplitude of the postsynaptic potential; and $\mathcal{S}_j$ is the subpopulation response function. The $\langle x\rangle$ represents the time-averaged value of $x(t)$. These equations describe the dynamical behaviour of a 1D line of cortical or thalamic tissue distributed along the x-axis; incorporating the second spatial dimension to model a 2D cortical sheet, as illustrated in

Fig. 5.1.(b), is straightforward.

Later in 1999, Wilson presented a simplification of equations (5.1.3) which sets the refractory period to zero, giving equations in which E and I now describe neural spike rates (rather than the proportion of E or I subpopulations which are active during unit time and unit area [Wilson, 1999]). The model describes the collective behaviour of cortical tissue in terms of a discrete *network* of laterally-connected localized aggregates of E and I populations representing cortical columns. The revised equations are:

$$\begin{aligned} \tau_E \frac{dE(x)}{dt} &= -E(x) + \mathcal{S}_E \left(\sum_x w_{EE}(x)E(x) - \sum_x w_{IE}(x)I(x) + P \right) \\ \tau_I \frac{dI(x)}{dt} &= -I(x) + \mathcal{S}_I \left(\sum_x w_{EI}(x)E(x) - \sum_x w_{II}(x)I(x) + Q \right) \end{aligned} \tag{5.1.4}$$

where the spatial convolutions have been replaced by discrete summations. For our investigations we choose to return these network equations to their continuum form,

$$\begin{aligned} \tau_E \frac{\partial}{\partial t} E(x,t) &= -E(x,t) + \mathcal{S}_E \Big[w_{EE}(x) \otimes E(x,t) - w_{IE}(x) \otimes I(x,t) + P \Big] \\ \tau_I \frac{\partial}{\partial t} I(x,t) &= -I(x,t) + \mathcal{S}_I \Big[w_{EI}(x) \otimes I(x,t) - w_{II}(x) \otimes I(x,t) + Q \Big] \end{aligned} \tag{5.1.5}$$

where $E(x)$ and $I(x)$ are again the mean firing rate of neurons at position x in $(\text{ms})^{-1}$, τ_E and τ_I are the time constant of each population (in ms), and P, Q (in mV) are the external voltage inputs to each population. The four w_{jk} $(j, k \in \{E, I\})$ are the connectivity functions that define the density (strength per unit length) of the synaptic coupling between and within populations. The coupling strength is assumed to decay exponentially with distance:

$$w_{jk}(x) = \frac{b_{jk}}{2\sigma_{jk}} \exp(-|x|/\sigma_{jk}) \tag{5.1.6}$$

where b_{jk} (in mV.ms) represents the maximum synaptic coupling strength between populations j and k, and σ_{jk} (in µm) is the space constant that controls the spread of connectivity. This form of normalization of the exponential decay has been chosen so that the integral of the connection density over the infinite 1D spatial domain gives the connection strength b_{jk}:

$$\int_{-\infty}^{\infty} w_{jk}(x)\, dx = b_{jk} \tag{5.1.7}$$

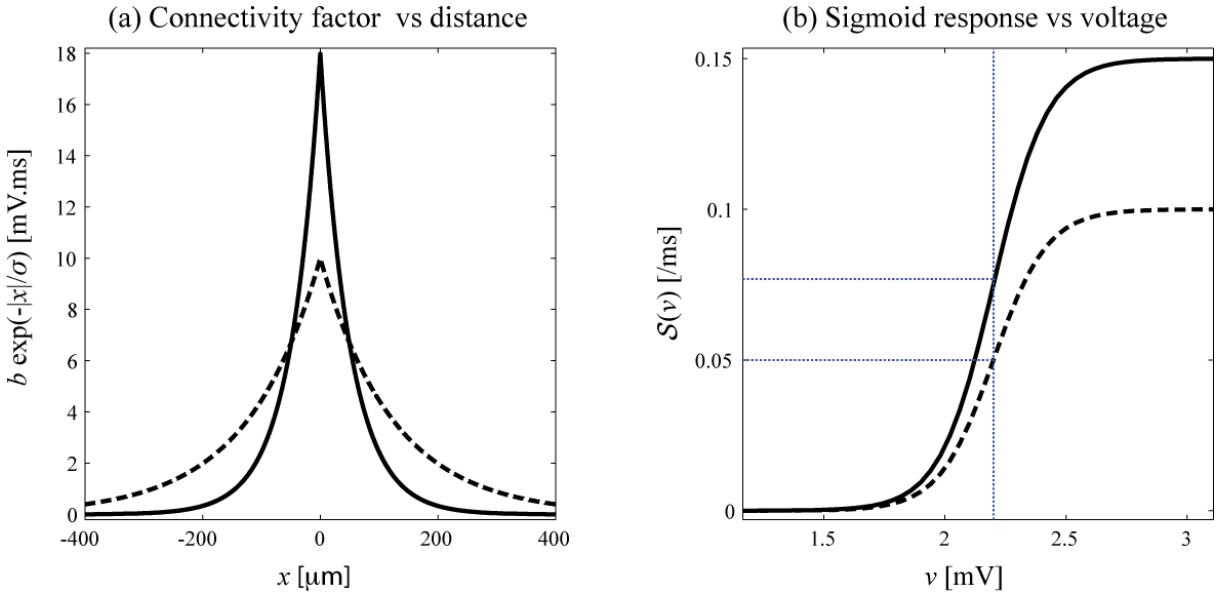

Figure 5.2: (a) The connectivity factor of Eq. (6.1.2) as defined by $b.\exp(-|x|/\sigma)$ versus distance x is plotted for two different sets of the coefficients, $[b/(\text{mV.ms}), \sigma/\mu\text{m}] = [18, 50],\ [10, 123.6]$, solid and dashed curves respectively. This function provides stronger connectivity for adjacent neurons compared to distant ones. (b) The sigmoidal response function as a function of membrane voltages for two sets of coefficients, $[\mathcal{S}_j^{\max}/(\text{ms})^{-1}, a/(\text{mV})^{-1}, \theta/\text{mV}] = [0.15, 9, 2.2], [0.1, 9, 2.2]$, solid and dashed curves respectively.

This follows after noting that

$$\int_{-\infty}^{\infty} \exp(-|x|/\sigma_{jk})\ dx = 2\int_{o}^{\infty} \exp(-x/\sigma_{jk})\ dx = 2\sigma_{jk}$$

This result is particularly useful when simplifying Eq. (5.1.5) to its spatially homogeneous limit (see next section). Figure 5.2(a) plots the synaptic connectivity factor $b\ \exp(-|x|/\sigma)$ versus x for typical values of $b,\ \sigma$. Wilson [1999] used the Naka–Rushton function to map from voltage to firing rate, but the sigmoidal function we elect to use in this thesis has the form,

$$S_j(v) = \frac{S_j^{\max}}{1 + \exp[-a_j(v - \theta_j)]}\ , \qquad j \in \{I, E\} \tag{5.1.8}$$

where θ (in mV) is the threshold voltage for half-maximum firing, a (in $(\text{mV})^{-1}$) sets the sigmoid slope at threshold, and $S_j^{\max}$ (in $(\text{ms})^{-1}$) is the maximum firing rate; see Fig. 5.2(b).

5.2 Wilson–Cowan model of a spatially-homogeneous cortex

As our simplest reference case, we wish to investigate the properties of a homogeneous 1D cortex in which the population firing rates are independent of position, i.e.,

$$E(x,t) \to E(t)\,, \qquad I(x,t) \to I(t)$$

so that the convolution integrals in Eqs.(5.1.5) simplify to constant scale factors multiplying the population activities. For example,

$$w_{EE}(x) \otimes E(x,t) = \int_{-\infty}^{\infty} w_{EE}(x')\ E(x-x',t)\ dx'$$

becomes

$$\begin{aligned} w_{EE}(x) \otimes E(t) &= \int_{-\infty}^{\infty} w_{EE}(x')\ E(t)\ dx' \\ &= E(t) \int_{-\infty}^{\infty} w_{EE}(x)\ dx \\ &= b_{EE}\ E(t) \qquad\qquad \text{from Eq. (5.1.7)} \end{aligned}$$

Applying the corresponding simplifications to the remaining three convolution integrals results in our final form for the Wilson–Cowan spatially-homogeneous cortex:

$$\begin{aligned} \tau_E \frac{dE}{dt} &= -E + \mathcal{S}_E(b_{EE}E - b_{IE}I + P) \\ \tau_I \frac{dI}{dt} &= -I + \mathcal{S}_I(b_{EI}E - b_{II}I + Q) \end{aligned} \tag{5.2.1}$$

Figure 5.3 illustrates the spatially homogeneous model with two interacting excitatory and inhibitory populations. P, Q (in mV) are the respective external inputs to excitatory and inhibitory populations. Synaptic weights are indicated by b_{jk} coefficients where $j, k \in \{E, I\}$. These weights represent the synaptic coupling strength from population j to k, and are proportional to the average number of synapses targeting the postsynaptic cell. The firing rate of each population is a sigmoidal function of its summed synaptic and external voltage inputs.

We now investigate the subthreshold dynamical behaviour of the spatially-homogeneous model. This analysis examines the dynamics of the cortex prior to occurrence of phase transitions in the homogeneous limit, and may provide insights about seizure generation mechanisms, since emergence of seizures can be well described by different bifurcation types.[1] We will see that white-noise-induced fluctuations of the model undergo critical slowing down, prior to two different bifurcation types: saddle-node and Hopf. Precursor signs will be extracted from the system's state prior to phase transitions which can have clinical significance in terms of seizure prediction.

[1] Our in vitro records from mouse brain slices (containing cortical and hippocampal areas) show different types of bifurcations responsible for seizure emergence and termination. See chapter 7 for more details.

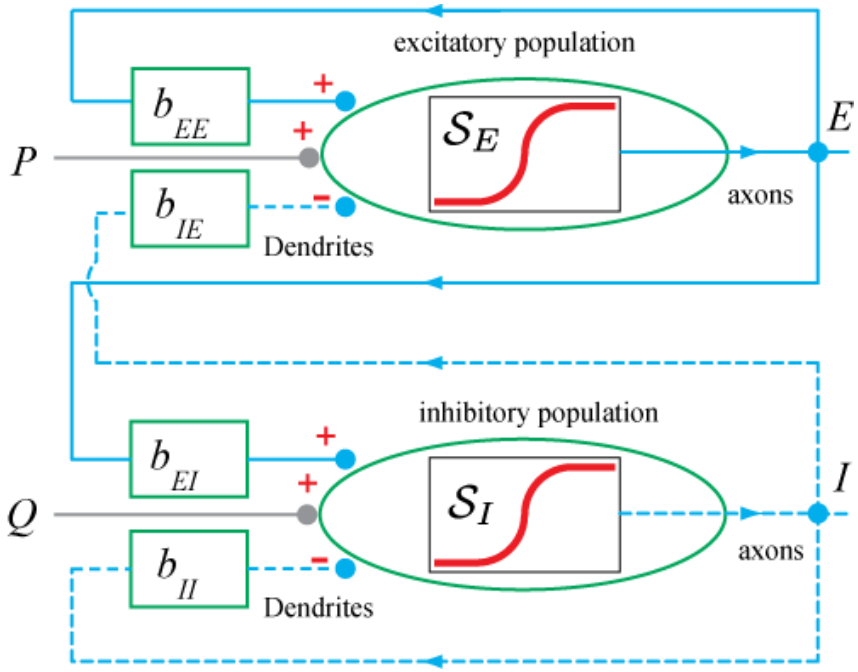

Figure 5.3: A diagrammatic representation of the Wilson–Cowan model of a spatially-homogeneous cortex. The inhibitory and excitatory connections are shown with dashed and solid lines respectively. P and Q are exogenous voltage inputs to the neural populations, and b_{jk} are the synaptic weights. The firing rates are sigmoidal function of synaptic and exogenous inputs.

5.2.1 Parameter values of the model

Although the homogeneous model of Eq. (5.2.1) is, by design, mathematically rather simple, it requires the specification of 14 numerical parameters (see Table 5.1). Choosing reasonable values for these 14 parameters is challenging, and requires biologically-inspired constraints to select or limit the range of values. The P, Q voltage inputs can take on a broad range of values since these parameters represent exogenous events such as external stimuli or incoming signals from neighbouring columns or distant brain parts such as thalamus or brainstem. Many parameters describe the spatially-averaged characteristics of cortical columns instead of individual neurons. For example, we choose $\tau_E = 10$ ms as a combination of decay times of all excitatory elements within a cortical column. Keeping the parameter values in the order of suggested values of a similar work by Wang *et al.* [2012], and considering biologically measured values, we fine-tuned some parameters. Specifically the sigmoidal parameters ($S^{\max}_{E,I}$, $a_{E,I}$, $\theta_{E,I}$) were tuned to get at least one non-monotone nullcline (a nullcline with regional negative and positive slopes, see E-nullcline in Fig. 5.4); and the P, Q voltage inputs were selected to give multi-root region in steady-state distribution curve as depicted in Fig. 5.5(a). Table 5.1 shows the parameter values.

It should be mentioned that the firing rates output from the Wilson–Cowan model are directly related to the axonal activity of neurons. As a result, the outputs are not quantitatively comparable with EEG waveforms.[1] However there is a reasonable correlation between mean

[1]Dendritic trees of cortical pyramidal neurons are aligned parallel to each other, and EEG is mainly produced by excitatory postsynaptic potentials of these neurons [da Silva, 2010]. The geometrical structure of cortical

Table 5.1: Symbol definitions and typical parameter values for the spatially-homogeneous Wilson–Cowan model. Although there is considerable uncertainty in the parameter values, they are selected to be in the range of a similar study by Wang et. al. [Wang *et al.*, 2012].

Symbol	Description	Value	Unit
E, I	Firing rates of E and I processes		$(\text{ms})^{-1}$
$\tau_{E,I}$	Time constants of E and I responses	10, 8	ms
S_E, S_I	Sigmoid functions mapping voltage to firing rate		$(\text{ms})^{-1}$
$b_{EE,EI,IE,II}$	Synaptic coupling strength	18, 10, 10, 0	mV.ms
$\sigma_{EE,EI,IE,II}$	Space constant	50, 110, 110, 20	µm
$S_{E,I}^{\max}$	Maximum firing rate	0.1, 0.15	$(\text{ms})^{-1}$
$a_{E,I}$	Sigmoid slope at threshold	9	$(\text{mV})^{-1}$
$\theta_{E,I}$	Threshold voltage for half-maximum firing	2.2	mV
P, Q	Exogenous voltage inputs to E and I populations	[1.3–2.1], 1.5	mV

firing rate of cortical neurons (as modelled by Wilson–Cowan equations), and amplitude (power) or phase of EEG potentials [Whittingstall and Logothetis, 2009] and [Ng *et al.*, 2013].

5.2.2 Equilibrium points of the homogeneous cortex

Although a numerical method is needed to study the temporal evolution of a highly nonlinear system such as Wilson–Cowan model, considerable insights about system dynamics can be obtained by examining the *equilibrium points* or *steady states*. Following Steyn-Ross *et al.* [2013], we consider the dynamics to have a fluctuating behaviour around, or relaxation towards, one or more fixed equilibrium points. These fixed points define resting states of a cortical column and are known as the equilibria or steady states of the system. The governing equations can be linearized about such states and then *linear stability analysis* (LSA) employed to theoretically predict conditions under which the system undergoes instabilities. All deviations from a stable state are predicted to decay back to steady state after removal of the perturbation. Even an unstable steady state can act to organize the system dynamics. Finally the existence of multiple stable and unstable steady states (as we will see shortly for Wilson–Cowan model) gives a rich dynamical behaviour to the system.

The equilibrium points of the system $(E^{\text{o}}, I^{\text{o}})$, are determined by setting all derivatives in Eq. (5.2.1) to zero to give the *nullcline* or *isocline* equations of the system

$$\begin{aligned} E^{\text{o}} &= \mathcal{S}_E(b_{EE}E^{\text{o}} - b_{IE}I^{\text{o}} + P), \qquad \text{(a) E-nullcline} \\ I^{\text{o}} &= \mathcal{S}_I(b_{EI}E^{\text{o}} - b_{II}I^{\text{o}} + Q), \qquad \text{(b) I-nullcline} \end{aligned} \tag{5.2.2}$$

pyramidals facilitates formation of synchronized strong *current dipoles* (as a result of ionic sink–sources around neurons). Theses dipoles produce electrical field normal to cortical surface, and can be recorded using scalp EEG electrodes.

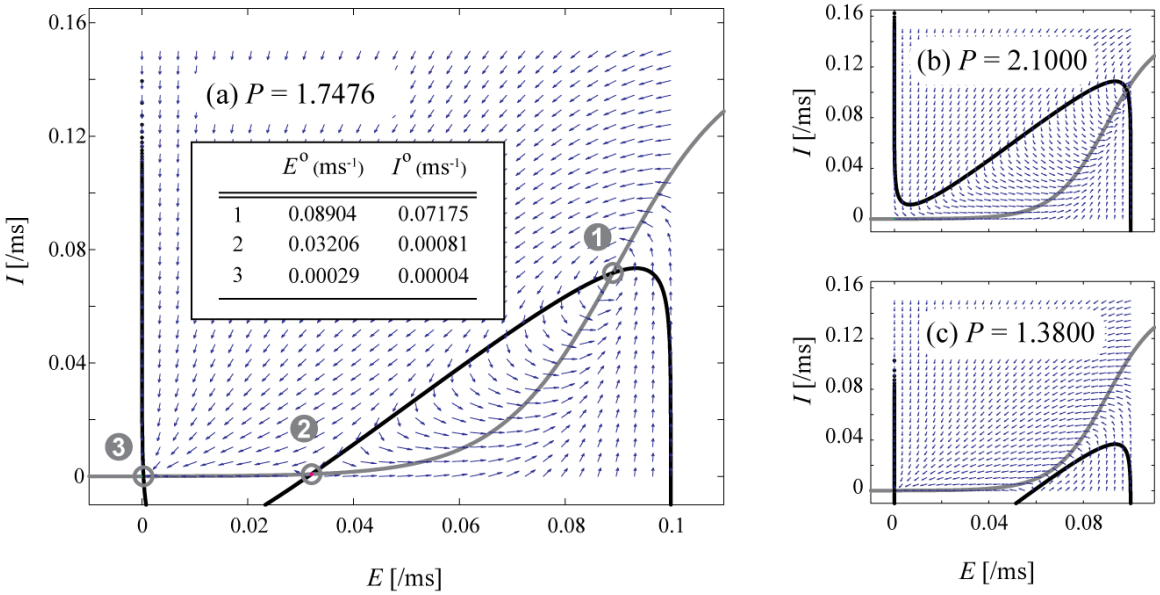

Figure 5.4: Phase-plane diagram of the spatially homogeneous Wilson–Cowan model (5.2.1). (a) The $dE/dt = 0$ (black) and $dI/dt = 0$ (grey) nullclines as described by Eqs. (5.2.2), with superimposed vector fields. The external input is $P = 1.7476$ mV. Refer to Table 5.1 for values of other parameters. The intersections of nullclines indicate three steady states with coordinates shown in the figure. Increasing and decreasing P shifts $dE/dt = 0$ nullcline up (b) and down (c) respectively, resulting in different set(s) of steady states. See Fig. 5.5(a) for distribution of steady states as a function of P. Linear stability analysis (LSA) reveals instability of two intersections (labelled 1, 2), and stability of third one (3) in (a).

These nullclines are plotted in Fig. 5.4(a) along with corresponding vector field[1]. Steady states of the system are located at the intersection of nullclines so satisfy both equations in (5.2.2) simultaneously.

Since these nullclines are highly nonlinear functions, an iterative numerical method employed by [Steyn-Ross, 2002] is used to find equilibrium points. In brief, we first select a set of finely-spaced candidate values of E in the range $[0 \;\; \mathcal{S}_{\max}]$ (excluding border values). Then we find the corresponding vector of I-values based on Eq. (5.2.2)(a) and substitute into Eq. (5.2.2)(b) to give a vector of E'-values. The sign changes in the resultant element-by-element subtraction of E and E' vectors reveals occurrence of intersections between nullclines. For each sign-change (representing a root) a bracketing interval is formed, and then a bisection technique (MATLAB's `fzero` function) is applied to find the root (see appendix C.3 for MATLAB code). The inset in Fig. 5.4(a) shows values of equilibrium points obtained by mentioned method.

Note that increasing and decreasing P shifts $dE/dt = 0$ nullcline (grey in the figure) up and down as shown in Fig. 5.4(b) and (c) respectively. As a result, the location and number

[1]The vector field (also called direction or velocity field) predicts the direction of movement of a system's state based on its current position in the phase plane [Izhikevich, 2007]. The dE/dt and dI/dt equations given in (5.2.1) are evaluated at selected discrete points on the phase plane to produce the vector field using MATLAB's `quiver` function (Fig. 5.4). The vector field provides qualitative graphical insights regarding the stability of steady states. The exact determination of stability of equilibrium points is given by linear stability analysis which is studied in section (5.2.3).

of intersections can vary. In section (5.2.4) we investigate how the distribution of equilibrium point changes as P is varied.

5.2.3 Linear stability analysis

We rewrite Eqs. (5.2.1) as

$$\begin{aligned}\frac{dE}{dt} &= B_1(E,I)\\ \frac{dI}{dt} &= B_2(E,I)\end{aligned} \tag{5.2.3}$$

where

$$\begin{aligned}B_1 &= \tau_E^{-1}\left[-E + \mathcal{S}_E(b_{EE}E - b_{IE}I + P)\right]\\ B_2 &= \tau_I^{-1}\left[-I + \mathcal{S}_I(b_{EI}E - b_{II}I + Q)\right]\end{aligned}$$

We linearize Eqs. (5.2.3) by assuming:

$$Z(t) = Z^{\mathrm{o}} + \hat{Z}$$

where $\hat{Z}$ is a small temporal perturbation of the form, $\hat{Z} = \delta Z(t)$, and $Z \in \{E, I\}$; Z^{o} is the equilibrium point. The question of interest asks if $\hat{E}$ and $\hat{I}$ perturbations grow or decay—as characteristic of unstable and stable equilibrium points. Replacing E, I with their perturbed forms, and using Taylor series expansions, (5.2.3) can be written in the form,

$$\begin{aligned}\frac{d\hat{E}}{dt} &= B_1(E^{\mathrm{o}} + \hat{E}, I^{\mathrm{o}} + \hat{I}) = B_1(E^{\mathrm{o}}, I^{\mathrm{o}}) + \left.\frac{\partial B_1}{\partial E}\right|_{\mathrm{o}} \hat{E} + \left.\frac{\partial B_1}{\partial I}\right|_{\mathrm{o}} \hat{I} + \cdots\\ \frac{d\hat{I}}{dt} &= B_2(E^{\mathrm{o}} + \hat{E}, I^{\mathrm{o}} + \hat{I}) = B_2(E^{\mathrm{o}}, I^{\mathrm{o}}) + \left.\frac{\partial B_2}{\partial E}\right|_{\mathrm{o}} \hat{E} + \left.\frac{\partial B_1}{\partial I}\right|_{\mathrm{o}} \hat{I} + \cdots\end{aligned}$$

Since $\hat{Z}$ is small, we neglect the higher order terms. Noting that $B_{1,2}(E^{\mathrm{o}}, I^{\mathrm{o}}) = 0$, we obtain,

$$\begin{aligned}\frac{d\hat{E}}{dt} &= \frac{\partial B_1}{\partial E}\hat{E} + \frac{\partial B_1}{\partial I}\hat{I}\\ \frac{d\hat{I}}{dt} &= \frac{\partial B_2}{\partial E}\hat{E} + \frac{\partial B_2}{\partial I}\hat{I}\end{aligned} \tag{5.2.4}$$

where the partial derivatives are evaluated at the equilibrium point. Equations (5.2.4) describe the evolution of the perturbations $\hat{E}, \hat{I}$. Noting that $\hat{E} = \delta E(t)$, $\hat{I} = \delta I(t)$ these equations can be written in linear matrix form,

$$\frac{d}{dt}\begin{bmatrix}\delta E(t)\\ \delta I(t)\end{bmatrix} = \begin{bmatrix}\frac{\partial B_1}{\partial E} & \frac{\partial B_1}{dI}\\ \frac{\partial B_2}{\partial E} & \frac{\partial B_2}{dI}\end{bmatrix}_{|\mathrm{o}} \begin{bmatrix}\delta E(t)\\ \delta I(t)\end{bmatrix} = \mathbf{J}\begin{bmatrix}\delta E(t)\\ \delta I(t)\end{bmatrix}$$

Table 5.2: The type and stability of the steady-states depends on the eigenvalues of Jacobian matrix.

		Node		Saddle	Focus	
		Unstable	Stable	Unstable	Unstable	Stable
eigenvalue1	Re{eig1}	+	−	−/+	+	−
	Im{eig1}	0	0	0	$\neq 0$	$\neq 0$
eigenvalue2	Re{eig2}	+	−	+/−	+	−
	Im{eig2}	0	0	0	$\neq 0$	$\neq 0$

where

$$\mathbf{J} = \begin{bmatrix} \frac{\partial B_1}{\partial E} & \frac{\partial B_1}{\partial I} \\ \frac{\partial B_2}{\partial E} & \frac{\partial B_2}{\partial I} \end{bmatrix}_{|_o} \tag{5.2.5}$$

is the *Jacobian matrix* of (5.2.1) evaluated at the equilibrium point (E^o, I^o) with B_1, B_2 as derivative functions defined in (5.2.3). The partial derivatives,

$$\begin{aligned} J_{11} &= \frac{1}{\tau_e}\left[-1 + E_{\max}\frac{ab_{EE}\exp(-a(b_{EE}E^o - b_{IE}I^o + P - \theta))}{(1+\exp(-a(b_{EE}E^o - b_{IE}I^o + P - \theta)))^2}\right] \\ J_{12} &= \frac{-1}{\tau_e}\left[E_{\max}\frac{ab_{IE}\exp(-a(b_{EE}E^o - b_{IE}I^o + P - \theta))}{(1+\exp(-a(b_{EE}E^o - b_{IE}I^o + P - \theta)))^2}\right] \\ J_{21} &= \frac{1}{\tau_i}\left[I_{\max}\frac{ab_{EI}\exp(-a(b_{EI}E^o - b_{II}I^o + Q - \theta))}{(1+\exp(-a(b_{EI}E^o - b_{II}I^o + Q - \theta)))^2}\right] \\ J_{22} &= \frac{-1}{\tau_i}\left[1 + I_{\max}\frac{ab_{II}\exp(-a(b_{EI}E^o - b_{II}I^o + Q - \theta))}{(1+\exp(-a(b_{EI}E^o - b_{II}I^o + Q - \theta)))^2}\right] \end{aligned} \tag{5.2.6}$$

give the elements of Jacobian matrix $\mathbf{J}$. Based on the theory of linear stability [Reichl and Prigogine, 1980], the exponential time-course for small perturbations around the steady state $(E^o,\ I^o)$ can be predicted from the eigenvalues of $\mathbf{J}$ matrix: when both eigenvalues are real and negative, or complex with negative real parts, then the steady state is *stable*; but when either eigenvalue is real and positive, or complex with positive real part, then the steady state is *unstable*. Table 5.2 summarizes the type and stability of steady states based on their eigenvalues.

5.2.4 Steady state distribution

The location of steady states can be modified by changing one (or both) of the external inputs P, Q. Figure 5.5(a) shows the distribution of steady state excitatory firing rate E^o as a function of P. It is clear that, with the parameter values in Table 5.1, the system can support up to

three steady states. The vertical line at $P = 1.7476$ [mV] demonstrates three roots (labelled 1–3 on the figure) corresponding to intersections of nullclines in Fig. 5.4(a).

Real and imaginary parts of both eigenvalues at each equilibrium point are plotted in Fig. 5.5(b) and (c) respectively. Based on the sign of real part of dominant eigenvalue, the unstable steady-states are highlighted with a grey background in Fig. 5.5(a). The state or phase transition happens at the border between stable and unstable equilibrium points. We study the subthreshold dynamics of the system prior to state transitions in the next section.

5.2.5 Critical slowing down prior to bifurcation points

At bifurcation points the qualitative behaviour of the system changes considerably. Cases like annihilation/emergence of states (via saddle-node annihilation) or change in the stability of the system (via Hopf bifurcation) are the most common and well-known types of bifurcations. The space-free Wilson–Cowan model demonstrates all of these bifurcation types implying a rich dynamical behaviour.

White-noise fluctuations are introduced to Eqs. (5.2.1) as *additive noises* to model continuous bombardment of neural membrane and ionic channels by ambient noise. This transforms the model equations to a pair of coupled *stochastic differential equations* (SDEs). We introduce the stochastic form of (5.2.1) as

$$\begin{aligned} \tau_E \frac{dE}{dt} &= -E + \mathcal{S}_E(b_{EE}E - b_{IE}I + P) + c_1\xi_1(t) \\ \tau_I \frac{dI}{dt} &= -I + \mathcal{S}_I(b_{EI}E - b_{II}I + Q) + c_2\xi_2(t) \end{aligned} \tag{5.2.7}$$

which can be linearized to give

$$\frac{d}{dt}\begin{bmatrix} E(t) \\ I(t) \end{bmatrix} = -\mathbf{A}\begin{bmatrix} E(t) \\ I(t) \end{bmatrix} + \sqrt{\mathbf{D}}\begin{bmatrix} \xi_1(t) \\ \xi_2(t) \end{bmatrix} \tag{5.2.8}$$

Here $\xi_1(t)$ and $\xi_2(t)$ (in $(\text{ms})^{-1/2}$) are two independent white-noise sources, and the $c_{1,2}$ (in $(\text{ms})^{-1/2}$) are corresponding rms noise amplitudes. Following Steyn-Ross *et al.* [2006], these white-noise sources are produced as Gaussian-distributed white noise of zero mean, infinite variance with zero autocorrelation everywhere except at lag $\tau = 0$,

$$\langle \xi(t) \rangle = 0 \ , \quad \langle \xi_j(t)\xi_k(t') \rangle = \delta_{j,k}\delta(t - t') \tag{5.2.9}$$

where $\delta_{j,k}$ is the dimensionless Kronecker delta[1] and $\delta(t)$ is the Dirac delta-function in $(\text{ms})^{-1}$.

[1]Kronecker delta function $\delta_{j,k}$ is defined $\delta_{j,k} = \begin{cases} 1 & \text{if } j = k \\ 0 & \text{if } j \neq k \end{cases}$

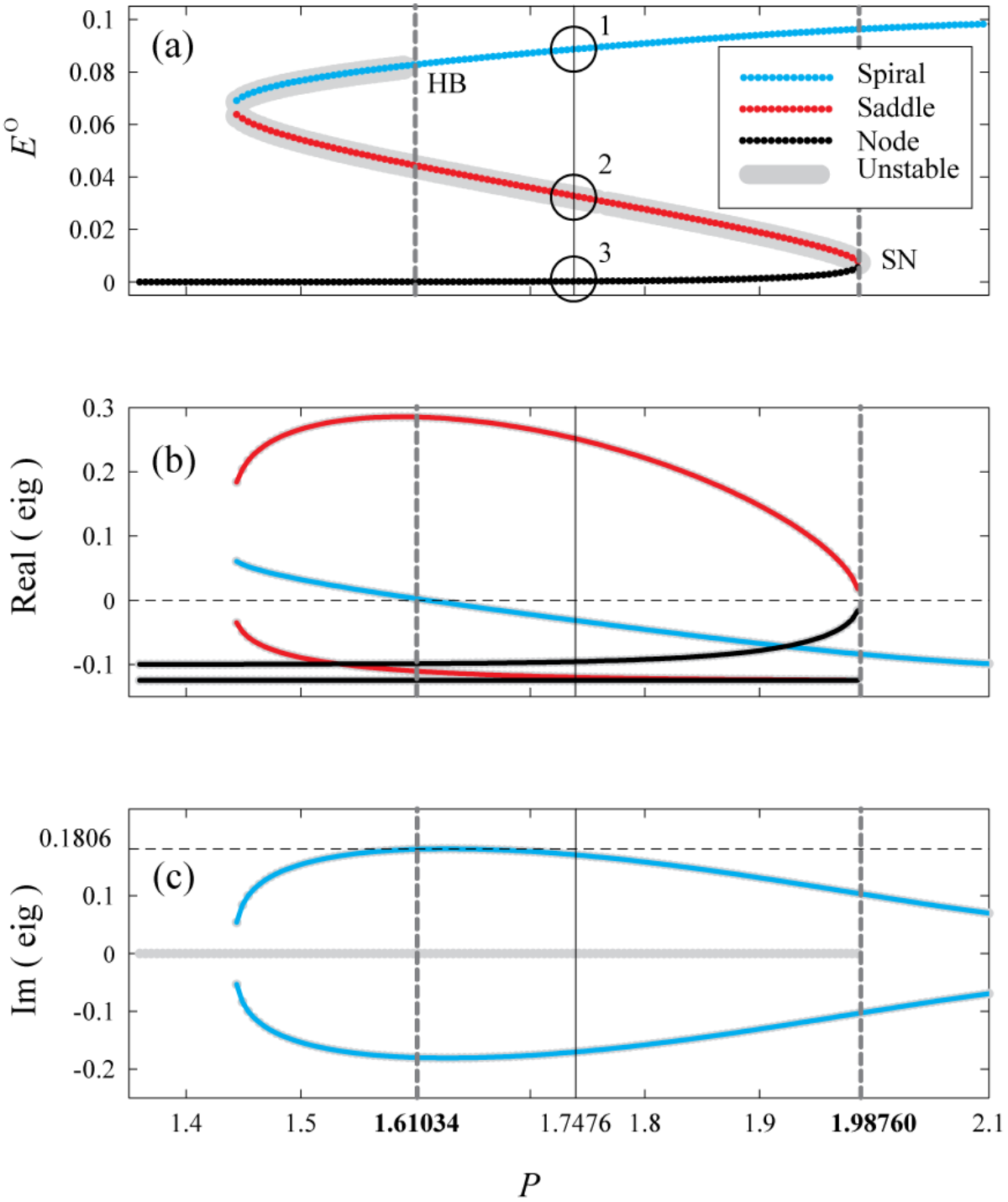

Figure 5.5: The steady state distribution (SSD) and eigenvalue diagram of the spatially homogeneous Wilson–Cowan model Eqs. (5.2.1). Hopf (HB) and saddle-node (SN) bifurcations happen at $P_{\text{Hopf}} = 1.610341975380000$ and $P_{\text{SN}} = 1.987601511600000$ mV respectively as indicated by vertical dashed lines. (a) SSD of excitatory firing rates E^{o} (ms^{-1}) as a function of external input P (mV). The grey background in SSD curve indicates unstable equilibrium points. (b) Real and (c) imaginary parts of eigenvalues of steady states (both in ms^{-1}) versus P. The bottom branch of SSD curve (black in (a)) has a pair of real negative eigenvalues (black traces in (b)), indicating a *stable node*. The middle branch (red in (a)) has pair of real opposite-sign eigenvalues (red traces in (b)), indicating an *unstable saddle*. The top branch (blue in (a)) has a pair of complex conjugate eigenvalues (blue traces in (b,c)) which can be stable or unstable for different P values. The top branch is a *stable spiraling-in focus* for $P > P_{\text{Hopf}}$ and an *unstable spiraling-out focus* for other P values. The frequency of perturbation-induced oscillations of top branch is determined from (c), e.g. the angular frequency of top branch at $P \simeq 1.61034$ is $\omega = 0.1806$ ms^{-1} which corresponds to $f \simeq 28.74$ Hz. Note that the eigenvalues of bottom and middle branches are real, and their zero imaginary parts are plotted as grey line in (c). The points labelled as 1–3 at $P = 1.7476$ mV correspond to intersections of nullclines in Fig. 5.4(a).

Samples from a zero-mean, unit-variance Gaussian random number generator (implemented by MATLAB's `randn` function) are used to generate this noise in numerical simulations. Noise samples are scaled by square-root of inverse of time step used in updating the numerical solution as

$$\xi(t) = \frac{\mathcal{R}_n(0,1)}{\sqrt{\Delta t}} \tag{5.2.10}$$

The $\mathbf{A}$ in (5.2.8) is the *drift* matrix equal to negative of the Jacobian matrix defined in (5.2.5), $\mathbf{A} = -\mathbf{J}$, and $\mathbf{D}$ is the *diffusion* matrix:

$$\mathbf{D} = \begin{bmatrix} c_1^2/\tau_E^2 & 0 \\ 0 & c_2^2/\tau_I^2 \end{bmatrix} \tag{5.2.11}$$

As with most nonlinear differential equations, generally it is not possible to find explicit analytical solutions. So numerical methods are used to approximately determine the solutions. Following Steyn-Ross [2002], the differential form of Eqs. (5.2.8) can be interpreted as an updating rule to be used in numerical simulations as:

$$\begin{aligned} E(t+dt) &= E(t) + \frac{dt}{\tau_E}\left[-E(t) + \mathcal{S}_E(b_{EE}E - b_{IE}I + P) + c_1\xi_1(t)\right] \\ I(t+dt) &= I(t) + \frac{dt}{\tau_I}\left[-I(t) + \mathcal{S}_I(b_{EI}E - b_{II}I + Q) + c_2\xi_2(t)\right] \end{aligned} \tag{5.2.12}$$

which is the form we use in our numerical simulations of the spatially-homogeneous Wilson–Cowan equations.

The stochastic differential equations in (5.2.8) describe a multivariate Ornstein–Uhlenbeck process for which one can make some theoretical predictions. We will use autocorrelations of E time-series to study the white-noise-induced dynamics of the system while approaching bifurcation points. In subthreshold regime—where all eigenvalues have negative real parts— the 2×2 stationary *covariance* matrix of this process (in $(\text{ms})^{-2}$), $\mathbf{\Sigma}$, is calculated from [Gardiner, 2004]

$$\mathbf{A\Sigma} + \mathbf{\Sigma A}^{\mathrm{T}} = \mathbf{D} \tag{5.2.13}$$

which can be reworked into the form

$$\mathbf{\Sigma} = \frac{\det(\mathbf{A})\mathbf{D} + [\mathbf{A} - \mathrm{tr}(\mathbf{A})\mathbf{I}]\mathbf{D}[\mathbf{A} - \mathrm{tr}(\mathbf{A})\mathbf{I}]^{\mathrm{T}}}{2\mathrm{tr}(\mathbf{A})\det(\mathbf{A})} \tag{5.2.14}$$

after a little algebraic manipulation. Here $\mathbf{I}$ is the 2×2 identity matrix; $\det(\cdot)$ and $\mathrm{tr}(\cdot)$ are

the determinant and trace operators. Following Gardiner [2004], the 2×2 steady-state time-correlation matrix of this system[1] is

$$\mathbf{C}(\tau) = \mathrm{e}^{-\mathbf{A}\tau}\mathbf{\Sigma}, \quad \tau \geq \mathbf{0} \tag{5.2.15}$$

where $\exp(-\mathbf{A}\tau)$ is the matrix exponential operator. The $C_{11}(\tau)$ gives theoretically predicted autocorrelation function $E(t)$ fluctuations which can be compared against experimental autocorrelations (from numerically generated $E(t)$ time-series). By examining theoretical and experimental autocorrelations, we will see how the fluctuations of the system become critical prior to occurrence of two different bifurcation types: saddle-node and Hopf.

Subthreshold behaviour prior to saddle-node annihilation

The steady-state distribution of spatially-homogeneous Wilson–Cowan model (5.2.1) is plotted again in Fig. 5.6(a) with the saddle-node bifurcation point labelled at $P \simeq 1.98760$ mV. A saddle-node bifurcation occurs at the point where the mid-branch saddle and bottom-branch node equilibria collide and annihilate.

Close to steady state, the response of the system to small perturbations can be predicted from the steady-state eigenvalues. Bottom branch eigenvalues are plotted in Fig. 5.6(b) and (c) as a function of subcortical drive P. Both eigenvalues are real and negative, so the bottom branch is stable. Perturbations away from this stable node will decay with two distinct time-scales, $T_{\text{slow}} = -1/\lambda_1$ and $T_{\text{fast}} = -1/\lambda_2$ where λ_1 and λ_2 are the dominant and second eigenvalues respectively. These time-scales are plotted in Fig. 5.6(d) and (e) showing a dramatic increase in slow time-scale while approaching the SN bifurcation. This behaviour results in slowing of system responsiveness, and is known as *critical slowing down*.

We calculate the variance and autocorrelation of numerically obtained E time-series to investigate system dynamics close to SN bifurcation, and compare against Ornstein–Uhlenbeck predictions by examining the Σ_{11} element of the covariance matrix $\mathbf{\Sigma}$ (see Eq. (5.2.14)).

The traces in Fig. 5.7(a) (from bottom to top) show white-noise-induced fluctuations of the model while approaching the SN point using external stimulation P as the control parameter. Fig. 5.7(b) shows the corresponding autocorrelation functions. Each blue trace is the average of three experimental autocorrelation (calculated with MATLAB's `xcov` function). Each black trace is the theoretical one-sided autocorrelation (Σ_{11} component of covariance matrix) for the linearized Wilson–Cowan model as an Ornstein–Uhlenbeck stochastic process. Growth in peak value (variance) and broadening of autocorrelation functions (corresponding to reduced decay rate) are evident on approach to SN bifurcation. Good agreement is observed between

[1] which is an OU system

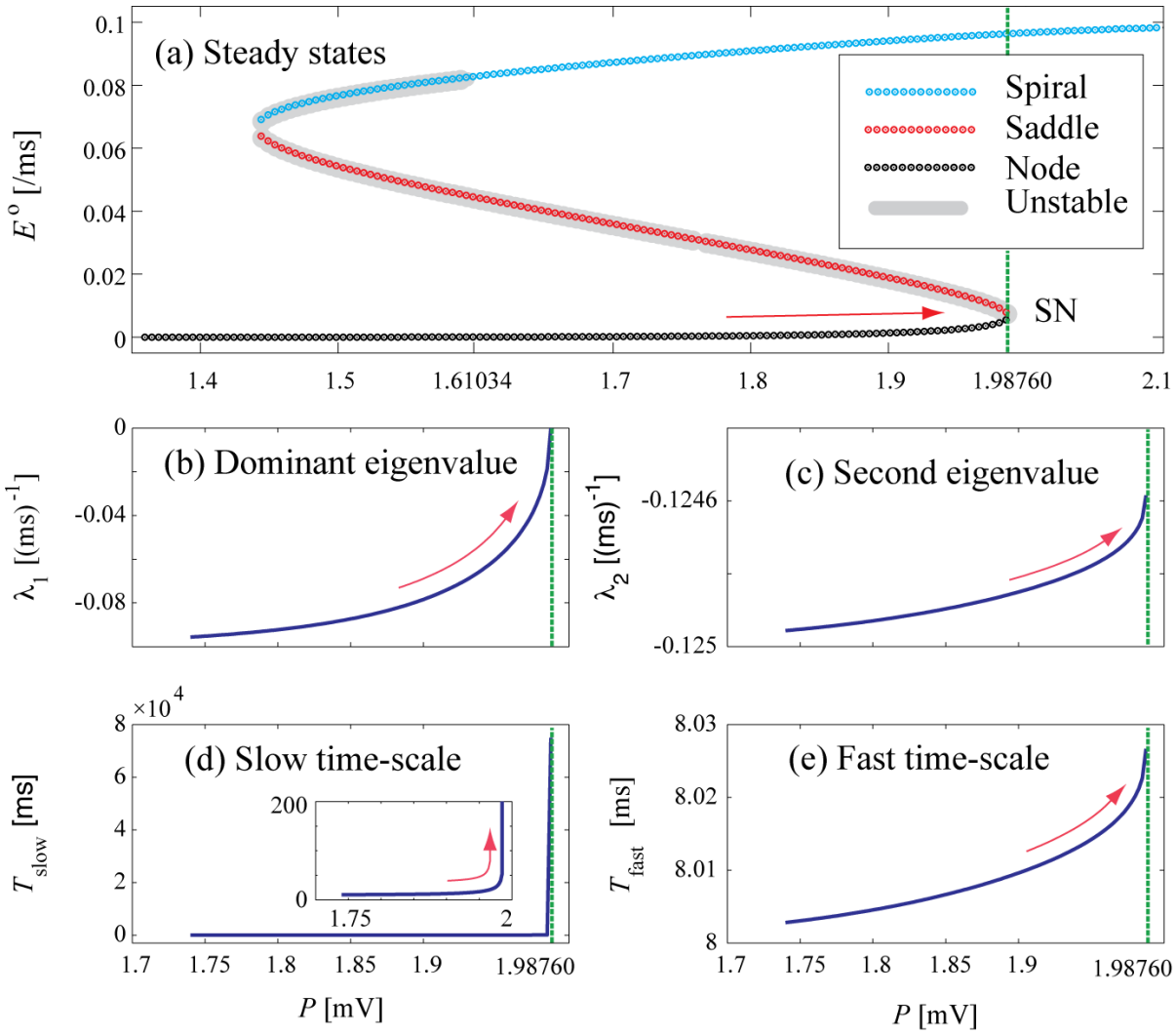

Figure 5.6: Steady states and eigenvalues of the spatially-homogeneous Wilson–Cowan model approaching a saddle-node (SN) bifurcation point. (a) Steady state distribution is replotted here versus P as the control parameter. Saddle-node bifurcation happens at $P \simeq 1.98760$ mV where two equilibrium points collide and annihilate. Eigenvalues of the lower branch are plotted in (b), (c) versus P. Both eigenvalues are real and negative, characteristc of a stable node. Dominant eigenvalue approaches zero when P pushes the system toward SN point. Time-scales defined as $T = 1/|\lambda|$ ms are plotted in (d), (e). Dramatic increment in slow time scale at SN point is a sign of critical slowing down.

theoretical prediction and numerical experiments. Note that obtaining comparable numerical and theoretical results become very challenging when the system is close to the SN point, and numerical settings need to be selected carefully [Steyn-Ross, 2002]:

- **Noise intensities:** The $c_{1,2}$ rms noise amplitudes should be sufficiently small to keep the system within the basin of attraction of stable node. This is more critical in the vicinity of SN point, where the basin of attraction shrinks considerably.
- **Simulation time:** The simulation time should be long enough to capture slow dynamics of the system. A rule of thumb is that simulation length should be at least $100 \times T_{\text{slow}}$. Again this is critical in the close vicinity of SN point, see T_{slow} in Fig. 5.6(e).
- **Numerical time-step:** The time-step of numerical update should be small enough to

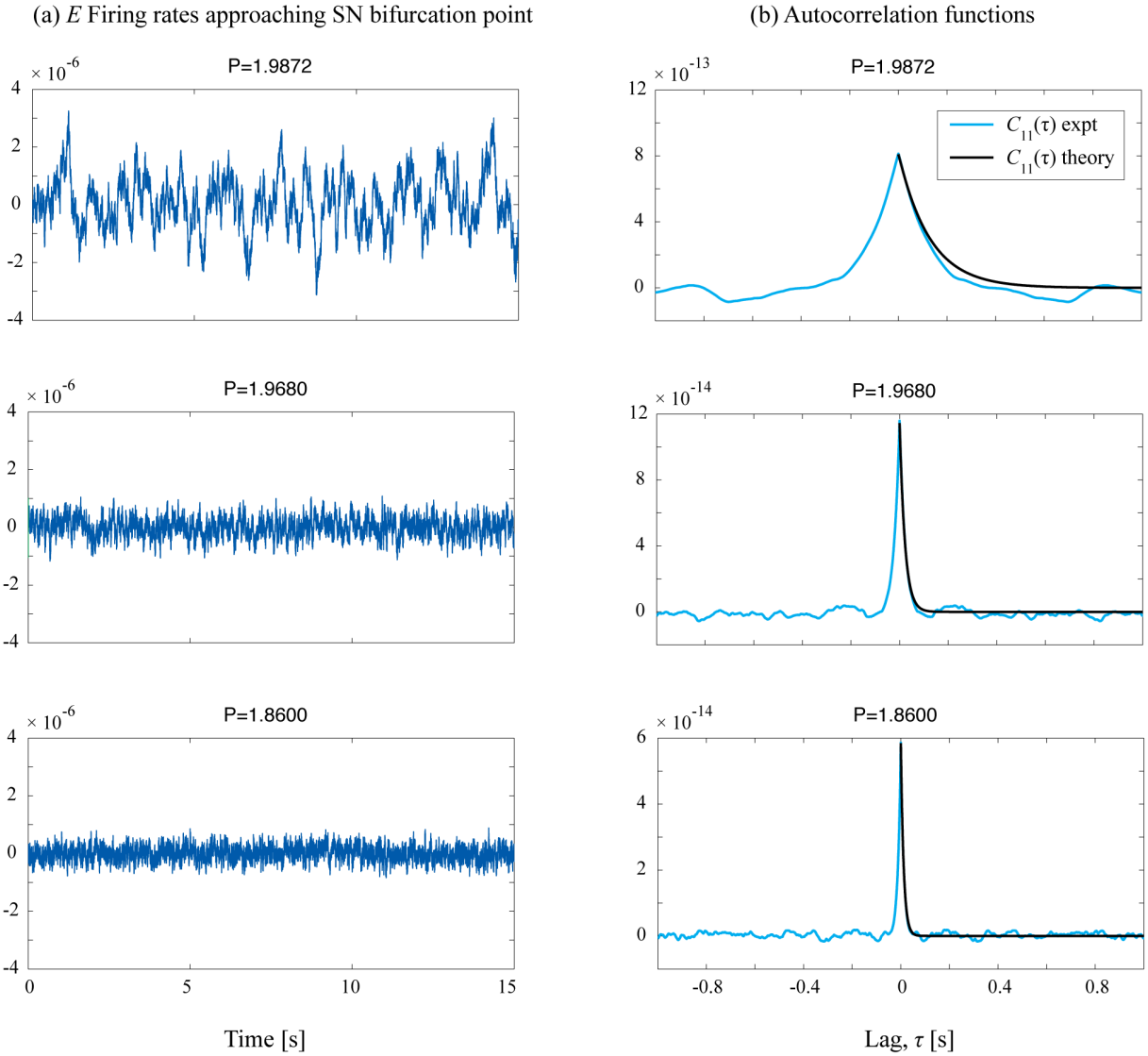

Figure 5.7: Numerical and theoretical analysis of white-noise-induced fluctuations in the spatially homogeneous Wilson–Cowan model approaching saddle-node (SN) bifurcation point. (a) Bottom to top are the numerically obtained firing rate of E neurons versus time approaching SN point. Values of control parameter P are shown for each case in mV. The time-step of numerical simulations is Δt=0.1 ms and the length of simulation is 15 s. Emergence of larger amplitude slow oscillations is evident as the state is driven toward SN point by increasing P. (b) Temporal autocorrelation functions of time-series of (a) are plotted (in blue) versus time-lag. Each blue trace is produced by averaging the autocorrelations obtained from three numerical experiments. Approaching bifurcation point increases peak value of autocorrelation function (equal to variance of the time series), and broadens the autocorrelation functions. Black curves are theoretically predicted one-sided autocorrelation functions described by $\Sigma_{11}(\tau)$ element of covariance matrix (5.2.14).

capture fast dynamics of the system as indicated by $T_{\text{fast}} = 1/|\lambda_2|$ where λ_2 is the second eigenvalue of the system. The time step should also be small enough to prevent numerical instabilities.

Excellent agreement between theory and numerical experiment is achievable when the simulations satisfy all three criteria. This is a challenging task in the vicinity of the SN point, where the slow time-scale dominates, demanding very long numerical simulations to capture slow dynamics. The results observed in top trace of autocorrelations in Fig. 5.7 can be improved by

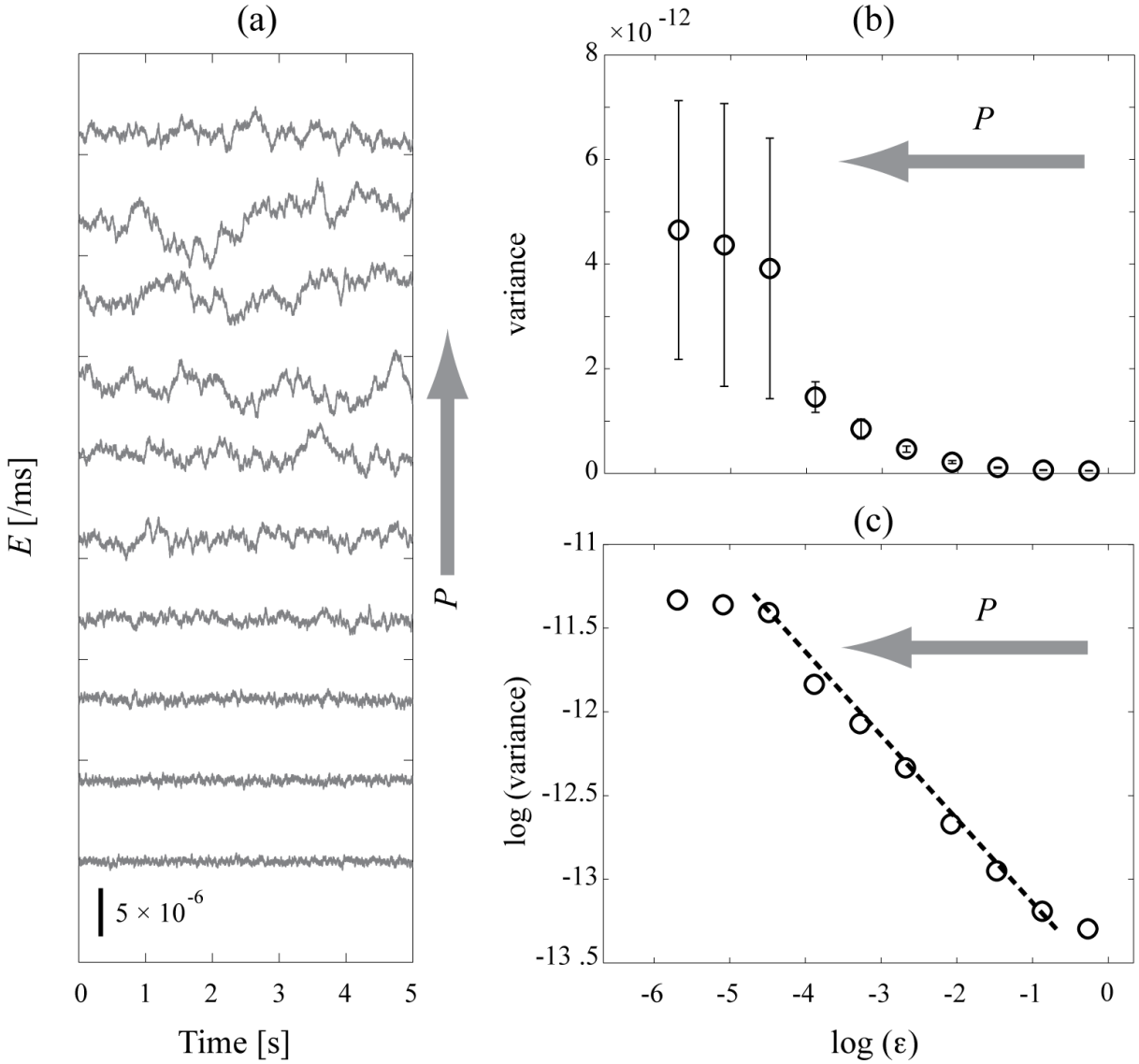

Figure 5.8: Variance of white-noise-induced fluctuations for the spatially homogeneous Wilson–Cowan model prior to saddle-node (SN) bifurcation. Arrows indicate moving toward SN point by increasing P. (a) From bottom to top are the time series of white-noise-induced fluctuations of E using different values of P. Proximity of the system to SN point is indicated by emergence of larger-amplitude slow oscillations in top traces. See Table 5.3 for the parameter values. (b) variance versus $\log(\epsilon)$ where $\epsilon_j = (P_{\rm SN} - P_j)/P_{SN} = 1/4^j$ with $j \in \{1,\ 2,\ ...,\ 10\}$, and $P_{\rm SN} = 1.9876015116$ mV. Each variance is a mean value obtained from 12 stochastic simulations. Error-bars show standard deviation of variances over 12 repeated experiments. (c) The logarithmic plot of variances versus $\log(\epsilon)$. The superimposed dashed line has the slope of -0.5.

performing longer simulations.

In order to extract the power-law relationship between fluctuation variance and closeness to the SN point, we generated 10 time-series corresponding to numerical simulations of Eqs. (5.2.7), using P as a control parameter to derive the system toward SN bifurcation point. We used $\epsilon_j = P_{\rm SN} - P_j$, $j \in \{1,\ 2,\ ...,\ 10\}$ as a measure of distance from bifurcation point. See Table 5.3 for full list of simulation parameters and their values. We repeated the numerical simulation 12 times per P value. Figure 5.8(a) shows sample time-series of E corresponding to each P value. White-noise-induced fluctuations show larger-amplitude slow oscillations while the system is

Table 5.3: Parameter values and simulation variables to produce Figs. 5.8 and 5.13

Symbol/Parameter	Description	Value	Value	Unit
		Fig. 5.8	Fig. 5.13	
$P_{\mathrm{SN,\,HB}}$	P at bifurcation point	1.9876015116	1.6103419764	mV
ϵ	$\epsilon_j = \frac{\lvert P_{\mathrm{HB\ or\ SN}} - P_j \rvert}{P_{\mathrm{HB\ or\ SN}}}$	$1/4^j$, $j \in \{1,\ 2,\ ...,\ 10\}$	$1/4^j$, $j \in \{1,\ 2,\ ...,\ 8\}$	
Δt	Time-step of Euler update	0.1	0.01	(ms)
T	Length of simulation	5	5	s
$c_{1,2}$	rms noise amplitudes	$1{\times}10^{-6}$	$1{\times}10^{-10}$	$(\mathrm{ms})^{-1/2}$

driven toward SN point. This is evident in top traces in (a), consistent with critical slowing down. For each P value, 12 variances are extracted from 12 simulation runs, and the mean of variances was recorded. Figure 5.8(b) shows mean variances as a function of $\log(\epsilon)$ with corresponding error-bars defined as standard deviation of variances. A pronounced increase in the variances, and their standard deviations, is evident prior to SN point. Figure 5.8(c) shows a logarithmic plot of variances. A line of slope -0.5 is superimposed to show the theoretically expected power-law growth for variance of white-noise-induced fluctuations prior to SN bifurcation [Steyn-Ross *et al.*, 2006],

$$\mathrm{var}\{E\} \sim 1/\sqrt{\epsilon} \tag{5.2.16}$$

Note that there is a good agreement for middle values of ϵ, confirming the validity of Ornstein-Uhlenbeck theory. Deviations of experimental variances from theoretical predictions is evident at the borders of range of ϵ values. When $\log(\epsilon) \gtrsim -1$, then $P \lesssim 0.9P_{\mathrm{SN}}$, and the system is far from SN point, so is little affected by slowing-down phenomenon. In the other hand when $\log(\epsilon) \lesssim -4.5$, then $P \gtrsim 0.9999683772P_{\mathrm{SN}}$, and the system is extremely close to SN point, extended simulation times are required (see Fig. 5.6(d)). Longer numerical simulations are expected to improve agreement between theory and experiment for these extreme cases.

Subthreshold behaviour prior to Hopf bifurcation

Recalling the eigenvalue structure of the top branch of Fig. 5.5, this branch has a pair of complex conjugate eigenvalues ($\lambda_{1,2} = -\alpha \pm j\omega$). The real part is positive for $P \lesssim 1.6103419764$ which results in an *unstable-spiraling out focus*; larger P values result in a negative real part, representative of *stable spiraling-in focus*. The evolution of Wilson–Cowan system around the top branch in the phase plane is demonstrated in Fig. 5.9(a) and (b).

Simulations start from two different points (indicated by star symbol) in each case. Trajectories are spiraling-out when the top branch is unstable (a), and spiraling-in when the top branch is stable (b). The corresponding time-series plotted in (c) and (d) both show oscillations whose

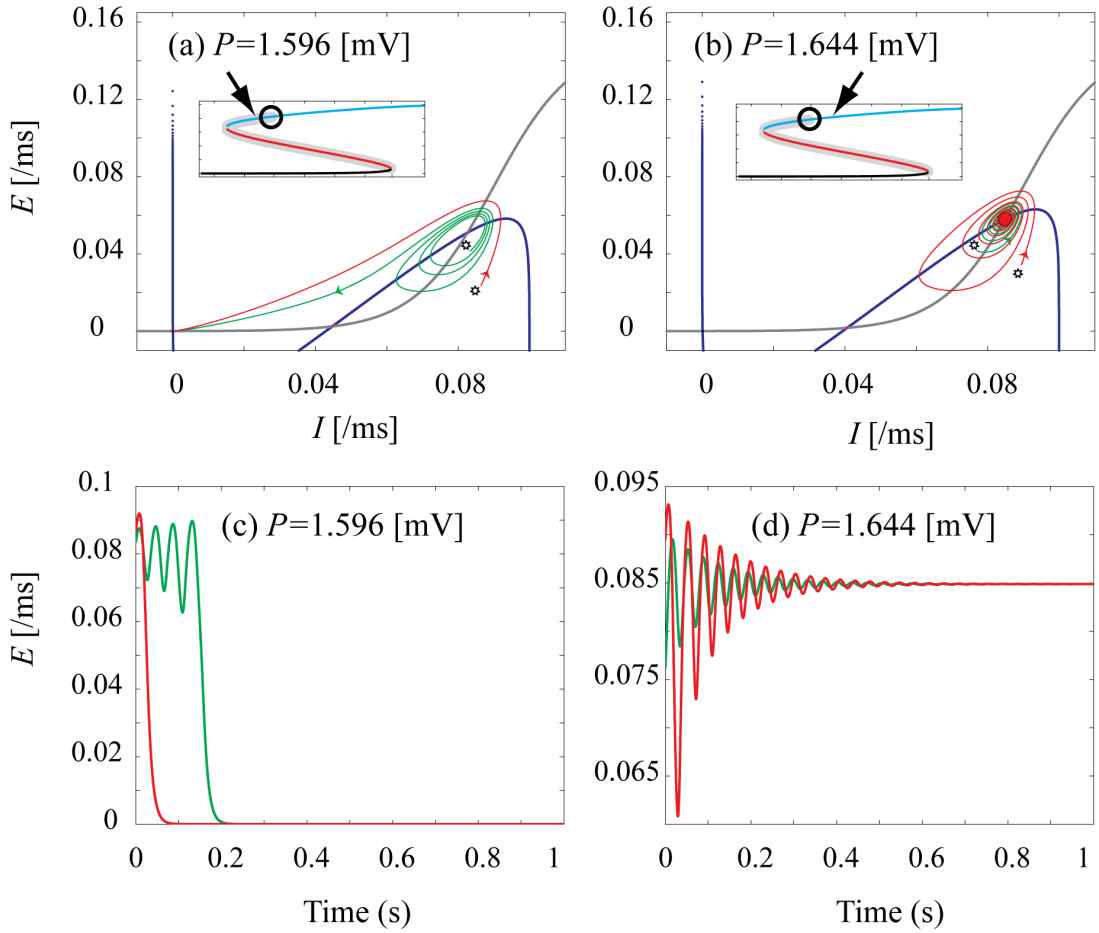

Figure 5.9: The spatially-homogeneous Wilson–Cowan model demonstrates unstable and stable spiral equilibrium points. Insets in (a), (b) show the steady state distribution with Hopf bifurcation (HB) point at $P \simeq 1.610341976400$ mV indicated by an open circle. (a) Phase plot at $P = 1.596$ mV demonstrating an unstable spiral point. Two numerical simulations starting at selected different points (indicated by stars) in the vicinity of spiral point demonstrate the instability. (b) Phase plot of the system at $P = 1.644$ mV demonstrating a stable spiral point for two numerical simulations. When the top branch is unstable, the states evolve to bottom branch after making a spiraling-out trajectory. When the state is stable, trajectories are attracted to top branch with a spiraling-in trajectory. Time series are plotted in (c) and (d). The frequency of oscillations are determined by the imaginary part of eigenvalues in both cases. The HB happens at the border between stable and unstable equilibria when the real part of eigenvalues is zero, leaving pure imaginary eigenvalues.

frequency can be predicted from the imaginary part of the eigenvalues. The *Hopf bifurcation*[1] (HB) happens at the border between stable and unstable spiral points ($P_{\text{HB}} = 1.6103419764$ mV, indicated by open circle in Fig. 5.9(a) and (b)) where the real part of eigenvalues changes the sign and the eigenvalues are purely imaginary $\lambda_{1,2} = \pm j\omega$.

We demonstrate how the HB causes the system to lose stability. The exogenous input P is chosen to be the bifurcation control parameter with the range of [1.68 1.50] mV. Continuous white-noises are added to to the system following Eqs. (5.2.7). Figure 5.10 depicts the system response to varying P (solid and dashed traces respectively).

[1] Sometimes called *Andronov-Hopf bifurcation*

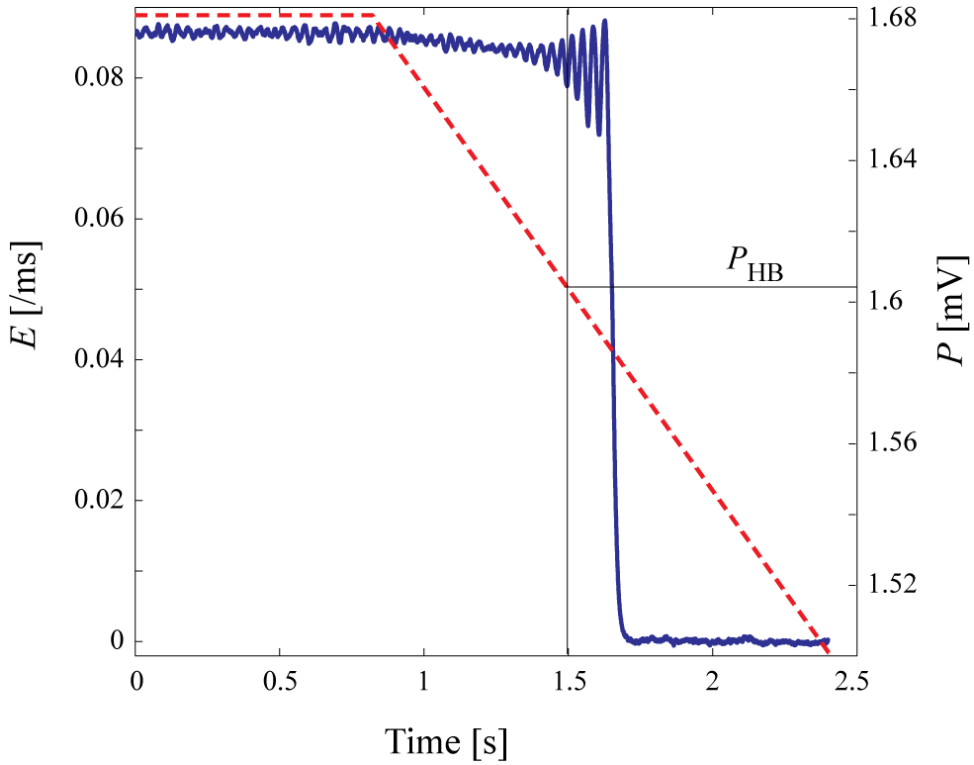

Figure 5.10: Induction of instability and state transition in spatially-homogeneous Wilson–Cowan model via Hopf bifurcation (HB). Excitatory exogenous input P is used as bifurcation parameter. The system's state (E) and P are plotted versus time (solid and dashed traces). The System is stable for $P > P_{\mathrm{HB}}$ where $P_{\mathrm{HB}} = 1.6103419764$ mV. Waxing-and-waning oscillations occur in this range due to white-noise-induced fluctuations. When the control parameter passes the P_{HB}, oscillations grow and enter to attraction domain of stable node on the bottom branch of steady-state distribution graph.

While P is held fixed for 0.8 s, the system shows white-noise-induced waxing-and-waning oscillations indicative of a stable focus point. By decreasing P, a small amplitude stable limit-cycle emerges at P_{HB} via a HB mechanism[1]. Note that when the system passes the bifurcation threshold, the linear stability analysis (as used previously for subthreshold regime) is no longer valid. Decreasing P is accompanied with growth in the amplitude of a stable limit cycle. Since this oscillatory state is not stable anymore (recall steady state distribution graph for $P < P_{\mathrm{HB}}$), the system enters the domain of attraction of the bottom branch and promptly settles there.

We are interested in subthreshold behaviour of the system where Wilson–Cowan model can be linearized into a Ornstein-Uhlenbeck formalism. The theoretical predictions regarding the model response when approaching Hopf bifurcation point (HB) are plotted in Fig. 5.11. Steady states are replotted in (a) showing HB point on the top branch. Reducing P drives the system toward HB as indicated by the red arrow. The slow time-scale is defined as $T_{\mathrm{slow}} = 1/|\alpha|$ where α is the real part of the eigenvalue. As shown in Fig. 5.11(b) and (d), the damping approaches zero

[1]This type of HB is called *supercritical Hopf bifurcation* where loss of stability is coincident with emergence of a stable limit-cycle. *Subcritical Hopf bifurcation* is the other type, where an unstable limit cycle shrinks to a stable equilibrium and makes it unstable. See [Wilson, 1999; Izhikevich, 2007] for more details. All the Hopf bifurcations in this chapter are supercritical, and we simply call them Hopf bifurcations.

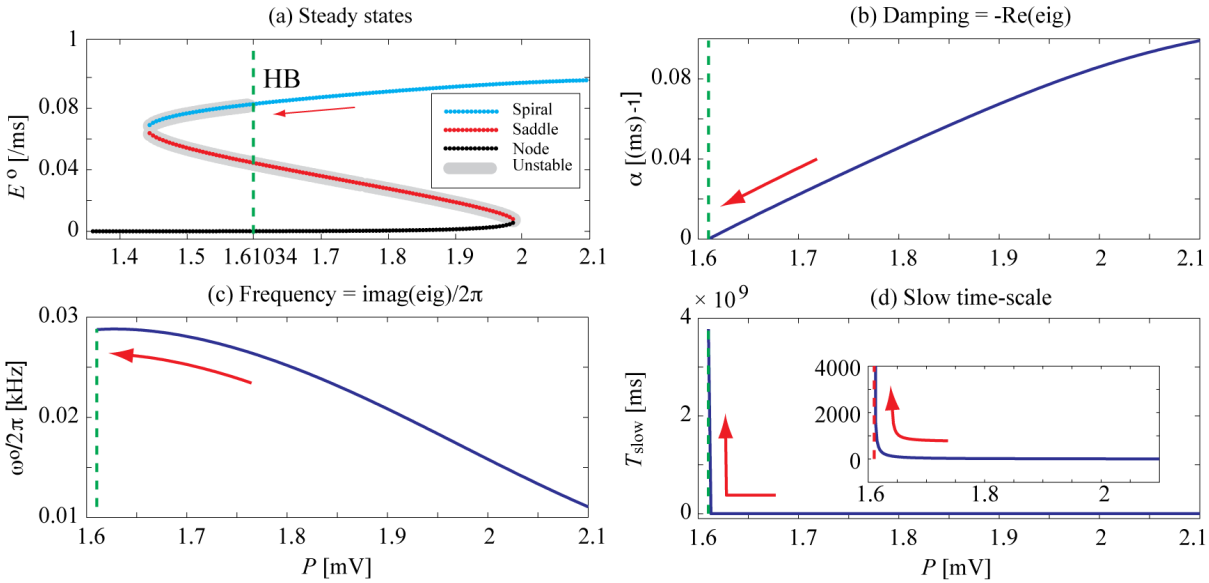

Figure 5.11: Theoretical analysis of the spatially-homogeneous Wilson–Cowan model prior to Hopf bifurcation (HB). (a) Steady state distribution with HB at $P \simeq 1.610341976400$ mV on top branch. The HB acts as a border between unstable (indicated by grey shadow)) and stable equilibria. Reducing P drives the system toward HB as indicated by red arrow. (b) Damping as defined by $\alpha = -\,\mathrm{real}\,(\mathrm{eig})$ is reduced while approaching HB. (c) Frequency of oscillations as defined by $f = \omega_0/2\pi$ where $\omega_0 = \mathrm{Im}(\mathrm{eig}/(2\pi))$. (d) Slow time-scale as defined by $T_{\mathrm{slow}} = 1/\alpha$. A dramatic increase in T_{slow} while approaching HB is predictive of critical slowing prior to HB. Inset shows a zoomed view of the T_{slow} curve.

prior to HB. As a result a dramatic increase in slow time-scale occurs before Hopf bifurcation, predicting critical slowing of the decay of white-noise-induced oscillations close to HB.

To capture the signs of slowing down as predicted by LSA, a series of numerical simulations were performed; see Fig. 5.12.(a) for three different values of P approaching HB point (from bottom to top in the figure). The observed oscillatory behaviour (with frequency of $f = \omega_0/2\pi$ where ω_0 is the imaginary part of eigenvalues) is the result of complex eigenvalues as predicted by LSA. Emergence of larger-amplitude oscillations (compared to noise amplitude) prior to HB bifurcation is evident in numerical results. We plot the corresponding autocorrelation function of the E time-series in Fig. 5.12.(b) (blue). Using Σ_{11} element of covariance matrix (5.2.14) we superimpose the theoretically predicted one-sided autocorrelations (black), and find excellent agreement.

We now examine the variance of fluctuations prior to Hopf bifurcation. Figure 5.13(a) shows series of simulations of the Wilson–Cowan model using a geometrically spaced set of P values to drive the system toward HB. The difference between each P and P_{HB} is selected as

$$\epsilon_j = \frac{P_j - P_{\mathrm{HB}}}{P_{\mathrm{HB}}} = 1/4^j \quad \text{where } j \in \{1,\, 2,\, ...,\, 8\}$$

The corresponding variance for each P is the mean of 12 experiments. Figure 5.13(b) shows that variances increase when approaching HB point. The variances are replotted in a logarithmic

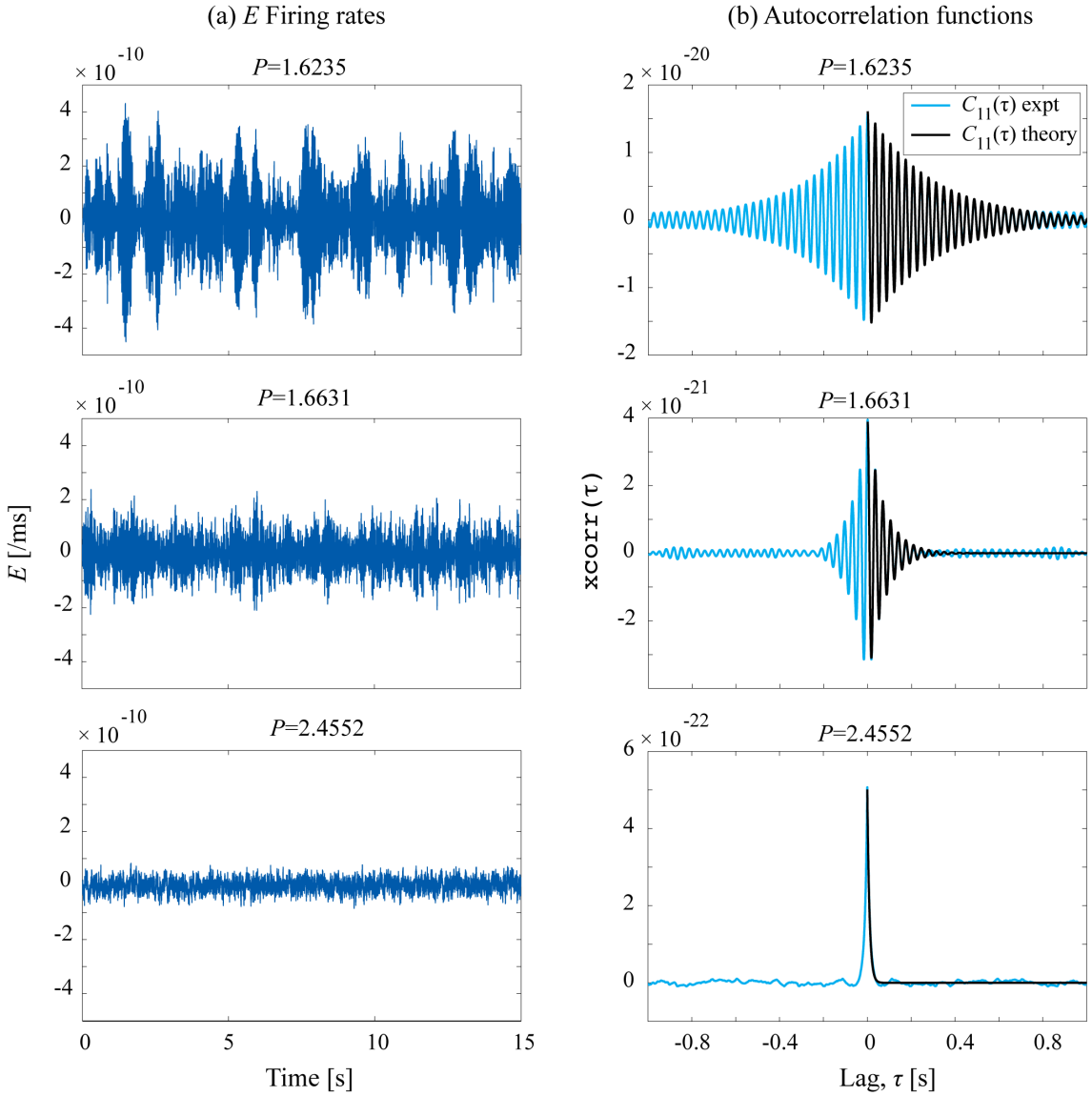

Figure 5.12: Numerical and theoretical analysis of white-noise-induced fluctuations in the spatially homogeneous Wilson–Cowan model approaching Hopf bifurcation (HB) point. (a) Bottom to top are the firing rate of E neurons versus time approaching HB point. Values of control parameter P are shown for each case in mV, and the time-step of numerical simulations is Δt=0.01 ms. Waxing and waning oscillations emerge as the state is driven toward HB by increasing P. Frequency of oscillations is $f = \omega_0/2\pi$ where ω_0 is the imaginary part of eigenvalues at corresponding P as plotted in Fig. 5.11(c). (b) Temporal autocorrelation functions of firing rate time-series of (a) are plotted (in blue) versus time-lag. Each blue trace is produced by averaging the autocorrelations obtained from three numerical experiments. Approaching the bifurcation point increases the peak value of autocorrelation function (equal to variance of the time series), and broadens the envelope of autocorrelation functions indicating increase in decay-time. Black curves are theoretically predicted one-sided autocorrelation functions described by $\Sigma_{11}(\tau)$ element of covariance matrix (2.2.13).

graph in Fig. 5.13(c) with a superimposed line of slope -1. We find good agreement with the theoretical power-law prediction prior to HB [Steyn-Ross *et al.*, 2006]:

$$\mathrm{var}\{E\} \sim 1/\epsilon \tag{5.2.17}$$

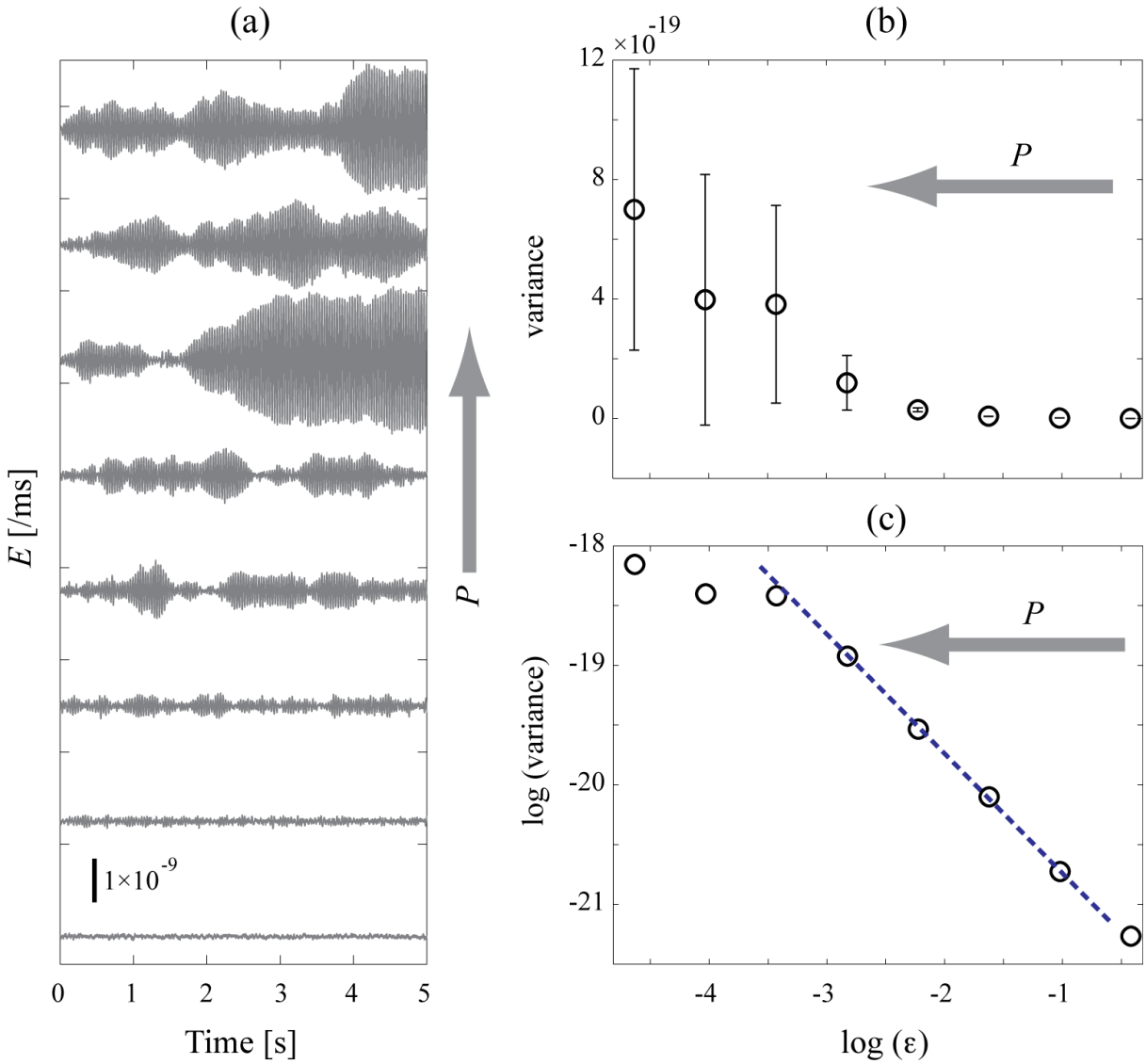

Figure 5.13: Variance of white-noise-induced fluctuations for the spatially homogeneous Wilson–Cowan model prior to Hopf bifurcation (HB). Arrows indicate moving toward HB point by increasing P. (a) From bottom to top are the time series of white-noise-induced fluctuations of E using different values of P to drive the system toward HB. Proximity of the system to bifurcation point is indicated by emergence of larger-amlitude oscillations (compared to noise amplitude). Frequency of these oscillations are in the range of 16–29 Hz, as presented by imaginary part of corresponding eigenvalues in Fig. 5.11(c). See Table 5.3 for parameter values. (b) Variance versus $\log(\epsilon)$ where $\epsilon_j = (P_j - P_{\rm HB})/P_{\rm HB}$ with $P_{\rm HB} = 1.6103419764$ mV. Each variance is a mean value obtained from 12 stochastic simulations. Error-bars showing standard deviation of variances in 12 experiments. (c) Logarithmic plot of variances versus ϵ. Superimposed dashed line has slope of -1.

5.3 Chapter Summary

A detailed investigation of the spatially-homogeneous Wilson–Cowan equations was introduced as a basic model of a homogeneous cortex, with rich dynamics. We demonstrated that saddle-node and Hopf bifurcations can occur in this model, and we studied their subthreshold dynamics prior to phase transitions. We demonstrated numerically clear evidences of critical slowing prior to state transitions in terms of increased variance and decay-time. The experimental findings agree with predictions from linear Ornstein-Uhlenbeck theory. Assuming that seizure-like events

emerge and terminate via different bifurcation types, we propose that leading indicators of critical slowing may accompany seizure emergence and termination phases. The findings of this chapter provide basic modelling support for our hypothesis about seizures. We will study space-dependent Wilson–Cowan model in the next chapter in an attempt to capture more realistic leading indicators.

Chapter 6

Subthreshold dynamics of Wilson–Cowan cortical rod

The dynamical behaviour of the spatially-homogeneous Wilson–Cowan cortical model investigated in Chapter 5 shows clear signs of critical slowing close to saddle-node and Hopf bifurcations. I now extend this work to investigate Wilson–Cowan dynamics in 1-D space, looking for signs of slowing down in both space and time as a potential precursor to state changes. The inclusion of space allows new dynamics to emerge, namely: spatial *Turing* patterns and spatiotemporal *Turing–Hopf* interactions.

After computation of the homogeneous steady states, our first step is to linearize the system around its steady states in order to compute the Jacobian matrix and eigenvalues of the linear system. This allows us to determine the stability of steady states and to perform bifurcation analyses. We extract dispersion curves from the wave-number-dependant Jacobian matrix to provide information about stability of the system with respect to different wave numbers and predict the possibility of development of Turing pattern. In addition to occurrence of saddle-node and Hopf bifurcations, we show that the *spatially non-homogeneous* cortex can destabilize spatially in favour of Turing pattern under certain conditions. We will see that the spatiotemporal instability via *Turing–Hopf* mixed mode instability can also be observed in this model. As the next step, we will transform the governing stochastic equations of the system to Ornstein-Uhlenbeck form with well-developed stochastic theories predicting its behaviour. This transformation will provide valuable theoretical tools to study the system statistics both in time and space. In a parallel step, we will adjust the parameters of the system to set it in a desired subthreshold state, just before occurrence of different bifurcations (e.g., saddle-node, Hopf, Turing, and Turing-Hopf) and will perform numerical simulations to solve the system equations. Then the temporal and spatial characteristics of the system will be investigated theoretically and numerically in a search for signs of slowing down prior to state transitions.

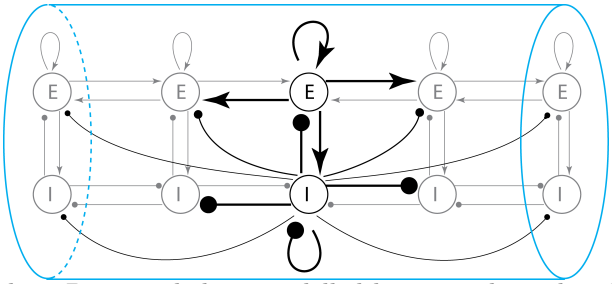

Figure 6.1: Schematic of the 1-D cortical sheet modelled by space-dependent Wilson–Cowan equations. There are dense all-to-all synaptic connections between all neurons. The strength of connections decays exponentially with distance. Connections are plotted completely just for central E and I neurons, with excitatory and inhibitory connections indicated by arrows and circles respectively. The thickness of connectors represent the strength of connection.

6.1 Space-dependent Wilson–Cowan model

Figure 6.1 depicts the structure of a network of laterally-connected localized aggregates of E and I populations, representing a 1-D sheet of cortical tissue. We use the continuum form of space-dependent Wilson–Cowan equations (5.1.5), repeated here for convenience,

$$\begin{aligned} \tau_E \frac{\partial}{\partial t} E(x,t) &= -E(x,t) + \mathcal{S}_E\Big[w_{EE}(x) \otimes E(x,t) - w_{IE}(x) \otimes I(x,t) + P\Big] \\ \tau_I \frac{\partial}{\partial t} I(x,t) &= -I(x,t) + \mathcal{S}_I\Big[w_{EI}(x) \otimes I(x,t) - w_{II}(x) \otimes I(x,t) + Q\Big] \end{aligned} \tag{6.1.1}$$

See Section (5.1) for parameter definitions. Recall that the coupling strength is assumed to decay exponentially with distance:

$$w_{jk}(x) = \frac{b_{jk}}{2\sigma_{jk}} \exp(-|x|/\sigma_{jk}) \tag{6.1.2}$$

where b_{jk} (in mV.ms) represents the maximum synaptic coupling strength from population j to k, and σ_{jk} (in µm) is the space constant that controls the spread of connectivity between corresponding populations. A schematic diagram of the 1-D space-dependent Wilson-Cowan model is displayed in Fig. 6.2. Compared with the structure of spatially-homogeneous model (see Fig. 5.3), the scaling by constant maximum synaptic strengths b_{jk} are replaced by corresponding convolutions with space-dependent synaptic densities w_{jk}. Equations (6.1.1) are equivalent to integro-differential forms

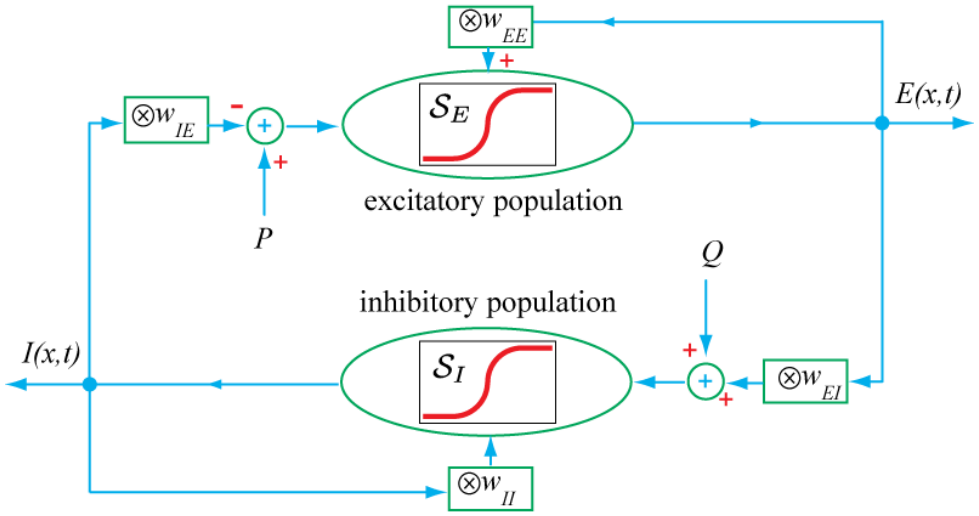

Figure 6.2: The schematic diagram of space-dependent Wilson–Cowan model of 1-D cortical sheet as described by Eqs. (6.1.1). The P and Q are exogenous excitatory voltage inputs to E and I neural populations respectively. Note that the main difference between this diagram and its spatially-homogeneous counterpart in Fig. 5.3 is the replacement of constant b_{jk} with $w_{jk}(x)$, the space-dependent coupling strengths from j to k. Firing rates are sigmoidal function of synaptic and exogenous voltage inputs.

$$\begin{aligned}
\tau_E \frac{\partial}{\partial t} E(x,t) &= -E(x,t) + S_E\big[b_{EE} \int_{-L/2}^{L/2} E(x',t)\, n_{EE}(x-x')\, dx' \\
&\quad - b_{IE} \int_{-L/2}^{L/2} I(x',t)\, n_{IE}(x-x')\, dx' + P\big], \\
\tau_I \frac{\partial}{\partial t} I(x,t) &= -I(x,t) + S_I\big[b_{EI} \int_{-L/2}^{L/2} E(x',t)\, n_{EI}(x-x')\, dx' \\
&\quad - b_{II} \int_{-L/2}^{L/2} I(x',t)\, n_{II}(x-x')\, dx' + Q\big]
\end{aligned} \tag{6.1.3}$$

where L is the length of integration domain, and n_{jk} is defined as:

$$n_{jk}(x-x') = \frac{1}{2\sigma_{jk}} \exp(-|x-x'|/\sigma_{jk}), \quad (j,\, k) \in \{E,\, I\} \tag{6.1.4}$$

Assuming that L is much greater than the length of spatial spread of excitatory and inhibitory connections (i.e. $L \gg \sigma_{ij}$, $i,j \in \{E,I\}$) the range of integrations in (6.1.3) can be extended to $\pm\infty$ (*infinite brain* assumption). We define ϕ_{Ek} and ϕ_{Ik} as excitatory and inhibitory input fluxes in $(\mathrm{ms})^{-1}$ to population of type k as

$$\begin{aligned}
\phi_{Ek}(x,t) &= \int_{-\infty}^{\infty} E(x',t)\, n_{Ek}(x-x')\, dx', \\
\phi_{Ik}(x,t) &= \int_{-\infty}^{\infty} I(x',t)\, n_{Ik}(x-x')\, dx', \qquad\qquad k \in \{E,I\}
\end{aligned} \tag{6.1.5}$$

Then $\phi_{Ek}(x,t)$, $\phi_{Ik}(x,t)$ obey[1]:

$$\begin{aligned}\left(\Lambda_{Ek}^2 - \frac{\partial^2}{\partial x^2}\right)\phi_{Ek}(x,t) &= \Lambda_{Ek}^2\, E(x,t)\\ \left(\Lambda_{Ik}^2 - \frac{\partial^2}{\partial x^2}\right)\phi_{Ik}(x,t) &= \Lambda_{Ik}^2\, I(x,t)\end{aligned} \tag{6.1.6}$$

where $\Lambda_{jk} = 1/\sigma_{jk}$ is the inverse length scale for connections. These equations are the wave equations for $\phi_{Ek,\,Ik}$ which describe, respectively, the propagation of flux activity from distant excitatory and inhibitory populations into the type k synaptic inputs of cortical column. As a result (6.1.3) can be written:

$$\begin{aligned}\tau_E\frac{\partial}{\partial t}E(x,t) &= -E(x,t) + S_E(b_{EE}\phi_{EE}(x,t) - b_{IE}\phi_{IE}(x,t) + P),\\ \tau_I\frac{\partial}{\partial t}I(x,t) &= -I(x,t) + S_I(b_{EI}\phi_{EI}(x,t) - b_{II}\phi_{II}(x,t) + Q)\end{aligned} \tag{6.1.7}$$

We may thus summarize as follows:

$$\begin{aligned}&\frac{\partial}{\partial t}E(x,t) = B_1(E,\phi_{EE},\phi_{IE})\\ &\frac{\partial}{\partial t}I(x,t) = B_2(I,\phi_{EI},\phi_{II})\\ &\left.\begin{aligned}\left(\Lambda_{Ek}^2 - \frac{\partial^2}{\partial x^2}\right)\phi_{Ek}(x,t) &= \Lambda_{Ek}^2\, E(x,t)\\ \left(\Lambda_{Ik}^2 - \frac{\partial^2}{\partial x^2}\right)\phi_{Ik}(x,t) &= \Lambda_{Ik}^2\, I(x,t)\end{aligned}\right\} \quad k \in \{E,\, I\}\end{aligned} \tag{6.1.8}$$

where

$$\begin{aligned}B_1 &= \tau_E^{-1}[-E(x,t) + S_E(b_{EE}\phi_{EE}(x,t) - b_{IE}\phi_{IE}(x,t) + P)],\\ B_2 &= \tau_I^{-1}[-I(x,t) + S_I(b_{EI}\phi_{EI}(x,t) - b_{II}\phi_{II}(x,t) + Q)]\end{aligned} \tag{6.1.9}$$

Equations (6.1.8) and (6.1.9) define the space-dependent Wilson-Cowan continuum model of Fig. 6.2, which will be called the *WC* from now on in this thesis. We start our analysis of this system by determining its *spatiotemporal equilibrium points* in Section (6.2). After linearization

[1]See Appendix A.1 for proof

of the system around its equilibria, we will see how the governing equations can be arranged as an Ornstein-Uhlenbeck system, with well-known theoretical knowledge regarding its autocorrelation and variance, based on the corresponding Jacobian matrix. We will see how the Jacobian matrix is a function of wave-number as well, resulting in introduction of *dispersion curves*. We will use P as a control parameter to extract the steady-state distribution and dispersion curves. A similar approach as used in Chapter 5 will be used in this chapter to study dynamics of WC model while approaching bifurcation thresholds.

6.2 Homogeneous equilibrium points of 1-D WC model

At homogeneous steady state, the $E(x,t)$ and $I(x,t)$ terms are replaced with their fixed-point values, independent of time and space. By setting to zero all time and space derivatives of Eqs (6.1.8) and using the definitions given at (6.1.9), the excitatory and inhibitory equilibrium firing rates ($E^{\mathrm{o}},\ I^{\mathrm{o}}$) can be computed as a function of excitatory exogenous input P:

$$\begin{aligned}
0 &= -E^{\mathrm{o}} + S_E(b_{EE}\phi_{EE}(x,t) - b_{IE}\phi_{IE}(x,t) + P) \\
0 &= -I^{\mathrm{o}} + S_I(b_{EI}\phi_{EI}(x,t) - b_{II}\phi_{II}(x,t) + Q) \\
\Lambda_{Ek}^2\,\phi_{Ek}(x,t) &= \Lambda_{Ek}^2\,E^{\mathrm{o}} \\
\Lambda_{Ik}^2\,\phi_{Ik}(x,t) &= \Lambda_{Ik}^2\,I^{\mathrm{o}}
\end{aligned} \tag{6.2.1}$$

Noting that at steady state excitatory and inhibitory fluxes (ϕ_{Ek} and ϕ_{Ik}) are equal to steady-state excitatory and inhibitory firing rates E^{o} and I^{o}, we obtain nullcline equations which are identical to those for the homogeneous case (see Eq (5.2.2)):

$$\begin{aligned}
E^{\mathrm{o}} &= S_E(b_{EE}E^{\mathrm{o}} - b_{IE}I^{\mathrm{o}} + P) \qquad \text{(E-nullcline)} \\
I^{\mathrm{o}} &= S_I(b_{EI}E^{\mathrm{o}} - b_{II}I^{\mathrm{o}} + Q) \qquad \text{(I-nullcline)}
\end{aligned} \tag{6.2.2}$$

which result in the same phase-plane diagram and vector-fields previously illustrated in Fig. 5.4.

Table 6.1 shows the parameter values of the model used in this chapter. Compared with the previous parameter values of Table 5.1, some minor changes are evident. Specifically, I boosted the inhibitory synaptic coupling strength b_{EI}, in order to shift the Hopf bifurcation (HB) point out of the multi-root region.[1] We will see in Section 6.3 how this modification is essential for

[1] Compare the position of Hopf bifurcation (HB) point on steady state distribution curves of Fig. 6.3(a) and Fig. 5.5(a).

Table 6.1: Symbol definitions and typical parameter values for the 1-D WC model. Parameter values are similar to the values of spatially-homogeneous model as given in Table (5.1) with some minor changes.

Symbol	Description	Value	Unit
E, I	Firing rates of E and I processes		$(\text{ms})^{-1}$
$\tau_{E,I}$	Time constants of E and I responses	10, 8	ms
S_E, S_I	Sigmoid functions mapping voltage to firing rate		$(\text{ms})^{-1}$
$b_{EE,EI,IE,II}$	Synaptic coupling strength	18, 19, 19, 0	mV.ms
$\sigma_{EE,EI,IE,II}$	Space constant	50, [119.1–148.5], [119.1–148.5], 20	µm
$S_{E,I}^{\max}$	Maximum firing rate	0.1, 0.15	$(\text{ms})^{-1}$
$a_{E,I}$	Sigmoid slope at threshold	9	$(\text{mV})^{-1}$
$\theta_{E,I}$	Threshold voltage for half-maximum firing	2.2	mV
P, Q	Exogenous voltage inputs to E and I populations	[0.9–3.3], 1.35	mV

generation of mixed mode Turing–Hopf oscillations.

6.2.1 Linear stability analysis

Following Steyn-Ross [2002] and Steyn-Ross *et al.* [2003], our working assumption is that the cortex normally operates in a state close to its homogeneous equilibrium. In this section I extract the linear form of 1-D WC model for a given spatiotemporally homogeneous steady-state. This gives the *Jacobian matrix* of the system at corresponding steady-state. Then I examine the eigenvalues of the Jacobian matrix to determine stability.

Equations (6.1.8) are linearized by assuming that $Z(x,t) \to Z^{\text{o}} + \hat{Z}(x,t)$, where Z^{o} is the homogeneous stationary state, and $\hat{Z}$ is a small spatiotemporal perturbation of the form, $\hat{Z}(x,t) = \delta_z \text{e}^{\lambda t}\text{e}^{iqx}$ around the steady state. Here δ_z is the amplitude of spatiotemporal perturbation (with same unit as Z^{o}), $\text{e}^{\lambda t}$ is the temporal perturbation, and e^{iqx} is the spatial perturbation mode at wave-number q, and $Z \in \{E,\, I,\, \phi_{Ek},\, \phi_{Ik}\}$. Thus in (6.1.9),

$$B_1 \Rightarrow B_1(E^{\text{o}} + \hat{E},\, \phi_{EE}^{\text{o}} + \hat{\phi}_{EE}, \phi_{IE}^{\text{o}} + \hat{\phi}_{IE})$$
$$B_2 \Rightarrow B_2(I^{\text{o}} + \hat{I},\, \phi_{EI}^{\text{o}} + \hat{\phi}_{EI}, \phi_{II}^{\text{o}} + \hat{\phi}_{II})$$

We expand B_1 using Taylor series while keeping just the first-order terms:

$$B_1 \approx B_1(E^{\text{o}}, \phi_{EE}^{\text{o}}, \phi_{IE}^{\text{o}}) + \left.\frac{\partial B_1}{\partial E}\right|_{\text{o}} \hat{E} + \left.\frac{\partial B_1}{\partial \phi_{EE}}\right|_{\text{o}} \hat{\phi}_{EE} + \left.\frac{\partial B_1}{\partial \phi_{IE}}\right|_{\text{o}} \hat{\phi}_{IE}$$

where derivatives are evaluated at stationary states. Noting that at stationary state,

$$B_1(E^{\text{o}},\, \phi_{EE}^{\text{o}},\, \phi_{IE}^{\text{o}}) = 0$$

we find

$$B_1 = \left.\frac{\partial B_1}{\partial E}\right|_{\mathrm{o}} \hat{E} + \left.\frac{\partial B_1}{\partial \phi_{EE}}\right|_{\mathrm{o}} \hat{\phi}_{EE} + \left.\frac{\partial B_1}{\partial \phi_{IE}}\right|_{\mathrm{o}} \hat{\phi}_{IE}$$

Similarly:

$$B_2 = \left.\frac{\partial B_2}{\partial I}\right|_{\mathrm{o}} \hat{I} + \left.\frac{\partial B_2}{\partial \phi_{EI}}\right|_{\mathrm{o}} \hat{\phi}_{EI} + \left.\frac{\partial B_2}{\partial \phi_{II}}\right|_{\mathrm{o}} \hat{\phi}_{II}$$

Thus equations (6.1.8) become[1]:

$$\begin{aligned}
&\frac{\partial}{\partial t}\hat{E} = \frac{\partial B_1}{\partial E}\hat{E} + \frac{\partial B_1}{\partial \phi_{EE}}\hat{\phi}_{EE} + \frac{\partial B_1}{\partial \phi_{IE}}\hat{\phi}_{IE} \\
&\frac{\partial}{\partial t}\hat{I} = \frac{\partial B_2}{\partial I}\hat{I} + \frac{\partial B_2}{\partial \phi_{EI}}\hat{\phi}_{EI} + \frac{\partial B_2}{\partial \phi_{II}}\hat{\phi}_{II} \\
&\Lambda_{Ek}^2 \phi_{Ek}^{\mathrm{o}} + \left(\Lambda_{Ek}^2 + q^2\right)\hat{\phi}_{Ek} = \Lambda_{Ek}^2 (E^{\mathrm{o}} + \hat{E}) \\
&\Lambda_{Ik}^2 \phi_{Ik}^{\mathrm{o}} + \left(\Lambda_{Ik}^2 + q^2\right)\hat{\phi}_{Ik} = \Lambda_{Ik}^2 (I^{\mathrm{o}} + \hat{I})
\end{aligned} \tag{6.2.3}$$

Noting $\Lambda_{Ek}^2 \phi_{Ek}^{\mathrm{o}} = \Lambda_{Ek}^2 E^{\mathrm{o}}$ and $\Lambda_{Ik}^2 \phi_{Ik}^{\mathrm{o}} = \Lambda_{Ik}^2 I^{\mathrm{o}}$, the two last equations of (6.2.3) become:

$$\hat{\phi}_{Ek} = \frac{\hat{E}\Lambda_{Ek}^2}{\Lambda_{Ek}^2 + q^2}, \qquad \hat{\phi}_{Ik} = \frac{\hat{I}\Lambda_{Ik}^2}{\Lambda_{Ik}^2 + q^2} \tag{6.2.4}$$

and the system will collapse to two dimensions by substituting (6.2.4) into the first two equations of (6.2.3) as:

$$\begin{aligned}
\frac{\partial}{\partial t}\hat{E}(x,t) &= \left[\frac{\partial B_1}{\partial E} + \left(\frac{\partial B_1}{\partial \phi_{EE}}\right)\frac{\Lambda_{EE}^2}{(\Lambda_{EE}^2 + q^2)}\right]\hat{E}(x,t) + \left[\left(\frac{\partial B_1}{\partial \phi_{IE}}\right)\frac{\Lambda_{IE}^2}{(\Lambda_{IE}^2 + q^2)}\right]\hat{I}(x,t) \\
\frac{\partial}{\partial t}\hat{I}(x,t) &= \left[\left(\frac{\partial B_2}{\partial \phi_{EI}}\right)\frac{\Lambda_{EI}^2}{(\Lambda_{EI}^2 + q^2)}\right]\hat{E}(x,t) + \left[\frac{\partial B_2}{\partial I} + \left(\frac{\partial B_2}{\partial \phi_{II}}\right)\frac{\Lambda_{II}^2}{(\Lambda_{II}^2 + q^2)}\right]\hat{I}(x,t)
\end{aligned} \tag{6.2.5}$$

where all partial derivatives at RHS of Eqs. (6.2.5) are calculated at steady state. Noting $\hat{E}(x,t) = \delta_E \mathrm{e}^{\lambda t}\mathrm{e}^{iqx}$, and $\hat{I}(x,t) = \delta_I \mathrm{e}^{\lambda t}\mathrm{e}^{iqx}$ equations (6.2.5) can be written in linear matrix

[1]Note that $\frac{\partial^2}{\partial x^2} Z(x,t) = \frac{\partial^2}{\partial x^2}(Z^{\mathrm{o}} + \hat{Z}) = \frac{\partial^2}{\partial x^2}\hat{Z}(x,t) = \frac{\partial^2}{\partial x^2}\delta_z \mathrm{e}^{\lambda t}\mathrm{e}^{iqx} = -q^2\hat{Z}(x,t)$

form:

$$\frac{d}{dt}\begin{bmatrix} \delta_E e^{\lambda t} \\ \delta_I e^{\lambda t} \end{bmatrix} = \begin{bmatrix} \dfrac{\partial B_1}{\partial E} + \dfrac{\partial B_1}{\partial \phi_{EE}} \dfrac{\Lambda_{EE}^2}{(\Lambda_{EE}^2 + q^2)} & \dfrac{\partial B_1}{\partial \phi_{IE}} \dfrac{\Lambda_{IE}^2}{(\Lambda_{IE}^2 + q^2)} \\ \dfrac{\partial B_2}{\partial \phi_{EI}} \dfrac{\Lambda_{EI}^2}{(\Lambda_{EI}^2 + q^2)} & \dfrac{\partial B_2}{\partial I} + \dfrac{\partial B_2}{\partial \phi_{II}} \dfrac{\Lambda_{II}^2}{(\Lambda_{II}^2 + q^2)} \end{bmatrix} \begin{bmatrix} \delta_E e^{\lambda t} \\ \delta_I e^{\lambda t} \end{bmatrix} \tag{6.2.6}$$

Equation (6.2.6) can be written as

$$\frac{d}{dt}\tilde{\mathbf{u}}(t) = \tilde{\mathbf{J}}(q) \cdot \tilde{\mathbf{u}}(t)$$

where

$$\tilde{\mathbf{u}}(t) = \begin{bmatrix} \delta_E e^{\lambda t} \\ \delta_E e^{\lambda t} \end{bmatrix}$$

is the perturbation column and

$$\tilde{\mathbf{J}}(q) = \begin{bmatrix} \dfrac{\partial B_1}{\partial E} + \dfrac{\partial B_1}{\partial \phi_{EE}} \dfrac{\Lambda_{EE}^2}{(\Lambda_{EE}^2 + q^2)} & \dfrac{\partial B_1}{\partial \phi_{IE}} \dfrac{\Lambda_{IE}^2}{(\Lambda_{IE}^2 + q^2)} \\ \dfrac{\partial B_2}{\partial \phi_{EI}} \dfrac{\Lambda_{EI}^2}{(\Lambda_{EI}^2 + q^2)} & \dfrac{\partial B_2}{\partial I} + \dfrac{\partial B_2}{\partial \phi_{II}} \dfrac{\Lambda_{II}^2}{(\Lambda_{II}^2 + q^2)} \end{bmatrix} \tag{6.2.7}$$

with units of $(\text{ms})^{-1}$ is the q-dependent stability matrix of the system. Stability is determined by the eigenvalues of $\tilde{\mathbf{J}}(q)$ at wave number q. The elements of $\tilde{\mathbf{J}}(q)$ evaluated at steady states

with units of $(\text{ms})^{-1}$ follow as:

$$\begin{aligned}
\tilde{J}_{11} &= \frac{1}{\tau_e}\Big[-1 + E_{\max}\frac{ab_{EE}\ \exp(-a(b_{EE}\phi_{EE} - b_{IE}\phi_{IE} + P - \theta))}{[1+\exp(-a(b_{EE}\phi_{EE} - b_{IE}\phi_{IE} + P - \theta))]^2}\cdot\frac{\Lambda_{EE}^2}{\Lambda_{EE}^2 + q^2}\Big] \\
\tilde{J}_{12} &= \frac{-1}{\tau_e}\Big[E_{\max}\frac{ab_{IE}\ \exp(-a(b_{EE}\phi_{EE} - b_{IE}\phi_{IE} + P - \theta))}{[1+\exp(-a(b_{EE}\phi_{EE} - b_{IE}\phi_{IE} + P - \theta))]^2}\cdot\frac{\Lambda_{IE}^2}{\Lambda_{EI}^2 + q^2}\Big] \\
\tilde{J}_{21} &= \frac{1}{\tau_i}\Big[I_{\max}\frac{ab_{EI}\ \exp(-a(b_{EI}\phi_{EI} - b_{II}\phi_{II} + Q - \theta))}{[1+\exp(-a(b_{EI}\phi_{EI} - b_{II}\phi_{II} + Q - \theta))]^2}\cdot\frac{\Lambda_{EI}^2}{\Lambda_{EI}^2 + q^2}\Big] \\
\tilde{J}_{22} &= \frac{-1}{\tau_i}\Big[1 + I_{\max}\frac{ab_{II}\ \exp(-a(b_{EI}\phi_{EI} - b_{II}\phi_{II} + Q - \theta))}{[1+\exp(-a(b_{EI}\phi_{EI} - b_{II}\phi_{II} + Q - \theta))]^2}\cdot\frac{\Lambda_{II}^2}{\Lambda_{II}^2 + q^2}\Big]
\end{aligned} \tag{6.2.8}$$

6.2.2 Steady state distribution and homogeneous ($q = 0$) stability

Using a numerical iterative method[1], we find the intersections of two nullclines described by Eqs. (6.2.2), and then locate the steady states as a function of varying external excitatory voltage drive P. We assume $q = 0$ to find the corresponding homogeneous eigenvalues using Eqs. (6.2.8).[2] The steady-states curve and corresponding eigenvalues of the model is plotted as a function of P in Fig. 6.3 which looks similar to steady-state diagram displayed in Fig. 5.5. Both steady state curves have a three-root region enclosed by two single-root regions. The corresponding eigenvalues have also similar structure. However the reader should note the difference in the position of HB point in two figures which is due to boosted inhibitory synaptic coupling strength $b_{IE} = 19$ mV.ms (previously $b_{IE} = 10$ mV.ms). This steady-state diagram shows that state transitions can emerge via two bifurcation types, saddle-node (SN) and Hopf (HB), as indicated by the eigenvalue structure. We will see in the next sections that how the q-dependent eigenvalue analysis of the system reveals the existence of other types of bifurcations in the 1-D WC model. Before studying this q-dependence, we perform some numerical simulations to investigate the system response for the homogeneous case.

The homogeneous ($q = 0$) steady-state curve is replotted in Fig. 6.4 with stable and unstable equilibria marked with black and red colours respectively. The phase plots at different P values corresponding to four distinct steady states are superimposed on the figure. We performed numerical simulations to test and demonstrate the validity of predictions of the linear stability analysis about the homogeneous system dynamics at different regions of steady state curve:

[1] See Section 5.2.2 for details.

[2] The stability for nonzero wavenumbers is studied in the next section.

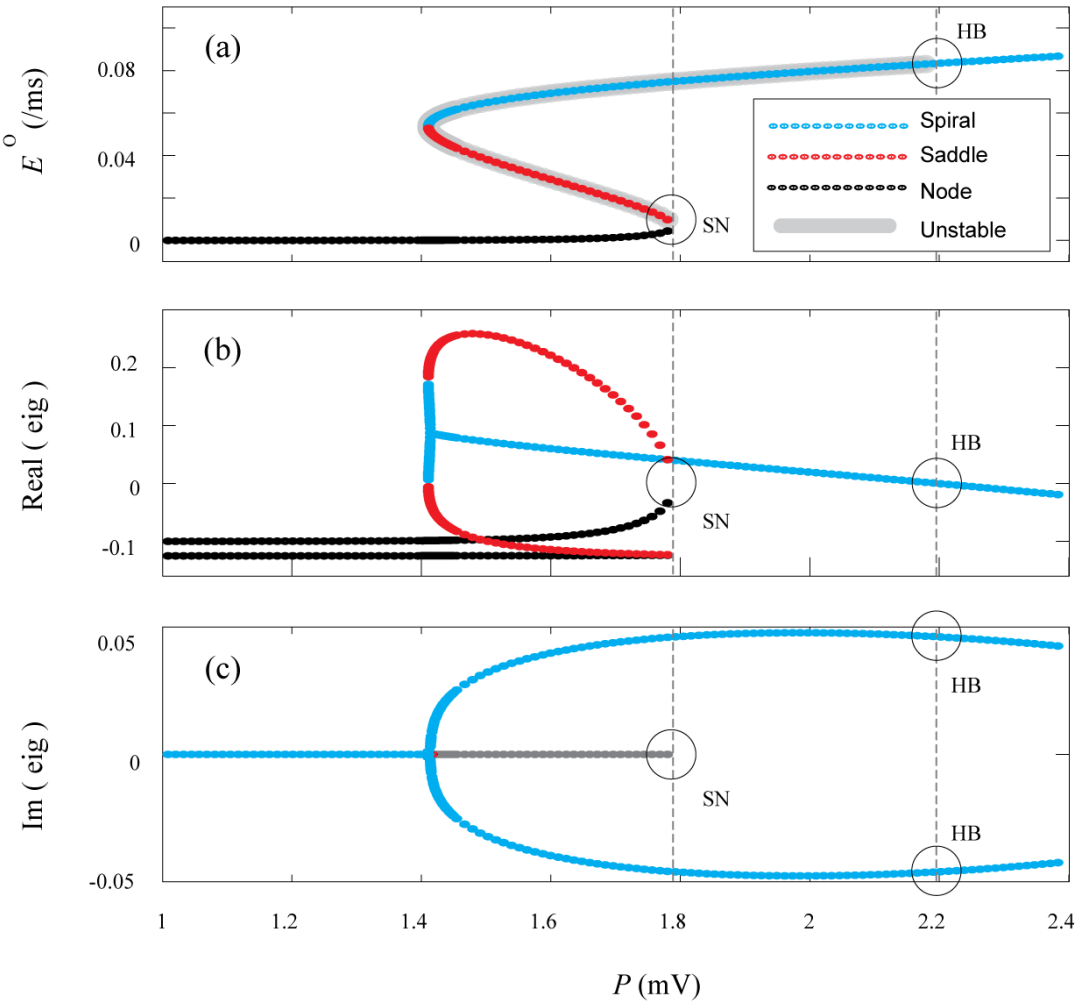

Figure 6.3: Steady state and eigenvalues of 1-D WilCo model, similar to Fig. 5.5. Note that the position of Hopf bifurcation (HB) point is different from the one in Fig. 5.5 due to boosted b_{IE} value in this chapter. (a) Steady state firing rate (E^o) as a function of external excitatory input voltage P. Saddle-node (SN) and Hopf (HB) bifurcations switch the stability of the steady state at $P = 1.7892426576,\ 2.1971513755$ mV respectively. See the caption for Fig. 5.5 for more descriptions. The real and imaginary parts of the eigenvalues of the stability matrix are displayed in (b) and (c) respectively.

(a) **Stable node**: For $P = 1.2$ mV, the two nullclines have one intersection corresponding to a stable node that is predicted to attract all trajectories of the phase plane such as the simulated one plotted in green.

(b) **Unstable focus, saddle, stable node**: For $P = 1.59$ mV, the two nullclines have three intersections $b_{1,2,3}$. The linear stability analysis predicts that all trajectories will be attracted to b_3, which is confirmed by simulations (solid green curve) being attracted to the bottom branch of the S-bend curve. Note that b_2 is an unstable saddle, and b_1 is an unstable spiraling-out focus point.

(c) **Unstable focus**: Panel (c) shows the phase plot diagram at the one-root region of the S-bend corresponding to $P = 2.1$ mV, predicted to be an unstable focus point. Starting from an arbitrary point in phase-plane, the numerical response settles down to a small-amplitude limit-cycle which surrounds the unstable focus point (inset shows detailed view

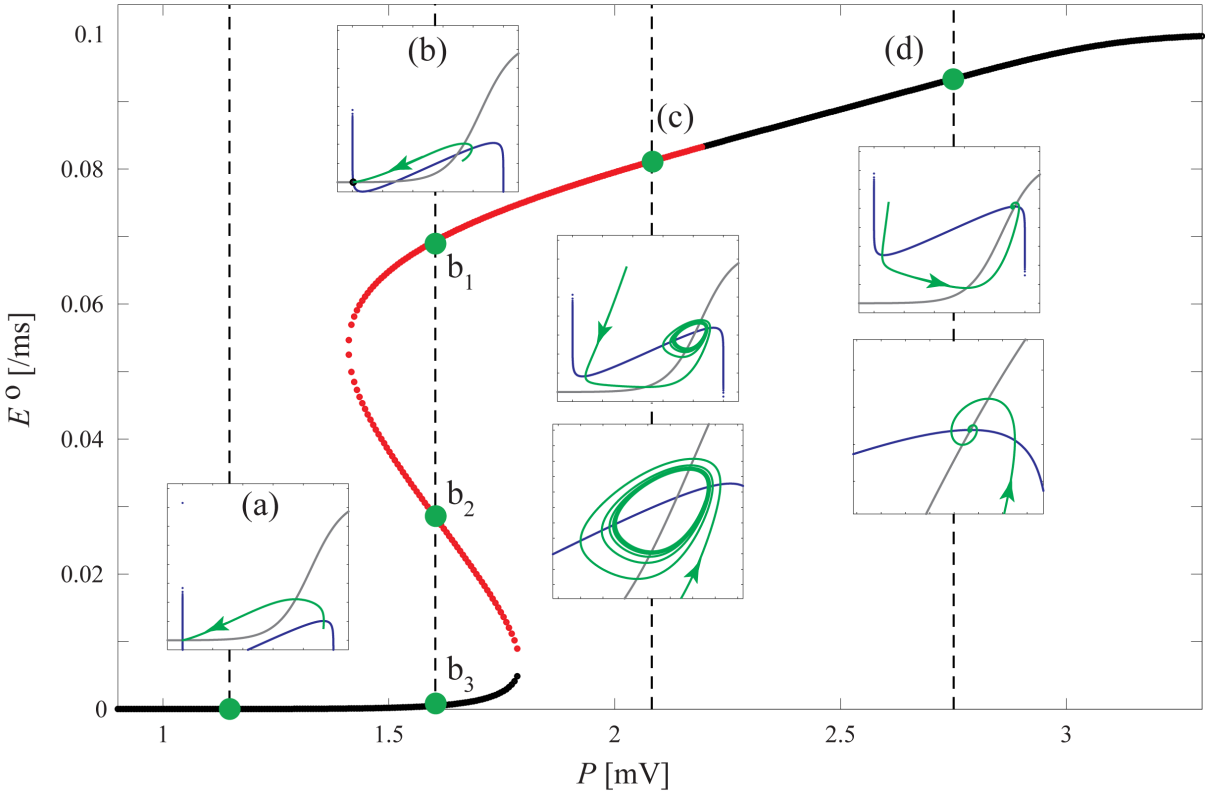

Figure 6.4: Confirmation of theoretical predictions about stability of homogeneous 1-D WC model with numerical simulations. The homogeneous ($q = 0$) steady state curve is plotted again for convenience. The nullclines and the numerically obtained system responses (green trajectories) in the vicinity of four distinct P values (a, b_{1-3}, c , d) are superimposed on steady state curve. The simulation results confirm theoretically predicted behaviour of corresponding equilibria as stated in Table 6.2. An Euler method with fixed time steps of $\Delta t = 0.05$ ms is used to obtain 200 ms-length numerical results. (a) Stable node, (b) unstable focus, saddle, and stable node, (c) unstable focus leading to limit cycle, and (d) is a stable focus.

of limit-cycle). Note that all trajectories will be attracted to this limit-cycle, regardless of their starting point.

(d) **Stable focus**: Panel (d) shows the phase plot diagram at $P = 2.75$ mV which corresponds to a stable spiraling-in focus. This point attracts all trajectories in the phase space. A sample trajectory is plotted in this panel with the inset showing detailed view.

Table 6.2 summarizes the predicted dynamical behaviour of four points corresponding to Fig. 6.4. Our numerical experiments confirm these theoretical predictions.

6.2.3 Stability for non-zero wavenumbers

The Eq. (6.2.7)—stability matrix of the 1-D WC model—depends on wavenumber q. We observed in the previous section that the system collapses to the homogeneous case when we set $q = 0$. I now explore the *non-homogeneous* 1-D WC model by studying the distribution of q-dependent eigenvalues of the $\tilde{\mathbf{J}}(q)$ matrix.

Unlike the homogeneous steady state curves where the steady state are plotted versus P, we now plot the real and imaginary parts of eigenvalues at a selected steady state as a function of

Table 6.2: Stability and types of equilibrium points on Fig. 6.4 based on homogeneous ($q = 0$) eigenvalues.

Panel	P	eig1	eig2	Stability & Type
a	1.2	-0.099	-0.124	stable node
	1.59	0.059+0.249i	0.059-0.249i	unstable focus
b	1.59	0.220	-0.114	unstable saddle
	1.59	-0.092	-0.124	stable node
c	2.1	0.009+0.296i	0.009-0.296i	unstable focus
d	2.75	-0.062+0.187i	-0.062-0.187i	stable focus

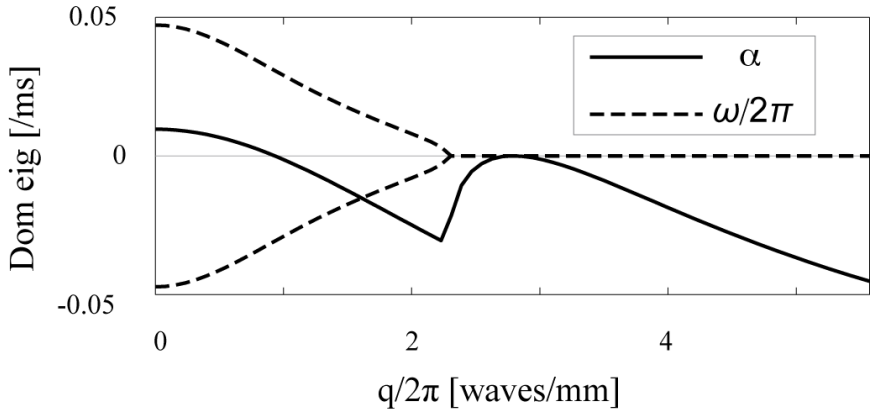

Figure 6.5: Dispersion curves corresponding to point (c) on Fig. 6.4. The solid α curve is the real part of the dominant eigenvalue while the dashed $\omega/2\pi$ curve displays the corresponding imaginary part. The system is unstable for $q/2\pi \lesssim 0.95$ waves/mm, which is accompanied with temporal oscillations indicated by $\omega/2\pi$ curve. The system is also very close to spatial instability with spatial frequency of $q \simeq 2.4$ waves/mm

$q/2\pi$ in units of waves/(unit length). This graph defines the *dispersion curve*. Assuming that λ is the q-dependent dominant eigenvalue of the system at a selected P,

$$\lambda(q)\big|_P = (\alpha(q) \pm \mathrm{j}\omega(q))\,\big|_P \tag{6.2.9}$$

we extract and plot α and $\omega/2\pi$ as a function of $q/2\pi$ using Eq. (6.2.7). We select $P = 2.1$ mV (corresponding to point (c) of Fig. 6.4) and the resulting dispersion curve is shown in Fig. 6.5. The positive values of the α curve predict spatial instability with corresponding spatial frequency in waves/mm, while the nonzero imaginary part (displayed as dashed $\omega/2\pi$ curve) shows the frequency of temporal oscillations in kHz.

We plot the dispersion curves of six distinct steady states as indicated in Fig. 6.6. The shapes of the various dispersion curves allow us to make predictions about the spatiotemporal dynamics of 1-D WC model at each P value:

- Panel (a): The real part is negative for all q values indicating spatiotemporal stability of the state. The imaginary part (not shown) is always zero.

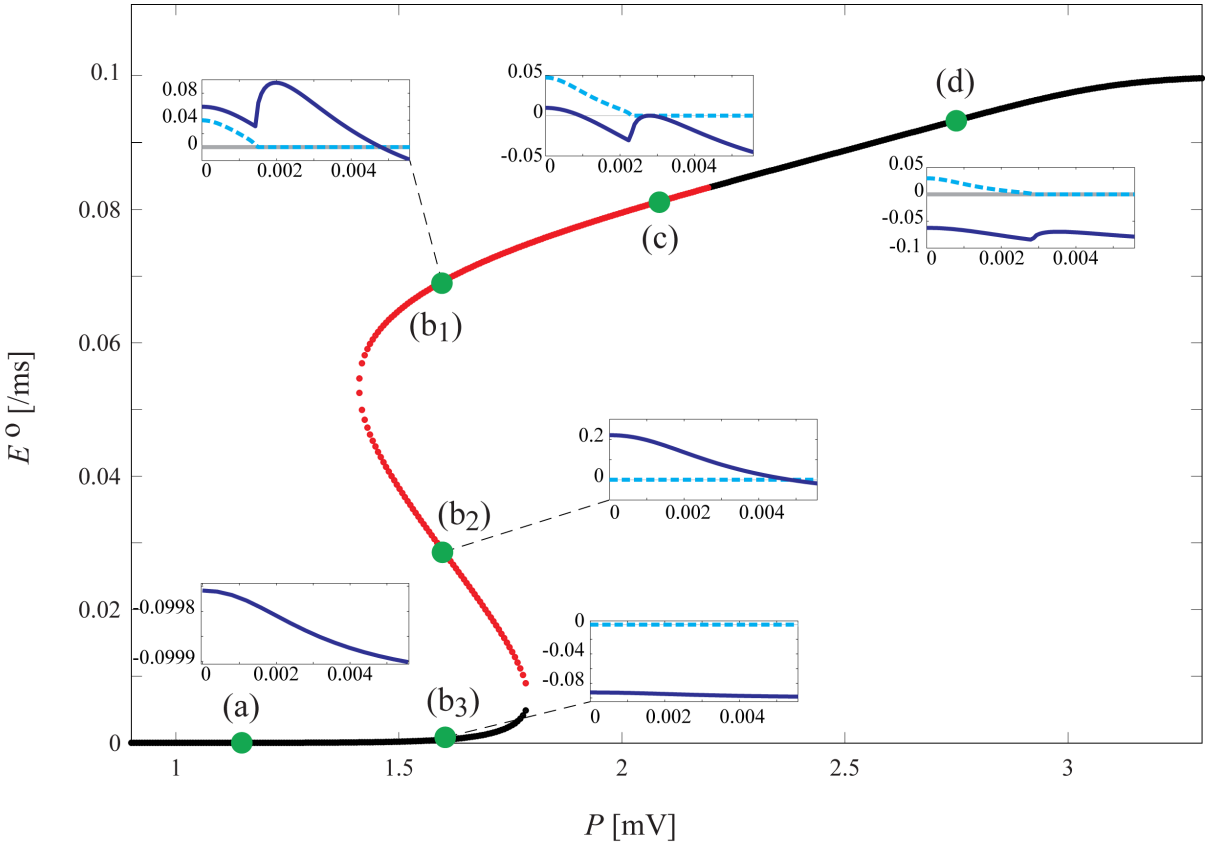

Figure 6.6: Distribution of steady states as a function of external excitatory input (P) along with dispersion curves at four different P values corresponding to six qualitatively distinct dynamics. Solid dark-blue traces show the real part of the dominant eigenvalue as function of wave number $q/2\pi$; dashed-blue traces indicate oscillation frequency (in kHz) $f = \omega/2\pi$ =Im(eig)/2π. (b_1) and (c) are temporally and spatially unstable since both have positive values for real part of dominant eigenvalue at $q = 0$ (temporal instability) and $q \approx 0.002, 0.0025$ waves/μm for b_1 and c respectively. (a) and (b_3) are always temporally and spatially stable, since the real part of dominant eigenvalues are negative for all q values. (b_2) is temporally and spatially unstable. (d) is temporally and spatially stable with a non-zero oscillation frequency which is the characteristic of a stable spiral point.

- Panels (b_1, b_2, b_3): This is a three-root region, with different dynamics for each equilibrium. While the (b_1) and (b_2) are spatiotemporally unstable, the system is spatiotemporally stable at (b_3).
- Panel (c): The real part of dominant eigenvalue is positive at some q values with nonzero imaginary part. This results in mixed mode spatiotemporal oscillations.[1]
- Panel (d): The real part of eigenvalue is always negative, so the system is spatiotemporally stable.

We see that the real part of the dominant eigenvalue can have *two* local peaks, one at the origin and the other at $q \neq 0$. Depending on the sign of the real part of the dominant eigenvalue, the system can support different spatiotemporal patterns. This topic is studied in the next section where we introduce Turing and mixed-mode instabilities of the 1-D WC model.

[1]Sometimes called Turing–Hopf oscillations

6.3 Bifurcations of 1-D WC model of cortical tissue

Four different bifurcation types of 1-D WC model are studied in detail in this section:

1. Saddle-Node (SN) annihilation
2. Hopf bifurcation (HB)
3. Turing instability
4. Turing–Hopf instability

While the SN and HB can induce *temporal* instabilities, the Turing produces *spatial* instabilities. In addition we will see that a Turing–Hopf bifurcation can induce *spatiotemporal* instabilities in the model.

6.3.1 Temporal instabilities

The **SN bifurcation**[1] happens when the midbranch of the S-bend curve collides with the bottom branch and annihilate at $P_{\mathrm{SN}} = 1.7892426576$ mV as displayed in Fig. 6.3(a). This bifurcation results in the disappearance of a pair of steady states, forcing the system to move to an alternate state. Assuming that the system is on the stable bottom branch (low firing rate), increasing P will push the system toward and then beyond SN, causing the system to jump to the upper branch which is an unstable focus point (see phase plot of a point on this branch in Fig. 6.4(c). As a result, the SN bifurcation changes the qualitative behaviour of all neurons in 1-D WC rod.

The **Hopf bifurcation** occurs when the real part of the complex eigenvalue pair changes sign at $P_{\mathrm{HB}} = 2.1971513755$ mV as indicated in Fig. 6.3(b), (c). This bifurcation also changes the qualitative behaviour of all neurons.

6.3.2 Spatial instabilities

The dispersion curves of the 1-D WC model corresponding to $P = 2.34$ mV are plotted in Fig. 6.7. Changing the inhibitory synaptic range constants σ_{EI} and σ_{IE} alters the dispersion curves. When $\sigma_{EI,IE} = 200$ μm, parts of the α-curve exhibit positive excursions implying the formation of spatial oscillations with spatial frequency of $q/2\pi \approx 1.6$ waves/mm.

We perform a numerical simulation to test these theoretical predictions about spatial instability and the resultant spatial oscillations. The synaptic space constant linking excitatory and inhibitory neurons is set at $\sigma_{EI,\,IE} = 200$ µm. The length of the 1-D cortex is $L = 3$ mm with spatial resolution of $\Delta x = 2$ μm. Initial states of the E and I neural populations are set to their steady state values corresponding to $P = 2.34$ mV. Spatiotemporal white noise is added

[1] Sometimes called a *fold* bifurcation

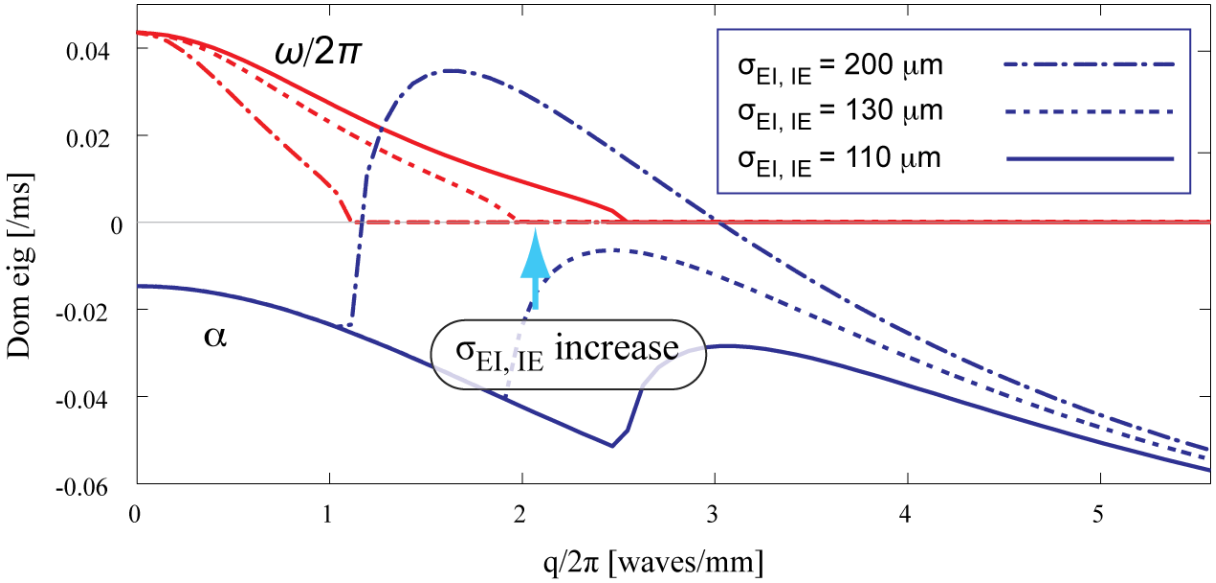

Figure 6.7: Prediction of emerged mixed mode oscillations in 1-D WC model at $P = 2.34$ induced by increased inhibitory synaptic space constant. The real and imaginary parts of dominant eigenvalue are plotted in blue and red respectively. Increasing the inhibitory synaptic space constants σ_{EI}, σ_{IE} increases the real part of dominant eigenvalue and causes its peak point to have positive values implying spatial instability.

to both exogenous voltage inputs P, Q to allow small deviations from steady state, encouraging evolution of any incipient spatial patterns.

Figure 6.8(a) shows the time-space evolution of the cortical rod, starting from homogeneous steady state $E \simeq 0.0859$ mV (corresponding to $P = 2.34$ mV) and developing into a full Turing pattern. The spatial Turing pattern has fully formed after about 0.5 sec. Panel (b) displays firing rates of the cortical tissue at $t = 0.55$ sec, clearly showing a spatial wave with spatial frequency of 5 waves/3mm which agrees nicely with prediction of linear stability analysis as shown by the location of the peak of the α-curve at Fig. 6.7 for $\sigma_{EI,IE} = 200$ μm.

6.3.3 Spatio-temporal instabilities

The *Turing-Hopf* spatiotemporal instability is a result of interacting Turing and Hopf bifurcations. This interaction happens when the conditions for both bifurcations are met simultaneously—i.e. the system is close to HB point, and the corresponding α dispersion curve has positive excursions at some nonzero q values. In this section I set up the conditions for formation of this pattern in the 1-D WC model, then validate the prediction by numerical simulation. I found that the selected steady point should be located *outside* the multi-root region of steady-state distribution curve; i.e. panel (c) of Fig. 6.6 is a proper choice, while panels (b_{1-3}) are not. This is because within the multi-root region, the state will be attracted to stable bottom branch, preventing the formation of spatiotemporal oscillating patterns.

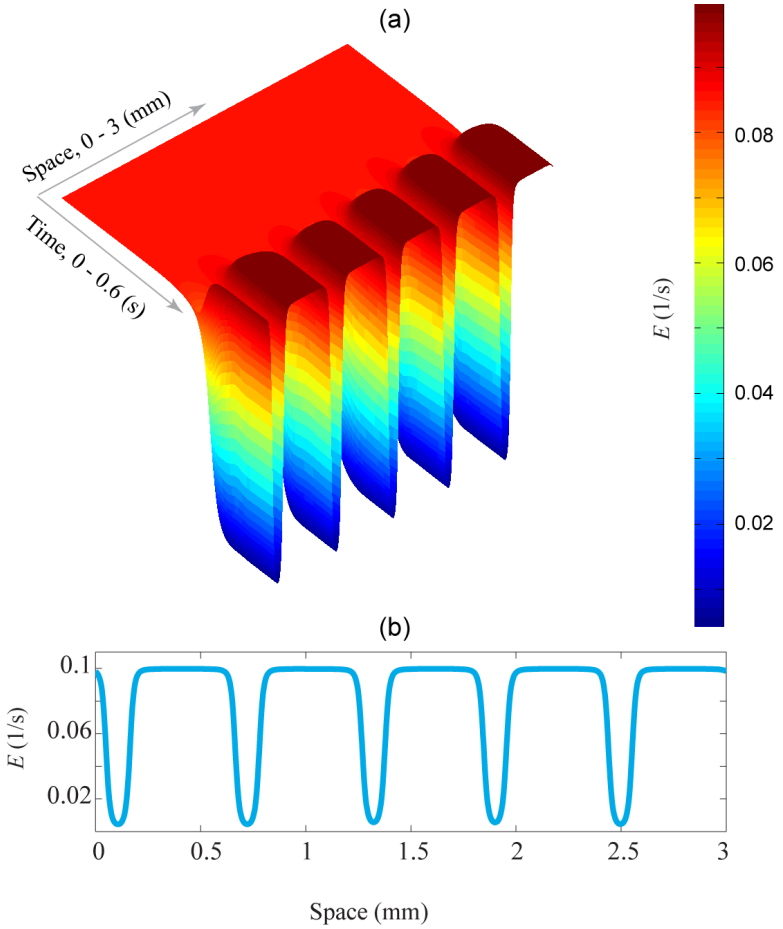

Figure 6.8: Formation of Turing spatial instability in the WC cortical rod. (a) Demonstration of state evolution of neurons from $E \simeq 0.0859$ mV to full Turing pattern as displayed by colour-coded spatio-temporal plot. (b) State of WC cortical rod at $t = 0.55$ s clearly shows spatial waveform with spatial frequency of 5 waves/3mm. A fourth-order Runge-Kutta method with time-step of Δt =0.05 ms is used to simulate the 3 mm length cortical column with spatial resolution of $\Delta x = 2$ μm.

.

We select $P = 2$ mV to put the system in an unstable Hopf mode on the top branch, and $\sigma_{EI,IE} = 112$ µm to induce a Turing instability (positive α for $q \neq 0$)[1]. (For the value of other model parameters see Table 6.1.)

Note that the system has only one steady state at this point indicated by a green circle in Fig. 6.9(a). The corresponding dispersion curve is shown in Fig. 6.9(b) with a pair of maxima of α curve at $q/2\pi \simeq 2.62$ and 0 waves/mm, indicating the possibility of simultaneous Turing and Hopf instabilities. The red curve of Fig. 6.9(b) predicts temporal frequency of $f \simeq 47$ Hz at the origin of the dispersion curve.

Numerical simulation results are shown in Fig. 6.10. The simulation starts from the steady state corresponding to $P = 2$ mV, and small amplitude continuous white noise is injected to each grid point at every time step. The white-noise induced evolution of the network is displayed in

[1]We select $\sigma_{EI,IE}$ values so that two peaks of α curve have similar magnitudes. Note that using higher $\sigma_{EI,IE}$ values increases the peak-value of α curve at $q \neq 0$ compared to its peak value at $q = 0$, making the Turing mode dominant, preventing development of Turing–Hopf mixed-mode oscillations.

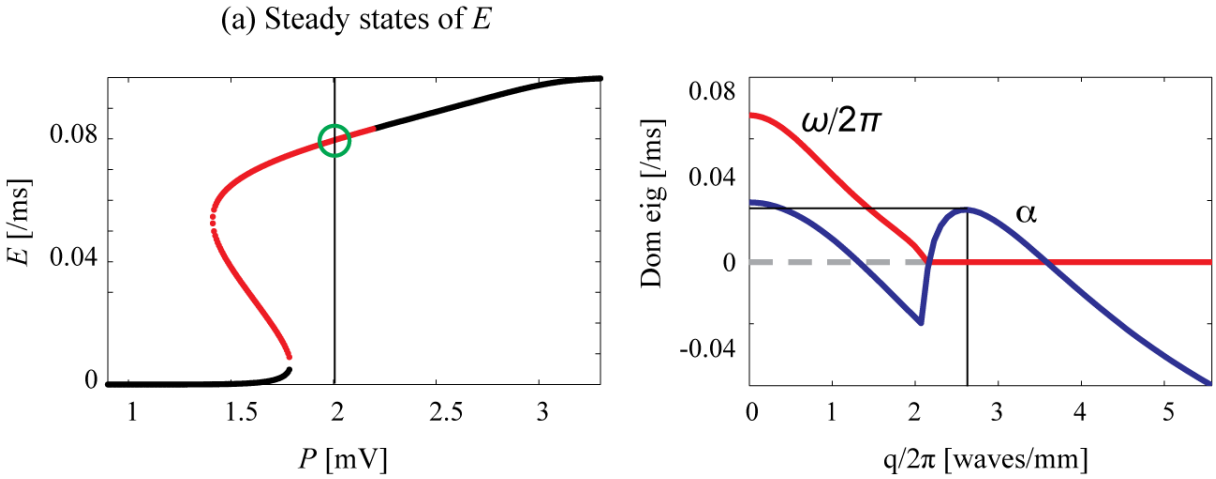

Figure 6.9: Theoretical prediction of mixed-mode oscillations in the 1-D WC model. (a) Steady state distribution curve and a selected point at $P = 2$ mV. The system has a Hopf instability at this state. (b) Dispersion curve of the system at the same state. The synaptic range constant between excitatory and inhibitory neurons are selected to be $\sigma_{EI,\,IE} = 112$ µm. See Table 6.1 for other parameter values. The dispersion curve shows the possibility of a Turing instability at spatial frequency of $q \simeq 2.62$ waves/mm. The dispersion curve also shows the frequency of temporal oscillations as $f \simeq 47$ Hz. (See the $\omega/2\pi$ value at the origin on dispersion curve.)

Fig. 6.10(a) as the colour-coded time-space plot. This plot shows the dominance of temporal Hopf oscillations at first. However a Turing instability emerges quickly until it pushes the system into mixed-mode oscillatory behaviour at $t \simeq 0.6$ s. Panel (b) displays a snapshot of 1-D cortical tissue at selected instant of $t = 1$ s. A basic examination of this graph reveals the spatial frequency of about $\simeq 2$ waves/mm which matches tolerably with predictions of linear stability analysis as shown in Fig. 6.9 (b) with $q/2\pi \simeq 2.6$ waves/mm. Better agreement may be obtained by increasing the length of domain L, but one should not expect perfect agreement between theory and experiments since the interaction between Turing and Hopf instabilities is a strongly nonlinear phenomenon, reducing the validity of predictions of linear stability analysis.

The 1-s evolution of a 0.75 mm-length part of the rod is depicted as a 3-D graph in (c). This graph shows how the temporal Hopf oscillations emerge and grow until they get mixed by spatial Turing oscillations, giving birth to mixed-mode oscillations. Firing rates of two selected grid points from the 1-D tissue are plotted in (d)[1]. The oscillatory behaviours at the two grid points are very similar at first, then become distinguishable after emergence of spatial oscillations. The differences can be described in terms of amplitude and phase, but their frequency is identical. Spectral analysis on one of the firing rate traces of (d) provides insights about the oscillatory behaviour[2]. We can partition the oscillatory behaviour into three distinct phases:

- emergence of Hopf
- Hopf-dominated

[1]The representing grid of the 1-D rod is composed of 1500 points with spatial resolution of $\Delta x = 2$ µm. The selected grid points are the 300th and 700th points.

[2]The grey trace of (d) is selected for spectral analysis.

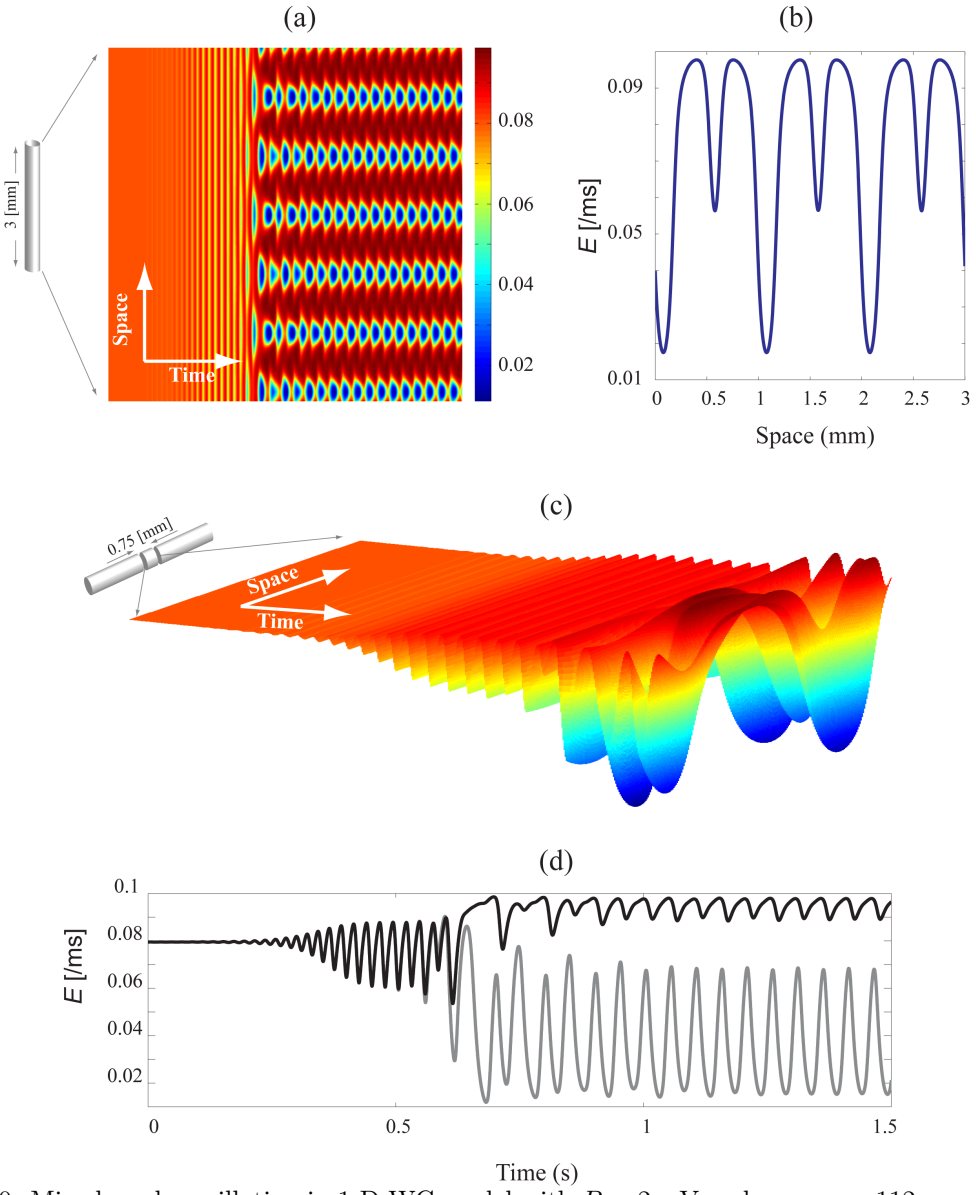

Figure 6.10: Mixed mode oscillation in 1-D WC model with $P = 2$ mV and $\sigma_{EI,\,IE} = 112$ µm. See Table 6.1 for other parameter values; steady state curve and corresponding dispersion curves at $P = 2$mV are depicted in Fig. 6.9. (a) Spatio-temporal evolution of the 3-mm cortical column in mixed mode. The simulation ran for 1.5 s, with spatial and temporal resolutions of $\Delta t = 0.05$ ms and $\Delta x = 2$ µm, and employed a fourth-order Runge–Kutta integrator. White noises was added to the system according to Eq. (6.4.2). (b) A sample snapshot of firing rates of 1-D cortical tissue at $t = 1$ s shows about 6 spatial waves within the domain length of $L = 3$ mm which corresponds to $q/2\pi \simeq 2$ waves/mm. (c) Detailed view of a selected part of 1-D cortical tissue showing its spatio-temporal evolution during first second of simulation. (d) Firing rates of two selected grid points from the network.

- mixed-mode

as highlighted in Fig. 6.11(a).

The figure shows the corresponding frequency of each phase. The initial state is selected to be an unstable spiraling-out point. Spectral analysis in (f) shows that the frequency of the emerged oscillations (stimulated by white-noise perturbation) is $f \simeq 45$ Hz. This temporal frequency agrees reasonably well with the LSA prediction of Fig. 6.9(b). Absence of higher-order harmonics for $t \leq 0.3$ s (evident in panel d) shows that the emerged oscillations are pure

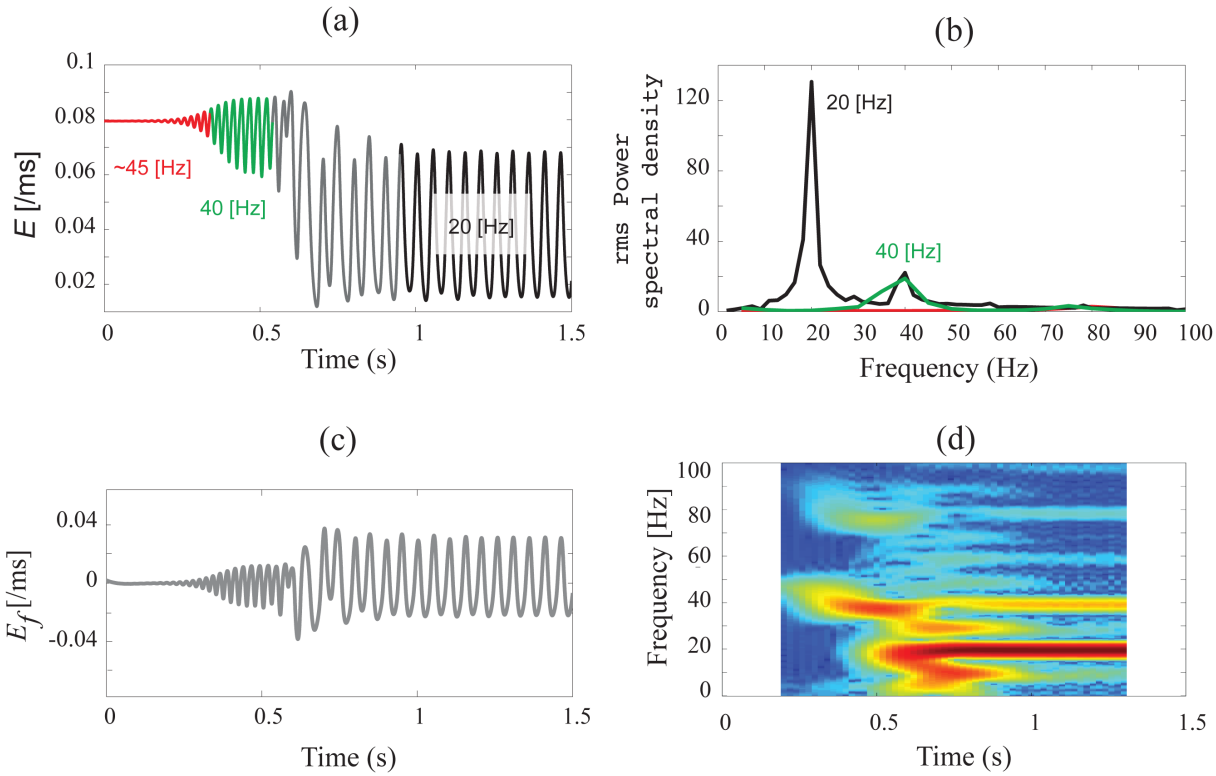

Figure 6.11: Spectral analysis of mixed mode oscillations in 1-D cortical rod. (a) Firing-rate trace of a grid point selected from Fig. 6.10(d) and partitioned into three phases: emergence (red), Hopf (green), and mixed-mode (black) periods. (b) The rms power spectral density for the time-series in (a). (c) High-pass filtered ($f_{\mathrm{HP}} = 5$ Hz, second-order Butterworth) view of firing rate shown in (a). (d) Time-frequency plot for filtered firing rate shown in (c). The different frequencies are the result of interaction between Hopf and Turing instabilities.

sine waves which again agrees with predictions of LSA. However the Turing instability interacts quickly with Hopf oscillations, and reduces the initial frequency down to 20 Hz at $t \simeq 0.5$. This is the result of a mixed-mode dynamics where temporal and spatial instabilities interact, leading to strong harmonic components of 40, 60, 80, 100 Hz on spectral graph of Fig. 6.10(d). This rich spectrum arises from nonlinear interacting dynamics, making the predictions of LSA less reliable.

To conclude this section, we have studied the different bifurcations of the 1-D WC cortical rod. Our numerical results confirmed predictions of theoretical analysis of the system regarding the frequency of spatial and temporal oscillations. We have showed how the spatiotemporal oscillatory behaviour of the system can be controlled using P and $\sigma_{\mathrm{EI,\ IE}}$ parameters.

In the following sections we will drive the system toward its different bifurcation points using the same control parameters. Considering our assumption about the role of different bifurcations in seizure generation and termination, we will study the subthreshold fluctuations of the 1-D rod close to different bifurcation types. We will demonstrate that the system undergoes a critical slowing prior to all four bifurcation types: saddle-node, Hopf, Turing, and Turing–Hopf. Our detailed examination of pre-bifurcation dynamics consist of theoretical investigations of the

system using well-stablished stochastic methods, confirmed by stochastic analysis simulations.

6.4 Linearized stochastic differential equations of WC model

In this section I describe how the ordinary differential equations of the WC model can be transformed into stochastic differential equations (SDEs) by adding white-noise perturbations. After introducing stochasticity, the governing equations will be reformed into a well-known stochastic process—the two-variable linear Ornstein-Uhlenbeck (OU) process—applying stochastic theory to its subthreshold fluctuation behaviour, namely its spatial and temporal variances, autocorrelations and power spectral densities. These theoretical predictions will be compared against experimentally-obtained quantities based on numerical simulation of the stochastic model.

The set of stochastic differential equations for WC model of cortical column follow:

$$\begin{aligned}
&\frac{\partial}{\partial t}E(x,t) = B_1(E,\phi_{EE},\phi_{IE}) \\
&\frac{\partial}{\partial t}I(x,t) = B_2(I,\phi_{EI},\phi_{II}) \\
&(\Lambda_{EK}^2 - \frac{\partial^2}{\partial x^2})\,\phi_{EK}(x,t) = \Lambda_{EK}^2\,E(x,t) \\
&(\Lambda_{IK}^2 - \frac{\partial^2}{\partial x^2})\,\phi_{IK}(x,t) = \Lambda_{IK}^2\,I(x,t)
\end{aligned} \tag{6.4.1}$$

where

$$\begin{aligned}
B_1 &= \tau_E^{-1}[-E(x,t) + S_E\,(b_{EE}\phi_{EE}(x,t) - b_{IE}\phi_{IE}(x,t) + P) + c_1\xi_1(x,t)], \\
B_2 &= \tau_I^{-1}[-I(x,t) + S_I(b_{EI}\phi_{EI}(x,t) - b_{II}\phi_{II}(x,t) + Q) + c_2\xi_2(x,t)]
\end{aligned} \tag{6.4.2}$$

with two stochastic terms $\xi_{1,2}$, selected to be independent zero-mean Gaussian-distributed δ-function-correlated spatiotemporal white-noise sources [Steyn-Ross *et al.*, 2003],

$$\langle\xi(x,t)\rangle = 0\ , \quad \langle\xi_m(x,t)\xi_n(x',t')\rangle = \delta_{mn}\delta(x-x')\delta(t-t') \tag{6.4.3}$$

where δ_{mn} is the dimensionless Kronecker delta, $\delta(\cdot)$ is the dirac delta with a dimensionless total area under its curve, and the $\langle\cdots\rangle$ is to be thought of as a "mean of" operator. As a result the variance term $\langle\xi_m(x,t)\xi_n(x',t')\rangle$ of Eq. (6.4.3) carries units of $1/(\text{ms}{\cdot}\mu\text{m})$. Therefore each $\xi(x,t)$ noise source has units of $1/\sqrt{\text{ms}{\cdot}\mu\text{m}}$. Considering Eqs. (6.4.2) the $c_{1,2}$[1] must carry units of $\sqrt{\mu\text{m}/\text{ms}}$. Samples from a zero-mean, unit-variance Gaussian random number generator

[1]The $c_{1,2}$ are small constants to ensure that the fluctuations are small.

(implemented by MATLAB's `randn` function) are scaled as

$$\xi(x,t) = \frac{\mathcal{R}_n(m,n)}{\sqrt{\Delta x \Delta t}} \tag{6.4.4}$$

to approximate an infinite-variance white-noise source $\xi(x,t)$ in numerical simulations at discrete position and time coordinates $x = m\Delta x$, $t = n\Delta t$. Here Δx is the grid spacing or the spatial resolution of the grid (in µm) and Δt is the time increment (in ms). To maintain consistency of units, the $\mathcal{R}_n$ noise samples are scaled as Eq. (6.4.4). The $\xi(x,t)$ noises have variance of $\sigma^2 = (\Delta x \Delta t)^{-1}$, with $\sigma^2 \to \infty$ in the continuous limit $\Delta x \to 0$, $\Delta t \to 0$. Following a similar method presented in Section 6.2.1, the linearization of Eqs. (6.4.1-6.4.2) results in

$$\frac{\partial}{\partial t}\begin{bmatrix} \hat{E}(x,t) \\ \hat{I}(x,t) \end{bmatrix} = \begin{bmatrix} \dfrac{\partial B_1}{\partial E} + \dfrac{\partial B_1}{\partial \phi_{EE}}\dfrac{\Lambda_{EE}^2}{(\Lambda_{EE}^2+q^2)} & \dfrac{\partial B_1}{\partial \phi_{IE}}\dfrac{\Lambda_{IE}^2}{(\Lambda_{IE}^2+q^2)} \\ \dfrac{\partial B_2}{\partial \phi_{EI}}\dfrac{\Lambda_{EI}^2}{(\Lambda_{EI}^2+q^2)} & \dfrac{\partial B_2}{\partial I} + \dfrac{\partial B_2}{\partial \phi_{II}}\dfrac{\Lambda_{II}^2}{(\Lambda_{II}^2+q^2)} \end{bmatrix} \begin{bmatrix} \hat{E}(x,t) \\ \hat{I}(x,t) \end{bmatrix} + \begin{bmatrix} (c_1/\tau_E)\,\hat{\xi}_1(x,t) \\ (c_2/\tau_I)\,\hat{\xi}_2(x,t) \end{bmatrix} \tag{6.4.5}$$

We make Eq. (6.4.5) amenable to theoretical analysis by transforming it into a two-variable Ornstein-Uhlenbeck (OU) system of equations as described by Chaturvedi *et al.* [1977] and Gardiner [2004]

$$\frac{\partial}{\partial t}\begin{bmatrix} \hat{E}(x,t) \\ \hat{I}(x,t) \end{bmatrix} = -\tilde{\mathbf{A}}(q)\begin{bmatrix} \hat{E}(x,t) \\ \hat{I}(x,t) \end{bmatrix} + \sqrt{\mathbf{D}}\begin{bmatrix} \hat{\xi}_1(x,t) \\ \hat{\xi}_2(x,t) \end{bmatrix} \tag{6.4.6}$$

where $\mathbf{D}$ is a diagonal 2×2 diffusion matrix

$$\mathbf{D} = \begin{bmatrix} (c_1/\tau_E)^2 & 0 \\ 0 & (c_2/\tau_I)^2 \end{bmatrix} \tag{6.4.7}$$

and $\tilde{\mathbf{A}}$ is the q-dependent drift matrix of the form

$$\tilde{\mathbf{A}}(\mathbf{q}) = \begin{bmatrix} \dfrac{-\partial B_1}{\partial E} - \dfrac{\partial B_1}{\partial \phi_{EE}}\dfrac{\Lambda_{EE}^2}{(\Lambda_{EE}^2+q^2)} & \dfrac{-\partial B_1}{\partial \phi_{IE}}\dfrac{\Lambda_{IE}^2}{(\Lambda_{IE}^2+q^2)} \\ \dfrac{-\partial B_2}{\partial \phi_{EI}}\dfrac{\Lambda_{EI}^2}{(\Lambda_{EI}^2+q^2)} & \dfrac{-\partial B_2}{\partial I} \end{bmatrix} \tag{6.4.8}$$

where we have assumed that $\Lambda_{II} = 0$, i.e., there is no self-inhibition in the system. The partial derivatives appearing in $\tilde{\mathbf{A}}(q)$ are

$$\begin{aligned}
\frac{\partial B_1}{\partial E} &= -\tau_E^{-1} < 0 \\
\frac{\partial B_1}{\partial \phi_{EE}} &= \tau_E^{-1} E_{\max} \frac{ab_{EE}\ \exp(-a(b_{EE}\phi_{EE} - b_{IE}\phi_{IE} + P - \theta))}{[1 + \exp(-a(b_{EE}\phi_{EE} - b_{IE}\phi_{IE} + P - \theta))]^2} > 0 \\
\frac{\partial B_1}{\partial \phi_{IE}} &= \tau_E^{-1} E_{\max} \frac{-ab_{IE}\ \exp(-a(b_{EE}\phi_{EE} - b_{IE}\phi_{IE} + P - \theta))}{[1 + \exp(-a(b_{EE}\phi_{EE} - b_{IE}\phi_{IE} + P - \theta))]^2} < 0 \\
\frac{\partial B_2}{\partial \phi_{EI}} &= \tau_I^{-1} I_{\max} \frac{ab_{EI}\ \exp(-a(b_{EI}\phi_{EI} - b_{II}\phi_{II} + Q - \theta))}{[1 + \exp(-a(b_{EI}\phi_{EI} - b_{II}\phi_{II} + Q - \theta))]^2} > 0 \\
\frac{\partial B_2}{\partial I} &= -\tau_I^{-1} < 0
\end{aligned} \tag{6.4.9}$$

which can be used to compute the q-dependent eigenvalues of the system. Regarding the sign of the partial derivatives, we simplify the drift matrix $\tilde{\mathbf{A}}(q)$, by defining five new positive constants as

$$\begin{aligned}
\alpha_1 &= -\frac{\partial B_1}{\partial E}, & \alpha_2 &= \frac{\partial B_1}{\partial \phi_{EE}}, & \alpha_3 &= -\frac{\partial B_1}{\partial \phi_{IE}} \\
\alpha_4 &= \frac{\partial B_2}{\partial \phi_{EI}}, & \alpha_5 &= -\frac{\partial B_2}{\partial I}, &
\end{aligned} \tag{6.4.10}$$

Considering that $b_{II} = 0$ and $\sigma_{EI} = \sigma_{IE}$ in our model[1], and recalling that $\Lambda = 1/\sigma$, the drift matrix can be written as

$$\tilde{\mathbf{A}}(\mathbf{q}) = \begin{bmatrix} \alpha_1 - \dfrac{\alpha_2 \cdot \Lambda_{EE}^2}{(\Lambda_{EE}^2 + q^2)} & \dfrac{\alpha_3 \cdot \Lambda_{IE}^2}{(\Lambda_{IE}^2 + q^2)} \\ \dfrac{-\alpha_4 \cdot \Lambda_{IE}^2}{(\Lambda_{EI}^2 + q^2)} & \alpha_5 \end{bmatrix} \tag{6.4.11}$$

which contains positive constants $\alpha_1, \alpha_2, \cdots, \alpha_5$[2].

Equation (6.4.6) is a two-variable OU process with well-documented stationary statistics. In the following sections I first derive the theoretical expressions for spatial power spectral density, autocorrelation and variance of Eq. (6.4.6). Next I will discuss a method showing how the temporal autocorrelation and variance of the system can be derived.

[1] See Table 6.1

[2] Knowing the sign of elements of $\tilde{\mathbf{A}}$ simplifies the computation of its space-domain counterpart using inverse Fourier transform.

6.4.1 Theoretical expressions for spatial power spectral density, autocorrelation and variance

The q-dependent 2×2 stationary *covariance* matrix of a two-dimensional system (sometimes referred to as the zero-time correlation matrix) is defined as [Chaturvedi *et al.*, 1977; Gardiner, 2004]

$$\tilde{\mathbf{G}}(q, q') = \lim_{t\to\infty} \begin{bmatrix} \Big\langle E(q,t)E(q',t)\Big\rangle & \Big\langle E(q,t)I(q',t)\Big\rangle \\ \Big\langle I(q,t)E(q',t)\Big\rangle & \Big\langle I(q,t)I(q',t)\Big\rangle \end{bmatrix} = 2\pi\delta(q+q')\tilde{\mathbf{G}}(q) \tag{6.4.12}$$

where the $\langle \cdot \rangle$ operator signifies the expected value. Following the stochastic methods described by Chaturvedi *et al.* [1977] and Gardiner [2004], the 2×2 steady-state Fourier-domain spatial covariance matrix[1] $\tilde{\mathbf{G}}$ of a system governed by Eq. (6.4.6) is computed as

$$\tilde{\mathbf{G}}(q) = \frac{\det(\tilde{\mathbf{A}})\mathbf{D} + [\tilde{\mathbf{A}} - \mathrm{tr}(\tilde{\mathbf{A}})\mathbf{I}]\mathbf{D}[\tilde{\mathbf{A}} - \mathrm{tr}(\tilde{\mathbf{A}})\mathbf{I}]^{\mathrm{T}}}{2\mathrm{tr}(\tilde{\mathbf{A}})\det(\tilde{\mathbf{A}})} \tag{6.4.13}$$

in which $\tilde{\mathbf{A}}$ is the q-dependent drift matrix, $\mathbf{I}$ is the 2×2 identity matrix; $\det(\cdot)$ and $\mathrm{tr}(\cdot)$ are the determinant and trace operators respectively[2]. Each element of the $\tilde{\mathbf{G}}$ matrix conveys spatial covariance information about fluctuation behaviour of the system. Namely $[\tilde{\mathbf{G}}(q)]_{11}$ is the spatial power spectral density of the excitatory firing rate E of the system. The inverse Fourier transform of $[\tilde{\mathbf{G}}(q)]_{11}$ gives the spatial autocorrelation of E fluctuations based on Wiener–Khinchin theorem[3] as:

$$[\mathbf{G}(x)]_{11} = \mathcal{F}^{-1}\{[\tilde{\mathbf{G}}(q)]_{11}\} \tag{6.4.14}$$

Also the area under the curve of power spectrum density function is equal to spatial variance of the process:

$$\text{spatial var} = \int_{-\infty}^{+\infty} [\tilde{\mathbf{G}}(q)]_{11}\, dq \tag{6.4.15}$$

These different statistical spatial measures, along with similar temporal measures, will be used extensively in our examination of pre-bifurcation dynamics of the WC system in the rest of the current current chapter.

[1] The $\tilde{\mathbf{G}}(q)$ matrix can also be interpreted as the spatial power spectrum of the system.

[2] The $\tilde{\mathbf{G}}(q)$ has units of $[E]^2 \times [x]$ where E is the excitatory firing rate in $(\mathrm{ms})^{-1}$ and x is the space variable, and the $[\cdots]$ should be thought as "units of" operator. In our case $[\tilde{\mathbf{G}}(q)] = \mu\mathrm{m}/(\mathrm{ms})^2$.

[3] Wiener–Khinchin theorem: The power spectrum density and the covariance functions are Fourier duals of each other [Chatfield, 2013].

We attempt to extract an analytical form for x-dependent spatial autocorrelation of excitatory firing rate $[\mathbf{G}(x)]_{11}$ using Eq. (6.4.14) in a similar approach as employed in Steyn-Ross *et al.* [2003]. By expanding Eq. (6.4.13) we obtain

$$\left[\tilde{\mathbf{G}}(q)\right]_{11} = \frac{\mathbf{D}_{11}}{2(\tilde{\mathbf{A}}_{11}+\tilde{\mathbf{A}}_{22})} + \frac{\tilde{\mathbf{A}}_{22}^2\mathbf{D}_{11}+\tilde{\mathbf{A}}_{12}^2\mathbf{D}_{22}}{2(\tilde{\mathbf{A}}_{11}+\tilde{\mathbf{A}}_{22})(\tilde{\mathbf{A}}_{11}\tilde{\mathbf{A}}_{22}-\tilde{\mathbf{A}}_{12}\tilde{\mathbf{A}}_{21})} \tag{6.4.16}$$

where all quantities are evaluated at steady state. Before transforming the $[\tilde{\mathbf{G}}(q)]_{11}$ to the space domain, some algebraic manipulations are carried out on Eq. (6.4.16). Note that all elements of $\tilde{\mathbf{A}}$ matrix except $[\tilde{\mathbf{A}}]_{22}$ are q-dependent. Replacing the elements of $\tilde{\mathbf{A}}$ by their equivalent from (6.4.11), the spatial power spectral density of E neurons $[\tilde{\mathbf{G}}(q)]_{11}$ can be written as

$$\begin{aligned}\left[\tilde{\mathbf{G}}(q)\right]_{11} =& \frac{D_{11}}{2\left(\alpha_1 - \dfrac{\alpha_2\cdot\Lambda_{EE}^2}{\Lambda_{EE}^2+q^2}+\alpha_5\right)} + \\ & \frac{\alpha_5^2 D_{11} + \left(\dfrac{\alpha_3}{\Lambda_{IE}^2+q^2}\right)^2 D_{22}}{2\left(\alpha_1 - \dfrac{\alpha_2\cdot\Lambda_{EE}^2}{\Lambda_{EE}^2+q^2}+\alpha_5)(\alpha_1\alpha_5 - \dfrac{\alpha_2\alpha_5\cdot\Lambda_{EE}^2}{\Lambda_{EE}^2+q^2} + \dfrac{\alpha_3\alpha_4\cdot\Lambda_{IE}^2}{(\Lambda_{IE}^2+q^2)^2}\right)}\end{aligned} \tag{6.4.17}$$

By defining a new variable[1] as

$$Q = \Lambda_{IE}^2 + q^2 \tag{6.4.18}$$

the expression for $[\tilde{\mathbf{G}}(q)]_{11}$ can be re written as a function of Q

$$\begin{aligned}\left[\tilde{\mathbf{G}}(q)\right]_{11} =& \frac{D_{11}}{2\left(\alpha_1 - \dfrac{\alpha_2\cdot\Lambda_{EE}^2}{Q-\Lambda_{IE}^2+\Lambda_{EE}^2}+\alpha_5\right)} + \\ & \frac{\alpha_5^2 D_{11} + \left(\dfrac{\alpha_3}{Q}\right)^2 D_{22}}{2\left(\alpha_1 - \dfrac{\alpha_2\cdot\Lambda_{EE}}{Q-\Lambda_{IE}^2+\Lambda_{EE}^2}+\alpha_5\right)\left(\alpha_1\alpha_5 - \dfrac{\alpha_2\alpha_5\Lambda_{EE}^2}{Q-\Lambda_{IE}^2+\Lambda_{EE}^2} + \dfrac{\alpha_3\alpha_4\Lambda_{IE}^2}{(Q)^2}\right)}\end{aligned} \tag{6.4.19}$$

[1] This new definition reduces the order of the equation.

After some algebraic manipulations we find

$$\begin{aligned}\Big[\tilde{\mathbf{G}}(q)\Big]_{11} =& \frac{D_{11}(Q-\Lambda_{IE}^2+\Lambda_{EE}^2)}{2\Big((\alpha_1+\alpha_2)\cdot(Q-\Lambda_{IE}^2+\Lambda_{EE}^2)-\alpha_2\cdot\Lambda_{EE}^2\Big)} \; + \\ & \left[\frac{(\alpha_5^2 D_{11}Q^2+\Lambda_{IE}^4\alpha_3^2 D_{22})(Q-\Lambda_{IE}^2+\Lambda_{EE}^2)^2}{(\alpha_1+\alpha_5)(Q-\Lambda_{IE}^2+\Lambda_{EE}^2)-\alpha_2\Lambda_{EE}^2}\right] \; \times \\ & \left[\frac{1}{(Q-\Lambda_{IE}^2+\Lambda_{EE}^2)(\alpha_1\alpha_2Q^2+\Lambda_{IE}^4\alpha_3\alpha_4)-\Lambda_{EE}^2\alpha_2\alpha_5Q^2}\right]\end{aligned} \tag{6.4.20}$$

Unfortunately, attempts to find analytically the inverse Fourier transform of Eq. (6.4.20) fail, despite the simplifications and algebraic manipulations made on $[\tilde{\mathbf{G}}(q)]_{11}$. The reason is that partial fraction decomposition cannot be used here to facilitate the inverse Fourier transformation of the Eq. (6.4.20) because of the cubic polynomial in the denominator of the second term. As a result a general *theoretical* formula cannot be extracted for the spatial autocorrelation function.[1] However, the *numerical* value of the inverse Fourier transform can be found straightforwardly if all parameters are replaced by their numerical values, and this is the approach used in this chapter (e.g., see Figs. 6.17(d-f), 6.21(g-i)).

6.4.2 Theoretical expressions for temporal autocorrelation and variance

Following Chaturvedi *et al.* [1977] and Gardiner [2004], one can express the 2×2 steady-state correlation matrix $\tilde{\mathbf{T}}$ exactly as the product of matrix exponential $\exp(-\tilde{\mathbf{A}}(q)\cdot\tau)$ with covariance matrix $\tilde{\mathbf{G}}(q)$:

$$\tilde{\mathbf{T}}(q,\tau) = \exp(-\tilde{\mathbf{A}}(q)\cdot\tau)\tilde{\mathbf{G}}(q), \quad \tau > 0 \tag{6.4.21}$$

with symmetry property $\tilde{\mathbf{T}}(q,-\tau) = [\tilde{\mathbf{T}}(q,\tau)]^T$. The $[\tilde{\mathbf{T}}(q,\tau)]_{11}$ element of $\tilde{\mathbf{T}}(q,\tau)$ matrix gives the theoretical expression for q and τ dependent autocorrelation function. We set the parameters of the model to bring the state of the system to the proximity of Hopf bifurcation and plot the scaled form of $[\tilde{\mathbf{T}}(q,\tau)]_{11}$ function in Fig. 6.12 defined as:

$$\tilde{\mathbf{T}}_s(q,\tau) = \tilde{\mathbf{T}}(q,\tau)/c_1^2 \tag{6.4.22}$$

[1] In addition to standard tables of Fourier transform pairs, I tried Mathematica software package in an attempt to find an analytical expression for the inverse Fourier transform of $[\tilde{\mathbf{G}}(q)]_{11}$.

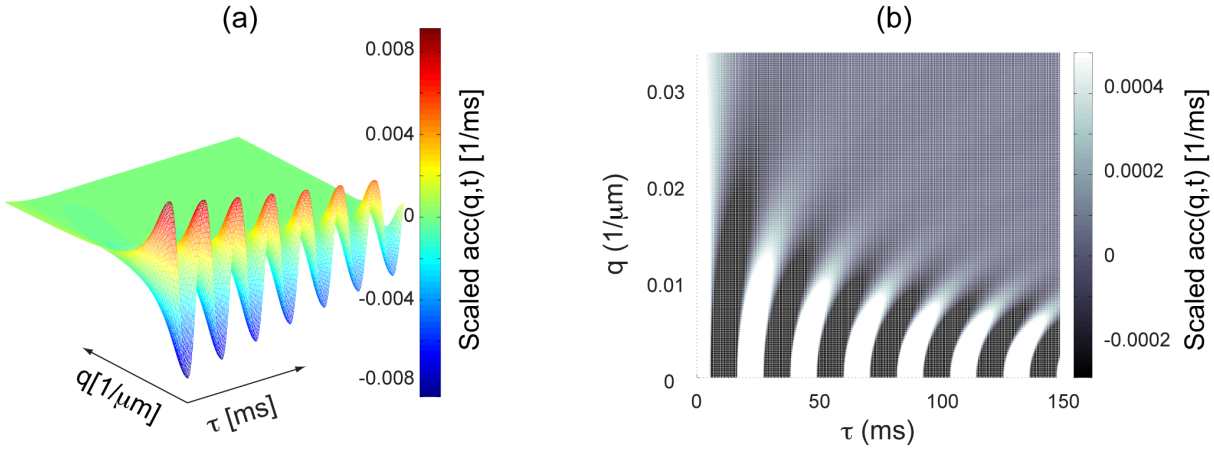

Figure 6.12: Theoretical τ and q dependent one-sided autocorrelation of E variable in linear regime, before emergence of Hopf instability. (a) The scaled autocorrelation of E variable as described by Eqs.(6.4.21), (6.4.22). Scaling is performed by dividing the autocorrelation values by noise intensity. Each temporal slice of this function is integrated over q-space to produce the temporal autocorrelation at the corresponding lag times. (b) Same scaled autocorrelation function plotted in 2-D. The vertical white stripe around $\tau = 0$ ms in this diagram shows considerable contributions of higher wave-numbers q for small τ values. The external excitatory input voltage is $P = 2.2416$ mV.

where c_1 is the amplitude of white noises introduced previously in Eqs. (6.4.2)[1]. The noise-induced oscillations in both τ and q domains are evident. To obtain numerical estimates for the theoretical temporal autocorrelation of the system at selected τ values, we integrate the $\tilde{\mathbf{T}}_s$ function along q dimension for selected τ values. More specifically we calculate the theoretical temporal autocorrelation at different τ values as:

$$\begin{aligned}
&\int_0^{q_{\max}} \tilde{\mathbf{T}}(q, \tau = 0)\, dq = \mathbf{C}(0), \\
&\int_0^{q_{\max}} \tilde{\mathbf{T}}(q, \tau = \tau_1)\, dq = \mathbf{C}(\tau_1), \\
&\int_0^{q_{\max}} \tilde{\mathbf{T}}(q, \tau = \tau_2)\, dq = \mathbf{C}(\tau_2), \\
&\vdots
\end{aligned} \tag{6.4.23}$$

to produce the temporal autocorrelation function $\mathbf{C}(\tau)$. Note that the theoretical temporal variance of the system can also be calculated: it is equal to the value of temporal autocorrelation at $\tau = 0$ ms as:

$$\mathrm{var}\{E\} = \mathbf{C}(0) \tag{6.4.24}$$

After introduction of the required theoretical tools to investigate spatiotemporal dynamics of the system, we are ready to perform a detailed examination of the WC model prior to its

[1]The c_1 coefficient is used for normalization since the $[\tilde{\mathbf{T}}(q, \tau)]$ is the autocorrelation of the E time-series. One can use c_2 to normalize the autocorrelation of the I time series.

bifurcation thresholds, both theoretically and numerically.

6.5 Spatiotemporal slowing down in noise-driven WC model

This section contains the theoretical and numerical examination of the 1D WC model prior to onset of different bifurcation types; we are looking for signs of critical slowing of fluctuations statistics. When the bifurcation type is Hopf or saddle-node, slowing down will be a temporal phenomenon captured by increased temporal variance, larger and wider temporal autocorrelations, and larger values of power spectral density at certain temporal frequencies. When there is a possibility of emergence of Turing pattern, the slowing down manifests as increased spatial variance, a larger and wider spatial autocorrelation function, and increased power spectral density at certain spatial frequencies. As we saw in the previous section, the 1D WC model is capable of producing mixed-mode oscillations in which the slowing down will be a spatiotemporal phenomenon. In the following sections I will use appropriate spatial and temporal measures (both theoretical and numerical) to examine network dynamics prior to four bifurcation classes that lead to state changes in the model.

6.5.1 Temporal dynamics prior to Hopf instability

The temporal autocorrelation function is a proper tool to study the temporal dynamics of the system prior to Hopf bifurcation. In Section 6.4.2, we discussed how one could compute the theoretical temporal autocorrelation of the WC model. We use the same integration method here to express the theoretical temporal autocorrelation, and normalize its value to make it independent of applied white-noise intensity as defined in Eq. (6.4.22). The q and τ dependent autocorrelation function was previously shown in Fig. 6.12. In order to make the theoretical predictions comparable with numerical results, we build a theoretical q vector based on spatial characteristics of 1-D network. By considering the properties of Fourier transform and keeping the Nyquist theorem in mind, one can determine the maximum spatial frequency q_{max} and the spacing in q domain Δq as

$$q_{\max} = \frac{\text{number of grid points}}{\text{length of network}} \tag{6.5.1}$$

or equivalently

$$q_{\max} = \frac{1}{\Delta x} \tag{6.5.2}$$

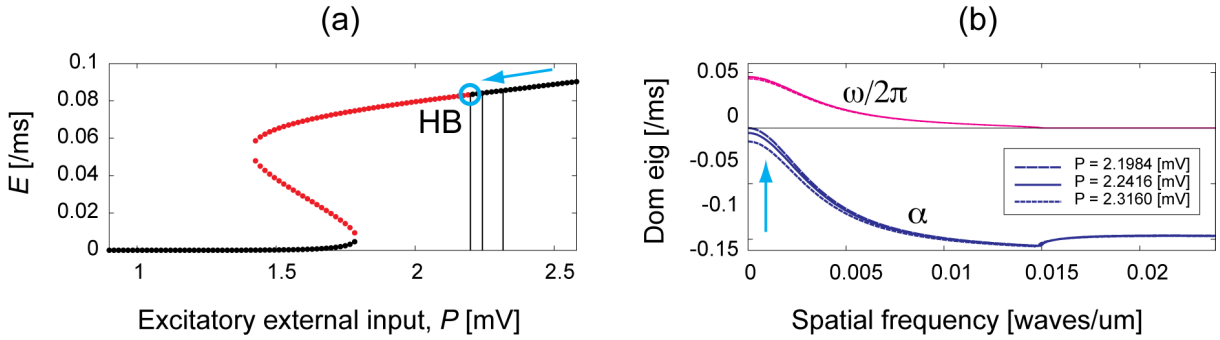

Figure 6.13: Demonstration of linear stability analysis of 1-D Wilson–Cowan model approaching Hopf instability. (a) Steady-state diagram of excitatory E variable as a function of excitatory external input P. The stable and unstable states are indicated by black and red color respectively. The Hopf bifurcation (HB) point is indicated by an open circle and the arrow expresses the approach to HB point by reducing the P value. The noise-induced dynamics of the system will be examined in three steady-state points as indicated by three vertical lines. See the legend of (b) for corresponding P values. (b) The dispersion curve of the system at three selected states close to HB threshold. For each P value the real part of dominant eigenvalue (α curves) and the scaled part of imaginary part ($\omega/2\pi$ curves) are plotted as a function of spatial frequency or wave number ($q/2\pi$). The upward arrow displays how steady state approaches the HB bifurcation.

where Δx is the spatial resolution of the 1-D network. The spacing in q domain is

$$\Delta q = \frac{1}{\text{length of network}} \tag{6.5.3}$$

By considering Fig.6.12(b) in which the colour map has been manipulated for display purposes[1], one can see the significant contributions from higher q values in the autocorrelation at small time lags.

The steady state distribution for the 1-D WC model is plotted again in Fig. 6.13(a) for convenience showing that the system undergoes Hopf bifurcation at $P_{\text{Hopf}} = 2.1971513755$ mV indicated by an open circle. We perform three experiments where the system's stable state is driven towards a Hopf bifurcation. This is accomplished by decreasing the excitatory exogenous input P down to P_{Hopf}. The three corresponding dispersion curves are plotted in Fig. 6.13(b) showing the approach to the Hopf instability. The frequency of temporal oscillations is theoretically predicted and displayed by the value of $\omega/2\pi$ curves at $q = 0$:

$$f \simeq 0.045 \times 1000 = 45 \text{ Hz} \tag{6.5.4}$$

Following the theoretical methods discussed in Section 6.4.2, the theoretical trend of temporal variance of E firing rates is extracted from the value of $\mathbf{T}(\tau)$ function at its origin[2]. Figure 6.14

[1] I manipulated the default colour map by shrinking it to a smaller range. This is helpful in terms of adding more details to the regions of the image with $q \geq 0.01$ 1/µm.

[2] The temporal variance can also be directly calculated from the value of $\tilde{\mathbf{G}}(q,\tau)_{11}$ function at the origin. Note that the spatial variance at $(q = 0, \tau = 0)$ will be equal to the temporal variance.

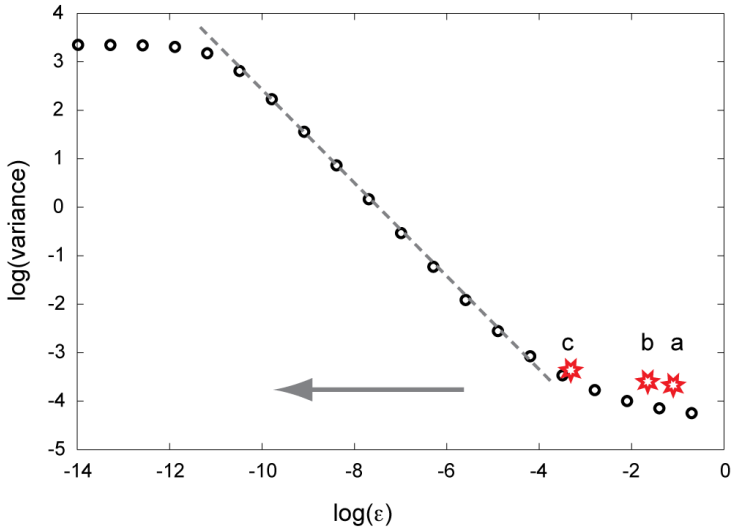

Figure 6.14: Theoretically predicted temporal variance of 1D WC model approaching Hopf instability. The theoretical variance is equal to the values of either $\tilde{\mathbf{G}}(q,\tau)_{11}$ or $\mathbf{C}(\tau)$ functions at their origin. The diagram shows the variances vs ϵ in a loglog graph where ϵ is a measure of distance from threshold of Hopf instability. The direction of approach to threshold is indicated by leftward arrow. As the system moves towards threshold, a dramatic increase in the variance of E time-series is observed. A line of slope -1 is superimposed on the graph indicating the slope of -1 for a middle range of ϵ values in agreement with the behaviour of homogeneous WC model studied in Chapter 5. The three points $a = (-0.9675, -3.5934), b = (-1.3946, 3.5686), c = (-3.2454, -3.3979)$ indicated by star symbols correspond to numerically obtained temporal variances whose detailed analysis is shown in Fig. 6.15.

displays the theoretical temporal variance in E fluctuations of the WC system with the arrow indicating the system's approach toward the threshold of Hopf instability. The variance is plotted as a function of ϵ, on a log-log graph; ϵ is a measure of the distance of control parameter (P) from Hopf threshold:

$$\epsilon_{\rm i} = \frac{P_{\rm i} - P_{\rm Hopf}}{P_{\rm Hopf}} \tag{6.5.5}$$

A line of slope -1 is superimposed on the theoretical trend showing a power-law growth for variance of white-noise-induced fluctuations prior to Hopf bifurcation. This is consistent with the asymptotic variance trend for the WC model of spatially-homogeneous cortical tissue (as shown in Chapter 5), and with the point-neuron model of a Wilson resonator studied in Steyn-Ross *et al.* [2006],

$$\mathrm{var}\{E\} \sim 1/\epsilon \tag{6.5.6}$$

We see power-law behaviour for $10^{-10} < \epsilon < 10^{-4}$. The saturated behaviour observed for $\epsilon < 10^{-10}$ is spurious and due to numerical limitations.

The result of numerical simulations of the 1D network are plotted in Fig. 6.15(a-c) as time-space graphs for the 1-D cortical rod. We see emergence of temporal oscillations as a vertical striped pattern whose contrast becomes amplified on approach to the Hopf point. See Appendix C.4 for a MATLAB code capable of reproducing Figs. 6.15(a-c).

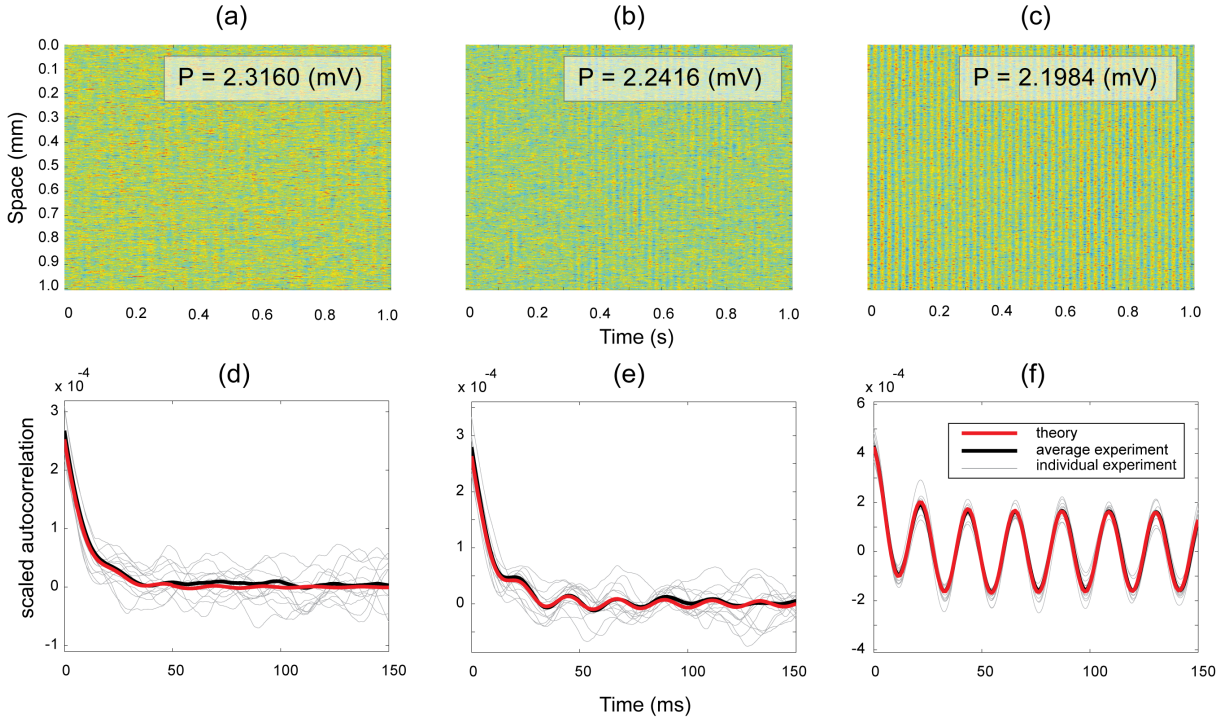

Figure 6.15: Growth of correlated fluctuations close to Hopf instability. (a-c) Time-space plots of E of 1-D WC model obtained using numerical simulation. A fixed-step Euler method ($\Delta t = 0.005$ ms) is used to numerically update the equations. The length of 1D network is $L = 1.005$ mm, with spatial resolution of $\Delta x = 1.5$ μm. By decreasing the external excitatory voltage P, the system is driven toward the threshold of Hopf bifurcation. In the vicinity of Hopf bifurcation, the white-noise induced perturbations result in temporal oscillation as evident by vertical striped pattern in the graphs. (d-f) The corresponding scaled theoretical and experimental temporal autocorrelation (tACC) functions. The scaled tACC is obtained by dividing tACC value by noise intensity. The theoretical tACC (red) is obtained using Eqs. (6.4.23). The experimental tACC is computed as the average of tACCs (thin grey traces) corresponding to 100 individual elements of the network evenly distributed along the cortical rod.

To extract the numerical autocorrelation trend, we calculate the normalized autocorrelation function of 670 grid points of the network using MATLAB's `xcorr` function (some are plotted as thin grey trends in Fig. 6.15 (d-e)), and report their average value as the corresponding experimental autocorrelation (thick black curve). We superimpose the theoretical temporal autocorrelation $\mathbf{C}(\tau)$ (thick red). Good agreement between the theoretical and experimental results is obtained for these pre-Hopf experiments. The approach to the Hopf threshold (from left to right in Fig. 6.15), is accompanied with an increase in the temporal variance as evident from the value of autocorrelation functions at $\tau = 0$ ms. However a significant increase in the amplitude of the side lobes of autoccorrelation function is observed prior to Hopf bifurcation as a sign of slowing down.

I found that extracting the experimental variance trend is very challenging for small ϵ values. This is because of the extreme sensitivity of the system to any perturbation (including the applied white noise, or the round-off error of numerical method), and the need for very small time steps to update the stochastic differential equations using a fixed-step Euler integrator.

6.5.2 Approaching saddle-node annihilation

The saddle-node bifurcation occurs when the stable bottom branch and unstable mid-branch steady states collide and annihilate at $P = 1.7892426576$ mV as shown in Fig. 6.16(a). Three dispersion curves with corresponding P values are plotted in Fig. 6.16(b). Increasing P shifts the α dispersion curve upward (indicated by vertical arrow), while it is always monotonic and negative. Note that the $\omega/2\pi$ curves are always equal to zero as expected of a stable node.

Numerical simulations of the stochastic equations using a fixed-step Euler integrator with $\Delta t = 0.1$ ms results in the time-space graphs displayed in Fig. 6.17(a-c). The length of 1D network is $L = 3000$ µm, with spatial resolution of $\Delta x = 1.5$ µm. A visual inspection of these numerical results reveals emergence of a dynamical pattern in the form of low frequency (asymptotically with zero frequency) fluctuations both in time and space; these become more strongly developed on close approach to the SN.

Some statistical measures can be used to quantify the pattern formation. We extract the spatial autocorrelations of excitatory firing rate of entire 1-D rod at 2000 selected instants (evenly spread between 0 and 10 s) and report their average value as the experimental spatial autocorrelation of the network. The theoretical spatial autocorrelation is calculated using the inverse Fourier transform of $\mathbf{G}(q)_{11}$ function. The results are plotted as one-sided spatial autocorrelations in Fig. 6.17(d-f).

The theoretical (red) and experimental autocorrelations are in good agreement, with both exhibiting fast and slow decay rates. The approach to SN (d to f) is accompanied with a significant increase in the slow decay times of the system. A slight increase in the variance of the system (equal to the value of autocorrelation function at the origin) is also evident. A significant increase would be expected in the very near vicinity of the threshold. However, such experiments are very challenging due to the need for very long numerical simulations.

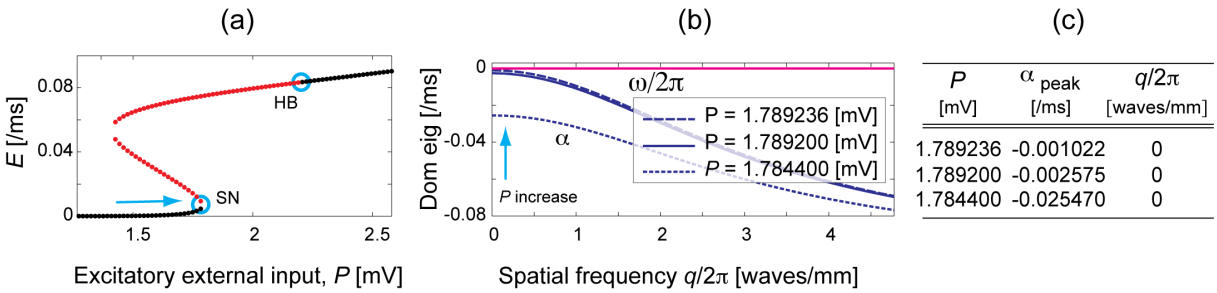

Figure 6.16: Linear stability analysis of 1-D Wilson–Cowan model approaching a saddle-node (SN) annihilation. (a) The steady state diagram is plotted again here with the arrow indicating the approach toward SN. (b) The dispersion curves of three steady-state points corresponding to three different P values. The real part of dominant eigenvalue α (blue) is always negative indicating a stable point, while the scaled imaginary part $\omega/2\pi$ (red) is always zero, characteristic of a stable node. By increasing P the α curves moves upward approaching the threshold of saddle-node instability. (c) The selected P voltages and corresponding α values indicating approach to SN threshold.

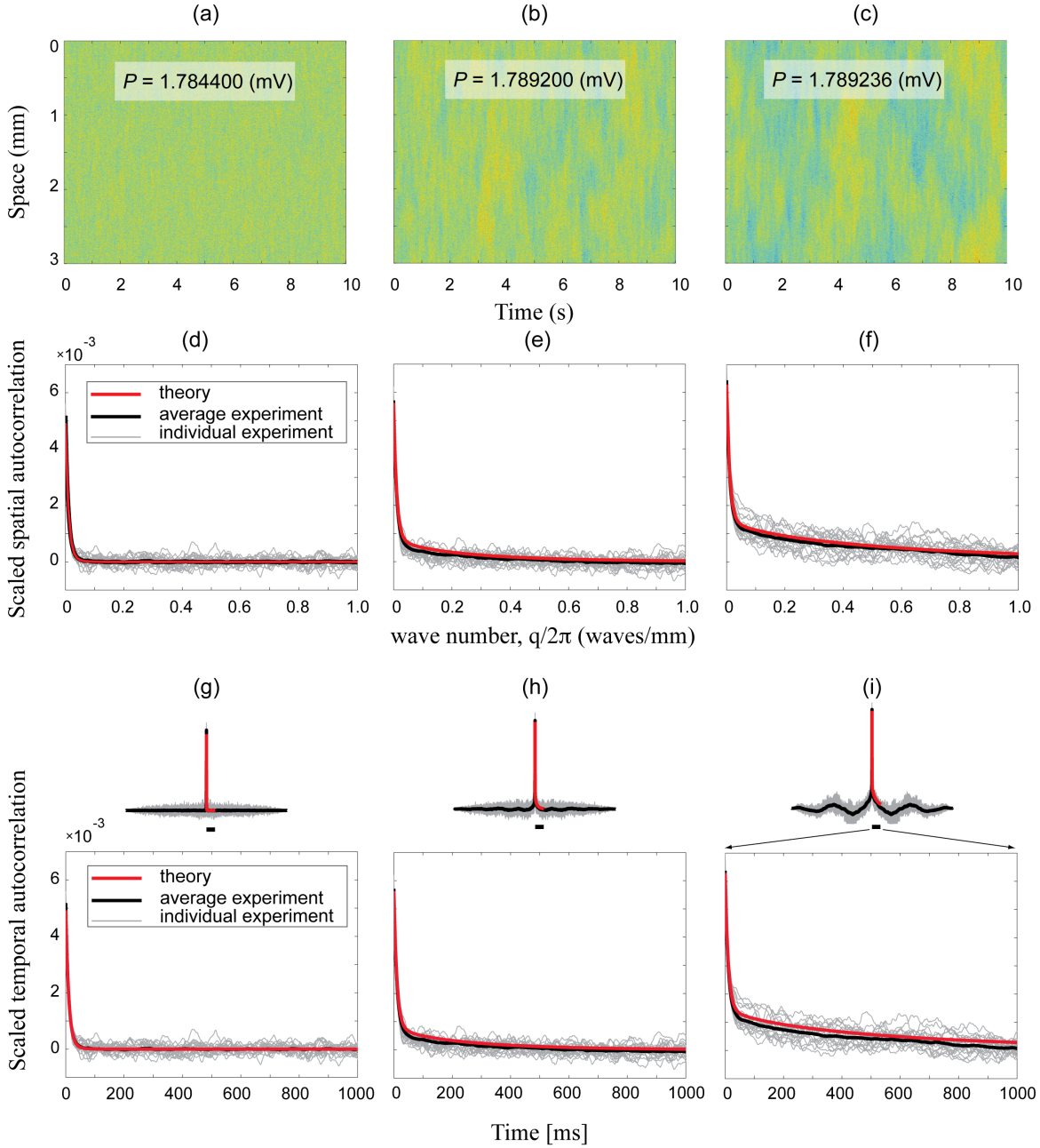

Figure 6.17: Slowing down in space and time in a 1-D Wilson–Cowan model prior to saddle-node annihilation. (a–c) The numerically obtained space-time diagram of the model approaching the threshold of saddle-node (SN) annihilation which happens at $P \simeq 1.7892426576$ mV (see Fig. 6.3). By approaching the SN, a spatiotemporal low frequency pattern emerges due to continuously applied white noises to elements of the network. A fixed-step Euler method with time steps of $\Delta t = 0.1$ ms is used to numerically update the model equations. (d–f) The experimental (black) and theoretical (red) spatial autocorrelations of E variable corresponding to experiments (a–c). The experimental curve is extracted as the average of 2000 individual spatial autocorrelations of entire 1-D network, captured in evenly distributed instants from $t = 0$ to $t = 10$ s. Some of these individual autocorrelations are superimposed in the figures (thin grey traces). The theoretical autocorrelation is extracted based on the inverse Fourier transform of $[\tilde{\mathbf{G}}(q)]_{11}$ function as described by Eq. (6.4.14). (g-i) The corresponding experimental (black) and theoretical (red) temporal autocorrelations. The experimental autocorrelation is the average of temporal autocorrelations obtained from 300 elements evenly distributed on the length of the cortical rod. I used the approach described in Section 6.4.2 to obtain the theoretical temporal autocorrelations. The temporal autocorrelations are displayed in two scales for each case. (The autocorrelations have been normalized by the intensity of applied white noise.)

The corresponding experimental and theoretical temporal autocorrelations are also displayed in Fig. 6.17(g-i) with two scales for each case. Driving the system towards the SN threshold (as moving from left to right panels in the figure) results in widening of the autocorrelation, appearance of side lobes and a slight increase in the autocorrelation amplitude in the origin. One should note the agreement between theoretical predictions and numerical results for the temporal autocorrelation. Considering the fact that the amplitude of both temporal and spatial autocorrelations at the origin are equal to the variance of the system, an excellent agreement has been achieved between the middle and bottom panels in the figure in terms of the variance value.

6.5.3 Approaching Turing threshold

We performed a series of experiments on the 1-D WC model while driving the system toward the threshold of spatial instability induced by formation of a Turing pattern. We set the excitatory stimulus voltage to a fixed value of $P = 1.74$ mV as indicated by star symbol on the steady state digram in Fig. 6.18(a). This choice of P sets the elements of the network on the stable part of the top branch where the type of steady state is stable focus. The dispersion curves of the system for different inhibitory space constant values $\sigma_{EI,IE}$ are plotted in Fig. 6.18(b). The α curve has a peak in $q \neq 0$ with a negative value, indicative of proximity to a Turing bifurcation. We drive the system toward the threshold by increasing the $\sigma_{EI,IE}$ values. See table in Fig. 6.18(c) for values of the parameters; the last column of the table displays the expected spatial frequency of the waves. Comparing the values at the two peaks of the α curves, one notices that between Hopf and Turing instabilities, the Turing is expected to be dominant.

I performed a series of three experiments corresponding to three selected $\sigma_{EI,IE}$ values as shown in Fig. 6.18(c). The results are displayed in Fig. 6.19(a-c). See Appendix C.4 for

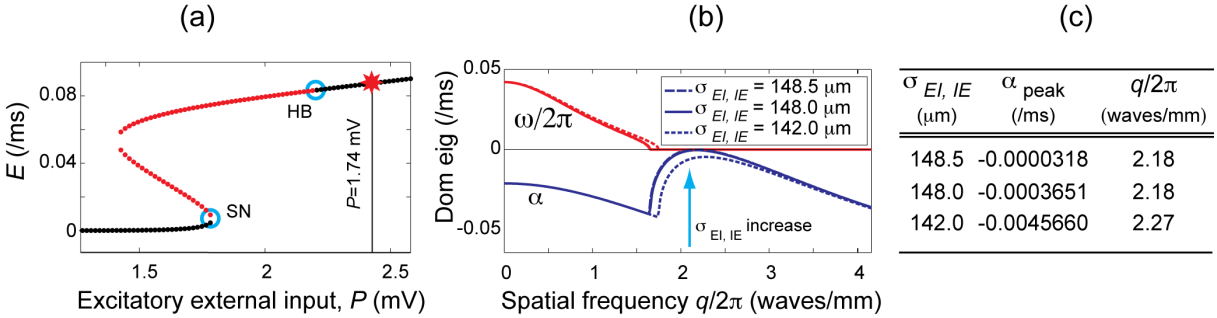

σ EI, IE (μm)	α peak (/ms)	q/2π (waves/mm)
148.5	-0.0000318	2.18
148.0	-0.0003651	2.18
142.0	-0.0045660	2.27

Figure 6.18: Demonstration of approach to Turing instability in 1-D Wilson–Cowan model. (a) Steady-state diagram of the model is plotted again for convenience. We set $P = 1.74$ mV to fix the state of the system at the stable values $E = 0.078$, $I = 0.082$ $(\text{ms})^{-1}$. (b) The dispersion curves of the system showing the real part α (blue) and scaled imaginary part $\omega/2\pi$ (red) of dominant eigenvalue of the system at $P = 1.74$ mV. By increasing the inhibitory space constants $\sigma_{EI,IE}$ as indicated by upward arrow, the peak of α curve approaches zero at $q \neq 0$. (c) The values of inhibitory space constants and the resultant peak values of dominant eigenvalue with corresponding wave numbers.

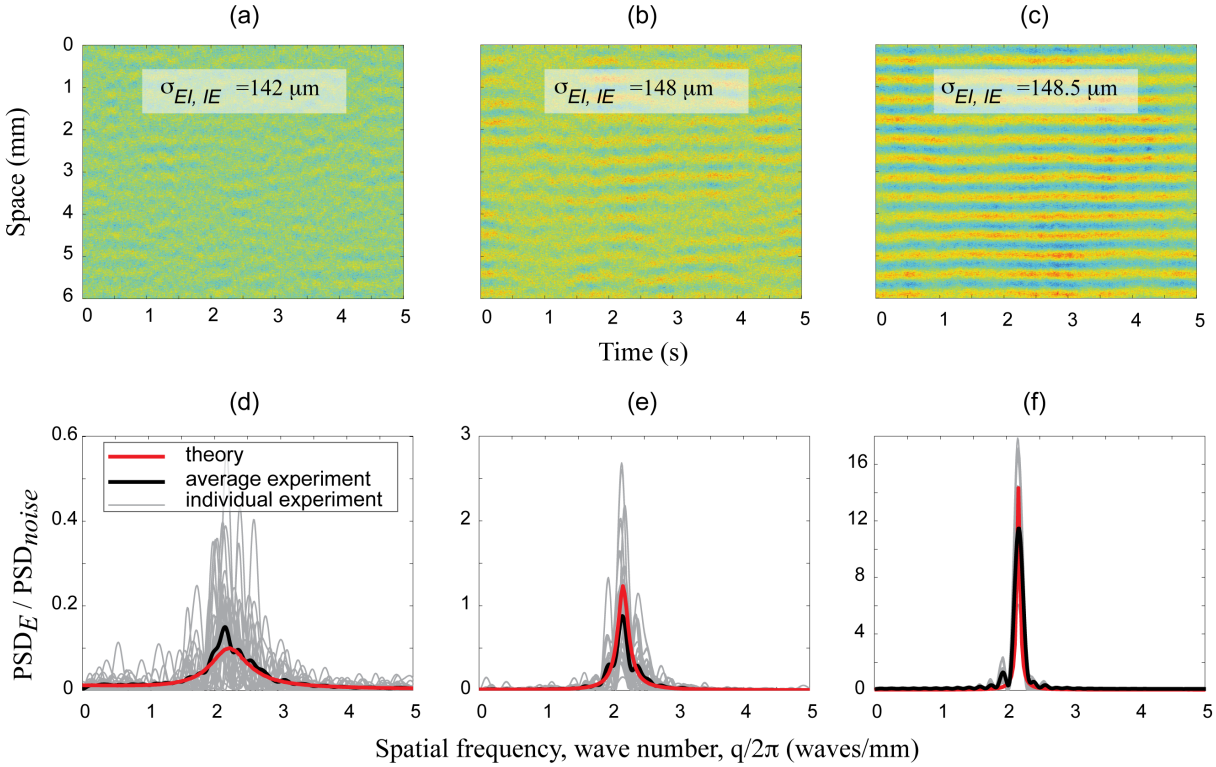

Figure 6.19: Theoretical and numerical demonstration of critical growth of spatial fluctuations prior to Turing instability in 1-D Wilson–Cowan model. (a–c) Spatiotemporal evolution of E variable of 1-D network on approach to Turing instability. The 1-D rod is set to a stable steady state as demonstrated in Fig. 6.18(a). Although the system is in a stable state, the proximity to spatial threshold of instability (see Fig. 6.18(b)) is responsible for emergence of white-noise induced spatial oscillations. A fixed-step Euler integrator with time steps of $\Delta t = 0.005$ ms is used for numerical simulation. The spatial spectral analysis of 1-D network approaching Turing instability is displayed in (d–f). The scaled average experimental spectrum (black) is obtained through averaging the spatial spectrum of 1-D network at 10000 distinct instants (some shown in thin grey). The scaled theoretical spatial spectrum (red) is superimposed on the graphs for comparison.

MATLAB implementation of numerical simulation. The spatial oscillations are evident as horizontal stripped patterns which strengthen with increasing $\sigma_{EI,IE}$. To quantify observed spatial dynamics, we extracted the spatial power spectral density; see Fig. 6.19(d-f). The theoretical PSD (red) is computed using $[\tilde{\mathbf{G}}(q)]_{11}$ function. The experimental PSD (black) is obtained via averaging individual spatial PSDs (thin grey). The individual PSD's are calculated from the E values of entire 1D network at 10000 instants evenly distributed between $t = 0$ and $t = 5$ s.

Very good agreement between theoretical and experimental PSDs is observed in these results. We note that the approach to the threshold of Turing instability is accompanied by significant increases in the peak value of spatial PSDs.

6.5.4 Approaching Turing-Hopf interaction instability

Here I inspect the behaviour of the 1-D WC network near emergence of mixed-mode Turing-Hopf instabilities. The parameter values of the system (except P and $\sigma_{EI,IE}$) are displayed in Table 6.1. In order to set the system near mixed-mode instability, the state of the system should

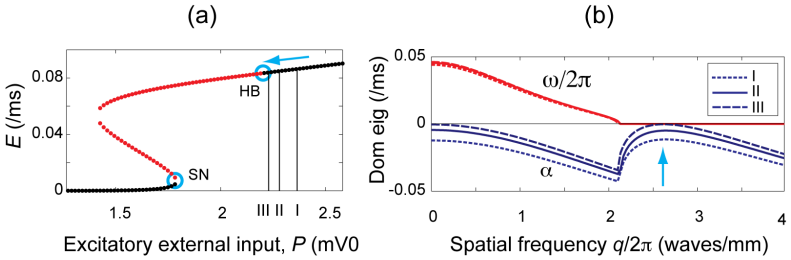

	P (mV)	σ EI, IE (μm)	α peak (/ms)	q/2π (waves/mm)	ω/2π (kHz)
I	2.3172	122.00	-0.0115	2.6420	44.02
II	2.2416	119.50	-0.0049	2.6420	45.45
III	2.2008	119.10	-0.0002	2.6100	46.08

Figure 6.20: Linear stability analysis of 1-D Wilson–Cowan model approaching mixed-mode Turing-Hopf instability. (a) Steady-state diagram of the system is plotted again for convenience, displaying three (I to III) settings for P to drive the state of the system toward Hopf bifurcation at $P = 2.1971513755$ mV. (b) Dispersion curves at three different parameter settings. By changing the inhibitory space constants σ_{EI}, σ_{IE} the system is kept in the proximity of Turing instability as well. The blue curves are the real part of the dominant eigenvalue α of steady state E; the red curves are the imaginary part ω of the same dominant eigenvalue divided by 2π. Frequency of the spatial Turing oscillations are predicted by the value of x axis at local maximum of α curves. Temporal Hopf frequency is predicted by the value of $\omega/2\pi$ curve at origin. (c) The values of two bifurcation parameters (P and $\sigma_{EI,IE}$) used to drive the system toward the threshold of Hopf-Turing instability. The two last columns show the spatial and temporal frequency of oscillations.

approach simultaneously both Hopf and Turing instability thresholds. Excitatory external input (P) can be adjusted to push the system towards Hopf bifurcation. We select three P values (indicated by $I - III$ in Fig. 6.20(a)) to move toward the Hopf threshold. For each P value, we adjust the $\sigma_{EI,\ IE}$ parameter in order to simultaneously move the system toward Turing instability. See the resultant dispersion curves and the value of parameters in Fig. 6.20(b, c). The dispersion curves indicate the temporal and spatial frequency of noise-induced subthreshold oscillations of the system. These frequencies are displayed as two last columns of the table in Fig. 6.20(c).

We performed a series of three numerical simulations corresponding to the parameter settings shown in Fig. 6.20(c). The results are displayed as time-space plots in Fig. 6.21(a-c): we see emergence of spatiotemporal patterns in response to white-noise stimulation. This pattern is composed of mixed vertical and horizontal stripes as a result of proximity to Hopf and Turing bifurcations respectively.

An analysis of spatial characteristics of the network is performed and the results are displayed as the normalized spatial power spectral density (sPSD) plots in Fig. 6.21(d-f). The normalized theoretical sPSD is calculated using the corresponding $[\tilde{\mathbf{G}}(q)]_{11}$ function, and is plotted in red showing two peaks at $q = 0$ and $q = 2.642, 2.642, 2.6100$ waves/mm for three experiments. We calculated the spatial PSD of the numerically simulated 1D network at 10000 individual instants (evenly distributed between $t = 0$ and $t = 0.5$ s) and normalize them by the spatial PSD of applied white noise. Some of individual PSDs are displayed as thin grey trends. The average of all individual PSDs is plotted as thick black trend showing a reasonable agreement with theoretical predictions. A significant increase in the spatial PSD is observed as the system is driven toward the instability threshold.

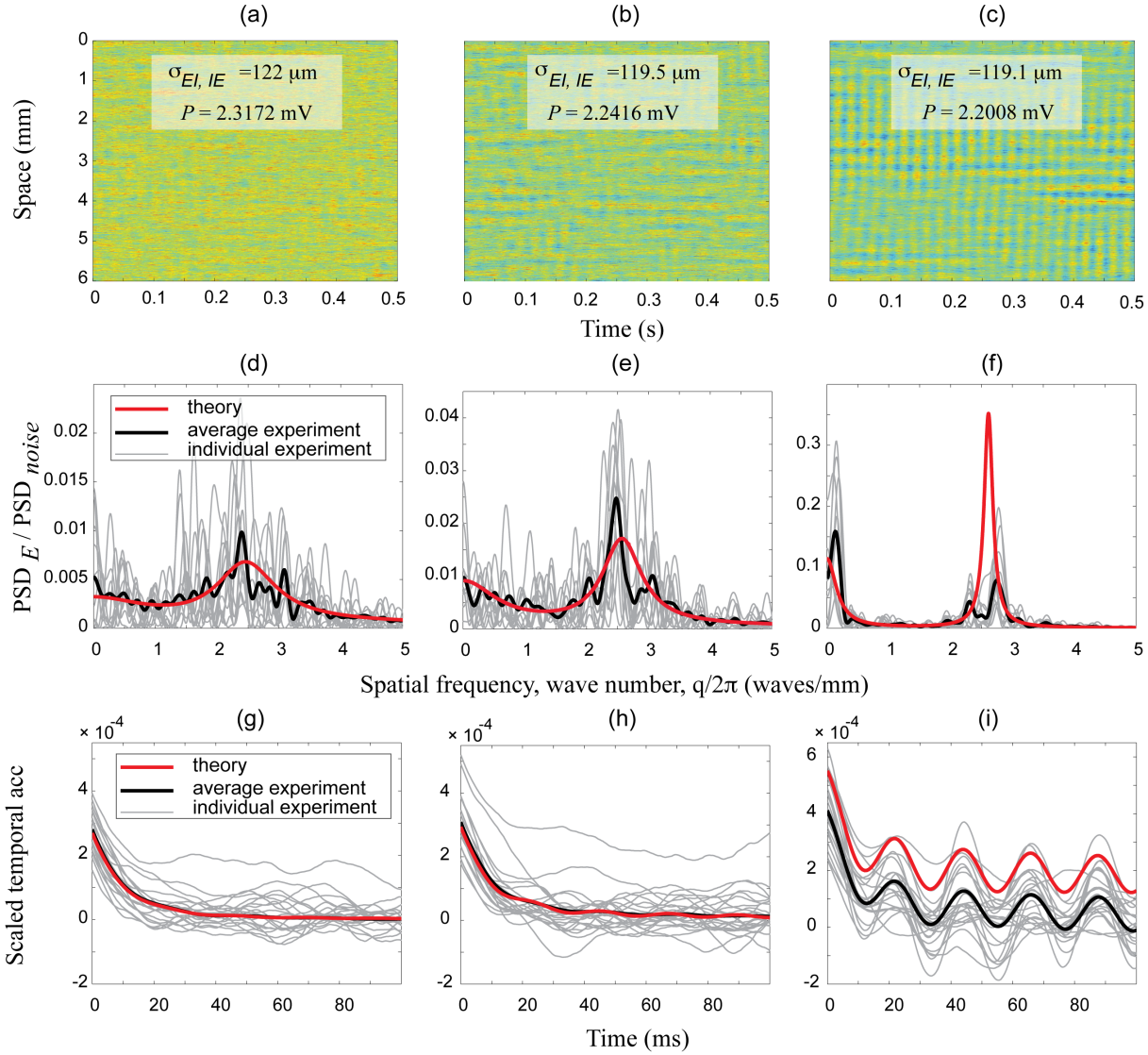

Figure 6.21: (a-c) Colour-coded plots of spatiotemporal evolution of the 1-D WC network. The white-noise induced oscillations in time and space emerge by approaching threshold of mixed-mode instability. A fixed-step Euler method ($\Delta t = 0.005$ ms) is used to numerically solve the stochastic differential equations of the network with domain length of $L = 6$ mm and spatial resolution of $\Delta x = 1.5$ μm. (d-f) Normalized spatial power spectral density (PSD). The average PSD (black) is extracted by averaging individual spatial PSD curves corresponding to 10000 distinct instants captured at every 0.05 ms (some are shown in thin grey). The scaled theoretical spatial spectrum (red) is superimposed on the graphs for comparison. (g-i) The scaled temporal autocorrelation functions. The theoretical trend (red) calculated using Eqs. (6.4.23) and scaled by the intensity of applied white noise. The individual experimental autocorrelations (some of them displayed as thin grey trends) obtained from related time-series of 400 individual elements of the network evenly distributed along the 1-D network. Scaled experimental temporal autocorrelation (black) is the average of 400 individual scaled experimental autocorrelations.

We perform a temporal investigation of the system by calculating the theoretical and experimental temporal autocorrelation (tACC) functions. The results are displayed in Fig. 6.21(g-i), showing the scaled theoretical and experimental tACCs in red and black respectively. The theoretical tACCs are computed using an approach described by Eqs. (6.4.23) and the experimental tACCs are computed as the average of numerically obtained time series of 400 individual excitatory neural elements evenly distributed along the entire 1D rod.

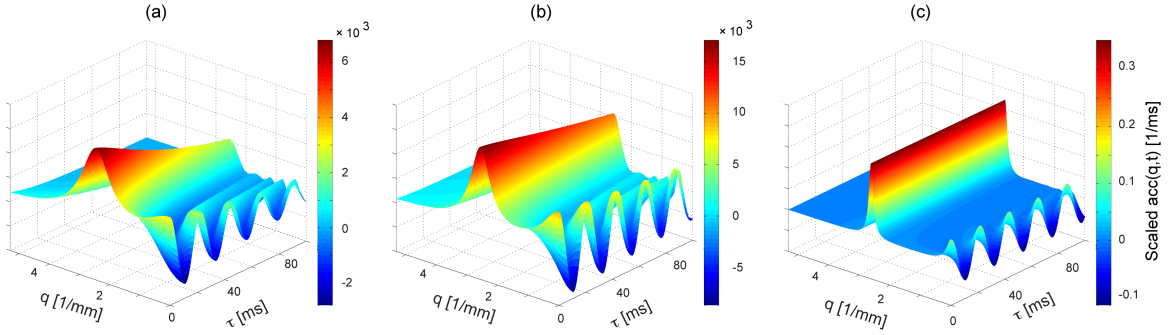

Figure 6.22: The normalized steady-state q and τ dependent autocorrelation of E variable $\tilde{\mathbf{T}}_{\mathbf{s}}(q,\tau)$ as described by Eq. (6.4.21). (a-c) The $\tilde{\mathbf{T}}_{\mathbf{s}}(q,\tau)$ function as the 1-D WC system approaches the threshold of Hopf-Turing instability, corresponding to three experiments displayed in Figs. 6.20 and 6.21. The Turing instability induces a regional increase of correlation function at $q \simeq 2.6$ waves/μm, while the Hopf instability induces an oscillatory behavior at small q values. The interaction of Turing and Hopf instabilities is evident in all diagrams.

A significant increase in the amplitude of side-lobes of tACC functions is evident while approaching the threshold of mixed-mode instability (from (g) to (i)). The emerged temporal frequency in (i) is in agreement with the one stated in Fig. 6.20(c) for experiment III. Figures (d) to (i) show a reasonable agreement between theoretical and experimental results, namely in terms of the values of spatial or temporal frequencies. However a discrepancy between the results is observed in Fig. 6.21(f, i) where the state is very close to the threshold of mixed-mode oscillations. Although the observed mismatch can be improved by increasing the size of cortical rod and the duration of simulation, one should not expect to eliminate the discrepancy completely. This is because the linear OU theory cannot expect to capture the nonlinear interactions between Hopf and Turing instabilities.

A plot of the corresponding $\tilde{\mathbf{T}}(q,t)$ autocorrelation functions as described by Eq. (6.4.21) is displayed in Fig. 6.22. One can observe the interaction of Turing and Hopf instabilities in these graphs. The slowing down phenomena are also observable in these graphs as indicated by very weak decays of Turing-induced regional peak at $q \simeq 2.6$ waves/mm and Hopf-generated oscillatory region for small q values.

6.6 Chapter summary

By introducing a spatial dimension, the Wilson-Cowan model of spatially homogeneous neural mass model was extended to a one-dimensional neural mass model in this chapter. The coupling strengths between E and I are no longer constants, but are now a decaying functions of distance between populations. Inclusion of space introduces excitatory and inhibitory fluxes as new variables to the system. We demonstrated that the fluxes obey the diffusion equations, giving a rich dynamics to the system. The analysis of the system started with determination of the homogeneous steady-states; these describe the time-and-space-independent response of

the system. The resulting steady-state diagram was slightly different from the one obtained for homogeneous model in previous chapter. The dissimilarity was due to some modifications in the value of model parameters (namely external excitatory voltage P and maximum inhibitory synaptic coupling strength b_{EI}, b_{IE}). These changes were needed in order to allow the possibility of spatial instabilities.

The steady-state analysis revealed two temporal bifurcations of the system: saddle-node (SN) and Hopf (HB) bifurcations. Using linear stability analysis we derived the q-dependent stability matrix of the linearized system. The behaviour of q-dependent dominant eigenvalues of the stability matrix is displayed by dispersion curves, predicting spatial behaviour of the system for different wave numbers. The possibility of Turing and mixed-mode Turing–Hopf instabilities was demonstrated. In the next step the zero-mean infinite-variance white-noise fluctuations were added to the E and I populations. The inclusion of white-noise transformed the model equations to stochastic differential equations. We presented the Ornstein-Uhlenbeck (OU) form of the stochastic model. Formal stochastic methods for the OU process were employed to derive analytical forms of some temporal and spectral characteristics of the Wilson–Cowan model, namely the variance, autocorrelation and power spectral density functions in time and space domains.

At this stage I was ready to pursue the main aim of the chapter; viz, looking for spatial and temporal evidence of critical slowing down prior to different bifurcation types in the Wilson–Cowan cortical rod. Four individual experiments were designed and carried out in which the system was driven towards one of the four possible bifurcations: Hopf, saddle-node, Turing, and Turing–Hopf. The dynamical behaviour of the system was investigated based on:

- spatial and temporal analysis of numerically obtained system responses
- theoretical predictions regarding behaviour of the system

while approaching the bifurcation points. Supported by the results of both approaches, we found clear symptoms of critical slowing down in time and space domains. More specifically we found that the variance, autocorrelation and power spectral density of E fluctuations grow in time and/or space before occurrence of phase transitions. These results are in good agreement with previously reported experimental and theoretical signs of critical slowing down in different biological, environmental and financial systems. This work shows that how the rich dynamics of Wilson–Cowan model of cortical rod provides a unique platform to investigate the subthreshold dynamics prior to distinct classes of bifurcations.

The theoretical and modelling investigations of this thesis is terminated here. Based on this theoretical background, I now describe how I attempted to observe experimental signs of critical

slowing down in slices of neural tissue extracted from cortical and hippocampal regions of mouse brain.

Chapter 7

Neural Dynamics in Mouse Brain Slices

A detailed study of neural models across different scales was presented in previous chapters of this thesis with an emphasis on the instabilities underlying state transitions. Using mathematical models I examined the subthreshold behaviour of neural systems prior to bifurcation points, where a sudden qualitative change of dynamical behaviour can occur.

Modelling results showed critical slowing down in the response to small perturbations, meaning that it takes increasingly longer for the system to recover its steady state. This increased sensitivity is manifest as increased fluctuation variance and correlation time, with increased fluctuation power at certain frequencies.

Ideally such theoretical predictions should be validated by relevant neurobiological experiments. This chapter demonstrates a series of *in vitro* experiments designed to seek empirical evidence for slowing-down phenomena prior to an impending state transitions.

The highly challenging nature of capturing early warning signals in real physical systems is consistent with the very small number of research reports in this field. Most of the empirical work has been done on lake ecology [Carpenter *et al.*, 2011], climate systems [Dakos *et al.*, 2008], social and financial transformations [Richter and Dakos, 2014], and recently on interconnected yeast populations [Dai *et al.*, 2013], dielectric fluids [Zhang and Zahn, 2014], cancer studies [Korolev *et al.*, 2014], percolation systems [Chen *et al.*, 2014], and human depression [van de Leemput *et al.*, 2014]. To my knowledge, only one study[1] has reported slowing down as an early warning signal before qualitative transitions in biological neural systems, in spite of its potential significance.

This chapter describes some experimental procedures employed to study subthreshold dynamical behaviour of cortical and hippocampal mouse brain slices prior to seizure initiation. Some successful observations of early warning signs prior to seizure onset are reported. At the end of the chapter a *neural probing* experiment is presented in which signs of critical slowing are captured using an active stimulation-based method.

[1] Wilson *et al.* [2008] looked at critical slowing down on leadup to an up state in slow-wave oscillations, *in vivo*.

7.1 Zero-Magnesium seizure-like events, an *in vitro* model of epileptic seizure

My motivation in studying epileptic seizures comes from the fact that epileptic seizures

- are one of the most common pathological transformers of normal neural activity, and
- represent a neurological phase transition.

The possibility of seizure prediction is of significance both for neuroscientists and for people suffering from epilepsy. In this chapter I study zero-Magnesium (zero-Mg) seizure-like events (SLEs) in cortico-hippocampal slices of the mouse brain in search of signs of seizure precursor.

The SLEs generated in slices of brain tissue have been used as an *in vitro* model of human seizure for a long time [Anderson *et al.*, 1986; Swartzwelder *et al.*, 1988; Tsau *et al.*, 1998]. Although *in vitro* models of epilepsy cannot exhibit motor and behavioural responses during seizure, a considerable advantage is that the temperature and constituents of the extracellular environment can be precisely controlled in these models in contrast to the *in vivo* case. SLEs can be induced by various pharmacological manipulations of the neural tissue. A common method is to remove the Mg^{2+} ions from the artificial cerebrospinal fluid (aCSF) used to keep the tissue alive *in vitro*. Elimination of extracellular Mg^{2+} activates excitatory N-methyl-D-aspartate (NMDA) ion channels. This results in a higher propensity for the tissue to produce recurrent excitatory currents which can result in the generation of SLEs. Another excitatory agent is carbachol[1] which activates muscarinic acetylcholine receptors and, via a G-protein-coupled mechanism, blocks potassium channels. This causes cell depolarization and excitation. I used a 100 mM solution of carbachol in most of my experiments to further promote seizure activity in brain slices which are already perfused with zero-Mg solution.

SLEs can be generated in both hippocampal and cortical tissue. Although many *in vitro* epileptogenesis studies are conducted on hippocampal SLEs[2], cortical SLEs have been investigated in Electrophysiology Laboratory of University of Waikatofrom 2009 [Voss *et al.*, 2009, 2010; Jacobson *et al.*, 2010; Voss *et al.*, 2012, 2013, 2014].

One main difference between cortical and hippocampal tissue is that the hippocampus can generate very long seizure-like events compared to the cortex (lasting for minutes rather than seconds). This may be due to the special structural arrangement of the excitatory and inhibitory neurons within the hippocampus [Traub and Miles, 1991; Andersen *et al.*, 2006]. These hippocampal structures are composed of recurrent neural networks which produce longer and larger SLEs with greater morphological complexity.

[1] Carbachol binds and activates the acetylcholine receptor. This drug can be used to alter the excitation level of the cortical tissue [Voss *et al.*, 2012].

[2] It is believed that the majority of partial seizures originate in hippocampus [Löscher, 1997].

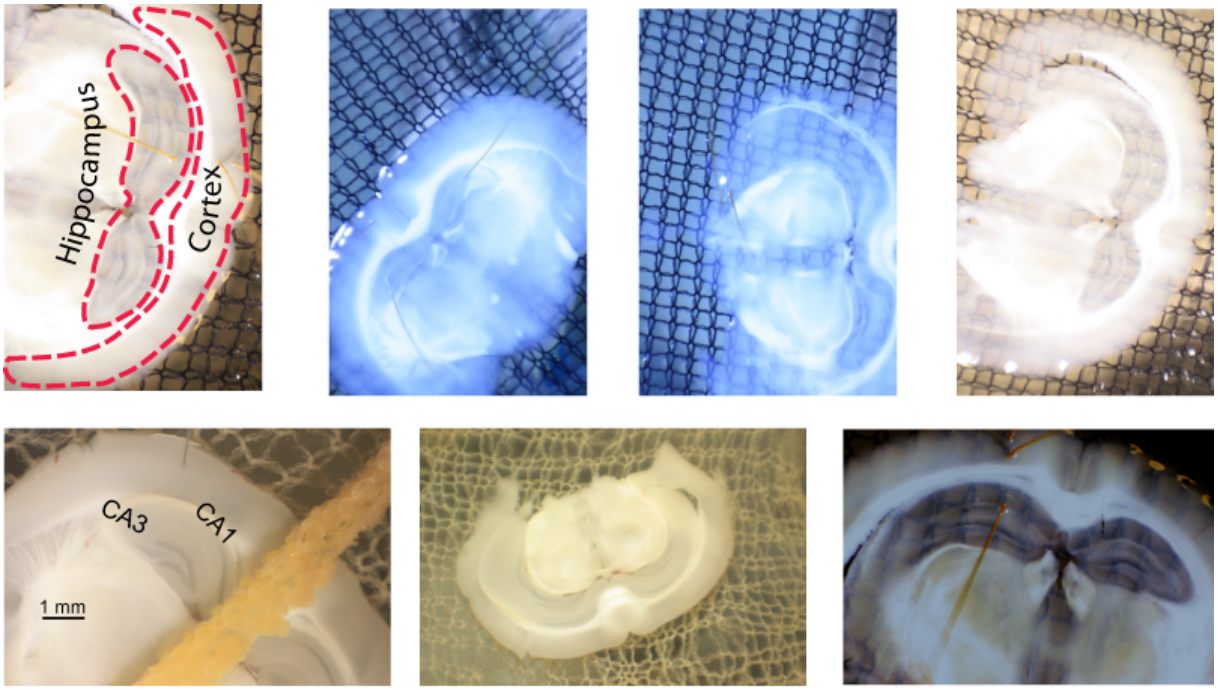

Figure 7.1: Coronal mouse brain slices containing both cortical and hippocampal parts. See Section 7.2.1 for details of slice preparation.

Most hippocampal SLE experiments are carried out on *rat* hippocampal slices after extraction and isolation of the hippocampus and preparation of 400-µm slices [Andersen *et al.*, 1980; Whittington *et al.*, 1995]. Although it is possible to prepare *mouse* hippocampal slices using similar methods, due to its smaller size, the tissue is more easily damaged during the preparation process.

To overcome the size and fragility issues in hippocampal extraction and slice preparation from the mouse brain, an alternative method is employed in this thesis. Examination of coronal cortical slices shows that occipital slices (belonging to the occipital lobe of the brain, which lies underneath the occipital bone) contain hippocampal regions. Figure 7.1 displays sample coronal slices that contain both cortical and hippocampal parts. Using these slices makes it possible to record simultaneous cortical and hippocampal SLEs from mouse brain slices without the need for isolation of the hippocampus.

7.2 Methods

This section describes the methods employed in these experiments. Some modifications to the standard methods for acquiring local field potential (LFP) activity were needed in order to capture signs of slowing down. These included

- careful optimisation of electrode configurations and grounding systems. As a result, the need for notch and high-pass filtering was eliminated, giving the possibility of DC mode

recording. This resulted in LFP signals containing DC and very low frequency components, thought most likely to contain the critical slowing down (CSD) signatures;

- very slow changes in the composition of aCSF. This slow modulation of aCSF was found to be essential in order to approach gradually the brink of seizure generation, which is crossed too abruptly if the increment in the seizure-inducing (or bifurcation control) parameter is uncontrolled.

I also performed simultaneous hippocampal and cortical recordings from which it became clear that stronger and more developed SLEs could be recorded from the hippocampus, compared to the cortex, thus increasing the likelihood of capturing signs of slowing-down. The details of slice preparation are discussed in the following section, then the electrical recording protocol is presented.

7.2.1 Animal and slice preparation

Standard solutions are prepared according to Nowak and Bullier [1996] and Voss *et al.* [2013] as needed, and are discarded after five days. These solutions are similar to the cerebrospinal fluid and keep the slices in a functioning condition for hours. They also act as a medium for delivering different drugs to the tissue. There are three standard solutions:

- Brain extract
- Normal artificial cerebrospinal fluid (aCSF)
- Zero-Mg aCSF

See Table 7.1 for the composition of the fluids. All fluids were bubbled with a mixture of 5% carbon dioxide and 95% oxygen gas (*carbogen*) for at least 20 min before use. The oxygen is needed for cell metabolism and the carbon dioxide buffers the pH of the solution.

After obtaining approval from the Waikato Animal Ethics Committee, 35 wild-type mice, 15–45 days old were used for the study regardless of their sex. A deep level of CO_2 anaesthesia was induced in the animal via delivery of carbon dioxide for 10 s. The responsiveness of animal was examined using the paw-pinch test. When irresponsive, decapitation was performed quickly, and the whole brain (excluding the brainstem) extracted in 3–4 minutes.

The extracted brain was transferred directly to ice-cooled brain-extract solution. Using a razor blade, the frontal and some part of occipital regions of the brain were cut away, and the brain glued to the base of the vibratome, which is used for slicing the brain tissue. The fixed brain was transferred to the holder of the vibratome containing ice-cooled carbogenated brain-extract solution. About 6–10 coronal slices of width 400 µm were cut from the brain and transferred directly to the holding chamber as shown in Fig. 7.2(a).

Table 7.1: Composition of the biological fluids used in different stages of slice preparation and maintenance in zero-Mg *in vitro* experiments. The displayed amounts of chemical component should be dissolved individually in 1 litre of distilled water to obtain the desired concentrations.

	Brain extract		Normal aCSF		zero-Mg aCSF	
Chemical compound	Concentration [mM]	Mass [g]	Concentration [mM]	Mass [g]	Concentration [mM]	Mass [g]
NaCl	92.7	5.42	125	7.31	124	7.25
KCl	3	0.22	2.5	0.19	5	0.37
$MgCl_2$	19	1.8	1	0.1	0.0	0.0
$CaCl_2$	0.0	0.0	2	0.22	2	0.22
NaH_2PO_4	1.2	0.14	1.25	0.15	1.25	0.15
$NaHCO_3$	24	2.02	26	2.18	26	2.18
Glucose	25	4.5	10	1.8	10	1.8

The holding chamber contained continuously carbogenated normal aCSF, or zero-Mg aCSF, depending on the type of the experiment. The slices are rested for at least an hour in the chamber to recover from trauma of the brain extraction and slicing. The composition of the holding fluid keeps the slices alive for several hours[1]. At this stage the slices are ready to be transferred to the recording chamber which also contains either continuously carbogenated normal or zero-Mg aCSF solution.

Figure 7.2(b, c) shows an individual slice resting on a nylon mesh in the recording chamber with the electrodes inserted in the cortical region. The recording is performed while the slice is either slightly immersed in the aCSF fluid, or kept at the interface of air and solution. The experimental setup (excluding main bioamplifiers, analogue-to-digital converter and the fluid circulation system) is shown in Fig. 7.2 (d), displaying the recording chamber, electrode holders and micromanipulators, headstages (preamplifiers) and the microscope, all inside a Faraday cage[2]. The room was also double-shielded on six sides by steel and aluminum layers to minimize interference from external electromagnetic sources. A brief review of the electrical aspects of the recording procedure is presented in the following section.

7.2.2 Electrophysiology setup and measurements

This section sets out the procedures used to record the local field potentials (LFPs) from the coronal cortical slices of the mouse brain. I first review the origin and significance of LFPs, then describe the configuration of the recording and ground electrodes, and the subsequent filtering, amplification, and noise management strategies.

[1] I have been able to record from slices for up to 24 hours before they stop producing electrical activity.

[2] Faraday cage specifications:

- Dimensions: 80 × 90 × 100 cm (H × W ×D)
- Material: Galvanized steel mesh, with solid brass grounding block

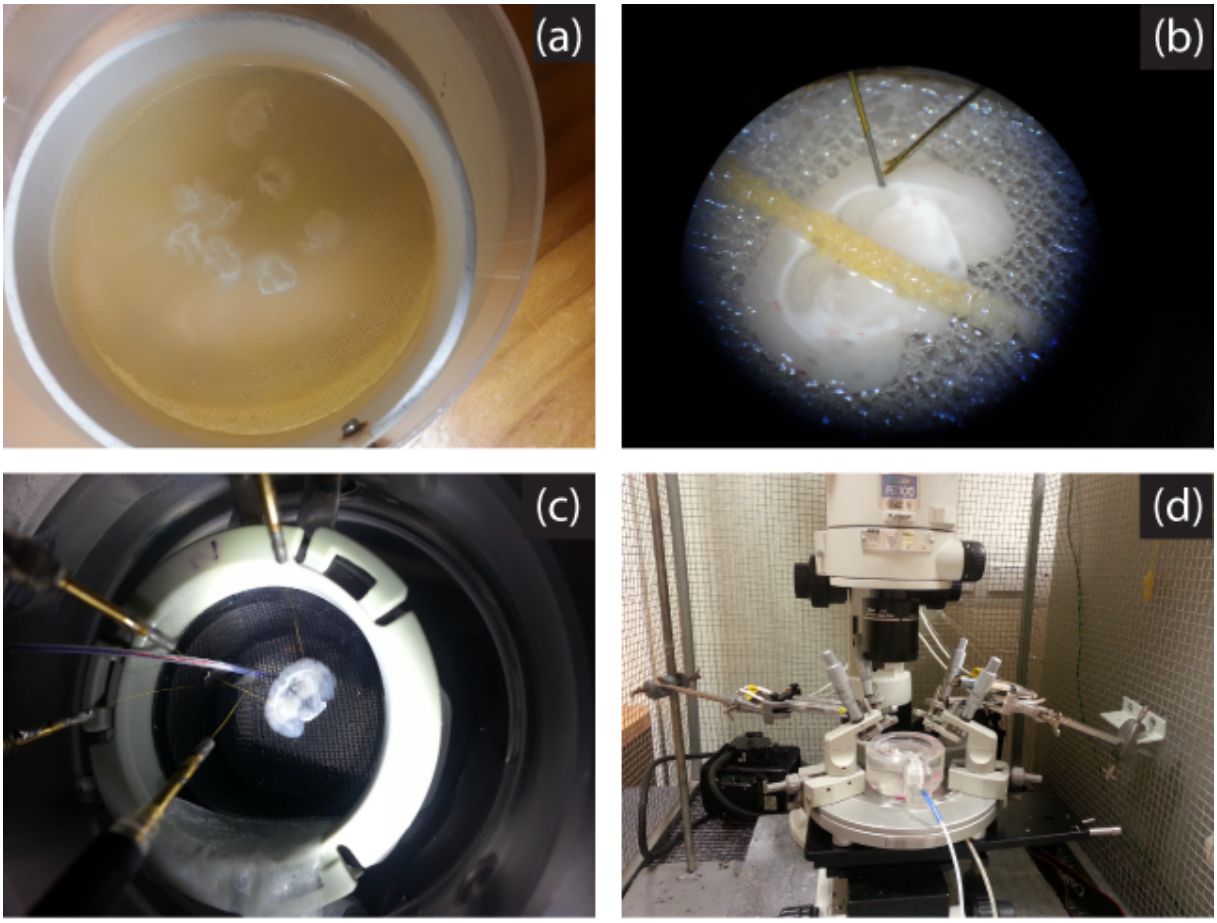

Figure 7.2: Experimental setup for recording local field potentials (LFP) from mouse brain slices *in vitro*. (a) The 400-µm coronal brain slices in the holding chamber. (b) A close-up view of the slice in the recording chamber resting on a mesh, slightly immersed ($\sim$ 1 mm) in the aCSF. The tips of the recording electrodes are visible. (c) The recording chamber, slice, metal microelectrodes with their gold-plated pin-headers and the temperature sensor (thick wire). (d) The recording chamber, electrode holders and micromanipulators, and the microscope all mounted inside a Faraday cage.

Local field potentials

The LFP is the electrical potential generated by populations of neurons, and can be recorded using microelectrodes (metal, silicon or glass micropipettes) placed in the extracellular space within the excitable tissue. Intracellular and electroencephalogram (EEG) recordings provide single unit and wide-field population activity of neurons, respectively. The LFP on the other hand provides an ensemble average of the activity of neurons confined mainly within a localized distance about 200–400 µm from recording electrode [Destexhe and Bedard, 2013][1]. As a result, independent LFPs can be recorded by electrodes separated by only a few hundred micrometers. LFPs are widely used by neuroscientists since they are:

- recordable through different electrode types and different recording configurations
- widespread in many brain regions

[1] Although there is some evidence that LFPs may spread over a centimeter scale [Kajikawa and Schroeder, 2011]

- recordable *in vivo* and *in vitro*
- unaffected by high-frequency filtering characteristics of the skull (unlike the EEG)

The EEG signal is strongly low-pass filtered due to signal propagation through CSF, skull and skin, resulting in loss of high-frequency content. However, this not an issue for LFP signals which are recorded directly from the neural tissue. Despite the differences between EEG and LFP signals, both show similar oscillatory behaviours since they both originate from synchronized synaptic currents of pyramidal neurons [Nunez and Srinivasan, 2006]. It has been shown that individual action potential spikes do not contribute significantly to the formation of LFP and EEG signals [Destexhe and Bedard, 2013]; this is due to the strong attenuation with distance of the high-frequency components comprising the action potential spike. Contribution from spikes is only possible when the tip of the recording electrode is placed in close proximity (within a few microns) of a neuron [Destexhe and Bedard, 2013]. Also it seems that technical factors like the position of the reference electrode can affect the interpretation of LFPs. For example, when the reference electrode is located in a distant position relative to the recording electrode, all signal generators between the pair could contribute to the recorded LFP [Kajikawa and Schroeder, 2011]. In the next sections I describe the electrodes and their configuration.

Electrode configuration

Considering the small physical working space between the microscope objective and the brain slice, the recording gear—including electrodes, electrode holders, micromanipulators, temperature sensor and ground electrode—need to be arranged and set up in a space-efficient way. Although increasing the number of recording channels provides more information about the state of the tissue, the constrained working area limits the number of the recording electrodes that can be used. Single monopolar recording is simple, but differential amplification is preferred because the differential method eliminates any common-mode noise contaminations such as DC drift. This makes it possible to record very low frequency components and reduces the need for high-pass filters. However, care should be taken not to eliminate the signal of interest by differential amplification: Ideally one electrode should detect the signal of interest plus the ambient noise, and the other should detect only the ambient noise.

Figure 7.3 illustrates four different configurations of a differential recording pair to obtain cortical LFP signals from the neocortical area of a mouse brain slice. The first electrode (indicated by $\oplus$) is placed in the tissue where the signal of the interest is likely to be generated, (e.g., cortical area); the second electrode (indicated by $\ominus$) can be placed (a) in the cortex very close to the first electrode, or (b) far from the first electrode in the cortex, or (c) in another brain

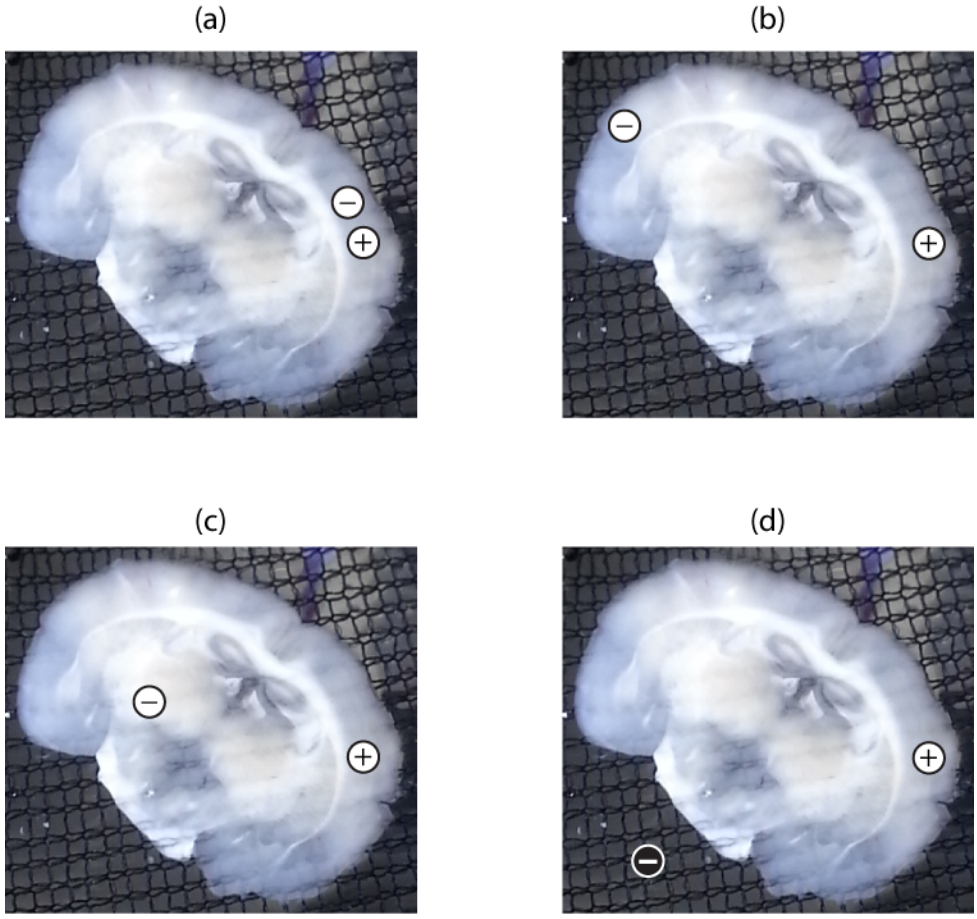

Figure 7.3: Different configurations of differential recording pairs from a brain slice. Two electrodes are indicated by (+) and (−) signs. The assumption is that the signal of interest is a cortical signal and is picked up from the cortical region where the (+) electrode is positioned. At least four configurations of the recording pair are possible based on the location of the (−) electrode. (a) Two electrodes are positioned in close proximity. The differential amplification eliminates both noise and the signal of interest since they are common to both two electrodes. (b) The (−) electrode is far from the (+) one, but is in a cortical area. Although ambient noise is removed in this case, all common biological signals will be eliminated as well. (c) The (−) electrode is placed in a non-cortical region far from the (+) electrode. The common signal including the ambient noise and common biological signals are eliminated. (d) The (−) electrode is placed in the solution in the vicinity of the slice, and receives only the ambient noise.

area such as thalamus, or (d) out of brain tissue immersed in the bath. These configurations are displayed in Fig. 7.3 (a-d) respectively.

I propose that the best configuration of the differential electrodes depends on the characteristics of the signal of interest. If we are looking for signs of critical slowing down, and assuming that this property is a general change in the characteristics of the whole slice, the arrangements as illustrated in Fig. 7.3 (a-c) may result in elimination of the signal of interest, since both electrodes are recording from the tissue. However the last configuration displayed in (d) may have more chance of picking up the signs of critical slowing since this signal is only picked up by

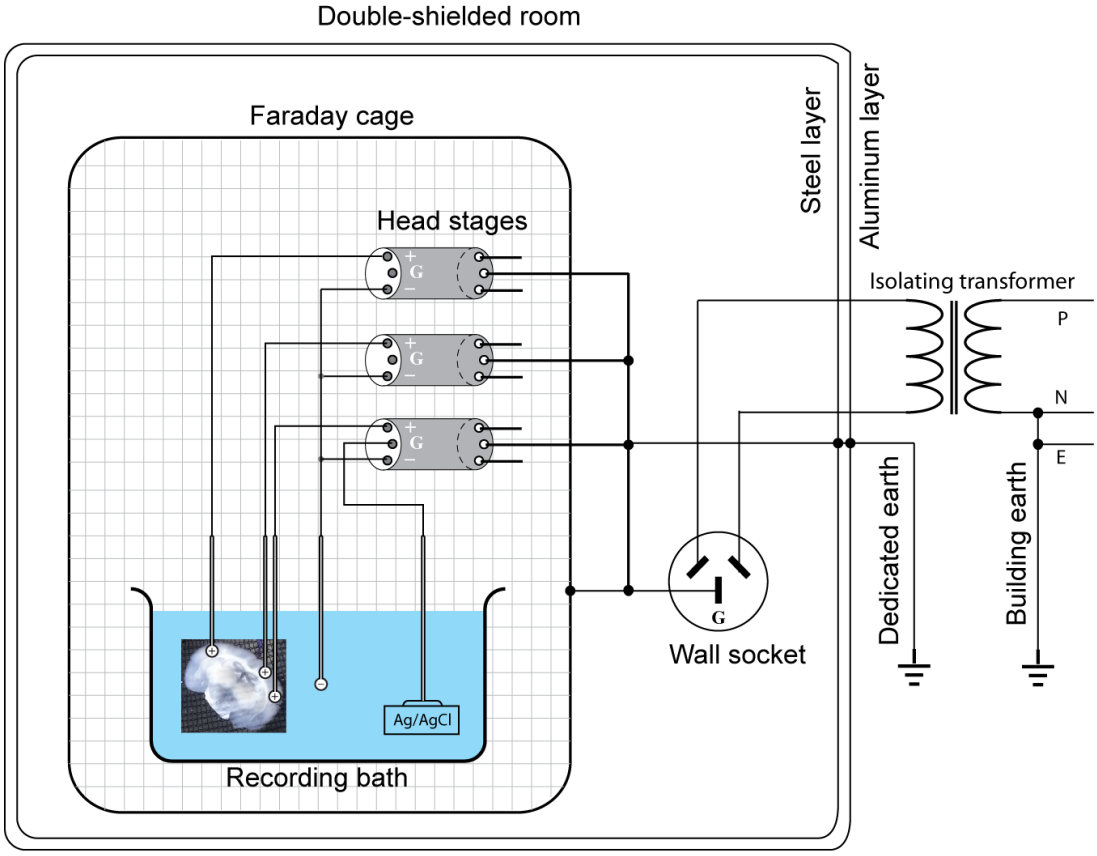

Figure 7.4: Schematic diagram of the LFP recording system. The bath is grounded by the Ag/AgCl disk electrode which is connected to the ground pin on one of the headstages. The ground pins on the other headstages should remain unconnected to ground electrode thus preventing formation of ground loops. (Ground loops provide a route for unwanted noise current due to subtle differences in the ground level voltage of different headstages and their related amplifier. Ground loops are also capable of conducting unwanted inductive noise.) The dedicated earth is completely independent of the mains earth that services the rest of the building. All three recording electrodes and the only reference electrode—relative to which the voltages are measured— are identical 50-µm Ag/AgCl electrodes, apart from slight differences in their lengths and some unavoidable microscopic differences in tip shape

⊕ electrode, and the common ambient noise[1] is differentially eliminated by the recording pair[2]. The configuration displayed in Fig. 7.3(d) was used in this thesis.

Reference electrode

The reference electrode (different from the ⊖ electrode), which is connected to the ground connection point on the bioamplifier, is immersed in the fluid in the recording chamber away from the recording site. This electrode is used to shunt all undesirable inductive signals, preventing them from being picked up by the recording pair. A silver/silver-chloride (Ag/AgCl) electrode is a common choice for ground electrode in many biological recordings, and was used in this work. Considering that the biological fluids used in these experiments contain ample chloride

[1]The ambient noise includes all noise sources from surrounding solution, tissue-electrolyte-electrode interface, and any inductive noise picked up by electrodes.

[2]We assume that the solution and the slice are affected similarly by the ambient noise and the biological signal generated by tissue is not conducted by the solution towards the ⊖ electrode.

ions, the electrical conductance through the Ag/AgCl electrode is described by the equilibria [Janz and Ives, 1968]

$$\mathrm{Ag}_{(\mathrm{solid})} \rightleftharpoons \mathrm{Ag}^{+}_{(\mathrm{solution})} + \mathrm{e}^{-}_{(\mathrm{metal\ phase})} \tag{7.2.1}$$

$$\mathrm{Ag}^{+}_{(\mathrm{solution})} + \mathrm{Cl}^{-}_{(\mathrm{solution})} \rightleftharpoons \mathrm{AgCl}_{(\mathrm{solid})} \tag{7.2.2}$$

Recording electrodes

Glass micropipettes and fine insulated tungsten microelectrodes are the most common electrode types used to record LFPs *in vivo* and *in vitro*. Different diameters (typically less than 100 µm) and tip profiles (standard, heat tapered, extra fine, or blunted tip) are widely used in experiments depending on the recording site and number of recording channels. In addition to tungsten, electrodes can be made from silver, stainless steel, platinum/iridium or pure iridium. Metal electrodes are insulated by a fine layer (≤ 3 µm) of teflon, Parylene-C or other polymer to provide electrical and moisture insulation and stiffness. The only conductive part of the exposed electrode is its tip. Tungsten and stainless steel are very stiff materials with high resistance against corrosion, making them biocompatible materials. Recently the noble metals and their alloys such as iridium and platinum/iridium have attracted interest in microelectrode fabrication, since they are extremely inert and resistant to corrosion. These electrodes also have very low tip electrical resistance making them excellent candidates for stimulus-recording purposes in neural implants.

Since I had selected Ag/AgCl as reference electrodes, and in order to minimize DC drift currents, I decided to use 50-µm insulated Ag/AgCl electrodes to record LFPs. Such electrodes are not normally used in *in vivo* experiments because of the possibility of production of toxic materials at the recording sites which is harmful for live animals. I fabricated the Ag/AgCl electrode by soldering an insulated 50-µm teflon-coated pure silver wire to a gold-coated pin-header. Before using the electrode, the silver tip was coated with a thin layer of AgCl by either electroplating or bleaching:[1]

- Electroplating with chloride (NaCl 0.9% or KCl 3M): making the silver wire positive with respect to the chloride solution, pass a current of about 1 mA/cm^2 for 10–15 seconds until a grey coating is formed
- Chloride bleaching: Soak the clean silver wire tip in household bleach (5% sodium hypochlorite) for about 20 minutes until a grey colour is observed

[1] Instructions from Warner Instrument Corporation,
`www.warneronline.com/pdf/whitepapers/chloriding_wire.pdf`

The spectral analysis of recordings from active seizing and silent cortical regions showed no significant difference in the performance of Ag/AgCl electrodes made by either method (see Appendix B.1 for results). Consequently, I used the simple bleaching method for electrode chloriding.

I now address the problem of DC drift and its minimization.

Baseline drift at DC and low frequency

A common phenomenon in low-frequency biological measurements is the slow drifting of the baseline voltage, frequently leading to saturation of the amplifiers. In many experiments it is desirable to record the full range of low frequencies, but the drift problem makes this very challenging. The drift voltage arises from the difference in the half-cell potential of the recording electrode pairs. For example, based on a table of half-cell potentials [Petrucci *et al.*, 1993], the potential drop between an Ag/AgCl reference electrode and a tungsten electrode is

$$+0.223 - (-0.58) = 0.803 \text{ (V)} \tag{7.2.3}$$

This potential difference between the two electrodes is large enough to cause a small DC current to flow between the electrodes, which may have very slow oscillating characteristics over time. Since the amplitude of the signal of interest is very small, the DC drift can be a major low-frequency noise source. (A sample recording containing baseline drift can be observed in Fig. B.1(a, b) of Appendix B.1; the drift is eliminated in Fig. B.1(c) by applying a 1-Hz high-pass filter.) Since the value of the half-cell potential is much larger than the measured signal (803 mV compared to 100–300 µV amplitude of SLEs) this DC voltage can easily saturate the preamplifier headstage. I found that the drift voltage can be minimized by carefully eliminating the possible sources of half-cell potentials between electrode pairs by—

- using the same materials for recording and ground electrodes
- removing contamination from the electrode tip
- electrical compensation of residual DC offset[1]
- minimizing movements of the electrodes, sample or recording bath to reduce the resultant change in the configuration of the charges in the electrode-electrolyte interface
- using geometrically identical microelectrodes (same tip profile, length and diameter)
- limiting the range of temperature changes at the recording site[2]

[1]The A-M Differential Amplifier used in my experiments has a DC offset knob which provides a variable DC offset voltage, and is summed with the input voltage. This feature may be used to compensate for DC offset.

[2]The temperature change is mainly due to variable temperature of circulated biological solutions. This circulation process is necessary to continuously provide a carbogenated solution to the alive tissue. See Fig. B.2 to observe the correlation between the temperature and DC drift in a slice experiment.

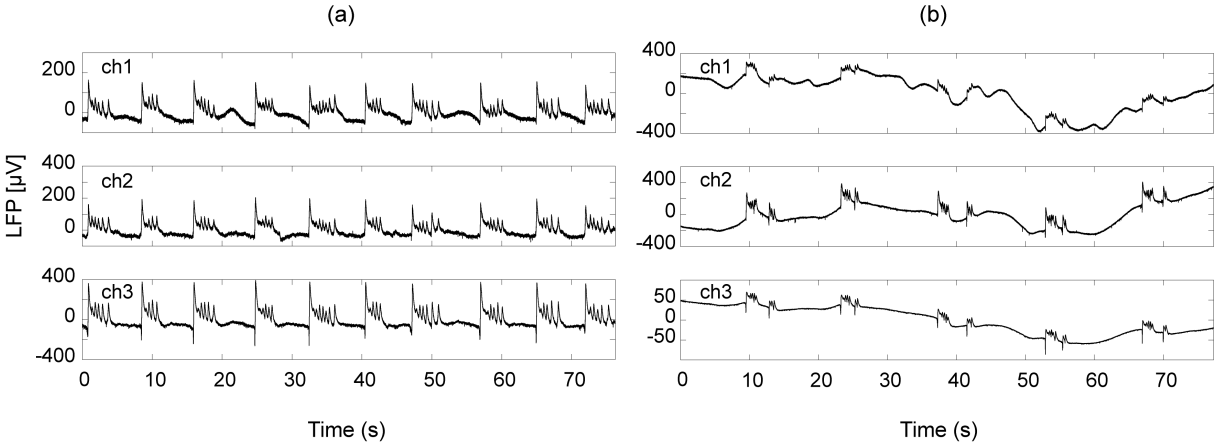

Figure 7.5: Near elimination of baseline drift in DC recordings. (a) A driftless three-channel cortical record of an active seizing slice. (b) Similar record as in (a) from a different slice containing some drift, but still small enough compared with the amplitude of individual SLEs. The LFPs were recorded using 50-μm Ag/AgCl electrodes, and low-pass filtered with $f_{\mathrm{LP}} = 1000$ Hz. Sample rate was 10000 per second per channel.

Employing this set of strategies made it possible to perform hour-length DC-mode recordings from seizing brain slices with very small drift voltages. This was not achievable using tungsten electrodes[1]. Figure 7.5 displays a three-channel cortical LFP recording containing almost no drift in (a), and a small but controllable drift in (b).

Bioamplifiers

A suite of single-channel A-M AC/DC Differential Amplifier, Model 3000[2] was used to amplify the LFPs. The instrument is designed for low-noise recordings from excitable tissue and offers different levels of amplification (up to $\times 10,000$) with different settings of low- and high-pass filtering. This amplifier is designed to be used with or without preamplifiers or *headstages*; all the experiments reported here were performed using the headstage. The headstage is a small-gain ($\times 50$) high input-resistance amplifier, positioned as close as possible to the signal source—tissue microelectrode in our case—within the Faraday cage. The high input-resistance of the headstage reduces the current drawn from the signal source thus minimizing signal distortion. I used four amplifiers to simultaneously record from four different regions of the brain slice.

All amplifiers should function identically to ensure comparable results. A custom-made low-amplitude signal generator was used to verify the identity of signal amplification by all four amplifiers. The signal generator is capable of producing 1-Hz and 10-Hz sinusoidal, triangular, square-wave test signals of amplitude of $\sim$90 μV_{pp}, which is in the range of typical EEG or LFP signals. (See Appendix B.3 for the schematic diagram of the signal generator and its output signals recorded using bioamplifiers.)

[1]Note that the change in the concentration of ions in the vicinity of electrode-electrolyte interface also contributes to DC drift. One can use Vycor glass to enclose the electrodes. This special type of glass provides electrical connectivity while preventing ionic mixing, keeping the ionic concentration of the solution fixed.

[2]A-M Systems, Inc., `http://www.a-msystems.com`

Noise management

The small range of LFP background activity ($\leq$ 25 µV) means the recordings can become contaminated easily by unwanted electrical noise. The noise sources include but are not limited to:

- capacitive electrical noise picked up by the electrodes through their stray capacitance
- inductive noise currents due to the existence of ground loops
- thermal noise of the electrodes

The complete elimination of noise is impossible but efforts should be made to minimize it as much as possible. My experiments were carried out in a double-shielded room which strongly attenuates external electromagnetic fields entering the room. Capacitive and inductive interference can be reduced by performing the experiments inside a Faraday cage. As shown in Fig. 7.4, the recording bath, preamplifiers and the microscope were placed inside a Faraday cage to prevent any electrical fields contaminating the records.

The formation of a ground loop is illustrated in Fig. 7.6 where two devices share a common ground point G. Assume that A is an electrical system consuming electricity, and B is the buffer circuit of the headstage of the amplifiers. Ideally the output of buffer circuit V_{out} should be equal to the LFP recorded from the slice. However if the common point connection to the earth has high resistivity, a voltage drop V_G appears on G where

$$V_G = V_1 - R_1 I \tag{7.2.4}$$

This voltage-drop forms a non-zero potential ground point, making the output voltage dependent on V_1

$$V_{\text{out}} = \text{LFP} - V_G = \text{LFP} - V_1 + R_1 I \tag{7.2.5}$$

This dependency creates an electrical connection between A and B. For example if A is a mains operated device, 50-Hz artifacts can easily contaminate V_{out}. Reducing R_G will reduce the effects of the ground loop. The voltage of the ground point can be minimized using an earth bar to ground all measuring devices via low-resistance cables.

The mains ground connection of the building may not be “clean” due to poor connections or the induced effect of other electrical devices via formation of multiple ground loops in the other parts of the building. A dedicated external earthing pin was installed during construction of the electrophysiology lab to provide a reliable ground reference that is completely independent of the building multiple-earth-neutral common connection.

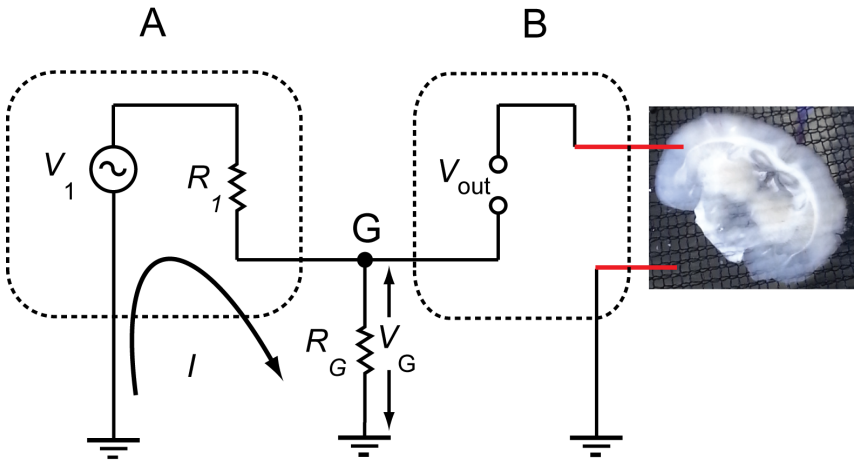

Figure 7.6: Formation of a ground loop

The bioamplifiers have inherent noise which cannot be reduced unless they are replaced by alternative low-noise devices. The inherent noise of amplifiers and associated ADC used in recording the LFPs are displayed in Fig. B.5.

I was able to minimize the noise levels by using the mentioned approaches. Specifically the 50-Hz interference and its harmonics (up to 200 Hz) were attenuated significantly, eliminating the need for 50-Hz notch filters when recording LFPs (see Fig. B.7).

7.3 Fluctuation-induced precursors of phase transitions in mouse brain slices

The electrical signals recorded from neural system always contain spontaneous background voltage fluctuations, arising from random variability in the structural and functional characteristics of ion channels and other neural elements. Other sources such as thermal fluctuations and spontaneous release of neurotransmitter at presynaptic vesicles also contribute to background fluctuations [Colquhoun and Sakmann, 1981; White *et al.*, 2000; Qian *et al.*, 2014]. This noisy behaviour results in some uncertainty in the spiking threshold of individual neurons. However these small fluctuations can also provide useful information about the closeness of the system to its tipping point or phase transition.

In a zero-Mg-induced seizing brain slice, I classify the phase transitions of LFPs into four categories. Two types of phase transitions can occur during the formation of an individual SLE as illustrated in Fig. 7.7(a):

a1 Onset of an individual SLE

a2 Termination of an individual SLE

A phase transition can also be assumed for the long-term LFPs recorded in (quiescent $\leftrightharpoons$ seizing) cycles as displayed in Fig. 7.7(b):

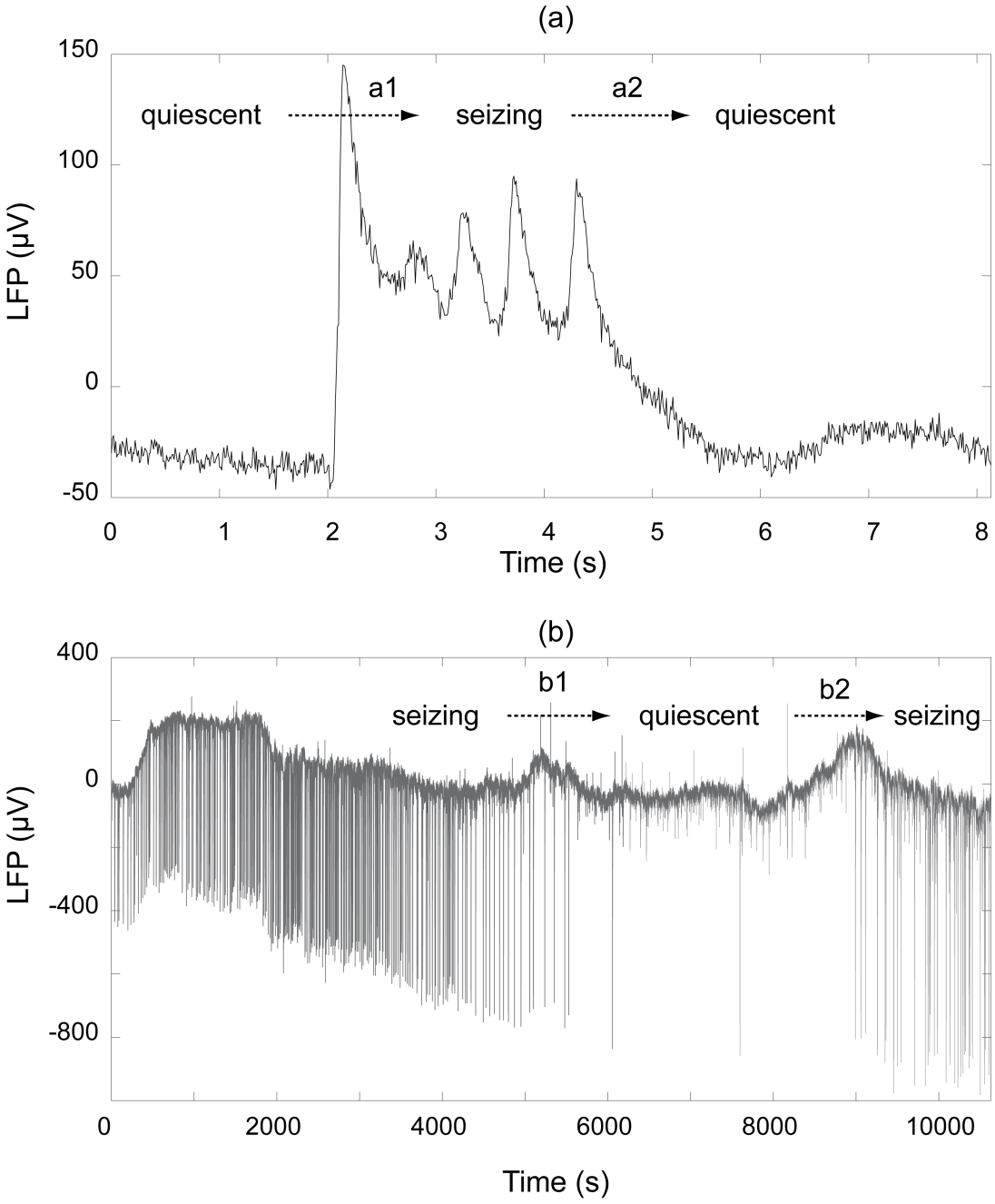

Figure 7.7: Phase transitions in seizing cortical slices in (a) an individual seizure-like event (SLE) and (b) long-term active/quiescent cycle. The SLEs in (a), (b) are induced by lowering the magnesium level, recorded from the cortical area of mouse brain slice, using 50-μm Ag/AgCl microelectrodes in DC mode, but from different animals. Increasing the magnesium level by slow application of brain extract solution induces the transition from the seizing to quiescence.

b1 Transition from seizing to quiescence

b2 Transition from quiescence to seizing

In this thesis only the a1 transition of a single SLE is examined in detail. The study of the transitions displayed in Fig. 7.7(b) are not practical based on my recorded data due to the very challenging task of inducing a *completely* quiescent state, sandwiched between seizing periods. The small spike-form activities as observed in the quiescent period of Fig. 7.7(b) may indicate

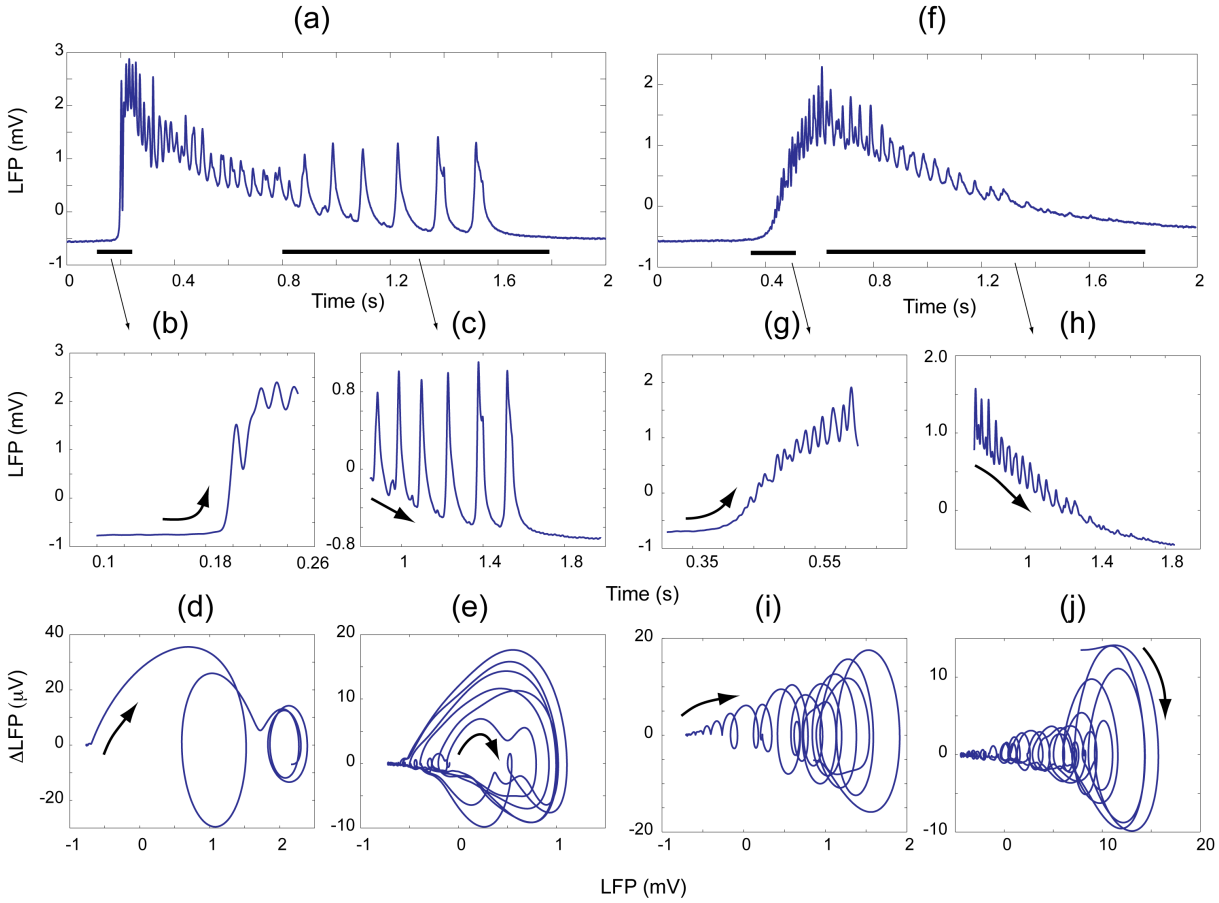

Figure 7.8: Qualitative analysis of the initiation and termination phases of hippocampal SLEs. (a) SLE with a sharp initiation and small growing events on the tail. The beginning and termination epochs are extracted and displayed in (b), (c). The corresponding phase plots are displayed in (d) and (e) with small arrows showing the start point and the direction of movement of trajectories in the phase plane. The phase plots are produced by plotting the first difference of the recorded voltage values ΔLFP as a function of recoded voltage LFP. Same analysis on a second SLE (f) with the results displayed in (g-j), showing qualitative differences in initiation and termination phases. LFPs are recorded using 50-μm Ag/AgCl microelectrodes, in DC mode with low-pass cutoff frequency of 1000 Hz and sampling rate of 10000 Hz.

that a phase transition to the completely quiescent state has not occurred yet.

7.3.1 Qualitative study of phase transitions in seizure like events

In this section I provide some qualitative evidence for state transitions in an epileptic neural system *in vitro*. By using *phase space* diagrams one can perform a qualitative analysis of a dynamical systems. I use phase diagrams to reveal the existence of phase transitions in epileptic mouse brain slices, then discuss experimental signs of critical slowing down prior to state transitions.

Two hippocampal SLEs are displayed in Fig. 7.8 (a), (f). Both events are likely to be the result of activity of bursting neurons in the vicinity of the electrode tip in the CA1 region of the hippocampus. These events show a state transition from quiescence to seizing, which persists

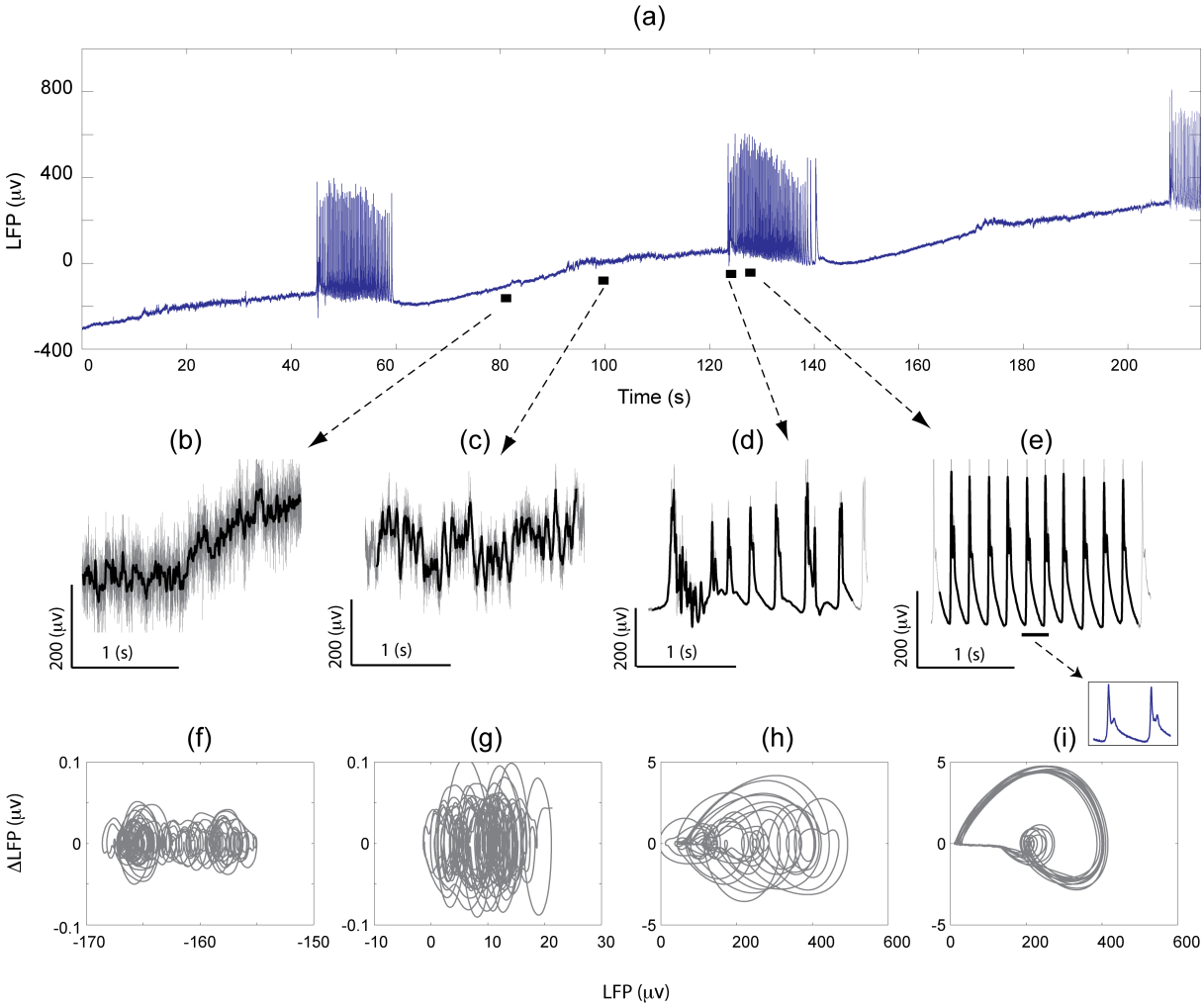

Figure 7.9: Qualitative dynamical analysis of hippocampal SLEs. (a) Same hippocampal SLEs as displayed in Fig. 7.11. Four selected 2-sec length epochs from different phases of LFP are extracted and displayed as (b, f) quiet inter-ictal, (c, g) sensitive pre-ictal, (d, h) seizure initiation, and (e, i) ictal or active seizing state. The raw signal is shown as the grey background and the smooth part of it is displayed in black in each case. The phase diagrams are plotted as the first difference of LFP time-series (ΔLFP) versus the LFP time-series in μV.

for about 2 s, followed by a transition back to the resting state. A closer look at the initiation and termination phases reveals some interesting differences between the two events. The first (a, b) starts with a sudden emergence of a large-amplitude limit cycle (d), while the second (f, g) initiates with a gradually growing-amplitude limit cycle (i). The limit cycles were generated by plotting the first difference of recorded voltage values (ΔLFP) versus the LFP time-series.

The transition from the silent resting state to oscillating limit cycle displayed in (d) is reminiscent of a saddle-node, saddle-node on invariant circle (SNIC) or subcritical Hopf bifurcation. The limit cycle in (i) suggests a supercritical Hopf bifurcation. Note that it is not possible to make further arguments regarding the type of bifurcations in these experiments only based on the presented phase plots. One may use spectral analysis of the voltage time-series to reveal any existing resonance which may indicate a Hopf bifurcation.

Bifurcation from limit cycle to the resting quiescent state at the end of the two SLEs is also quite different for the two events. The first bifurcates to silence via an increase in the amplitude of the limit cycle (c, e) , while the second one bifurcates through a smooth reduction in the amplitude of the limit cycle (h, j). These transitions are also suggestive of different bifurcation types as described by the theory of dynamical systems.

Here I present the results of another qualitative analysis of epileptic data. Figure 7.9 demonstrates a sample hippocampal LFP containing consecutive SLEs and the corresponding phase diagrams. Four different epochs are selected for qualitative analysis and are displayed in (b-e). The gray trace in the background is the raw signal and the superimposed black trace is the corresponding smooth part of the signal extracted using a *Whittaker* smoother[1]. Each epoch is representative of a distinct mode of neural activity:

(b) Quiet interictal period

(c) Increased sensitivity pre-ictal phase

(d) Seizure initiation

(e) Active seizing (ictal state)

The corresponding phase diagrams are displayed in Fig. 7.9(f-i). The qualitative difference between phase plots reveals several state transitions in this epileptiform LFP. The visually irregular pattern (higher complexity) in (f) expands and shows small-amplitude limit cycles (decreased complexity or increased regularity) in (g) as a result of increased sensitivity in the preictal period. The seizure initiation is reflected in the sudden and rapid transformation of the phase diagram in (h) where small-amplitude limit-cycles give birth to large-amplitude ones. The phase plot in (i) displays regular repetitive trajectories corresponding to the active seizing state. Note that an extra loop developed in (i) corresponding to bursting activity (inset displays a selected burst activity in (i)). I observed comparable sequential state changes in many similar records—containing strong SLEs with rich morphological patterns. Similar qualitative observations are also reported for hippocampal seizures in rat and mouse slices by Jiruska *et al.* [2010] and Filatov *et al.* [2011].

These observations provide experimental evidence for the existence of phase transitions in the epileptic mouse brain[2]. My attempts to capture warning signals prior to these observed phase transitions are presented in the next section.

[1] See Appendix C.1 for more details.

[2] In a comprehensive work one could quantify the state changes using entropy or complexity measures in a series of *in vitro* experiments.

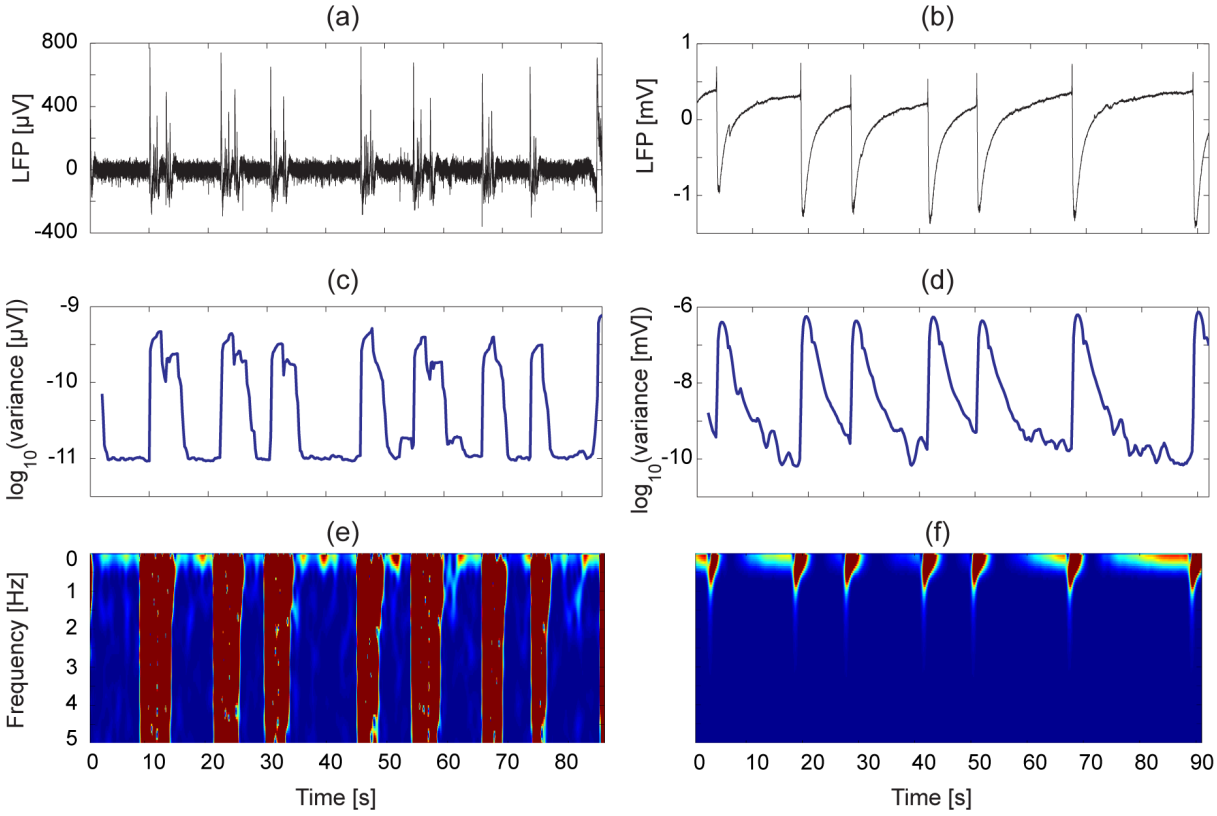

Figure 7.10: Variance and spectral analysis of cortical SLEs. The zero-Mg induced seizures (a, b) are recorded using 50-µm Ag/AgCl electrodes. The low- and high-pass filter settings, amplification and sampling rate are 1000 Hz, DC, ×1000, 10 kHz respectively. The instantaneous variance (c, d) and the time-frequency (e, f) plots are obtained using a 4-sec rolling window, with 90% overlap. The logarithm of variance is displayed for more clear demonstration of any existing trend.

7.3.2 Spectral and variance analysis of LFPs prior to the onset of individual SLEs

The modelling results of Chapters 3, 5, and 6 indicated increased variance, autocorrelation and power spectral density in certain frequencies prior to state transitions. Inspired by these results and the methods employed in other research fields to unmask the precursors of state transitions, I use similar methods to analyze the LFPs prior to SLE occurrence. The spectrum and variance are the two analytical tools that are used to uncover the possible signs of critical slowing down (CSD) prior to onset of individual SLEs.

Figure 7.10 (a, b) displays two sample *cortical* LFPs each containing several SLEs recorded from two slices, each from a different animal. The SLEs are induced by application of zero-Mg solution. There is no obvious increase in fluctuation variance prior to SLE initiation, in the instantaneous variance graphs in (c), (d)[1]. Note that the estimated variance (calculated using the MATLAB `var` function) is equal to the real variance only if the time-series is of infinite length. As a result one should not expect to obtain an accurate estimate of variance from the relatively

[1]The instantaneous *skewness* and *kurtosis* also did not show any trend prior to individual SLEs (results not shown).

short time series corresponding to the brief quiescent periods between consecutive SLEs. The power spectral density (PSD) curves of the time-series are displayed in (e) and (f), and they show slightly different behaviour. While the low frequency activity occurs almost randomly before appearance of each SLE in (e), a gradual increase in the low-frequency activity before initiation of some SLEs is evident in (f). This low-frequency activity pattern was not observed consistently in other cortical SLE recordings in this study. However I noticed that this precursive low-frequency activity was more likely to be captured when the corresponding SLE had a large amplitude, long period, or a rich morphology. A morphologically rich SLE is a long event (> 2 s) having a large initial deviation followed by multiple smaller events on the tail.

Motivated by these observations, two methods were employed to increase the chance of capturing evidence of critical slowing down:

- Enhancing SLE activity by adding carbachol to the perfused zero-Mg aCSF
- Focusing on *hippocampal* (rather than cortical) SLEs to obtain stronger and longer SLEs sustained by the recurrent excitatory neural networks within the hippocampus

Figure 7.11(a) displays three consecutive SLEs recorded from the hippocampal CA1 area. The SLE events are zero-Mg induced seizures strengthened by application of carbachol (100 mM). These large amplitude (∼600-µm peak-to-peak) and long-lasting (∼20 s) SLEs with their

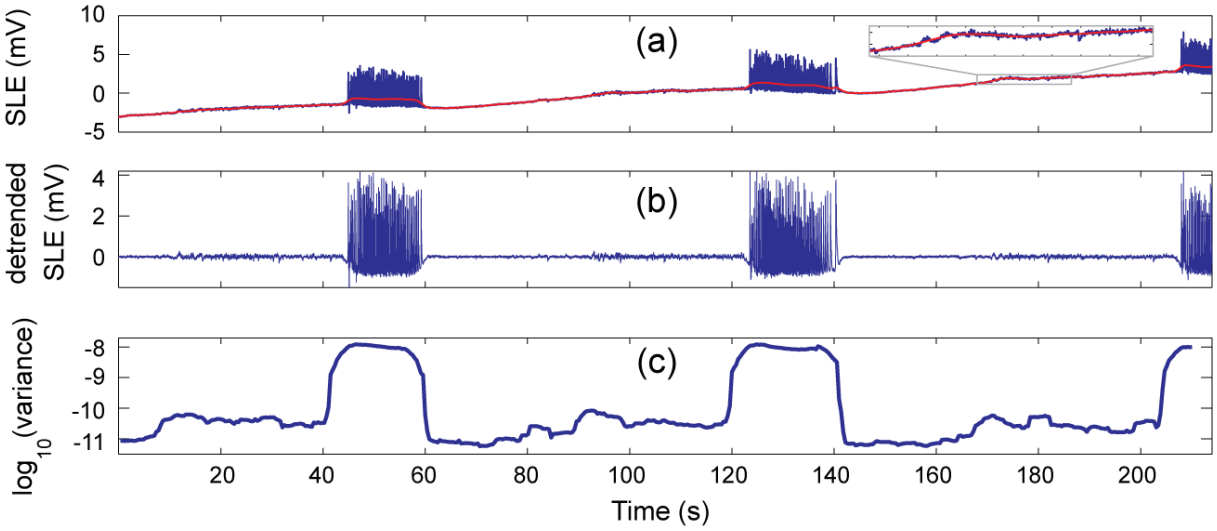

Figure 7.11: Increased tissue sensitivity prior to seizure onset in hippocampal area CA1. (a) Representative LFP showing consecutive zero-Mg SLEs recorded from coronal slices containing hippocampal area CA1. The large-amplitude and long SLEs are the result of very slow (1 mL/min) application of carbachol. The volume of zero-Mg solution was 50 mL before addition of carbachol. LFPs are recorded using 50-µm Ag/AgCl microelectrodes, in DC mode with low-pass cutoff frequency of 1000 Hz and sampling rate of 10000 Hz. Increased background activity is evident in the LFPs ∼25 s prior to seizure onset. The superimposed red trace is the low-frequency trend of the signal (see inset for details). (b) Corresponding detrended LFP signal. (c) Instantaneous variance of the detrended signal in a logarithmic scale. The (estimated) variance is obtained using a rolling window algorithm, with window length of 4 s and 90% overlap. The fluctuation variance increases by about an order of magnitude prior to each SLE.

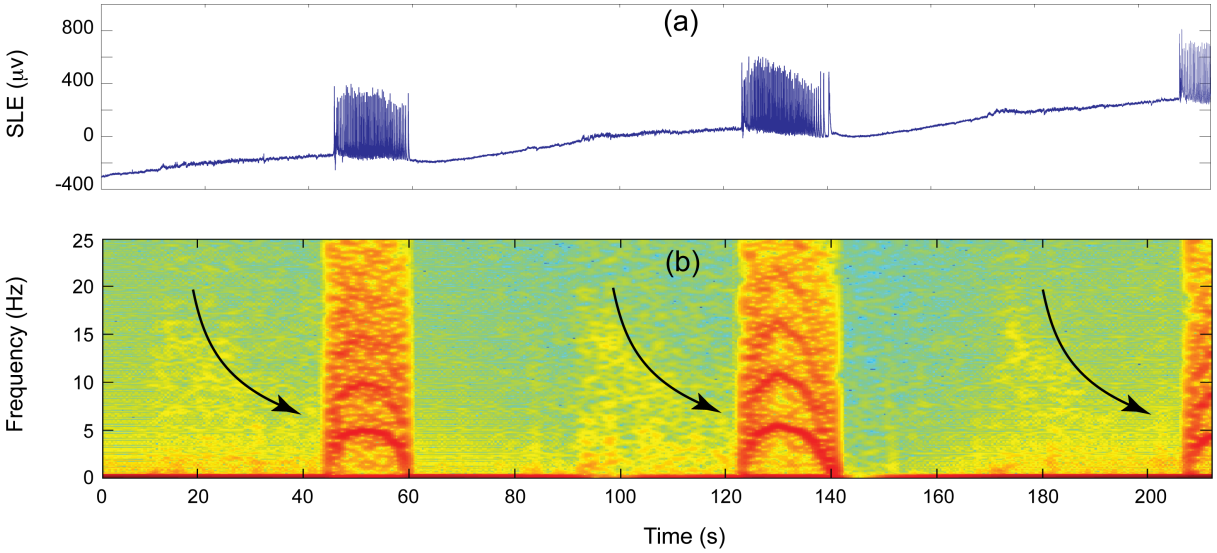

Figure 7.12: Low-frequency activity prior to seizure onset in hippocampal area CA1. (a) Same events as displayed in Fig. 7.11(a). (b) The corresponding power spectral density function showing appearance of low-frequency activity and characteristic "down-chirp" (drift to lower frequencies) in spectral activity as SLE onset is approached (arrows). The power spectral density is obtained using MATLAB's `spectrogram` function using window length of 4 s with 90% overlap.

rich morphological structure may have been recorded from the vicinity of a seizure source. An increased "fizziness" is evident in the time-series before the initiation of each event. Using a Whittaker smoother, I extracted the trend or low-frequency part of the LFP (red), and superimposed it on the raw signal. I detrended the signal by subtracting the DC drift to produce a signal with a stable baseline as displayed in (b). Now a rolling-window variance extractor can be employed to track the instantaneous variance of the detrended signal. Figure 7.11(c) shows an increase in the variance of the signal prior to SLE initiation plotted on a logarithmic scale.

The spectral analysis of these SLE time-series, displayed in Fig. 7.12, shows appearance of low-frequency activity prior to SLE onset. This activity has spectral energy that initially extends to ∼20 Hz, but drops to lower frequencies as onset approaches, forming a characteristic "down-chirp" pattern. This increased variance and power density at low-frequencies is a consistent feature across 40 consecutive hippocampal seizure-like events spanning a time period of ∼2.5 hours.

Figure 7.13 displays the result of the variance analysis on 40 consecutive inter-SLE periods. The first inter-SLE period is displayed in (a). Three epochs are extracted belonging to the first, third and last second of the inter-SLE period (epoch1, epoch2, epoch3). Every epoch was divided into four non-overlapping 250 ms segments, and the variance of detrended segments (using Whittaker smoother) was calculated.

The variance of the epoch was calculated as the average value of the variances of five segments. As a result three variance values (var1, var2, var3) were extracted for every inter-SLE period. The trend of three variances is displayed in Fig. 7.13 (b). The bar plot displayed in

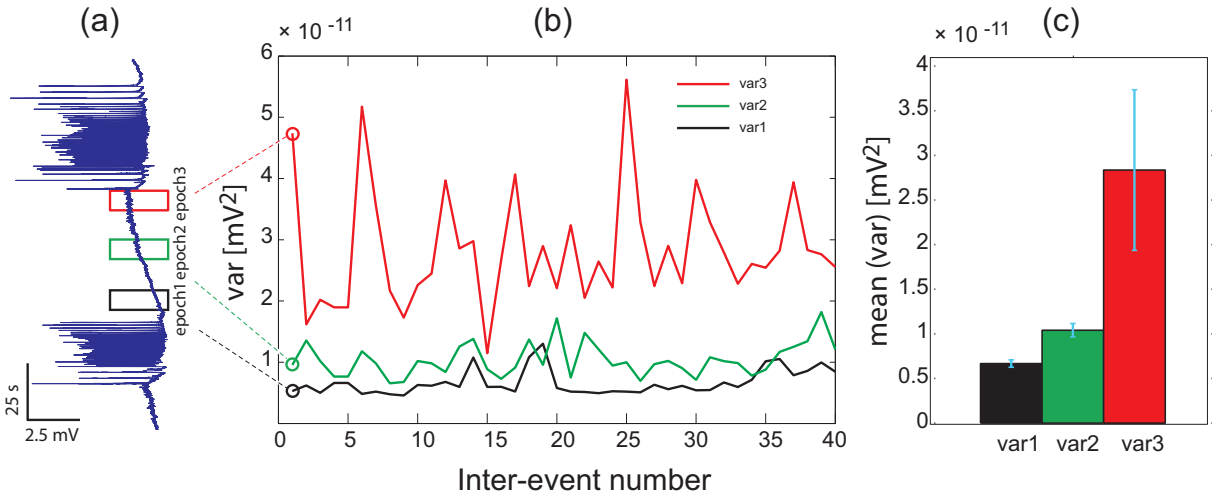

Figure 7.13: Increased variance prior to hippocampal seizure like activities (SLEs). (a) A sample inter-SLE period. Three epochs are selected belonging to the first, third and last second of the period. The variance of each epoch is calculated (see text for more details). (b) The trend of corresponding variances of three epoch displayed in (a) across 40 pre-SLE periods. (c) Average value of the trends displayed in (b). The error bars correspond to the variances of the trends in (b). See Fig. 7.11 for the experimental method.

Fig. 7.13 (c) corresponds to the average value of three variances and summarizes the analysis results. A consistent increase (∼88%) in the variance of inter-SLE fluctuations prior to SLE occurrence over 40 samples is evident.

The increased variance and low-frequency activity prior to SLE generation is also conserved across analysis of another data set obtained from a different mouse as presented in Fig. 7.14, again showing an increase in low-frequency power and fluctuation variance prior to hippocampal seizure onset (the experimental method is described in the caption of Fig. 7.11). Figure 7.14(a) displays an ∼11-min LFP record from hippocampal CA1 region on a mouse brain slice. The DC part of the signal is removed using a Whittaker filter, and the driftless signal is plotted in black. The power spectral density is displayed as a color-coded time-frequency graph in (b) showing increased low-frequency activity prior to individual SLEs with the more obvious increases highlighted by by arrows. A further analysis is done on one of the SLEs and the results are displayed in Fig. 7.15. The appearance of low-frequency activity and increased variance is evident in the figure.

7.3.3 Bistability and flickering prior to seizure initiation

Bistability is a common feature of dynamical systems with coexisting multiple steady states in which the system's output can alternate between states due to the effect of intrinsic or external subthreshold stimulation. There is increasing evidence supporting the bistability of neural systems under epileptic conditions [Wu and Shuai, 2012; Barnett *et al.*, 2013; Koppert

et al., 2013]. *Flickering* is defined as a transient rapid alternation of the state of the system, and can precede the corresponding bifurcation point in bistable or multistable systems. This phenomenon is considered as another precursor of state transitions [Scheffer *et al.*, 2009] and interestingly is observed prior to occurrence of some SLEs in our experiments.

Figure 7.16 displays four selected SLEs preceded by flickering activity. Individual flickers marking isolated events are indicated by arrows. These precursor events show how the neural activity apparently toggles between quiescent and seizing regimes prior to seizure initiation. The observed flickers suggest the extreme sensitivity of the neural tissue to noise-induced perturbations, and its tendency to phase transition. The region (b) of the steady state diagram presented in Fig. 6.6 of Chapter 6 might be appropriate for investigating flicker dynamics underlying bistability in a neural model. But note that flickering is a *suprathreshold* event and is not modelled in this thesis.

7.4 Prolongation of evoked potentials in the seizure promoting state

Inspired by modelling and experimental evidence for critical slowing down, I identified noise-induced precursors of phase transitions in the Izhikevich and Wilson-Cowan models in Chapters 3, 5, 6 respectively, and in *in vitro* experiments in the current chapter. These results predict existence of critical slowing signs in a system probed by external impulses. Kalitzin *et al.* [2002] first performed a *probing* experiment in which they analyzed magnetoencephalogram (MEG) and EEG signals while periodic light stimulation of visually sensitive epileptic patients. They

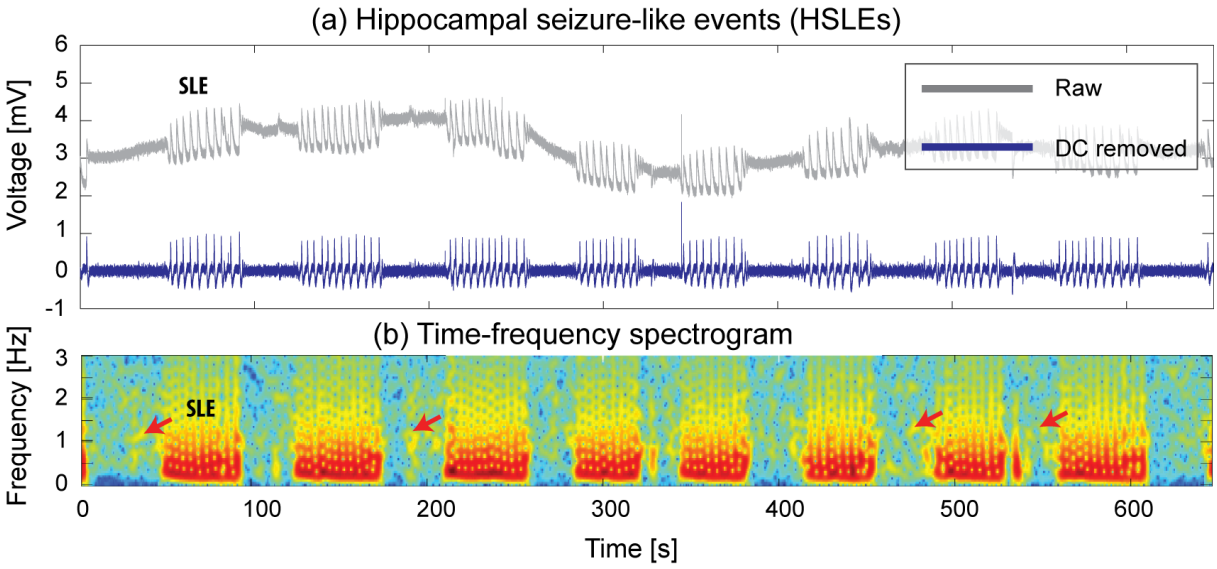

Figure 7.14: Increased spectral power prior to some hippocampal seizures. (a) The raw and DC-removed hippocampal LFP signal containing consecutive SLEs. (b) Power spectral density of DC-removed signal showing increased low-frequency activity prior to some of SLEs (arrows).

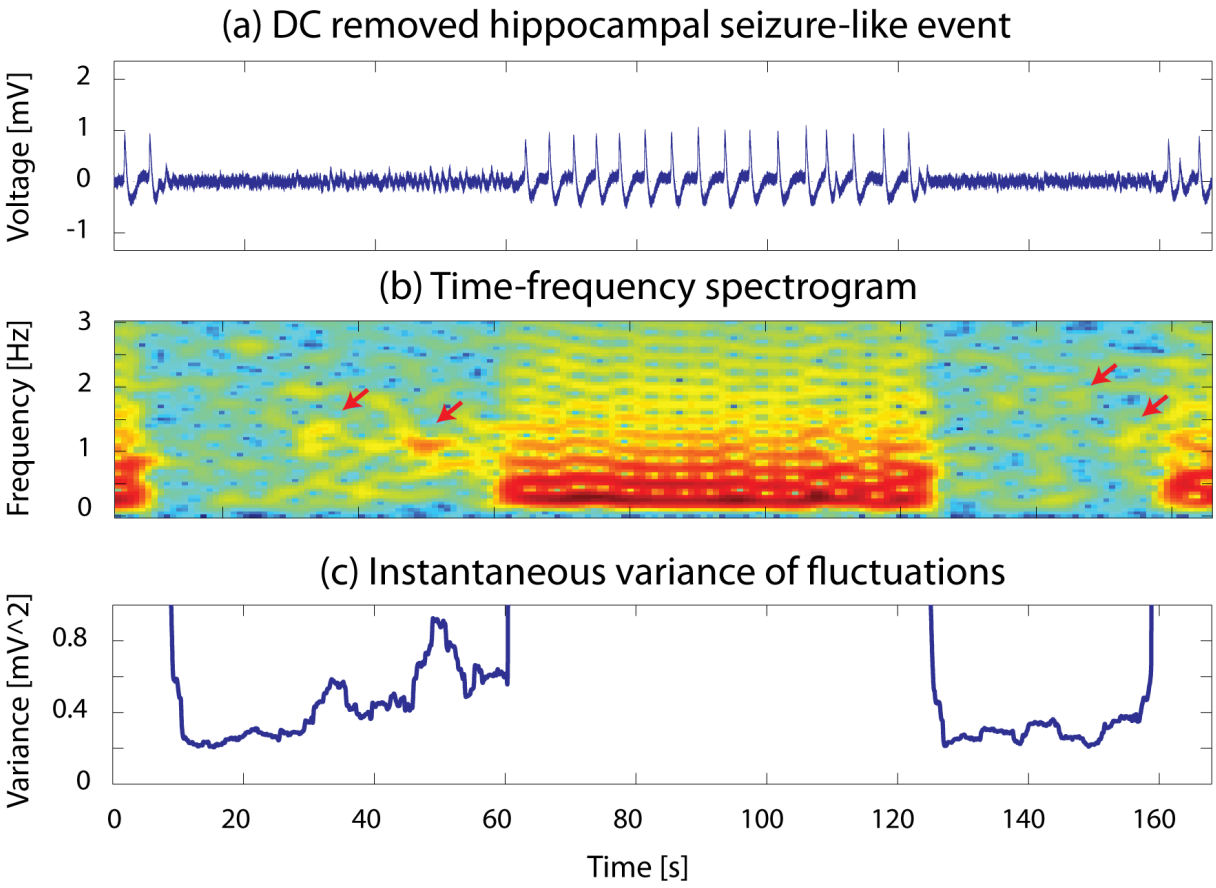

Figure 7.15: Spectral and variance analysis of an individual hippocampal seizure event. (a) DC removed LFP. (b) Spectrogram and (c) instantaneous variance showing incresed spectral power and variance prior to seizure initiation.

introduced rPCI (relative phase clustering index) as a measure of phase clustering of harmonically related frequency components of evoked MEG/EEG responses, and showed enhanced phase clustering in gamma band frequency (30–120 Hz) before transition to seizing. They extended their previous method using subthreshold electrical stimulation as a probe for neural excitability [Kalitzin *et al.*, 2005]. They showed enhanced rPCI values in seizure onset sites, and demonstrated the correlation between rPCI and the time to next seizure occurrence in a group of six patients with temporal lobe epilepsy. This study provided a proof of principle for neural probing approach.

Freestone *et al.* [2011] introduced a cortical probing method in which the excitability of cortical circuits (as reflected by larger EEPs) was used to anticipate the proximity to seizure occurrence. They introduced mean phase variance (MPV) of EEPs as a measure of excitability and demonstrated the correlation between higher excitability and possibility of impending seizure.

We hypothesize that results of probing experiments may be correlated with universal slowing-down properties prior to phase transitions. It seems reasonable to relate the concept of increased

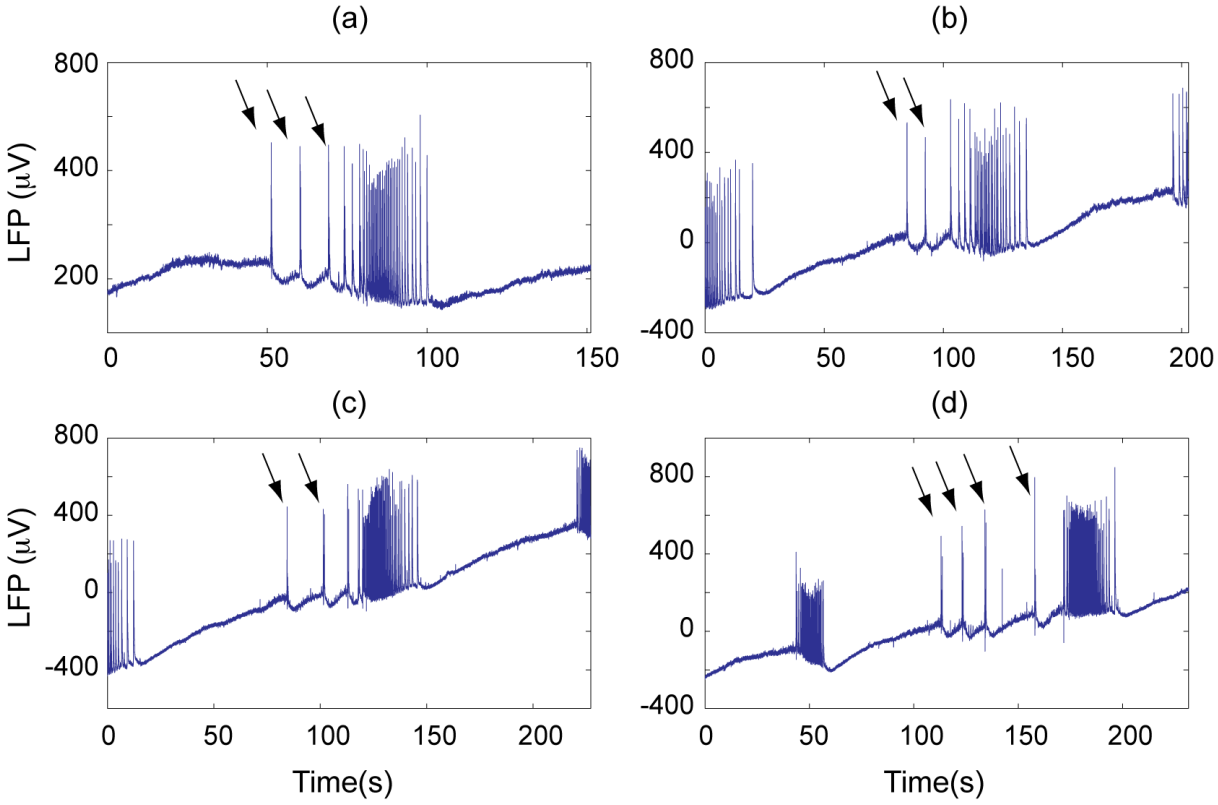

Figure 7.16: Flickering or bistability prior to seizure onset in hippocampal area CA1. Four represented hippocampal CA1 SLEs preceded with flickering activity. The flickers are indicated by arrows. See caption of Fg. 7.11 for more more description about the data.

excitability (larger EEPs) to elevated noise-induced spatiotemporal variances, thus linking the previous work in this thesis to the *in vivo* neural probing experiments of Kalitzin *et al.* [2002, 2005] and Freestone *et al.* [2011].

Using an *in vitro* setting, we report a prolongation of evoked potentials (EPs) while the neural populations are *nudged* towards the seizing mode by slow application of the zero-Mg solution in this section. This serendipitous observation was made during an experiment in the electrophysiology laboratory of University of Waikato by Dr Logan Voss. See Appendix B.5 for methods.

The extracted and time-aligned EPs are displayed in Fig. 7.17(a). The colour shades from black to light grey representing the EPs recorded from the beginning (normal aCSF) to the end (zero-Mg) of the experiment, respectively. Comparing the light-grey traces with the darker ones, an amplification and prolongation of the EPs is evident when the tissue is biased towards the threshold of the seizing state by application of zero-Mg solution. The bird's-eye view of all aligned EPs is displayed in (b) where the amplitude of the EPs is colour coded using an arbitrary scaling to demonstrate the temporal evolution of the EPs. Comparing the amplitude of EPs in normal and zero-Mg aCSF modes reveals the gradual increase in amplitude and period of EPs

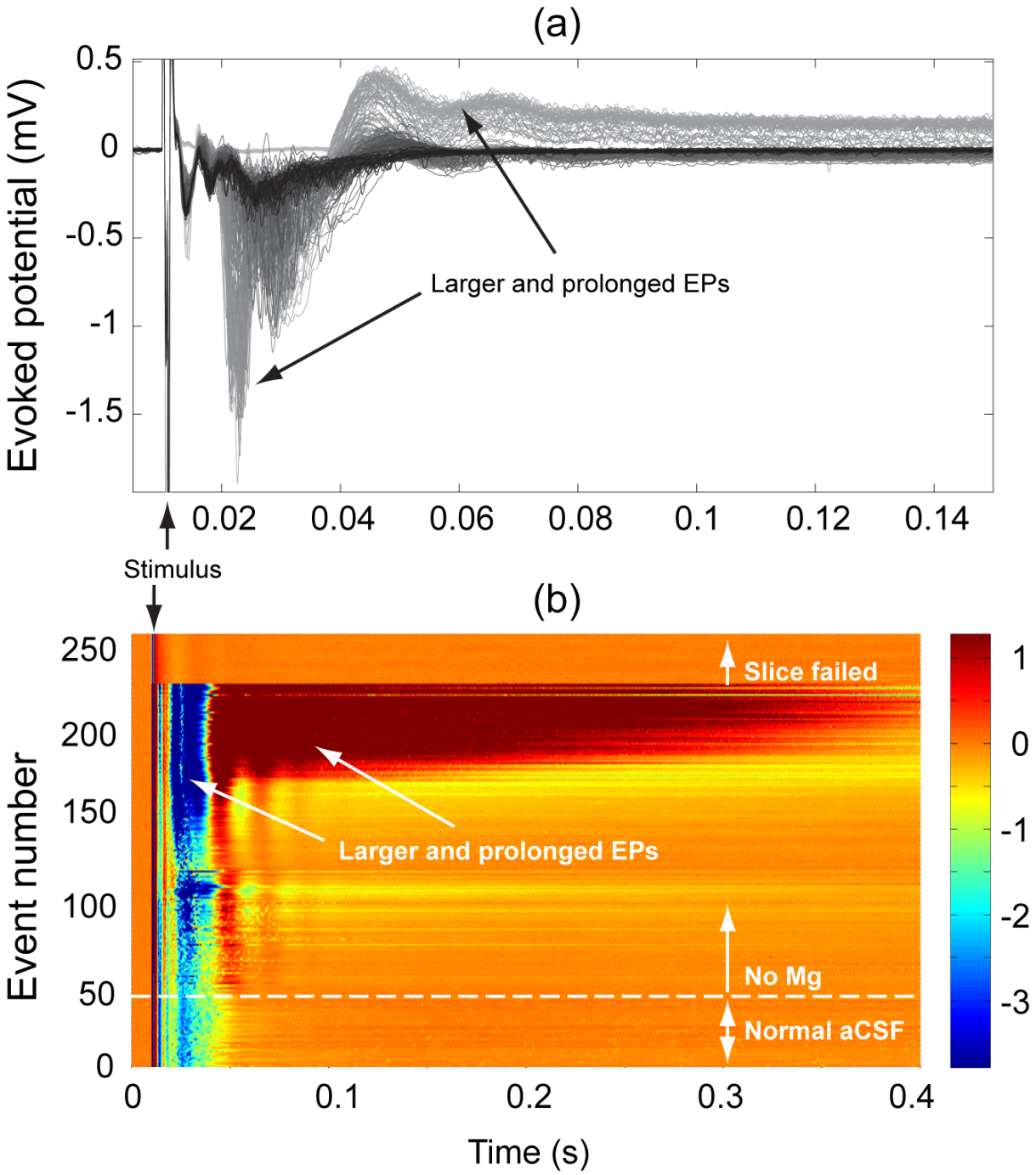

Figure 7.17: Prolongation of electrically evoked potentials (EPs) after gradual introduction of zero-Mg solution to mouse brain slices. Fifty EPs were recorded in normal aCSF, then zero-Mg solution was introduced to recording bath with the rate of 0.2 mL/s. The slice failed responding to electrical stimuli after producing 180 EPs.

as indicated by the dark-blue and dark-red colours.

Amplification and prolongation of evoked potentials is evident in this experiment. The gradual introduction of zero-Mg solution acts as a control parameter of the system and forwards it towards the threshold of state transition—seizure production in this case. Based on the

modelling work presented in previous chapters, and the experimental observations showing noise-induced signs of critical slowing prior to bifurcation points, I would expect to see corresponding precursors in stimulus or probing experiments as well. Based on these preliminary results, one could perform a comprehensive experimental *in vitro* study using a large number of animals to examine the effectiveness of neural probing for seizure prediction.

7.5 Chapter summary

The transition from the quiescent to the seizing state is a major qualitative change in the state of an epileptic neural circuit. In the theory of dynamical systems such changes are known as phase or state transitions, and bifurcation theory can be used to classify and study the behaviour of systems prior to such phase transitions. Prediction of phase transitions is shown to be theoretically possible, due to the occurrence of critical slowing down prior to the initiation of a phase transition at a turning point. For a critically slowed system, it takes divergently longer times to relax to rest in response to small perturbations. I presented slowing down in the Izhikevich and Wilson-Cowan models of individual neurons and neural populations in Chapters 3, 5 and 6, manifest as increased variance, autocorrelation and spectral power (at certain frequencies) as signs of close approach to the bifurcation point. Supported by this theoretical background, and motivated by the importance of seizure prediction, I have presented some preliminary experimental evidence for critical slowing down in the current chapter.

An *in vitro* animal model of human epilepsy was studied in which seizure-like events (SLEs) were induced in cortical and hippocampal circuits of mouse brain slices. The 400-µm coronal slices containing both cortical and hippocampal regions were perfused with an artificial cerebrospinal fluid (aCSF) to provide the *in vitro* platform for this study. By washing out the magnesium ions, excitatory NMDA receptor blockade was removed from the neurons, resulting in the development of cortical and hippocampal SLEs.

By constructing phase-plot diagrams, I performed a qualitative analysis of different stages of the epileptic neural activity, i.e., interictal, pre-ictal, seizure initiation, ictal, and seizure termination periods. This suggested the existence of a cascade of consecutive state transitions during progress through seizure generation, maintenance and termination. Distinct bifurcation types may be responsible for seizure generation and termination. Based on similar results Jirsa *et al.* [2014] have recently presented their "Epileptor" model and identified some universal features shared by the various seizure types.

The next step was to capture evidence of critical slowing down prior to state transition. I studied the LFP time-series before transition from the quiescent to seizing state. The challenging task of tracking the subtle changes in the variance, autocorrelation and power spectrum of the

time-series underscored the importance of recording *clean* LFPs. By applying proper electrical grounding and shielding methods, appropriate bipolar recording configurations, and selecting the same material for recording and ground electrodes, I recorded LFPs that were minimally corrupted by ambient noise, with negligible baseline drift. This allowed the frequency content of the biological signals to be kept intact in the range of 0–1000 Hz. The very low frequency components of the signal are of importance since they are presumed to carry information about critical slowing down.

I observed that precursors of bifurcations are more evident in larger and well-separated SLEs which also contain more morphological complexity in their pattern. Consequently, I focused on these hippocampal SLEs, intensified by the application of carbachol. This resulted in the generation of very long (∼20 s) seizure episodes. I was able to demonstrate signs of critical slowing in terms of increased variance and low-frequency spectral power. Flickering as another warning symptom was also observed in the recordings. I learned that uncovering signs of critical slowing is a very challenging task in slice experiments, and requires–

- minimization of noise sources in order to reduce the need for high-pass, low-pass, and notch filtering and consequent information loss, particularly at low frequencies
- elimination of DC drifts by using matched Ag/AgCl electrodes
- carefully paced slow delivery of seizure-inducing perfusion fluids to ensure very slow driving of the neural tissue towards seizure threshold

Considering all these factors, I found that only the generation of the strong, long and morphologically rich seizures are accompanied with identifiable precursor signals. In agreement with the "sick column" hypothesis presented by Stead *et al.* [2010][1], I argue that the slowing down signals may be captured if the LFP recording is obtained from the sick column or seizure-generating zone. This may describe why seizure precursors are not evident prior to every SLE. The chapter concluded with the presentation of the results of a neural probing experiment. Electrical stimuli were delivered to the cortical region, while the seizure promoting factor (removal of magnesium ions) was applied. The characteristics of the evoked potential (EPs) were investigated. An increase in the amplitude of the EPs and its temporal prolongation were observed while the system was being forwarded towards the seizing state.

To my knowledge these preliminary results for spontaneous tissue responses are the first reported observations of critical slowing down in an *in vitro* neural system. Its significance is in the confirmation of model predictions, and providing basic knowledge and background for developing novel seizure prediction algorithms.

[1]The sick column hypothesis states that the sparse small (comparable with the size of cortical microcolumns) cortical columns are the anatomical substrate of focal neocortical epilepsy.

Chapter 8

Summary and Future Work

8.1 Summary

This thesis has investigated some of the underpinning mechanisms of phase transitions in neural systems using mathematical and computer-based modelling as well as *in vitro* approaches. Employing concepts from dynamical systems theory, I was looking specifically for precursor indicators of sudden regime shifts. Phase transitions were studied at three different scales: single neuron, network and continuum. Models of single spiking neurons and networks of these were constructed using the Izhikevich formalism. Modifications were made to the original cortical and thalamic forms to generate realistic neural phenomena such as burst-suppression, gamma oscillations and sleep spindles. Precursor signs prior to phase transition were observed.

The spiking-neuron investigations were complemented by investigation of the Wilson–Cowan (WC) mean-field description of cortical networks. A range of spatiotemporal phase transitions were identified, and clear indications of critical slowing down prior to transition were observed both in time and space.

Motivated by these theoretical findings, the thesis moved onto a series of *in vitro* investigations of phase transition-like behaviour in slices of neural tissue. Different bifurcation classes were proposed to be responsible for the genesis and suppression of seizure-like events (SLE) in mouse brain slices. Promising signs of slowing down were observed prior to SLE onset and offset.

Phase transition in single spiking neurons

Two cortical (excitatory regular spiking RS, and inhibitory fast spiking FS) and two thalamic (excitatory thalamic relay TC and inhibitory reticular nucleus RTn) neural types were investigated with an emphasis on their subthreshold dynamics. The original Izhikevich RS model was altered to demonstrate metabolic-rate related cortical burst-suppression. The thalamic TC neuron was modified by incorporating a slow hyperpolarization-activated cation current (I_h) which plays an important role in sleep spindles. The types of bifurcation responsible for spike generation was identified for each neuron class. Noise-induced subthreshold fluctuations showed signs

of slowing down prior to spike generation. Increased sensitivity was observed for the modified RS neuron prior to burst-suppression, and for the modified TC neuron prior to bursting.

Precursors of phase transition in networks of spiking neurons

Two networks were constructed using both the original and modified forms of the Izhikevich spiking neuron:

- A cortical network composed of RS and FS neurons capable of producing gamma oscillations. A form of local field potential (LFP) was extracted from the network showing 30-Hz gamma oscillations as an emergent network activity. Transition from gamma to lower frequencies due to induction of anaesthesia was investigated. The network LFP displayed flickering (as a precursor of regime shift), bistability and hysteresis across the transition from gamma to slow oscillations.
- A three-neuron thalamocortical network composed of RS, TC and RTn neurons that generates sleep spindles. The output was comparable with *in vitro* results. The subthreshold fluctuations of the TC neuron showed increased variance as an early warning of spindle initiation.

Subthreshold dynamics of spatially homogeneous Wilson–Cowan model

A detailed investigation of the spatially homogeneous Wilson–Cowan (WC) mean-field model was presented. Saddle-node and Hopf mediated phase transitions were observed in the excitatory firing-rate time-series. Numerical analysis showed clear signs of slowing down in form of increased variance and autocorrelation functions prior to bifurcation. These numerical findings were in agreement with predictions from linear Ornstein–Uhlenbeck theory.

Spatiotemporal phase transitions in Wilson-Cowan cortical rod

The homogeneous WC model was extended to a one-dimensional neural mass (a "rod") by incorporating space-dependent excitatory and inhibitory fluxes. Obeying diffusion equations, these fluxes brought a rich dynamics to the system, supporting four type of phase transition: temporal saddle-node and Hopf, spatial Turing, and a mixed-mode Turing–Hopf interaction. Noise-induced subthreshold fluctuations demonstrated signs of critical slowing both in time and space, consistent with Ornstein–Uhlenbeck predictions.

In vitro experimental evidence of slowing down

These model-based theoretical findings encouraged me to look for experimental evidence of phase transition precursors. Zero-magnesium induced seizure-like events (SLEs) in mouse corticothalamic slices were selected as an *in vitro* model of neural phase transition. By ensuring proper differential recording methods with a carefully selected arrangement for recording, reference and ground electrodes, "clean" local field potential (LFP) signals were recorded from cortex and hippocampus, minimally contaminated with DC drift and 50-Hz interference. This ensured the fidelity of the SLEs in the frequency range 0–1000 Hz. A qualitative phase-plot analysis of the SLEs suggested a cascade of state transitions during onset, maintenance and termination of seizure events. Precursor signs of SLEs were observed only on large-amplitude, long and morphologically rich SLEs, and were evident as increased variance and spectral power at low frequencies. In addition to noise-induced signs of slowing down, I presented evidence for critical slowing in a neural probing experiment. An increase in the amplitude of the electrically evoked potentials was observed while the brain slice was being forwarded towards the seizing state by wash-out of magnesium ions.

8.2 Future Work

An obvious limitation of the neuron-by-neuron modelling studies of Chapter 4 is the small size of the presented networks. Networks with larger numbers of neurons should be developed to examine precursor signs prior to anaesthesia-induced phase transition, and before spindle initiation. In addition, the robustness of obtained results should be examined after introduction of heterogeneity to neuron parameter values.

Hopf–Turing instability was introduced as the only mixed-mode oscillation of 1-D WC model of cortical tissue in Section 6.3. It would also be interesting to study the dynamics of other codimension-2 mixed-mode interactions such as the saddle-node-Turing instability.

Section 7.4 demonstrated prolongation of evoked potentials prior to phase transition in mouse brain slice. The uniformity of presented results should be investigated in a comprehensive *in vitro* study using a large number of slice measurements. In parallel it would be informative to develop the equivalent mathematical and computer-based models of these experiments, and study the dynamics of the spatiotemporal indicators of phase transition onset.

Appendix A

A.1 Verification of wave equations in 1-D Wilson–Cowan model

Recall the definition of excitatory and input fluxes to population of type K as

$$\begin{aligned}\phi_{Ek}(x,t) &= \int_{-\infty}^{\infty} E(x',t)\, n_{Ek}(x-x')\, dx', \\ \phi_{Ik}(x,t) &= \int_{-\infty}^{\infty} I(x',t)\, n_{Ik}(x-x')\, dx' \qquad\qquad , \quad k \in \{E,I\}\end{aligned} \tag{A.1.1}$$

Here we proof the equations stated in 6.1.6, Chapter 6. Define Fourier transforms:

$$\begin{aligned}\tilde{\phi}_{Ek}(q,t) &= \frac{1}{2\pi}\int_{-\infty}^{+\infty} dx\ \phi_{Ek}(x,t)\mathrm{e}^{-iqx} \\ \tilde{E}_{Ek}(q,t) &= \frac{1}{2\pi}\int_{-\infty}^{+\infty} dx\ E_{Ek}(x,t)\mathrm{e}^{-iqx}\end{aligned} \tag{A.1.2}$$

and the corresponding inverse mappings:

$$\begin{aligned}\phi_{Ek}(x,t) &= \int_{-\infty}^{+\infty} dq\ \tilde{\phi}_{Ek}(q,t)\mathrm{e}^{iqx} \\ E_{Ek}(x,t) &= \int_{-\infty}^{+\infty} dq\ \tilde{E}_{Ek}(q,t)\mathrm{e}^{iqx}\end{aligned} \tag{A.1.3}$$

Considering the first equation in Eq. (A.1.1) as a convolution, its Fourier domain equivalent is

$$\tilde{\phi}_{Ek}(q,t) = 2\pi\tilde{E}(q,t)\cdot\tilde{n}(q) \tag{A.1.4}$$

Substitute (A.1.2, A.1.3) in first equation of (6.1.6)

$$\frac{1}{2\pi}\int_{-\infty}^{+\infty}(\Lambda_{Ek}^2+q^2)\tilde{\Phi}_{Ek}(q,t)\mathrm{e}^{-iqx}\ dq = \frac{1}{2\pi}\int_{-\infty}^{+\infty}\Lambda_{Ek}^2\tilde{E}(q,t)\mathrm{e}^{-iqx}\ dq \tag{A.1.5}$$

Equating integrands:

$$(\Lambda_{Ek}^2 + q^2)\tilde{\Phi}_{Ek}(q,t) = \Lambda_{Ek}^2 \tilde{E}(q,t) \tag{A.1.6}$$

using (A.1.4):

$$\tilde{n}(q) = \frac{1}{2\pi}\left(\frac{\Lambda_{Ek}^2}{\Lambda_{Ek}^2 + q^2}\right) \tag{A.1.7}$$

Note: From (6.1.4) :

$$\begin{aligned}
\tilde{n}(q) &= \frac{1}{2\pi}\left(\frac{\Lambda_{jk}}{2}\int_{-\infty}^{+\infty} dx\ \mathrm{e}^{-\Lambda_{jk}|x|}\mathrm{e}^{-iqx}\right) \\
&= \frac{\Lambda_{jk}}{2(2\pi)}\left\{\int_{-\infty}^{0} dx\ \mathrm{e}^{\Lambda_{jk}x - iqx} + \int_{0}^{\infty} dx\ \mathrm{e}^{-\Lambda_{jk}x - iqx}\right\} \\
&= \frac{\Lambda_{jk}}{2(2\pi)}\left\{\left[\frac{\mathrm{e}^{\Lambda_{jk}x - iqx}}{\Lambda_{jk} - iq}\right]_{-\infty}^{0} + \left[\frac{\mathrm{e}^{-\Lambda_{jk}x - iqx}}{-(\Lambda_{jk} + iq)}\right]_{0}^{+\infty}\right\} \\
&= \frac{\Lambda_{jk}}{2(2\pi)}\left[\frac{1}{\Lambda_{jk} - iq} + \frac{1}{\Lambda_{jk} + iq}\right] \\
&= \frac{\Lambda_{jk}}{2(2\pi)}\left[\frac{\Lambda_{jk} + iq + \Lambda_{jk} - iq}{\Lambda_{jk}^2 + q^2}\right] = \frac{1}{2\pi}\left(\frac{\Lambda_{jk}^2}{\Lambda_{jk}^2 + q^2}\right)
\end{aligned} \tag{A.1.8}$$

which is the same result as (A.1.7). Thus $n(x) = \frac{\Lambda_{Ek}}{2}\mathrm{e}^{-\Lambda_{Ek}|x|}$ and $\Phi_{Ek}(x,t)$ satisfy Eq. (6.1.6).

Appendix B

B.1 Chemically versus electrically chlorided Ag/AgCl microelectrodes

Figure B.1 shows that the two Ag/AgCl electrodes made by two chloriding methods have comparable performance when recording from brain tissue in its silent regime (normal aCSF). These results are based on simultaneous recordings from two different points on a slice.

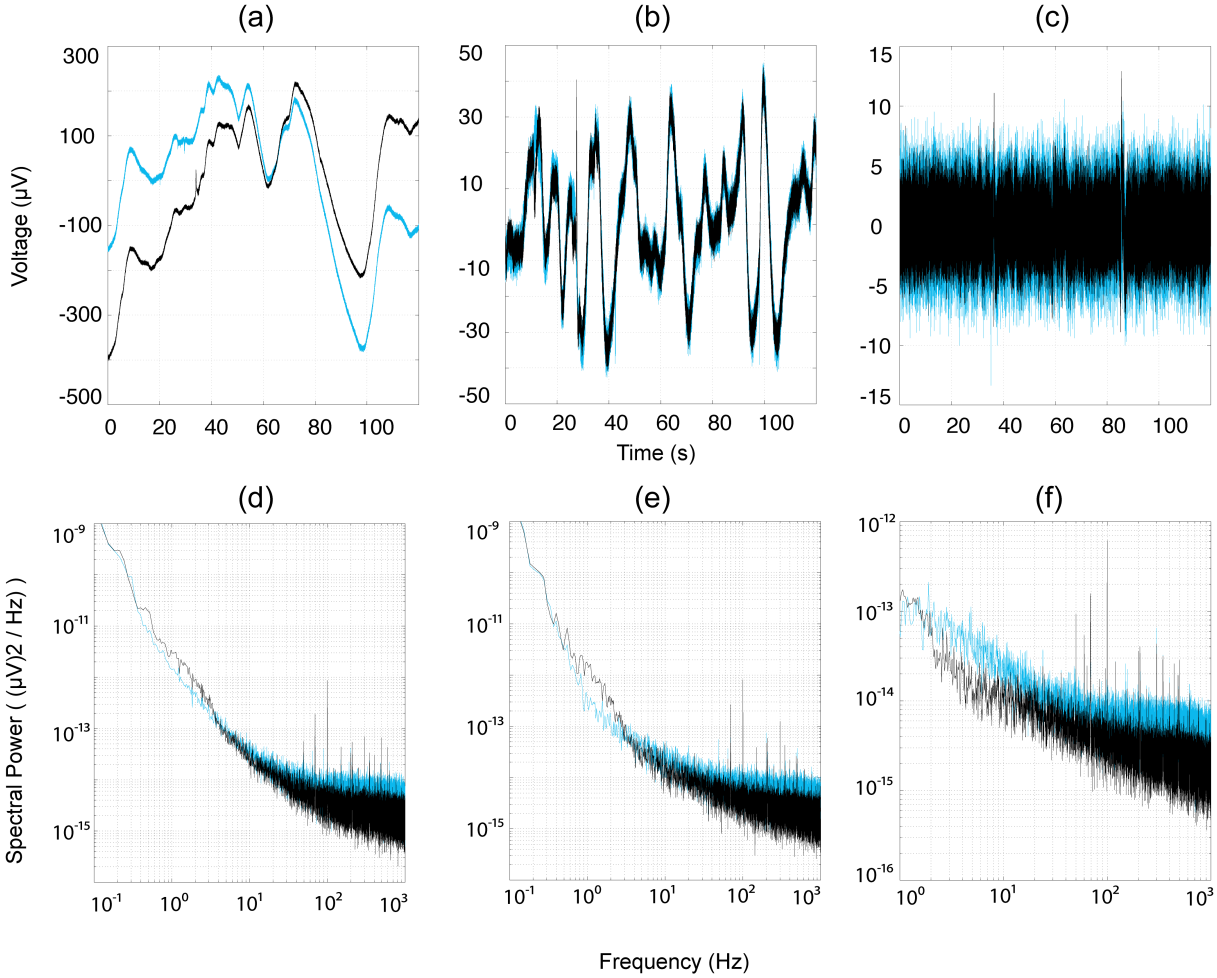

Figure B.1: Comparison between the performance of electrically (black) and chemically (blue) chlorided 50 micron Ag/AgCl electrodes. (a-c) The voltage signals from a non-seizing cortical slice with different high-pass filter settings, 0, 0.1, 1 Hz respectively. The low-pass cut-off frequency is 1000 Hz for all records. Both signals look similar in terms of peak to peak amplitude. The corresponding spectral graphs shown in (d-f) reveal similar spectral content.

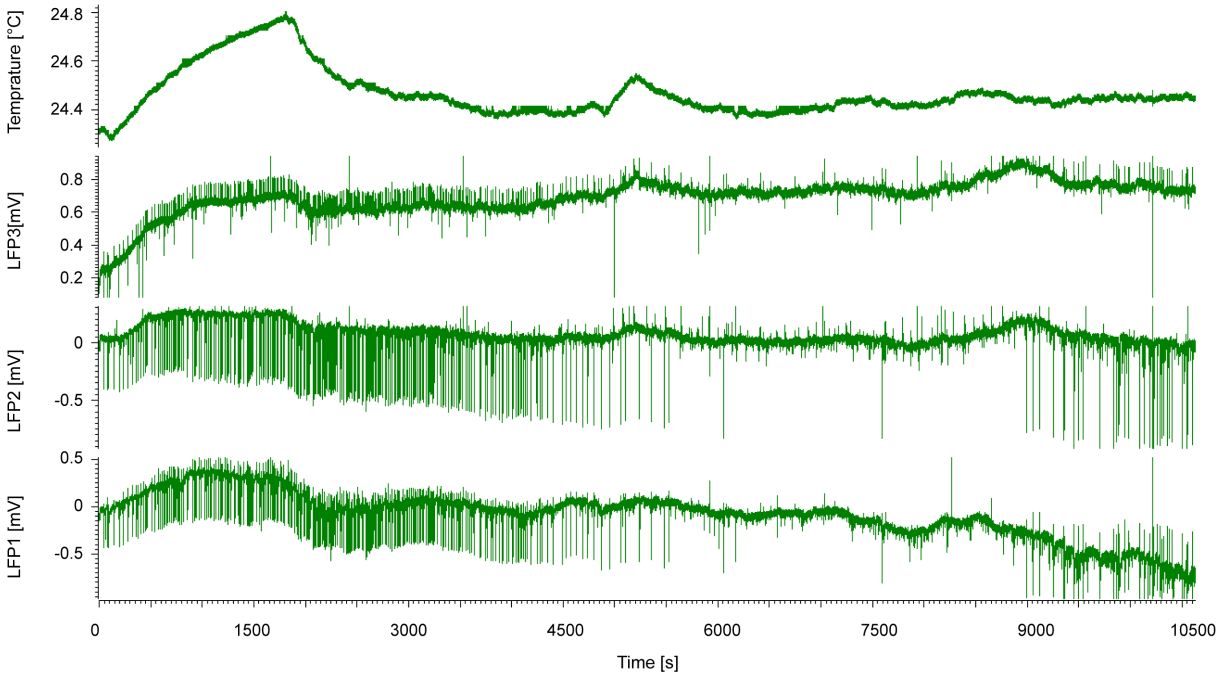

Figure B.2: ACSF temperature and baseline drift. Top to bottom are the temperature of the recording bath and the three LFP signals recorded from distinct points on the cortical region of an active seizing mouse brain slice. The 50 µm Ag/AgCl electrodes are arranged in differential mode to record LFPs. The settings for dc recording and low-pass filter are 0 and 1000 Hz respectively. A small variation of the temperature of recording bath induces baseline drift in all three channels. The individual spikes are zero-magnesium seizure-like events.

B.2 Correlation between temperature and DC offset

Here I demonstrate a possible correlation between aCSF temperature and the DC offset voltage in brain slices. Figure B.2 displays the temperature of the recording chamber (top) and simultaneous LFP records from three distinct cortical points in the mouse brain slice (three bottom traces). A visual inspection suggests a correlation between temperature and baseline drift.

B.3 Low-amplitude signal generator

The low-amplitude signal generator[1] was used to test the operational performance of the bioamplifiers. The reference signal produced with this device can be fed into different bioamplifiers and their outputs monitored for possible discrepancies. The schematic diagram of the low-amplitude signal generator is displayed in Fig. B.3. The main component of the device is the MAX038CPP 9741 integrated circuit (IC 1 in the figure), a precision function generator configured here to generate 1-Hz and 10-Hz sinusoidal, triangular, square-wave test signals of amplitude of $\sim$90 μV_{pp}, which is in the range of typical EEG and LFP signals.

[1]Designed by Jon Henderson, built by technician Stewart Finlay

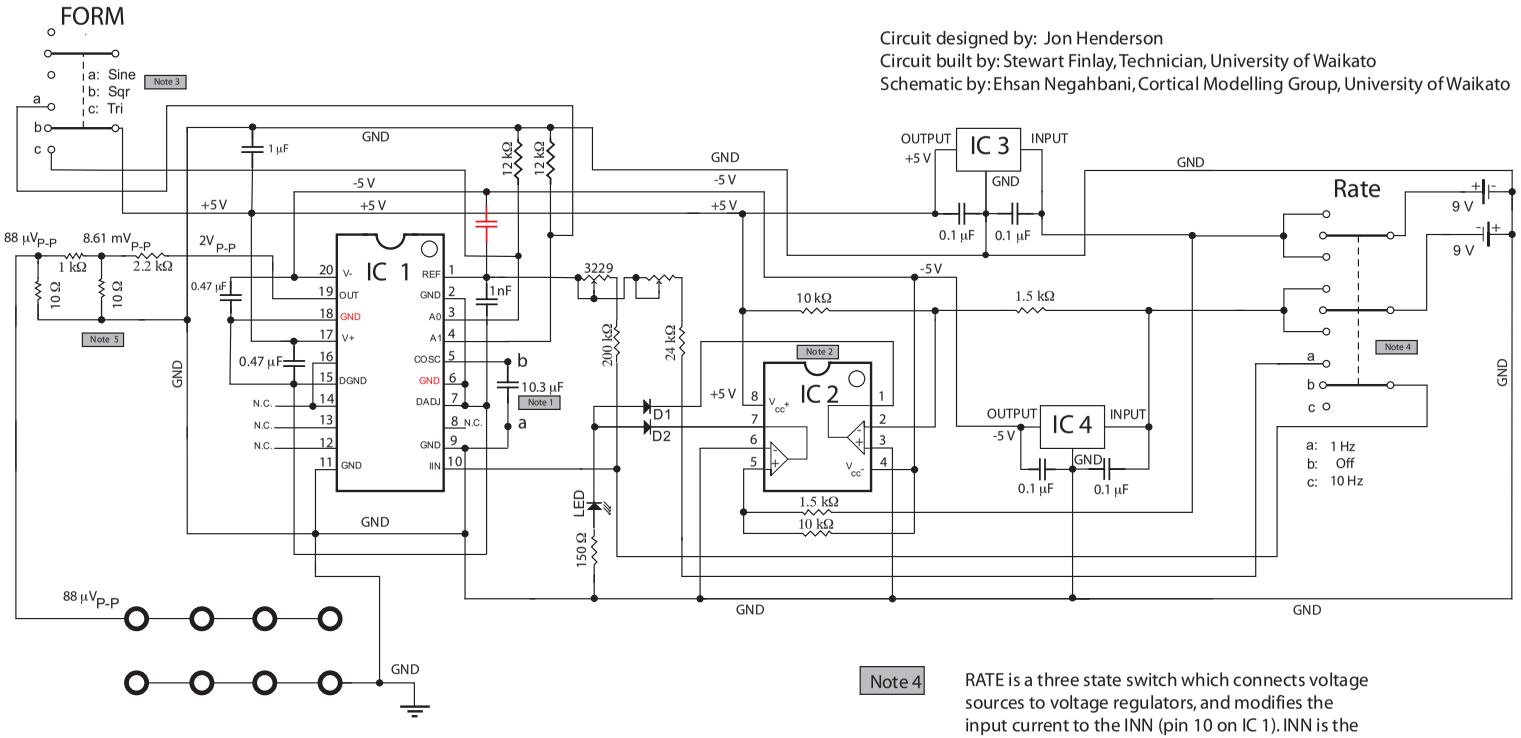

Note 1 A 10.3 μF polyester capacitor has a large dimension that made it impossible to use in a small case. 5 smaller capacitors were used in parallel to have a small case., as shown:

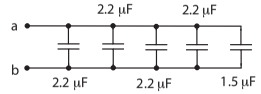

Note 2 IC 2 provides a power supply battery-low circuit, as shown:

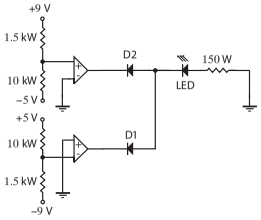

Note 3 FORM is a three state switch works as a waveform selector. This switch provides 0 volt or +5 volt to the TTL/CMOS-logic address pins (A0, A1), as shown:

A0	A1	Wave Form
X	1	Sine Wave
0	0	Square Wave
1	0	Triangle Wave

Note 4 RATE is a three state switch which connects voltage sources to voltage regulators, and modifies the input current to the INN (pin 10 on IC 1). INN is the current input for frequency control. A reference voltage (+2.5 Volts) s applied to two variable resistors (which can be selected by RATE switch) and is applied to INN input. Variable resistors can be adjuusted to achive 1 Hz and 10 Hz in the output pin.

Note 5 The output signal for all waveforms is a 88.71 μVP-P signal that is symmetrical around ground. A ladder attenuator is used to get a 90 μV_pp as the output for EEG callibration. Detailes are as shown:

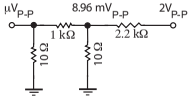

IC 1 MAX038CPP 9741: Is a high-frequency, precision function generator producing accurate, high-frequency triangle, sawtooth, sine, square, and pulse waveforms with a minimum of external components.

IC 2 TL062CN 91A701: Low power J-FET dual operational amplifiers

IC 3 7805 : 3-terminal positive regulator (+5 Volts)

IC 4 7905 : 3-terminal negative regulator (-5 Volts)

D1, D2 : 1N4001

Figure B.3: Schematic diagram for low-amplitude signal generator

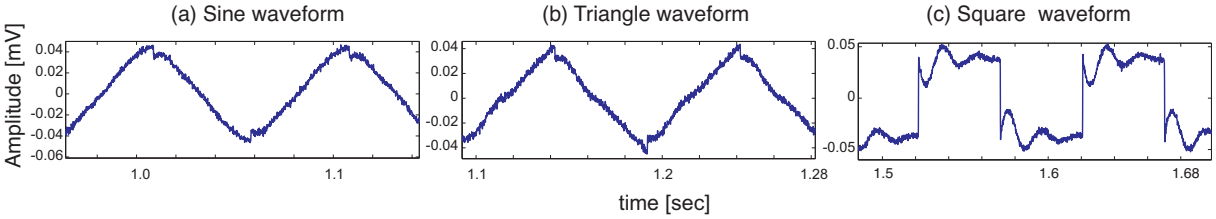

Figure B.4: Low voltage calibration signals. (a) sine, (b) triangle, and (c) square waveforms as recorded with bioamplifiers. The output frequency is 10 Hz. The amplification is $\times 10,000$ and the cutoff frequency settings on the bioamplifier are 0.1 and 3000 Hz for high- and low-pass filters. To plot the recorded signals, the amplitudes have been divided by the gain of the amplifier.

A sample record of the three different 10-Hz waveforms produced by this small-amplitude signal generator is shown in Fig. B.4.

B.4 Inherent noise of A-M bioamplifiers and CED analogue-to-digital converter

Figure B.5 shows the result of simultaneous recordings by four different amplifiers and a direct recording via analogue-to-digital converter (ADC) with their respective inputs configured as short circuits. This figure shows the results of an experiment to ensure that the performance of amplifiers is similar and comparable. Since all amplifiers have identical settings, one expects similar outputs which represent the amplifier's internal noise levels. Any channel showing different behaviour should be considered faulty and may need repair or calibration. Based on the connection diagram on the top panel of Fig. B.5, the input terminals of each of the four headstages (preamplifiers with fixed gain of $\times 50$) were connected together to make the short circuit. Headstage outputs were connected to the amplifiers with a bandpass range of 0–1000 Hz and amplification gain of $\times 200$. Each amplifier output was fed into the ADC with sampling frequency of 2 kHz. The sample records are displayed in Fig. B.5 (b–e), corresponding to the internal noise levels of each amplifier. The power spectra are depicted on the right panel (g-j). Note that all voltage traces and power spectra are comparable, indicating matched amplifiers. Panels (f) and (k) show the result of the record from a short-circuit connection applied directly to one of the ADC channels in order to capture the noise level of the ADC.

B.5 Methodology of neural probing experiments

This experiment was performed on a 400-µm slice of coronal mouse brain tissue. Electrical stimulation was delivered to white matter underlying the cortex using a voltage source capable of delivering a preset voltage waveform regardless of variations in the impedance of the target tissue. The voltage stimulation is applied via a bipolar configuration of 75-µm tungsten electrodes. The

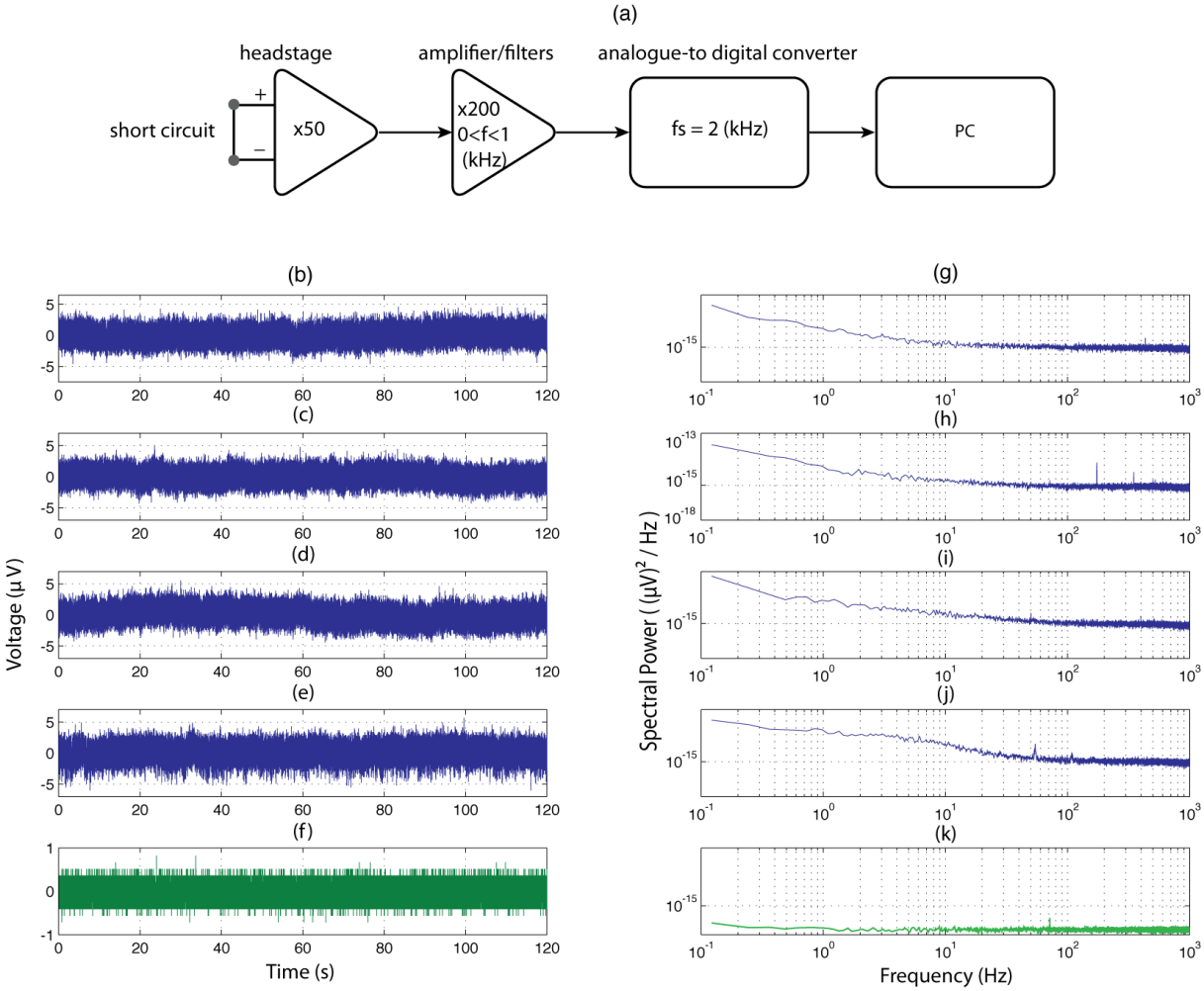

Figure B.5: Simultaneous monitoring of the inherent noise levels of A-M bioamplifiers and the CED analogue to digital converter (ADC). (a) Schematic diagram of the experimental setup showing a connection between a headstage (HDSTG), a bioamplifier and the ADC. The experiments are carried out using same amplifier gains (×1000) and frequency ranges (0–1000 Hz), without using the notch filter. The four bioamplifiers are connected to four input channels on the ADC. A short circuit is applied to the headstages. The four resultant digital outputs of ADC are displayed in panels (b–e). The inherent noise level of the ADC is obtained by applying a short-circuit to its fifth input and the resultant voltage is displayed in (f). For each voltage trace, the related power spectrum is displayed on the right panels (g-k).

evoked potentials (EPs) were recorded from neocortex directly above the stimulation area (using a 25-µm tungsten recording electrode in the tissue and a platinum electrode as the reference electrode in the recording bath) in bipolar mode. A large circular Ag/AgCl electrode was used as the ground in the bath. The recorded signal was filtered, amplified, digitized and recorded for further analysis. The high- and low-pass filter settings, amplifier gain and sampling frequency were 0.1 Hz, 1000 Hz, ×1000, 1 kHz respectively. The stimulation voltage was set to be a biphasic ±1 V square impulse pair, 100 ms per pulse, with a pulse separation of 1 ms as displayed in Fig. B.6.

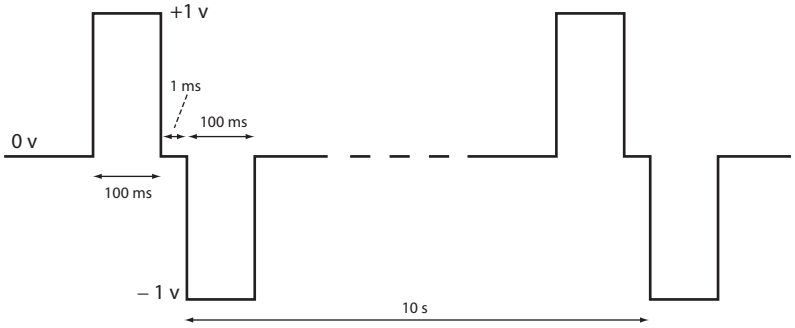

Figure B.6: The biphasic voltage stimulation in evoked potential experiment

This biphasic stimulus pattern was delivered every 10 s. The tissue was kept shallow submerged, but was prevented from drying. About 50 EPs were recorded while the slice was perfused with normal aCSF. Thereafter, the normal solution was replaced by zero-Mg solution while the stimulation and recording processes were continued for about 200 more EP tracks. At that point the slice failed to generate EPs due to mechanical disturbance generated in the holding bath. Large-amplitude artifacts were removed from the LFP recording by visual inspection. Individual EPs were extracted and time-aligned based on the stimulus start point. Data were recorded using `Spike2` software, and the event extraction and other preliminary signal processing methods were implemented in MATLAB.

B.6 Performance of notch filter

The A-M bioamplifiears have a notch filter designed to eliminate 50 Hz mains interference while keeping other frequency content intact. The specific attenuation of the notch filter is -50 dB. The User Manual emphasizes that the notch filter should only be used if other noise reduction techniques such as proper grounding and shielding are inadequate, since this filter causes some signal distortion for frequency components below 100 Hz. Here I demonstrate the effect of the notch filter to remove 50 Hz interference. Two 10 s voltage signals (one with notch filter off and the other with notch on) are recorded from artificial cerebreospinal fluid (aCSF), and the resulting power spectra displayed in Figure B.7 in logarithmic (a) and linear (b) frequency scales. The spectra show the result of notch filtering as an attenuation around 50 Hz, and an attenuation of only the second harmonic at 100 Hz; all other harmonics of 50 Hz are still present. Note that using differential (rather than monopolar) electrode configuration enables us to attenuate the 50-Hz interference considerably without using the notch filter: see Fig. B.8. The low frequency component of the background noise ($f < 10$ Hz) is also reduced considerably compared to monopolar record.

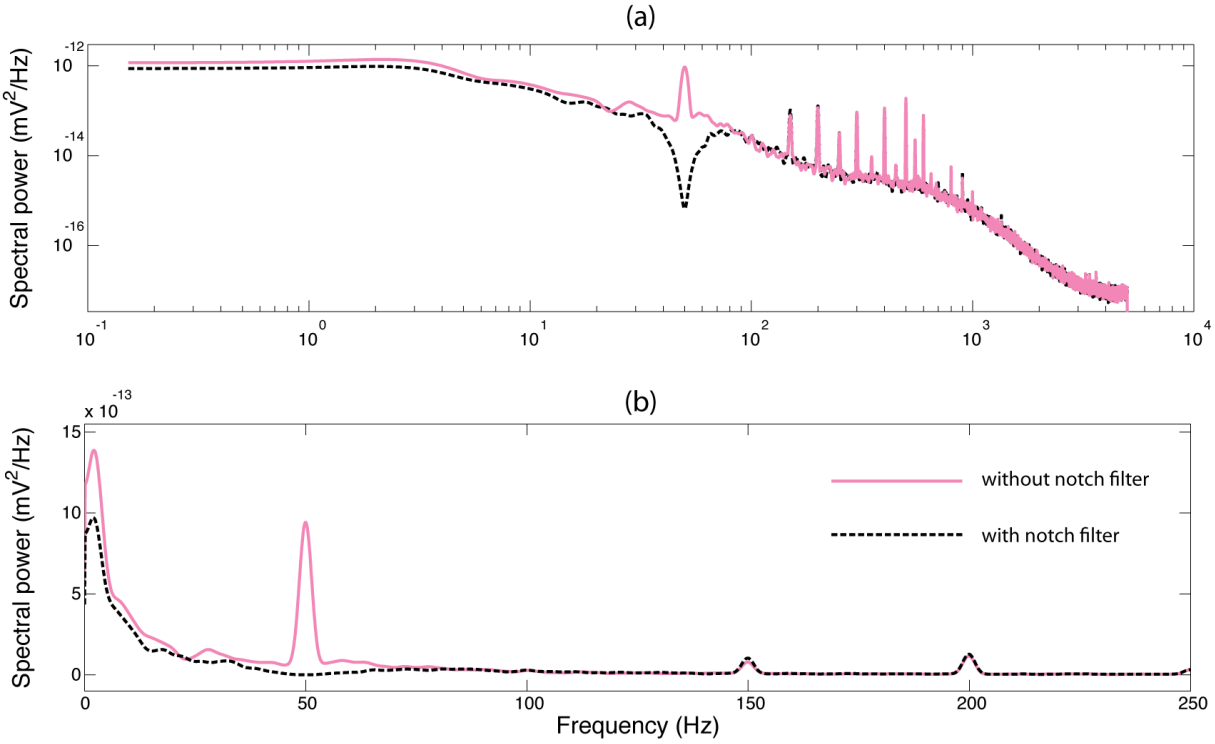

Figure B.7: Spectra of sample records from normal artificial cerebrospinal fluid (aCSF) in the recording bath to demonstrate the effect of notch filtering. The signal was recorded using a monopolar configuration while the door of Faraday cage and door of the shielded room were left open, causing the trace to be contaminated by 50-Hz mains noise. (a) Resulting power spectra without (solid line) and with (dashed line) 50-Hz notch filter in logarithmic, and (b) linear frequency scales. The sampling frequency was 10 kHz and the signal length was 10 s. The signal was recorded using 50 µm Ag/AgCl recording electrode and a disk shaped reference electrode made from the same material.

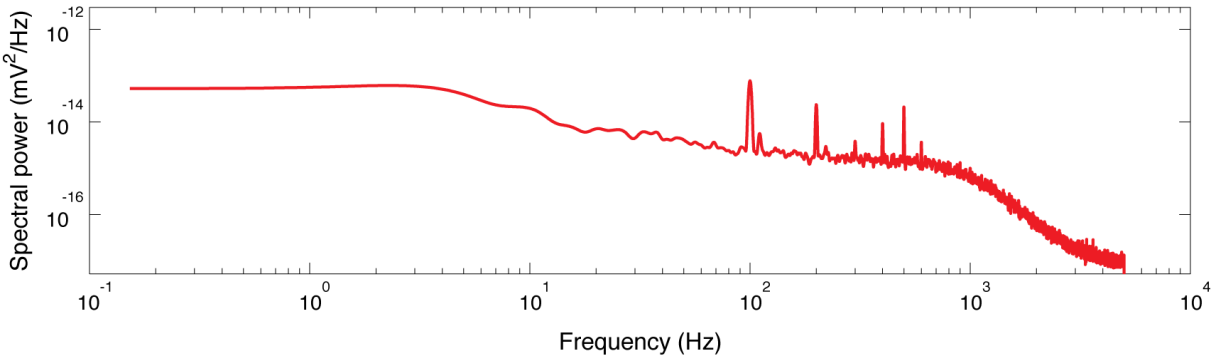

Figure B.8: Differential mode eliminates the common-mode 50-Hz interference. The recording is similar to the ones demonstrated in Fig. B.7, but here a differential mode is used instead of monopolar configuration.

Appendix C

C.1 Whittaker smoother

The Whittaker smoother is a computationally efficient method to extract the trend of fluctuating data. It is mainly used for noise-removal purposes, but is used as a trend extractor in this thesis. See Eilers [2003] for more details. The method can easily be implemented in MATLAB as below:

Whittaker.m

```
function [xsmooth, xrough] = whittaker(x, Fs, smo)
% function [xsmooth, xrough] = whittaker(x, Fs, smo)
% Decompose x into smooth and rough components using Whittaker filter
% ASR: Feb 22, 2006, based on Jamie Sleigh's code
% JWS: Input Fs and smoothing parameter smo (usually ~50)

lambda = smo*Fs;
m = length(x);
E = speye(m);
D = diff(E, 2);
if size(x, 1) == 1
    x = x';
end
z = (E + lambda * (D' * D)) " x;
xsmooth = z;
xrough = x - z;
```

C.2 Spindle extraction

Here I describe the algorithm and MATLAB code to automatically extract simulated spindles as displayed in Fig. 4.8(a). I apply a low-pass filter to extract a smooth waveform from the mean-removed and rectified membrane voltage of the regular spiking (RS) cortical neuron. The amplitude of the filtered signal is compared against a threshold to locate the onset and termination of a spindle, corresponding to a bundle or burst of action potentials. The filter characteristics and the threshold setting were determined by trial-and-error. I obtained good results using a third-order Butterworth filter with normalized cutoff frequency of 0.00008. The mean-removed

rectified signal is filtered in forward and reverse directions (using MATLAB `filtfilt`) to eliminate phase distortion. Then a threshold value of 2.6 mV is used to detect spindle events. The corresponding MATLAB code is presented here. After locating the spindles, it is easy to calculate their width and interspindle gaps (see Fig. 4.8(b, c)). Except for the false identification of an event as a spindle (the first "spindle" in Fig. 4.8), the spindle extraction is generally quite reliable.

Spindle-extraction.m

```
function [spindle] = Spindle-extraction(vrs) % vrs is the voltage of RS neuron
% design a simple first-order Butterworth filter
[B,A] = butter(3, 0.00008);       % order, normalized cut-off freq
vrs = vrs-mean(vrs);
vrs = vrs.*(vrs>0);
% apply Butterworth filter to synthetic data
y2 = filtfilt(B, A, vrs); % zero phase distortion filtering
% apply threshold test to y2 to locate the spindles
spindle = (y2 > 2.6);
```

C.3 Steady state locator

The `steady-state-locator.m` is a MATLAB function capable of locating steady states of Wilson–Cowan model. Based on an iterative numerical algorithm and employing MATLAB's standard `fzero` function, `steady-state-locator.m` requires two input arguments (`P` external excitatory stimulus and `Nsearch` number of search iterations) to return any existing excitatory and inhibitory steady states.

Steady-state-locator.m

```
function [E_root, I_root] = WiCo_ss_finder(P, Nsearch)
if nargin == 0
        [P] = deal(0.075);
        Nsearch = 8000;
end
global H; A = cell(3,5);
H = WiCo_init_globs_q; % recall model parameters and constants
n_roots = 0;
Nsearch_max = 5000000;
while ((n_roots == 0) && Nsearch <= Nsearch_max)
    % define search span of E and I
    E_1 = [linspace(0+eps, 1e-3, 1e6) linspace(1e-3, H.Emax-1e-3, 1e5),...
             linspace(H.Emax-1e-3, H.Emax-eps, 1e5)]';
    I_1 = [linspace(0+eps, 1e-3, 1e6) linspace(1e-3, H.Imax-1e-3, 1e5),...
             linspace(H.Imax-1e-3, H.Imax-eps, 1e5)]';
    [err_E] = E_resid(E_1, P);
    % Count the number of E roots (look for sign-change in residuals)
    chs_E = err_E(1:end-1) .* err_E(2:end);
    chs_E_index = find(chs_E < 0);
    n_roots = length(chs_E_index);
    if (n_roots == 0 || n_roots == 2)
```

```
        Nsearch = 2*Nsearch;
        disp(['Doubling Nsearch to ' num2str(Nsearch)]);
    end
end
if n_roots == 0
    msg1 = '...failed to find a root at';
    msg2 = '  [H.Pcent, H.Qcent, R, P] =';
    fprintf('"n%s "n %s "n   [ %g  %g  %g  %g ] ---skipped!"n"n', ...
        msg1, msg2, ...
        [H.Pcent, H.Qcent, H.R, P]);
end
% Form a bracketting interval for each root
if n_roots >= 1
    brack_E = [E_1(chs_E_index )  E_1(chs_E_index + 1)];
    % Check for NaN at either end of bracket
    if any(isnan(brack_E(:)))
        error('Detected NaN in a bracket!');
    end
end
% Polish each E root, and retrieve corresponding I root
[E_root I_root] = deal(NaN*ones(n_roots, 1));
for i = 1: n_roots
    E_root(i) = fzero(@ E_resid, brack_E(i,:), [], [], P);
    %         using dE/dt isocline to find I_root:
    I_root(i) = dE_dt_isocline(E_root(i), P);
end
[E_root, IX] = sort(E_root, 'descend');
I_root_temp = NaN(size(I_root));
for i=1:length(IX)
    I_root_temp(i) = I_root(IX(i));
end
I_root = I_root_temp;
% ---------------------------------------------------------------------
% Solve the dE/dt and dI/dt isocline equations, and report discrepancy
% between initial E_1 values and derived E_3 values.
function [err_E] = E_resid(E_1, P)
I_2 = dE_dt_isocline(E_1, P);
% now solve dI/dt=0 isocline using I_2 to give E_3
E_3 = dI_dt_isocline(I_2, P);
err_E = E_3 - E_1;
end
% ---------------------------------------------------------------------
% Given E_ss, solve the dE/dt isocline equation for I_ss.
function I_ss = dE_dt_isocline(E_ss, P)
global H
I_ss = (invEsig(E_ss) - H.bb(1, 1)*E_ss+H.bb(1, 3)*P - H.Pcent)./-H.bb(1, 2);
if I_ss>H.Imax; I_ss = H.Imax-eps;end
if I_ss<0; I_ss = eps;end
end
% ---------------------------------------------------------------------
% Given I, solve the dI/dt isocline equation for E.
function E_ss = dI_dt_isocline(I_ss, P)
```

```
74 global H
75 E_ss = (invIsig(I_ss) + H.bb(2, 2)*I_ss + H.bb(2, 3)*P - H.Qcent)./H.bb(2, 1);
76 if E_ss>H.Emax; E_ss = H.Emax-eps;end
77 if E_ss<0; E_ss = eps;end
78 end
79 %---------------------------------------------------------------------
80 % Inverse of excitatory sigmoid function; output in millivolts
81 function  invsig = invEsig(val)
82 global H
83 invsig = NaN*ones(size(val));
84 ok = find(val > 0 & val < H.Emax);
85 % without these checks, the algorithm fails
86 % to find the third root which is very close to the origin:
87 invsig(ok) = H.theta - (1/H.a)*log(H.Emax./val(ok) - 1);
88 invsig(val < 0) = H.theta - (1/H.a)*log(H.Emax./eps - 1);
89 invsig(val > H.Emax) = H.theta - (1/H.a)*log(H.Emax./(1-eps) - 1);
90 end
91 %---------------------------------------------------------------------
92 % Inverse of excitatory sigmoid function; output in millivolts
93 function  invsig = invIsig(val)
94 global H
95 invsig = NaN*ones(size(val));
96 ok = find(val > 0 & val < H.Imax);
97 % without these checks, the algorithm fails
98 % to find the third root which is very close to the origin:
99 invsig(ok) = H.theta - (1/H.a)*log(H.Imax./val(ok) - 1);
100 invsig(val < 0) = H.theta - (1/H.a)*log(H.Imax./eps - 1);
101 invsig(val > H.Imax) = H.theta - (1/H.a)*log(H.Imax./(H.Imax - eps) - 1);
102 end
103 % ---------------------------------------------------------------------
104 % Matlab's standard fzero function:
105 function b = fzero(FunFcn, x, tol, trace, varargin)
106         % A copy Matlab's standard fzero function comes here
107 end
```

C.4 Numerical simulation of 1-D Wilson–Cowan network

The Euler implementation of 1-D Wilson–Cowan model is presented in this Appendix. The code demonstrates pre-Turing and pre-Hopf simulations (using `TurHopf` flag) in response to delta function or continuously applied white noise (using `ImpStoch` flag). One can reproduce Figs. 6.15(a-c), Fig. 6.19(a-c) by setting `ImpStoch=0`.

Initial values for E and I firing rates set to the steady state values extracted from intersection of model nullclines.

Lines 48–53 demonstrate how white noise is added to the initial steady-state values. To expedite Turing emergence, the network is energized with boosted noise at the first time-step, then the noise amplitude is attenuated (line 48) thereafter.

The fixed-step Euler method uses model derivatives (computed by nested function `EI_derivs` on line 92) to update E and I activities. Spatiotemporally uncorrelated white noise is generated using `Matlab`'s `randn` function at every time step (lines 98, 99), but is inactivated (`sf`=0 for the impulse runs).

Very long simulations are needed (`Last=1000, 5000` for pre-Hopf and pre-Turing cases respectively) with very fine time-steps (`dt=0.005` ms) in order to obtain fully evolved patterns similar to Figs. 6.15(a-c), Fig. 6.19(a-c).

```
1  function JMNS_demo_code
2  % Demonstration code for integrating the Wilson-Cowan 1-D neural equations
3
4  %% flags
5  ImpStoch = 1;  % 1 for impulse response, 0 for stochastic simulation
6  TurHopf = 1;   % 1 for pre-Turing, 0 for pre-Hopf simulation
7
8  %% Define the 1-D space domain
9  L = 6000;                   % length of cortical rod (um)
10 dx = 1.5;                   % spatial resolution (um)
11 X = [-L/2: dx: L/2]';       % cortical rod as a column vector (um)
12 N = length(X);              % number of elements in the rod
13
14 %% Define the Eq. (4) connectivity kernels
15 if TurHopf % pre-Turing:
16    [b_EE  b_EI  b_IE  b_II]  = deal(18, 10, 19, 0);   % synaptic strength
17    [sigEE sigEI sigIE sigII] = deal(50, 148.5, 148.5, 20);% synaptic range
18 else     % pre-Hopf:
19    [b_EE  b_EI  b_IE  b_II]  = deal(18, 10, 19, 0);   % synaptic strength
20    [sigEE sigEI sigIE sigII] = deal(43, 42, 42, 20);  % synaptic range
21 end
22 wEE = b_EE/(2*sigEE) * exp(-abs(X)/sigEE);
23 wEI = b_EI/(2*sigEI) * exp(-abs(X)/sigEI);
24 wIE = b_IE/(2*sigIE) * exp(-abs(X)/sigIE);
25 wII = b_II/(2*sigII) * exp(-abs(X)/sigII);  % (not used since b_II = 0)
26
27 %% Set up the time-base
28 dt = 0.005*10;        % integration time step (ms)
29 Last = 1000;          % duration of simulation (ms)
30 tspan = 0: dt: Last;            Nsteps = length(tspan);
31
32 %% Initialize the noise attenuation and the noise scaling factor
33 if ImpStoch,     noise_att = 0; else   noise_att = 1e-10; end
34 sf = noise_att./sqrt(dt*dx);          % noise scaling factor
35
36 %% Sigmoid definitions
37 [a, theta] = deal(9, 2.2);      % sigmoid gain (1/mV) and threshold (mV)
38 [Emax Imax] = deal(0.1, 0.15);  % maximum firing rates (1/ms)
39
40 SigmoidE = @(v) Emax./(1 + exp(-a*(v - theta)));
41 SigmoidI = @(v) Imax./(1 + exp(-a*(v - theta)));
42
43 %% Initial conditions and other parameter settings
44 [tau_E, tau_I] = deal(10, 8);      % ms
45 E = zeros(N, Nsteps);       I = zeros(N, 1);
46 if TurHopf % pre-Turing (refer to Fig.  4 and Table 1 for P, Q values):
```

```
    [P, Q] = deal(2.4, 1.35);      % mV
    E(:, 1) = 0.087034901273651 + randn(N, 1)*sf; sf = 0.1*sf;
    I(:, 1) = 0.081851136336899 + randn(N, 1)*sf;
else    % pre-Hopf (refer to Fig.  4 and Table 1 for P, Q values):
    [P, Q] = deal(2.1984, 1.35);   % mV
    E(:, 1) =  0.083346268256679 + randn(N, 1)*sf;
    I(:, 1) =  0.069458670491093 + randn(N, 1)*sf;
end

if ImpStoch      % apply delta-like spike to central grid point
    E(round(N/2),1) = 0.1;    I(round(N/2),1) = 0.110;
end

%% Euler integration of Wilson-Cowan equations
for i = 2:length(tspan)

    EI_derivs = WilCo_dot();

    E(:, i) = E(:, i-1) + dt*(EI_derivs(:, 1));  % record E-activity
    I = I + dt*(EI_derivs(:, 2));      % (but don't save I-activity)

    if mod(i, 100) == 1         % show progress graphs
        if TurHopf
            figure(2); clf; hold on; plot(X, [E(:, i)]);
            title(sprintf('pre-Turing E-activity:: i = %d/%d', i,...
                length(tspan)), 'fontsize', 16);
            xlabel('X (um)', 'fontsize', 14); zoom on; grid on;
        else
            figure(2); clf; hold on;
            plot(tspan(1:i-1), E(round(N/2), 1:i-1));
            xlabel('t (ms)'); ylabel('E (1/ms)');
            title(sprintf('pre-Hopf activity, central point:: i = %d/%d'...
                ,i,length(tspan)), 'fontsize', 16);
        end
    end
end

%% Plot the time-space graphs
figure(5); clf; imagesc(tspan(length(tspan)/10:end), X, ...
        E(:, (length(tspan)/10):end)); colorbar;
xlabel('t (ms)'); ylabel('X (um)');
if TurHopf,  title('pre-Turing'); else title('pre-Hopf'); end

%% Stochastic Wilson-Cowan DEs in one spatial dimension,
% with uncorrelated noise in time and space
    function EI_derivs = WilCo_dot()

      Evolt = ifftshift( cconv(wEE, dx*E(:, i-1), N) - ...
            cconv(wIE, dx*I, N) ) + P;
        Ivolt = ifftshift( cconv(wEI, dx*E(:, i-1), N)  ) + Q;

        deriv1 = ( -E(:, i-1) + SigmoidE(Evolt) + randn(N, 1)*sf)/tau_E;
        deriv2 = ( -I         + SigmoidI(Ivolt) + randn(N, 1)*sf)/tau_I;

        EI_derivs = [deriv1, deriv2];
    end

end
```

References

Abbott, L. and Kepler, T. Model neurons: From Hodgkin–Huxley to Hopfield. In *Statistical Mechanics of Neural Networks*. Springer, 1990.

Akrawi, W. P., Drummond, J. C., Kalkman, C. J., and Patel, P. M. A comparison of the electrophysiologic characteristics of EEG burst-suppression as produced by isoflurane, thiopental, etomidate, and propofol. *Journal of Neurosurgical Anesthesiology*, 8(1):40–46, 1996.

Amari, S.-I. Characteristics of randomly connected threshold-element networks and network systems. *Proceedings of the IEEE*, 59(1):35–47, 1971.

Amari, S.-I. Characteristics of random nets of analog neuron-like elements. *Systems, Man and Cybernetics, IEEE Transactions on*, (5):643–657, 1972.

Amari, S.-i. Dynamics of pattern formation in lateral-inhibition type neural fields. *Biological cybernetics*, 27(2):77–87, 1977.

Ames III, A. CNS energy metabolism as related to function. *Brain Research Reviews*, 34(1):42–68, 2000.

Andersen, P., Dingledine, R., Gjerstad, L., Langmoen, I., and Laursen, A. M. Two different responses of hippocampal pyramidal cells to application of gamma-amino butyric acid. *The Journal of Physiology*, 305(1):279–296, 1980.

Andersen, P., Morris, R., Amaral, D., Bliss, T., and O'Keefe, J. *The Hippocampus Book*. Oxford University Press, 2006.

Anderson, W. W., Anderson, W. W., Lewis, D. V., Scott Swartzwelder, H., and Wilson, W. A. Magnesium-free medium activates seizure-like events in the rat hippocampal slice. *Brain Research*, 398(1):215–219, 1986.

Astori, S., Wimmer, R. D., and Lüthi, A. Manipulating sleep spindles–expanding views on sleep, memory, and disease. *Trends in Neurosciences*, 36(12):738–748, 2013.

Ayoub, A., Mölle, M., Preissl, H., and Born, J. Grouping of meg gamma oscillations by eeg sleep spindles. *Neuroimage*, 59(2):1491–1500, 2012.

Barnett, W., O'Brien, G., and Cymbalyuk, G. Bistability of silence and seizure-like bursting. *Journal of Neuroscience Methods*, 220(2):179–189, 2013.

Bazhenov, M. and Timofeev, I. Thalamocortical oscillations. *Scholarpedia*, 1(6):1319, 2006.

Bazhenov, M., Timofeev, I., Steriade, M., and Sejnowski, T. J. Computational models of thalamocortical augmenting responses. *The Journal of neuroscience*, 18(16):6444–6465, 1998.

Bazhenov, M., Timofeev, I., Steriade, M., and Sejnowski, T. J. Model of thalamocortical slow-wave sleep oscillations and transitions to activated states. *The Journal of Neuroscience*, 22(19):8691–8704, 2002.

Bojak, I. and Liley, D. Modeling the effects of anesthesia on the electroencephalogram. *Physical Review E*, 71(4):041902, 2005.

Bonjean, M., Baker, T., Lemieux, M., Timofeev, I., Sejnowski, T., and Bazhenov, M. Corticothalamic feedback controls sleep spindle duration in vivo. *The Journal of Neuroscience*, 31(25):9124–9134, 2011.

Borisyuk, R. M. and Kirillov, A. B. Bifurcation analysis of a neural network model. *Biological Cybernetics*, 66(4):319–325, 1992.

Braitenberg, V. and Schüz, A. *Anatomy of the Cortex: Statistics and Geometry (Studies of Brain Function)*. Springer, February 1991.

Breakspear, M., Roberts, J., Terry, J. R., Rodrigues, S., Mahant, N., and Robinson, P. A unifying explanation of primary generalized seizures through nonlinear brain modeling and bifurcation analysis. *Cerebral Cortex*, 16(9):1296–1313, 2006.

Buzsaki, G., Lai-Wo S., L., and Vanderwolf, C. H. Cellular bases of hippocampal EEG in the behaving rat. *Brain Research Reviews*, 6(2):139–171, October 1983.

Carpenter, S. R., Cole, J. J., Pace, M. L., Batt, R., Brock, W., Cline, T., Coloso, J., Hodgson, J. R., Kitchell, J. F., and Seekell, D. A. Early warnings of regime shifts: a whole-ecosystem experiment. *Science*, 332(6033):1079–1082, 2011.

Chatfield, C. *The Analysis of Time Series: An Introduction*. CRC press, 2013.

Chaturvedi, S., Gardiner, C., Matheson, I., and Walls, D. Stochastic analysis of a chemical reaction with spatial and temporal structures. *Journal of Statistical Physics*, 17(6):469–489, 1977.

Chen, W., Schröder, M., D'Souza, R. M., Sornette, D., and Nagler, J. Microtransition cascades to percolation. *Physical Review Letters*, 112(15):155701, 2014.

Ching, S., Cimenser, A., Purdon, P. L., Brown, E. N., and Kopell, N. J. Thalamocortical model for a propofol-induced α-rhythm associated with loss of consciousness. *Proceedings of the National Academy of Sciences*, 107(52):22665–70, 2010.

Ching, S., Purdon, P. L., Vijayan, S., Kopell, N. J., and Brown, E. N. A neurophysiological-metabolic model for burst suppression. *Proceedings of the National Academy of Sciences*, 109(8):3095–3100, 2012.

Colquhoun, D. and Sakmann, B. Fluctuations in the microsecond time range of the current through single acetylcholine receptor ion channels. *Nature*, 294:464–466, 1981.

Cowan, J. A personal account of the development of the field theory of large-scale brain activity from 1945 onward. In *Neural Fields*, pages 47–96. Springer, 2014.

Cunningham, M. O., Pervouchine, D. D., Racca, C., Kopell, N. J., Davies, C. H., Jones, R. S. G., Traub, R. D., and Whittington, M. A. Neuronal metabolism governs cortical network response state. *Proceedings of the National Academy of Sciences*, 103(14):5597–5601, 2006.

da Silva, F. L., Hoeks, A., Smits, H., and Zetterberg, L. Model of brain rhythmic activity. *Kybernetik*, 15(1):27–37, 1974.

Silva, F. L.da , Rotterdam, A.van , Barts, P., Heusden, E.van , and Burr, W. Model of neuronal populations. the basic mechanism of rhythmicity. ma corner, df swaab (eds) progress in brain research. *Elsevier, Amsterdam*, 45:281–308, 1976.

Silva, F. L.da , Blanes, W., Kalitzin, S. N., Parra, J., Suffczynski, P., and Velis, D. N. Epilepsies as dynamical diseases of brain systems: basic models of the transition between normal and epileptic activity. *Epilepsia*, 44(s12):72–83, 2003.

da Silva, F. L. EEG: Origin and Measurement. In *EEG-fMRI*. Springer, 2010.

Dai, L., Korolev, K. S., and Gore, J. Slower recovery in space before collapse of connected populations. *Nature*, 496(7445):355–358, 2013.

Dakos, V., Scheffer, M., van Nes, E. H., Brovkin, V., Petoukhov, V., and Held, H. Slowing down as an early warning signal for abrupt climate change. *Proceedings of the National Academy of Sciences*, 105(38):14308–14312, 2008.

Deco, G., Jirsa, V. K., Robinson, P. A., Breakspear, M., and Friston, K. The dynamic brain: From spiking neurons to neural masses and cortical fields. *PLoS Computational Biology*, 4(8):e1000092, 2008.

Destexhe, A. and Babloyantz, A. A model of the inward current I_h and its possible role in thalamocortical oscillations. *Neuroreport*, 4(2):223, 1993.

Destexhe, A. and Bedard, C. Local field potential. *Scholarpedia*, 8(8):10713, 2013.

Destexhe, A., Contreras, D., and Steriade, M. Mechanisms underlying the synchronizing action of corticothalamic feedback through inhibition of thalamic relay cells. *Journal of neurophysiology*, 79(2):999–1016, 1998.

Eilers, P. H. A perfect smoother. *Analytical Chemistry*, 75(14):3631–3636, 2003.

Filatov, G., Krishnan, G. P., Rulkov, N. F., and Bazhenov, M. Dynamics of epileptiform activity in mouse hippocampal slices. *Journal of Biological Physics*, 37(3):347–360, 2011.

Fisher, R. S., Boas, W. v. E., Blume, W., Elger, C., Genton, P., Lee, P., and Engel, J. Epileptic seizures and epilepsy: definitions proposed by the International League Against Epilepsy (ILAE) and the International Bureau for Epilepsy (IBE). *Epilepsia*, 46(4):470–472, 2005.

FitzHugh, R. *Mathematical Models of Excitation and Propagation in Nerve*. Biological Engineering. New York: McGraw-Hill, 1966.

Freeman, S., Sharp, J. C., and Harrington, M. *Biological Science*. Pearson Prentice Hall, 2005.

Freeman, W. J. *Mass Action in the Nervous System*. Academic Press, 1975.

Freestone, D. R., Kuhlmann, L., Grayden, D. B., Burkitt, A. N., Lai, A., Nelson, T. S., Vogrin, S., Murphy, M., D'Souza, W., Badawy, R., Nesic, D., and Cook, M. J. Electrical probing of cortical excitability in patients with epilepsy. *Epilepsy Behav*, 22 Suppl 1:S110–8, Dec 2011.

Friedman, E. B., Sun, Y., Moore, J. T., Hung, H.-T., Meng, Q. C., Perera, P., Joiner, W. J., Thomas, S. A., Eckenhoff, R. G., and Sehgal, A. A conserved behavioral state barrier impedes transitions between anesthetic-induced unconsciousness and wakefulness: evidence for neural inertia. *PLoS ONE*, 5(7):e11903, 2010.

Garcia, P. S., Kolesky, S. E., and Jenkins, A. General anesthetic actions on $GABA_A$ receptors. *Current Neuropharmacology*, 8(1):2, 2010.

Gardiner, C. *Handbook of Stochastic Methods: for Physics, Chemistry and the Natural Sciences*, volume 13 of *Series in Synergetics*. Berlin: Springer, 2004.

Golubitsky, M., Schaeffer, D. G., and Stewart, I. *Singularities and Groups in Bifurcation Theory*. Springer New York, 1988.

Granger, R. H. and Hearn, R. A. Models of thalamocortical system. *Scholarpedia*, 2(11):1796, 2007.

Held, H. and Kleinen, T. Detection of climate system bifurcations by degenerate fingerprinting. *Geophysical Research Letters*, 31(23), 2004.

Hlinka, J. and Coombes, S. Using computational models to relate structural and functional brain connectivity. *European Journal of Neuroscience*, 36(2):2137–2145, 2012.

Hodgkin, A. L. and Huxley, A. F. A quantitative description of membrane current and its application to conduction and excitation in nerve. *The Journal of Physiology*, 117(4):500, 1952.

Hughes, J. R. Extreme stereotypy in the burst suppression pattern. *Clinical Electroencephalography*, 17(4):162–168, 1986.

Izhikevich, E. M. and Edelman, G. M. Large-scale model of mammalian thalamocortical systems. *Proceedings of the National Academy of Sciences*, 105(9):3593–3598, 2008.

Izhikevich, E. Simple model of spiking neurons. *IEEE Transactions on Neural Networks*, 14(6):1569–1572, 2003.

Izhikevich, E. *Dynamical Systems in Neuroscience: The Geometry of Excitability and Bursting*. MIT press, 2007.

Jacobson, G. M., Voss, L. J., Melin, S. M., Mason, J. P., Cursons, R. T., Steyn-Ross, D. A., Steyn-Ross, M. L., and Sleigh, J. W. Connexin36 knockout mice display increased sensitivity to pentylenetetrazol-induced seizure-like behaviors. *Brain Research*, 1360:198–204, 2010.

Jansen, B. H. and Rit, V. G. Electroencephalogram and visual evoked potential generation in a mathematical model of coupled cortical columns. *Biological cybernetics*, 73(4):357–366, 1995.

Jansen, B. H., Zouridakis, G., and Brandt, M. E. A neurophysiologically-based mathematical model of flash visual evoked potentials. *Biological cybernetics*, 68(3):275–283, 1993.

Janz, G. J. and Ives, D. J. G. Silver, silver chloride electrodes. *Annals of the New York Academy of Sciences*, 148(1):210–221, 1968.

Jirsa, V. K., Stacey, W. C., Quilichini, P. P., Ivanov, A. I., and Bernard, C. On the nature of seizure dynamics. *Brain*, 137(8):2210–2230, 2014.

Jiruska, P., Csicsvari, J., Powell, A. D., Fox, J. E., Chang, W.-C., Vreugdenhil, M., Li, X., Palus, M., Bujan, A. F., Dearden, R. W., and others, . High-frequency network activity, global increase in neuronal activity, and synchrony expansion precede epileptic seizures in vitro. *The Journal of Neuroscience*, 30(16):5690–5701, 2010.

Joeken, S. and Schwegler, H. Predicting spike train responses of neuron models. *CiteSeer*, 1995.

Kajikawa, Y. and Schroeder, C. E. How local is the local field potential? *Neuron*, 72(5):847–858, 2011.

Kalitzin, S., Parra, J., Velis, D. N., and Silva, F. H. L.da . Enhancement of phase clustering in the eeg/meg gamma frequency band anticipates transitions to paroxysmal epileptiform activity in epileptic patients with known visual sensitivity. *Biomedical Engineering, IEEE Transactions on*, 49(11):1279–1286, 2002.

Kalitzin, S., Velis, D., Suffczynski, P., Parra, J., and Silva, F. L.da . Electrical brain-stimulation paradigm for estimating the seizure onset site and the time to ictal transition in temporal lobe epilepsy. *Clinical neurophysiology*, 116(3):718–728, 2005.

Kandel, E. R., Schwartz, J. H., and Jessell, T. M. *Principles of Neural Science*. McGraw-Hill New York, 2000.

Kann, O., Papageorgiou, I. E., and Draguhn, A. Highly energized inhibitory interneurons are a central element for information processing in cortical networks. *Journal of Cerebral Blood Flow and Metabolism*, 2014.

Katznelson, R. Normal modes of the brain: neuroanatomical basis and a physiological theoretical model. *Electric fields of the brain: The neurophysics of EEG*, 1:401–442, 1981.

Kelso, J., Holt, K. G., Rubin, P., and Kugler, P. N. Patterns of human interlimb coordination emerge from the properties of non-linear, limit cycle oscillatory processes: theory and data. *Journal of motor behavior*, 13(4):226–261, 1981.

Kelso, J., Scholz, J., and Schöner, G. Nonequilibrium phase transitions in coordinated biological motion: critical fluctuations. *Physics Letters A*, 118(6):279–284, 1986.

Kelso, J. Phase transitions and critical behavior in human bimanual coordination. *American Journal of Physiology-Regulatory, Integrative and Comparative Physiology*, 246(6):R1000–R1004, 1984.

Knoblich, U. *Contributions of Distinct Interneuron Types to Neocortical Dynamics*. PhD thesis, Massachusetts Institute of Technology. Dept. of Brain and Cognitive Sciences., 2011.

Kopell, N., Borgers, C., Pervouchine, D., Malerba, P., and Tort, A. *Gamma and Theta Rhythms in Biophysical Models of Hippocampal Circuits*. Springer Series in Computational Neuroscience. Springer, 2010.

Koppert, M., Kalitzin, S., Velis, D., Da Silva, F. L., and Viergever, M. A. Reactive control of epileptiform discharges in realistic computational neuronal models with bistability. *International Journal of Neural Systems*, 23(01), 2013.

Korolev, K. S., Xavier, J. B., and Gore, J. Turning ecology and evolution against cancer. *Nature Reviews Cancer*, 14(5):371–380, 2014.

Kroeger, D. and Amzica, F. Hypersensitivity of the anesthesia-induced comatose brain. *The Journal of Neuroscience*, 27(39):10597–10607, 2007.

Latham, P., Richmond, B., Nelson, P., and Nirenberg, S. Intrinsic dynamics in neuronal networks. I. Theory. *Journal of Neurophysiology*, 83(2):808–827, 2000.

Ledoux, E. and Brunel, N. Dynamics of networks of excitatory and inhibitory neurons in response to time-dependent inputs. *Frontiers in Computational Neuroscience*, 5, 2011.

Lewis, L. D., Ching, S., Weiner, V. S., Peterfreund, R. A., Eskandar, E. N., Cash, S. S., Brown, E. N., and Purdon, P. L. Local cortical dynamics of burst suppression in the anaesthetized brain. *Brain*, 136(9):2727–2737, 2013.

Liley, D. T. and Walsh, M. The mesoscopic modeling of burst suppression during anesthesia. *Frontiers in Computational Neuroscience*, 7, 2013.

Liley, D. T., Cadusch, P. J., and Dafilis, M. P. A spatially continuous mean field theory of electrocortical activity. *Network: Computation in Neural Systems*, 13(1):67–113, 2002.

Livina, V. N. and Lenton, T. M. A modified method for detecting incipient bifurcations in a dynamical system. *Geophysical Research Letters*, 34(3), 2007.

Logothetis, N. K. The underpinnings of the BOLD functional magnetic resonance imaging signal. *The Journal of Neuroscience*, 23(10):3963–3971, 2003.

Löscher, W. Animal models of intractable epilepsy. *Progress in Neurobiology*, 53(2):239–258, 1997.

Lukatch, H. S. and MacIver, B. M. Synaptic mechanisms of thiopental-induced alterations in synchronized cortical activity. *Anesthesiology*, 84(6), 1996.

Lytton, W. W. and Sejnowski, T. J. Simulations of cortical pyramidal neurons synchronized by inhibitory interneurons. *Journal of Neurophysiology*, 66(3):1059–79, 1991.

Maruyama, Y., Kakimoto, Y., and Araki, O. Analysis of chaotic oscillations induced in two coupled Wilson–Cowan models. *Biological Cybernetics*, 108(3):355–363, 2014.

Mazzoni, A., Panzeri, S., Logothetis, N. K., and Brunel, N. Encoding of naturalistic stimuli by local field potential spectra in networks of excitatory and inhibitory neurons. *PLoS Computational Biology*, 4(12):e1000239, 2008.

McCarley, R. W. and Sinton, C. M. Neurobiology of sleep and wakefulness. *Scholarpedia*, 2(10):3313, 2007.

Meijer, H. G. E. and Coombes, S. Travelling waves in a neural field model with refractoriness. *Journal of Mathematical Biology*, 68:1249–1268, 2013.

Meiss, J. Dynamical systems. *Scholarpedia*, 2(2):1629, 2007.

Ng, B. S. W., Logothetis, N. K., and Kayser, C. EEG phase patterns reflect the selectivity of neural firing. *Cerebral Cortex*, 23(2):389–398, 2013.

Nowak, L. G. and Bullier, J. Spread of stimulating current in the cortical grey matter of rat visual cortex studied on a new in vitro slice preparation. *Journal of Neuroscience Methods*, 67(2):237–248, 1996.

Nunez, P. L. and Srinivasan, R. *Electric Fields of the Brain: The Neurophysics of EEG*. Oxford University Press, 2006.

Nunez, P. L. and Srinivasan, R. Neocortical dynamics due to axon propagation delays in cortico-cortical fibers: EEG traveling and standing waves with implications for top-down influences on local networks and white matter disease. *Brain Research*, 1542:138–166, 2014.

Nunez, P. L. Wavelike properties of the alpha rhythm. *IEEE Transactions on Biomedical Engineering*, 21(6):473–482, 1974.

Ohtahara, S., Ohtsuka, Y., Yamatogi, Y., and Oka, E. The early-infantile epileptic encephalopathy with suppression-burst: developmental aspects. *Brain and Development*, 9(4):371–376, 1987.

Pasillas-Lepine, W. Delay-induced oscillations in Wilson and Cowan's model: an analysis of the subthalamo-pallidal feedback loop in healthy and parkinsonian subjects. *Biological Cybernetics*, 107(3):289–308, 2013.

Petrucci, R. H., Harwood, W. S., Herring, F. G., and Perry, S. S. *General Chemistry: Principles and Modern Applications*. Macmillan New York, 1993.

Peyrache, A., Battaglia, F. P., and Destexhe, A. Inhibition recruitment in prefrontal cortex during sleep spindles and gating of hippocampal inputs. *Proceedings of the National Academy of Sciences*, 108(41):17207–17212, 2011.

Press, W., Teukolsky, S., Vetterling, W., and Flannery, B. *Numerical Recipes in Fortran 77: The Art of Scientific Computing*. Cambridge University Press, New York, 1992.

Qian, H., Zhang, X.-J., and Qian, M. Stochastic dynamics of electrical membrane with voltage-dependent ion channel fluctuations. *Europhysics Letters*, 106(1):10002, 2014.

Reichl, L. E. and Prigogine, I. *A Modern Course in Statistical Physics*. University of Texas press Austin, 1980.

Richter, A. and Dakos, V. Using economic information to anticipate transitions in social-ecological systems. Wageningen University Working Paper, 2014.

Rinzel, J. Excitation dynamics: insights from simplified membrane models. In *Federation Proceedings*, volume 44, pages 2944–2946, 1985.

Roberts, J. A., Iyer, K. K., Finnigan, S., Vanhatalo, S., and Breakspear, M. Scale-free bursting in human cortex following hypoxia at birth. *The Journal of Neuroscience*, 34(19):6557–6572, 2014.

Robinson, P. A., Rennie, C. J., and Wright, J. J. Propagation and stability of waves of electrical activity in the cerebral cortex. *Physical Review E*, 56(1):826, 1997.

Robinson, P., Rennie, C., Wright, J., and Bourke, P. Steady states and global dynamics of electrical activity in the cerebral cortex. *Physical Review E*, 58(3):3557, 1998.

Robinson, P., Rennie, C., and Rowe, D. Dynamics of large-scale brain activity in normal arousal states and epileptic seizures. *Physical Review E*, 65(4):041924, 2002.

Rodrigues, S., Terry, J. R., and Breakspear, M. On the genesis of spike-wave oscillations in a mean-field model of human thalamic and corticothalamic dynamics. *Physics Letters A*, 355(4):352–357, 2006.

Sakaguchi, H. Oscillatory and excitable behaviors in a population of model neurons. *Progress of Theoretical Physics*, 79(5):1061–1068, 1988.

Scheffer, M., Carpenter, S., Foley, J. A., Folke, C., and Walker, B. Catastrophic shifts in ecosystems. *Nature*, 413(6856):591–596, 2001.

Scheffer, M., Bascompte, J., Brock, W. A., Brovkin, V., Carpenter, S. R., Dakos, V., Held, H., van Nes, E. H., Rietkerk, M., and Sugihara, G. Early-warning signals for critical transitions. *Nature*, 461(7260):53–59, 2009.

Schiff, N. D., Nauvel, T., and Victor, J. D. Large-scale brain dynamics in disorders of consciousness. *Current Opinion in Neurobiology*, 25:7–14, 2014.

Shadlen, M. N. and Newsome, W. T. Noise, neural codes and cortical organization. *Current Opinion in Neurobiology*, 4(4):569–579, 1994.

Sherman, S. M. and Guillery, R. W. *Exploring the Thalamus and Its Role on Cortical Function*. Elsevier, 2001.

Sherman, S. M. Tonic and burst firing: dual modes of thalamocortical relay. *Trends in Neurosciences*, 24(2):122–126, 2001.

Sherman, S. M. Thalamus. *Scholarpedia*, 1(9):1583, 2006.

Shlizerman, E. and Holmes, P. Neural dynamics, bifurcations, and firing rates in a quadratic integrate-and-fire model with a recovery variable. I: Deterministic behavior. *Neural Computing*, 24(8):2078–2118, 2012.

Sleigh, J. W., Vizuete, J. A., Voss, L., Steyn-Ross, D. A., Steyn-Ross, M. L., Marcuccilli, C. J., and Hudetz, A. G. The electrocortical effects of enflurane: experiment and theory. *Anesthesia and Analgesia*, 109(4):1253, 2009.

Spruston, N. Pyramidal neuron. *Scholarpedia*, 4(5):6130, 2009.

Srinivasan, R., Thorpe, S., and Nunez, P. L. Top-down influences on local networks: basic theory with experimental implications. *Frontiers in Computational Neuroscience*, 7:29, 2013.

Stead, M., Bower, M., Brinkmann, B. H., Lee, K., Marsh, W. R., Meyer, F. B., Litt, B., Van Gompel, J., and Worrell, G. A. Microseizures and the spatiotemporal scales of human partial epilepsy. *Brain*, 133(9):2789–2797, 2010.

Steriade, M. and McCarley, R. W. *Brain Control of Wakefulness and Sleep*. Springer, Boston, MA, 2005.

Steriade, M. and Timofeev, I. Neuronal plasticity in thalamocortical networks during sleep and waking oscillations. *Neuron*, 37(4):563–576, 2003.

Steriade, M., Amzica, F., and Contreras, D. Cortical and thalamic cellular correlates of electroencephalographic burst-suppression. *Electroencephalography and Clinical Neurophysiology*, 90(1):1–16, 1994.

Steriade, M., Jones, E. G., and McCormick, D. A. *Thalamus*. Elsevier, 1997.

Steriade, M., Timofeev, I., and Grenier, F. Natural waking and sleep states: a view from inside neocortical neurons. *Journal of Neurophysiology*, 85(5):1969–1985, 2001.

Steriade, M. Sleep, epilepsy and thalamic reticular inhibitory neurons. *Trends in Neurosciences*, 28(6):317–324, 2005.

Steriade, M. Grouping of brain rhythms in corticothalamic systems. *Neuroscience*, 137(4):1087–1106, 2006.

Steyn-Ross, M. L., Steyn-Ross, D. A., Sleigh, J. W., and Liley, D. Theoretical electroencephalogram stationary spectrum for a white-noise-driven cortex: Evidence for a general anesthetic-induced phase transition. *Physical Review E*, 60(6):7299, 1999.

Steyn-Ross, M. L., Steyn-Ross, D. A., Sleigh, J. W., and Whiting, D. Theoretical predictions for spatial covariance of the electroencephalographic signal during the anesthetic-induced phase transition: Increased correlation length and emergence of spatial self-organization. *Physical Review E*, 68(2):021902, 2003.

Steyn-Ross, M. L., Steyn-Ross, D. A., and Sleigh, J. W. Modelling general anaesthesia as a first-order phase transition in the cortex. *Progress in Biophysics and Molecular Biology*, 85(2):369–385, 2004.

Steyn-Ross, D. A., Steyn-Ross, M. L., Wilson, M. T., and Sleigh, J. W. White-noise susceptibility and critical slowing in neurons near spiking threshold. *Physical Review E*, 74(5), 2006.

Steyn-Ross, M. L., Steyn-Ross, D. A., Wilson, M. T., and Sleigh, J. W. Modeling brain activation patterns for the default and cognitive states. *NeuroImage*, 45(2):298–311, 2009.

Steyn-Ross, M. L., Steyn-Ross, D. A., and Sleigh, J. W. Interacting Turing-Hopf instabilities drive symmetry-breaking transitions in a mean-field model of the cortex: A mechanism for the slow oscillation. *Physical Review X*, 3(2):021005, 2013.

Steyn-Ross, D. A., Steyn-Ross, M. L., and Sleigh, J. W. Equilibrium and nonequilibrium phase transitions in a continuum model of an anesthetized cortex. In *Neural Fields*. Springer, 2014.

Steyn-Ross, D. A. *Modelling the anaestheto-dynamic phase transition of the cerebral cortex*. PhD thesis, University of Waikato, 2002.

Strogatz, S. H. *Nonlinear Dynamics and Chaos: With Applications to Physics, Biology, Chemistry, and Engineering*. MA: Addison-Wesley Publishing Co, 1994.

Swartzwelder, H., Anderson, W., and Wilson, W. Mechanism of electrographic seizure generation in the hippocampal slice in Mg^{2+}-free medium: the role of $GABA_A$ inhibition. *Epilepsy Research*, 2(4):239 – 245, 1988.

Terry, J. R., Benjamin, O., and Richardson, M. P. Seizure generation: the role of nodes and networks. *Epilepsia*, 53(9):e166–e169, 2012.

Timofeev, I. and Bazhenov, M. Mechanisms and biological role of thalamocortical oscillations. In *Trends in Chronobiology Research*, pages 1–47. Nova Science Publishers New York, NY, 2005.

Traub, R. D. and Miles, R. *Neuronal Networks of the Hippocampus*. Cambridge University Press, 1991.

Traub, R. D., Contreras, D., Cunningham, M. O., Murray, H., LeBeau, F. E. N., Roopun, A., Bibbig, A., Wilent, W. B., Higley, M. J., and Whittington, M. A. Single-column thalamocortical network model exhibiting gamma oscillations, sleep spindles, and epileptogenic bursts. *Journal of Neurophysiology*, 93(4):2194–2232, 2005.

Tsau, Y., Guan, L., and Wu, J.-Y. Initiation of spontaneous epileptiform activity in the neocortical slice. *Journal of Neurophysiology*, 80(2):978–982, 1998.

Tuckwell, H. *Introduction to Theoretical Neurobiology*, volume 1. Cambridge University Press, 1988.

Ullah, G. and Schiff, S. J. Models of epilepsy. *Scholarpedia*, 4(7):1409, 2009.

Ursino, M. and Cara, G.-E. L. Travelling waves and EEG patterns during epileptic seizure: Analysis with an integrate-and-fire neural network. *Journal of Theoretical Biology*, 242(1):171–187, 2006.

van de Leemput, I. A., Wichers, M., Cramer, A. O., Borsboom, D., Tuerlinckx, F., Kuppens, P., van Nes, E. H., Viechtbauer, W., Giltay, E. J., and Aggen, S. H. Critical slowing down as early warning for the onset and termination of depression. *Proceedings of the National Academy of Sciences*, 111(1):87–92, 2014.

van Nes, E. H. and Scheffer, M. Slow recovery from perturbations as a generic indicator of a nearby catastrophic shift. *The American Naturalist*, 169(6):738–747, 2007.

Veraart, A. J., Faassen, E. J., Dakos, V., van Nes, E. H., Lürling, M., and Scheffer, M. Recovery rates reflect distance to a tipping point in a living system. *Nature*, 481(7381):357–359, 2012.

Voss, L. J., Jacobson, G., Sleigh, J. W., Steyn-Ross, D. A., and Steyn-Ross, M. L. Excitatory effects of gap junction blockers on cerebral cortex seizure-like activity in rats and mice. *Epilepsia*, 50(8):1971–1978, 2009.

Voss, L. J., Melin, S., Jacobson, G., and Sleigh, J. W. GABAergic compensation in connexin36 knock-out mice evident during low-magnesium seizure-like event activity. *Brain Research*, 1360:49–55, 2010.

Voss, L. J., Brock, M., Carlsson, C., Steyn-Ross, D. A., Steyn-Ross, M. L., and Sleigh, J. W. Investigating paradoxical hysteresis effects in the mouse neocortical slice model. *European Journal of Pharmacology*, 675(1):26–31, 2012.

Voss, L. J., van Kan, C., and Sleigh, J. W. Quantitative investigation into methods for evaluating neocortical slice viability. *BMC Neuroscience*, 14(1):137, 2013.

Voss, L. J., Gauffin, E., Ringqvist, A., and Sleigh, J. W. Investigation into the role of gap junction modulation of intracortical connectivity in mouse neocortical brain slices. *Brain Research*, 2014.

Wang, Y., Goodfellow, M., Taylor, P. N., and Baier, G. Phase space approach for modeling of epileptic dynamics. *Physical Review E*, 85(6):061918, 2012.

Warlaumont, A. S., Lee, H. C., Benayoun, M., Stevens, R. L., and Hereld, M. Systematic comparison of the behaviors produced by computational models of epileptic neocortex. *Journal of Clinical Neurophysiology*, 27(6):479–483, 2011.

White, J. A., Rubinstein, J. T., and Kay, A. R. Channel noise in neurons. *Trends in Neurosciences*, 23(3):131–137, 2000.

Whittingstall, K. and Logothetis, N. K. Frequency-band coupling in surface EEG reflects spiking activity in monkey visual cortex. *Neuron*, 64(2):281–289, 2009.

Whittington, M. A., Traub, R., and Jefferys, J. Erosion of inhibition contributes to the progression of low magnesium bursts in rat hippocampal slices. *The Journal of Physiology*, 486(Pt 3):723–734, 1995.

Whittington, M. A., Traub, R. D., Kopell, N., Ermentrout, B., and Buhl, E. H. Inhibition-based rhythms: experimental and mathematical observations on network dynamics. *International Journal of Psychophysiology*, 38(3):315–336, 2000.

Wiggins, S., Wiggins, S., and Golubitsky, M. *Introduction to Applied Nonlinear Dynamical Systems and Chaos*. Springer, 1990.

Wilson, H. R. and Cowan, J. D. Excitatory and inhibitory interactions in localized populations of model neurons. *Biophysical Journal*, 12(1):1–24, 1972.

Wilson, H. R. and Cowan, J. A mathematical theory of the functional dynamics of cortical and thalamic nervous tissue. *Kybernetik*, 13(2):55–80, 1973.

Wilson, M. T., Barry, M., Reynolds, J. N., Hutchison, E., and Steyn-Ross, D. A. Characteristics of temporal fluctuations in the hyperpolarized state of the cortical slow oscillation. *Physical Review E*, 77(6):061908, 2008.

Wilson, H. R. *Spikes, Decisions, and Actions: The Dynamical Foundations of Neuroscience*. Oxford University Press Oxford, 1999.

Wright, J. J. and Liley, D. T. Simulation of electrocortical waves. *Biological Cybernetics*, 72(4):347–356, 1995.

Wu, X.-X. and Shuai, J. Multistability in a neuron model with extracellular potassium dynamics. *Physical Review E*, 85(6):061911, 2012.

Young, G. B. The EEG in coma. *Journal of Clinical Neurophysiology*, 17(5):473–485, 2000.

Zhang, X. and Zahn, M. Electro-optic precursors of critical transitions in dielectric liquids. *Applied Physics Letters*, 104(5):052914, 2014.